Kinematics of neutral hydrogen in interacting galaxies in two groups from the MeerChoirs survey

Sriram Sankar

Thesis presented for the degree of
Master of Science in Astronomy
Department of Astronomy
University of Cape Town

South African Astronomical Observatory
Cape Town
South Africa

Supervisors: Moses Mogotsi & Matthew Bershady
June 2023

quiet revolutions in my mind
silent resolutions taken in kind
invaluable legacies left behind
picking up intricacies entwined
fruits of the forest from seeds once sown
lessons inherited from lives unknown
offshoots of thought grown with fraught
quiet revelations yearning to be sought
each forming a bridge between disparate worlds
I am but one, but the thoughts are more than just one's

Abstract

It is well known that galaxies shape and are shaped by their environments, but the relative contribution of environmental and internal galactic processes remains poorly understood. HI 21 cm is the ideal tracer to study the role of environments in shaping galaxies in the local universe as the extended distribution of neutral hydrogen makes it susceptible to a wide range of environmental effects that produce peculiar HI morphologies. Moreover, HI enables the study of how galaxies obtain and lose cold gas. The HI distribution of galaxies often exhibits warps, lopsidedness, and the presence of anomalous gas (AG) such as the Extraplanar Gas (EPG). In this era of resolved, sensitive HI observations, one exciting possibility is the identification of AG associated with galaxies experiencing a wide range of environmental effects. However, the task of separating AG and the disc is non-trivial due to fundamental limitations induced by instrumental effects (e.g., spatial and spectral resolution), projection effects, and systematic effects (e.g., assumptions, methods). In this work, we demonstrate a method we developed to separate anomalous gas from the disc based on physically motivated Gaussian decomposition and kinematic tagging. We perform a comprehensive analysis of the kinematics of the neutral gas in two nearby low-mass, gas-rich, late-type dominated, and relatively isolated groups from the MeerChoirs survey. The two groups, HIPASS J1250-20 and HIPASS J1403-06, both contain interacting pairs in the centre that showcase unique HI morphologies. In the groups, we investigate the impact of two ongoing co-rotating minor mergers, an intermediate-stage counter-rotating major merger, and an intermediate-stage co-rotating major merger. Additionally, we characterize several previously known and unknown dwarfs in the groups and the extended fields. We extract the kinematics of the extended, warped, and lopsided discs of the interacting galaxies using 3D tilted ring modelling. Employing techniques we developed, we detect and examine copious amounts of anomalous gas produced in the interactions in the form of leading gas, lagging gas, extended envelopes, tails, and bridges. By combining the kinematics, deep optical images, and ancillary evidence from the literature we relate the anomalous gas to star formation in the discs and the interactions. We detect gas exchange between the interacting pairs and enhanced star formation in the galaxies experiencing inflow. Notably, we report the farthest characterised EPG to date in HIPASS J1403:06 at a distance of 40 Mpc, which is also among the most massive EPG reservoirs ever studied. Furthermore, the 150 kpc long envelope of HIPASS J1250-20:S1 with a total HI mass of log $M_{HI} \sim 10.72$ $M_{\odot}$ is among the most HI-rich galaxies in the literature. We posit plausible formation scenarios for the extended envelope in HIPASS J1250-20:S1 and the $\sim$ 90 kpc long unidirectional transverse tails observed in HIPASS J1403-06. We suspect misaligned gas accretion from companions for the former and a combination of collisional and tidal origin for the latter. Such studies of gas kinematics and galaxy dynamics across different environments will deepen our understanding of the baryon cycle, galaxy interactions, and the impact of the environment on galaxy evolution.

Acknowledgements

Throughout the course of my degree, I have been most excited to write this section. For, I truly realise that I might not be here doing what I love, if not for the kindness and support offered by people around me. The nurturing environment at SAAO coupled with the invaluable interactions that I was lucky to have during my time on this project has fostered both my professional and personal development in profound ways. I express my utmost gratefulness to the numerous teachers who have played pivotal roles in shaping my journey thus far in astronomy.

I extend my deepest gratitude to my primary supervisor, Dr. Moses Mogotsi, for his wisdom, guidance, and mentorship, and also for allowing me to dream big while keeping me tethered to reality. I express my sincere thanks to my co-supervisor, Prof. Matthew Bershady, for his encouragement and support, and for always answering questions. I am extremely thankful for the generous financial support provided by the South African Astronomical Observatory (SAAO) through the SALT-SAAO Prize Scholarship 2021.

I express my sincere appreciation to: Dr. Julia Healy for patiently introducing me to SoFiA and CARACAL; Dr. Kelley Hess for her kind encouragement, the scientific discussions, and guidance with SoFiA Image Pipeline; Prof. Marc Verheijen for scientific discussions and guidance on image plane continuum subtraction; Prof. Filippo Fraternali for scientific discussions, advice on kinematic modelling, and his kind encouragement; Dr. Jonathan Stern for the lessons on cooling flows, scientific discussions, and his kind encouragement; Prof. Curtis Struck and Prof. Beverly Smith for the scientific discussion and advice on Arp 271; Prof. Se-Heon Oh and Mr. Minsu Kim for their kind assistance with BAYGAUD and technical discussions about Gaussian decomposition; Prof. Thijs van der Hulst for introducing me to iDaVIE and his encouragement. Prof. Erwin de Blok for hosting me at Kapteyn, for scientific discussions, and for his encouragement. Prof. D.J. Pisano for scientific discussions, advice on spatial smoothing, and his encouragement. Dr. Krishna Sekhar for discussions on primary beam correction and for kindly offering career advice. I express my indebtedness to Prof. Anand Narayanan for patiently introducing me to astronomy, for allowing me to audit classes, for giving me an opportunity to experience research first-hand, and for recommending me for this position. I extend my wholehearted thanks to Prof. Jane Charlton for her kind encouragement and for recommending me for this position. I am deeply grateful to the late Prof. Blair Savage for his kind encouragement and support. I extend my thanks to Prof. Srianand Raghunathan for his guidance and advice prior to this position.

I express my earnest appreciation to all the SAAO staff who have been integral in creating a nurturing environment at SAAO - Prof. Petri Väisänen for his unwavering support and encouragement; Prof. Patricia Whitelock and Mrs. Valencia Cloete for their kind attention to the well-being of students; Dr. Vanessa McBride, Dr. Retha Pretorius, and Dr. Zara Randriamanakoto for their support with student activities; Mr. Iriwaan Simon for sharing his knowledge and wit, and also for assisting with all IT-related matters. I express profound appreciation to Mrs. Roslyn Daniels and Mrs. Valencia Cloete for their invaluable assistance with all administrative matters at UCT and SAAO respectively. I thank Prof. Patrick Woudt, HoD of the astronomy department at UCT for his leadership. Mr. Ayanda Mgwatyu, Mrs. Sanchia Lewis, and Mr. Eugene Lakey for their attention to all site-related matters and for allowing me to assist with

waste management on site. Jenny (Mrs. Jennifer Harding) and Zainu (Mrs. Zainunesa) for their efforts to ensure the cleanliness of the student housing and offices. Dr. Daniel Cunnama, Mr. Pranesthan Govender, and Mr. Christian Hettlage for allowing me to assist with open nights and other outreach-related activities. Dr. Vanessa Mcbride, Mrs. Glenda Snowball and Mrs. Dalene Fischer for their kind support with financial matters. I express my thanks to the UCT/SAAO extragalactic discussion group for all the insightful discussions. I extend my gratitude to Dr. Kate Le Roux and the writing circle for tips and feedback on writing. I extend my genuine appreciation to Dr. Hannah Worters for the fun late-night corridor conversations, her kind encouragement, and for training me to perform service observations.

I extend my wholehearted thanks to Andrew Firth for the comradery, lessons, and discussions, and also for ensuring that I spent time away from work. I express my genuine appreciation to my office mates Andrew Firth, Mikhail de Villiers, Gideon de Beer, Kyle Solomons, and Lisa Seconna for making the Master's office a fun place. I am grateful to my group mates, Petro Janse van Rensburg and Mikhail for the fun and insightful discussions. I wholeheartedly thank all the people who made me feel at home in Cape Town, especially, Dr. Bynish Paul, Dr. Jessymol Thomas, Mrs. Narima Panday, Dr. Sabyasachi Chattopadhyay, Mrs. Sujata Majumdar, Dr. Sunil Chandra, and Dr. Siddharth Maharana. I thank Mrs. Minna Väisänen for her kind hospitality on numerous occasions. I thank Anke Van Dyk, Anja Genade, Christian van der Merwe, Nazir Makda, Antoine Mahoro, and the SAAO postgrads for their friendship and adventures throughout my studies. I thank Lennart Heino, Mokhine Motsoaledi, Venu Prayag, Kira Hanmer, Sumari Faul, and the UCT postgrads for always making me feel welcome at the astronomy department at UCT.

I express deep gratitude to my friends and family from back home who consistently root for me and celebrate my victories as their own. I extend my heartfelt gratitude to my parents for their selfless sacrifices, enabling me to conceive and pursue my cherished dream of studying the Universe. I express my utmost gratefulness to my sister, Swetha Sankar, and brother-in-law, Venkatesh Nandakumar for their unconditional encouragement and support. I express my special thanks to my best friend, Aiswarya Arun, for her unwavering companionship, relentless encouragement, and heartfelt support throughout my journey in astronomy.

I express my gratitude to the organizers and participants of the conferences and schools I had the privilege of attending during my studies: What Matters Around Galaxies (WMAG 2022) conference held in September 2022 in Aosta Valley, Italy; the European Radio Interferometry School (ERIS) held in September 2022 in JIVE/ASTRON, the Netherlands; and the Meeting of the SKA Pathfinder HI Survey Coordination Committee (PHISCC) held in March 2023 in Cape Town.

The MeerKAT telescope is operated by the South African Radio Astronomy Observatory, which is a facility of the National Research Foundation, an agency of the Department of Science and Innovation. We graciously acknowledge the use of the ilifu cloud computing facility - www.ilifu.ac.za, a partnership between the University of Cape Town, the University of the Western Cape, the University of Stellenbosch, Sol Plaatje University, the Cape Peninsula University of Technology and the South African Radio Astronomy Observatory. The ilifu facility is supported by contributions from the Inter-University Institute for Data Intensive Astronomy (IDIA - a partnership between

the University of Cape Town, the University of Pretoria and the University of the Western Cape), the Computational Biology division at UCT and the Data Intensive Research Initiative of South Africa (DIRISA).

This work made use of the CARTA (Cube Analysis and Rendering Tool for Astronomy) software (DOI 10.5281/zenodo.3377984 - https://cartavis.github.io; Comrie et al. 2021). This work also made use of CASA (McMullin et al. 2007; Team et al. 2022); SoFiA2 (Serra et al. 2015; Westmeier et al. 2021); SIP (Hess et al. 2022a); ^{3D}BAROLO (Di Teodoro & Fraternali 2015); GaussPy+ (Riener et al. 2019); BAYGAUD (Oh et al. 2018); PySpecKit (Ginsburg et al. 2022a); SlicerAstro (Punzo et al. 2017); AstroPy (Astropy Collaboration et al. 2022); Matplotlib (Hunter 2007); CMASHER (van der Velden 2020). We acknowledge the usage of the HyperLeda database (http://leda.univ-lyon1.fr). This research has made use of the NASA/IPAC Extragalactic Database (NED), which is funded by the National Aeronautics and Space Administration and operated by the California Institute of Technology. This research has made use of the SIMBAD database, operated at CDS, Strasbourg, France

Plagiarism Declaration

I, Sriram Sankar, am familiar with the meaning of plagiarism and declare that all the work in this document, other than that which is properly credited, is my own.

Contents

1 Introduction

Over a century of collective learning has unravelled an ever-growing picture of an unfathomably vast universe filled with billions of galaxies, each with millions of stars like the Sun, all governed by the same fundamental mathematics and physics that dictate our life here in our home we call Earth.

Galaxies in the universe can be classified based on various characteristics ranging from star-forming spirals to quenched ellipticals, from isolated to those residing in massive clusters with thousands of other galaxies. A disc galaxy is characterized by a coherently rotating structure of stars, dust, and gas embedded in a dark matter potential. Our Galaxy, the Milky Way is a disc galaxy that resides in a group with over 54 galaxies of diverse shapes and sizes. This study explores disc galaxies similar to the Milky Way, residing in low-mass groups, and experiencing varied levels of interactions with their nearby companions.

Figure 1.1: Image of the SALT telescope in Sutherland, South Africa, with the Arch of the Milky Way and its interacting companion dwarf, the Large Magellanic Cloud, in the background. Picture captured by an SAAO-commissioned photographer.

1.1 The Baryon Cycle

In a disc galaxy, in addition to the stars, there exist copious amounts of gas and dust from which new stars form. These along with radiation constitute the Interstellar Medium (ISM) which supplies the fuel for and retains signatures of star formation (see recent review by Saintonge & Catinella 2022). These discs are embedded in gaseous haloes known as the Circumgalactic Medium (CGM) that extend out to the virial radii defined by the dark matter potential (see figure 1.2). The CGM forms a reservoir that regulates the flow of gas originating from various internal processes within the galactic disc, as well as external environmental influences (see review by

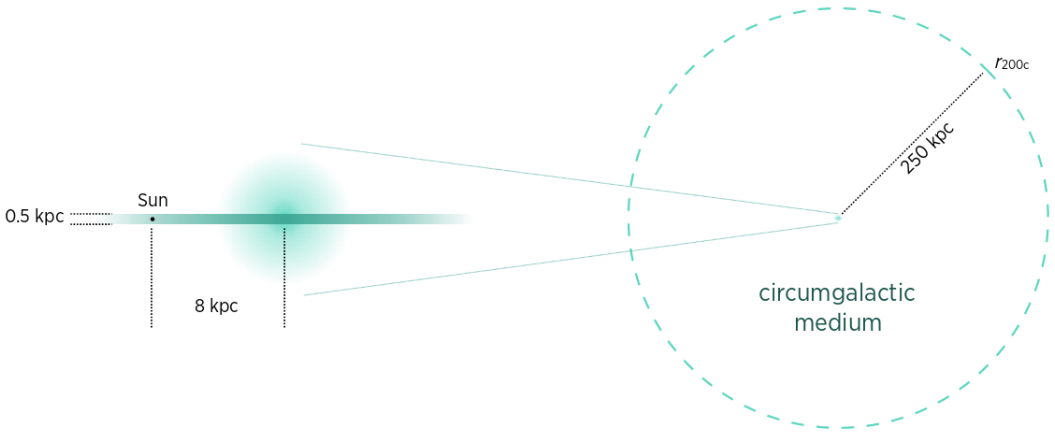

Figure 1.2: Schematic diagram taken from Donahue & Voit (2022) showing the extent of the Milky Way's CGM. The distances shown are approximate and are not to scale.

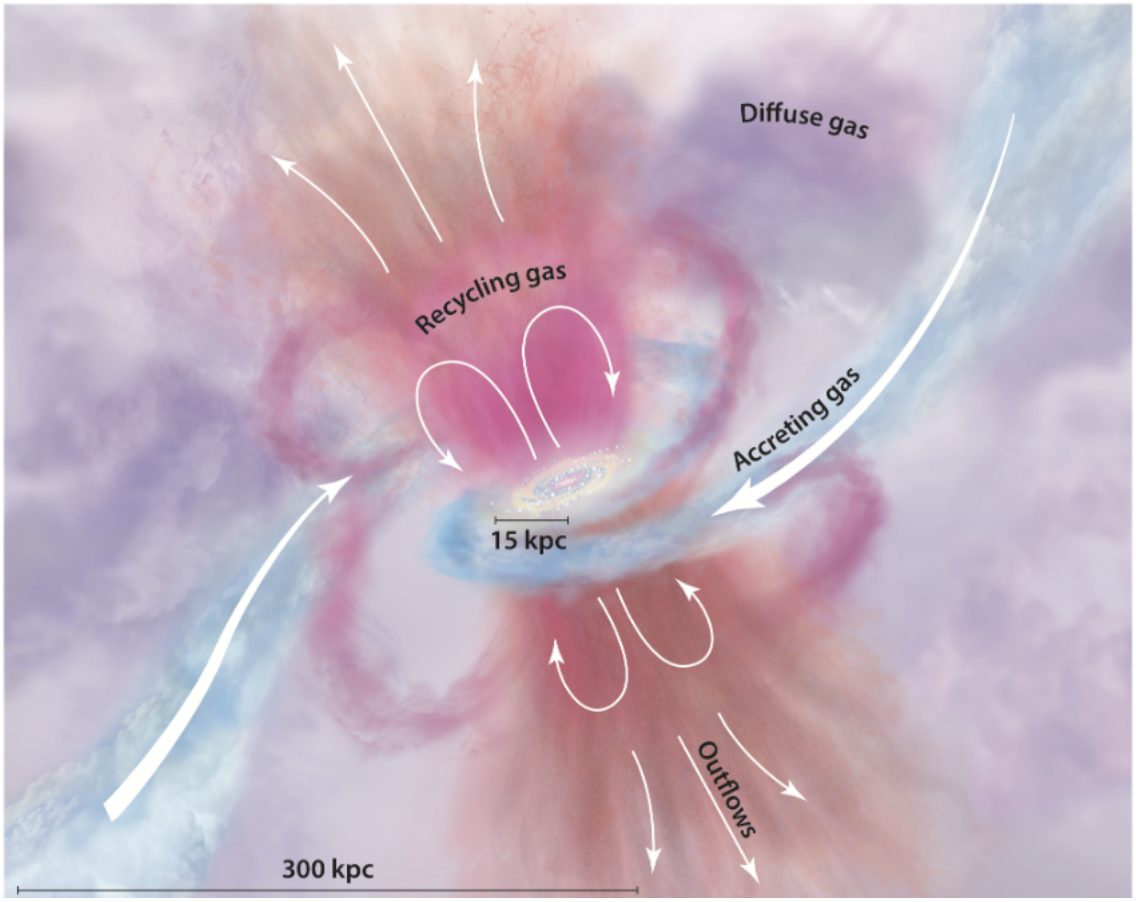

Figure 1.3: An artist's representation of the CGM taken from Tumlinson et al. (2017) showing some of the processes seen in the CGM. The blue filaments show accretion from the cosmic web. The pink structures show galactic fountains, orange shows outflows from the disc, and the diffuse gas is shown in varying tones of purple. We additionally note that the CGM is observed to be an in-homogeneous multi-phase medium which is difficult to represent. Furthermore, longitudinal accretion is still debated.

Tumlinson et al. 2017). The gaseous environments in groups and clusters are known as Intra-Group Medium (IGrM) and Intra-Cluster Medium (ICM) respectively. These environments serve

as both reservoirs and sinks; supplying gas to as well as removing gas from galaxies. The gas in the large-scale structure of the universe forming the cosmic web is known as the Inter-Galactic Medium (IGM) and galaxies are expected to accrete pristine gas from the IGM (see review by Meiksin 2009).

The baryon cycle can be thought of as the flow of multiphase gas within and between three broad settings (a) the ISM, (b) the CGM, and (c) the extended environment (IGrM, IGM, ICM). It encapsulates all the processes from the infall of gas into galactic potentials, collapse into and processing by stars, outflow due to stellar and/or AGN feedback, and even "mixing"[1] driven by cooling. Although the gas in these environments undergo various physical processes, it also initiates and facilitates some of them. These complex phenomena can be studied using multi-wavelength observations. For example, star formation in galaxies and the baryon cycle are interlinked phenomena that affect one another. Thus, both carry signatures of physical processes responsible for observables in the other. The gas in all these environments exists in multiple phases and is exposed to varied physical processes which enable us to explore a range of rich physics crucial for understanding key questions in galaxy evolution. Over the last several decades, numerous tracers and techniques have been employed to study the multi-phase baryon cycle and its role in galaxy evolution (see review by Péroux & Howk 2020).

1.2 Tracers of the Baryon Cycle

The non-luminous gas cycling through the galaxy and the environment can be studied using spectroscopy using ground-based and space-based telescopes. In this section, we provide a brief overview of the multi-wavelength spectroscopy of both absorption lines observed in the continuum of background sources and emission lines. While the latter is restricted to regions with high-column density gas typically observed close to the disc, the former is capable of tracing diffuse gas farther from the galaxy, but with the caveat that the spatial density of background sources is sparse. Due to the cosmic abundance of hydrogen, several tracers of hydrogen seen in both emission and absorption have been exploited to study the various baryon reservoirs.

1.2.1 Absorption line spectroscopy

The neutral hydrogen traced by the Lyman transitions (Ly$\alpha \sim 1215\,$Å) along with other metal lines (MgII, OIII, OVI, CIV, SiII, etc.) are employed extensively in absorption line spectroscopy of background sources (stars, QSOs, GRBs, lensed galaxies, galaxies, etc.) to study gas with column densities ranging from $\sim 10^{12}$ cm^{-2} to 10^{22} cm^{-2} in the IGM, IGrM, ICM, CGM, and ISM. The vantage point offered by absorption against a background source extends across a wide range of densities, redshifts, metals, ionizations, and environments. This has enabled the characterisation of the IGM through the detection of low column density, low-metallicity gas seen as Lyman α forests at high redshifts (see review by Meiksin 2009). However, the information is typically limited to a projected, pencil-beam view usually along a single line of sight through a reservoir. In certain fortuitous cases, multiple sightlines passing through the same foreground structure have been employed to study small-scale variations of the gas (e.g., Keeney et al. 2013;

[1] To some extent

Lehner et al. 2020; Sameer et al. 2022). Recent developments in Integral-Field Spectroscopy have unlocked the use of lensed galaxies, and galaxies as background sources (e.g., Péroux et al. 2018; Tejos et al. 2021). 3D spectroscopy (see the next sub-section) of extended background sources allows the estimation of the coherence scales of foreground gas by probing "contiguous sightlines". From these studies, we find a trend of decreasing absorption strength of hydrogen with increasing impact parameter in the CGM. The emerging picture of the CGM from high-resolution simulations and observational studies employing component-by-component multiphase modelling of metal line absorbing clouds is that of clumpy low-ionization gas ($\sim 10^4$ K) embedded in a diffuse hot corona ($\sim 10^6$ K) (e.g., McCourt et al. 2018; Zahedy et al. 2019; Hummels et al. 2019; Peeples et al. 2019; Martin et al. 2019; Rudie et al. 2019; Sankar et al. 2020). With current X-ray instrumentation, the direct detection of the hot coronae has been limited to the innermost few tens of kpc in massive galaxies with stellar mass greater than 10^{11} $M_\odot$ (Anderson & Bregman 2011; Anderson et al. 2013; Walker et al. 2015; Anderson et al. 2016). But indirect evidence from studying gas content and stripping in dwarf galaxies in the local group indicates the presence of hot gas even beyond the virial radii (Putman et al. 2021). The observations of highly ionized metal lines in absorption line systems also confirm the existence of a hot corona (see Tumlinson et al. (2017) for a review). Recently, the presence of hot ionized gas (WHIM, coronal gas, ICM, etc.) has been confirmed with dispersion measures from Fast Radio Bursts (FRBs; Ravi et al. 2019; Macquart et al. 2020). The ionized, hot, and diffuse gas in the IGrM and ICM is expected to be in thermal equilibrium with the dark matter potential, having temperatures in the range of $\sim 10^6 - 10^7$ K. But cold gas has also been discovered in the IGrM and ICM, and it is speculated to have originated from a variety of sources such as galaxy-galaxy interactions, accretion from the IGM, precipitation from the hot medium, etc. (e.g., Pradeep et al. 2020; Sameer et al. 2022; Nielsen et al. 2022). The ubiquitous presence of cool clouds in extreme environments has led to various theoretical explorations and debates in an attempt to explain the origin and fate of the cool gas far from the discs (e.g., McCourt et al. 2018; Gronke & Oh 2020; Afruni et al. 2021, 2022, Donahue & Voit 2022).

1.2.2 Emission line spectroscopy

Various emission lines are employed to study the different phases of the ISM and regions closely connected to galaxies (see reviews by Haffner et al. 2009 and Saintonge & Catinella 2022). Emission lines in an extragalactic source can be observed broadly in 4 ways: (i) Multi-object & slit-less spectroscopy, (ii) Long-slit spectroscopy, (iii) Narrow-band imaging, and (iv) 3D spectroscopy (FP/IFU/Radio/X-ray). Multi-object & slit-less spectroscopy are typically employed in large volumetric surveys of unresolved targets such as dwarfs and high-z galaxies. This approach collects all the emission from the source and produces an integrated 1D spectrum which is ideal for obtaining a redshift for the source. Long-slit spectroscopy produces a spectrum per resolution element within a slit placed on a source. Such a method produces 2D spectra which can be useful for deriving rotation curves, if the slit were placed parallel to the major axis. Narrow-band imaging involves using filters to capture all the emission flux in a specific region to produce a spatial map of the emission. Even though narrow-band imaging does not provide line-of-sight information, it can be useful for studying the spatial distribution of emissions, such as HII regions in a galaxy, through photometric methods. Finally, 3D spectroscopy captures the spatial and

spectral information in a spectral cube which contains spectra taken from multiple spatial points across the object. In optical and Infra-Red (IR) wavelengths, spectral cubes can be obtained using either Integral Field Spectroscopy (IFS) or Fabry-Perot Spectroscopy (FP). In sub-mm and radio, spectral cubes are produced by both single-dish telescopes and multi-dish interferometers (see chapter 2 for a detailed discussion). For completeness, X-ray observations produce spectral cubes by leveraging fast readout electronics to count photons. γ-ray interferometers that detect Cherenkov radiation also produce spectral cubes. The observed emission lines can provide information on various physical and chemical properties, such as kinematics, ionization parameter, stellar populations, and chemical abundances. However, the type of emission line and the properties of the gas traced are closely related, and some lines are more sensitive to certain properties than others. A review in terms of studying the disc kinematics using emission lines is presented in section 3.4. We note that in addition to the emission lines, the continuum at different wavelengths also provides valuable information on star formation. In the remainder of this section, we will briefly review certain interesting applications of emission lines for probing different phases of the ISM.

1. The Balmer lines (Hα $\sim$ 6563 Å; Hβ $\sim$ 4861 Å), Paschen lines (Paα $\sim$ 1875 nm), and even higher order Bracket lines (Brγ $\sim$ 2166 nm) observed in the optical and IR can be utilized to study the Warm Ionized Gas (WIM or Diffuse Ionized Gas; DIG; T $\sim 10^4$ K) of the ISM. Several other metal emission lines such as [MgII], [OII], [NII], etc. also probe the WIM (see review by Kewley et al. 2019). These metal lines along with Balmer lines are routinely employed to decode numerous physical and chemical properties of the ISM, such as, sources of ionization, metallicity gradients, stellar population histories, and extraplanar Diffuse Ionized Gas (eDIG) (e.g., Haffner et al. 2009; Dopita et al. 2014; Väisänen et al. 2017; Kewley et al. 2019).
2. The 21 cm hyperfine transition of hydrogen (explored in detail in the next subsection 1.2.3) is used to trace neutral gas in the ISM, which exists as both warm neutral gas (WNM, T $\sim$ 5000 K) and cold neutral gas (CNM, T $\sim$ 100 K). The HI spectral line is a powerful tool for studying the kinematics and morphologies of atomic gas reservoirs in galaxies. In addition to these applications, the HI mass function and numerous scaling relations based on HI are used as constraints in galaxy evolution models. For example, the Tully-Fisher relation can be employed to determine distances to and peculiar motions of galaxies (for a review of the cold ISM see Saintonge & Catinella 2022). The 21 cm line is also being adopted for intensity mapping at high-z. Furthermore, 21 cm absorption in the spectra of strong continuum sources is also utilized to study high column density HI along the line of sight. In addition to HI, the sodium doublet (Na D; 5890 Å) absorption line seen in the optical is also used as a tracer for studying the neutral ISM.
3. The warm molecular gas (T $\sim 50-300$ K) in the ISM can be traced by various vibrational states of H_2 seen in IR (e.g., Väisänen et al. 2017). In the millimetre regime, the J = 1 $\longrightarrow$ 0 rotational transition of carbon monoxide (CO) is used as a proxy for molecular hydrogen (H_2) in the ISM. H_2 along with dust form the key ingredients for star formation and numerous studies have explored the correlation between the molecular gas and SFR (see Saintonge & Catinella (2022) for a review). Molecular lines including several rotational and vibrational transitions of CO observed at mm wavelengths are employed to probe both

warm and cold (T $\sim 10 - 20$ K) molecular gas in the ISM.

1.2.3 21 cm hydrogen

The magnetic interaction between the electron and nuclear quantum mechanical spins cause the *1s* ground state of atomic hydrogen to split into two hyperfine levels: one with parallel spins and the other with anti-parallel spins. The higher energy state of the two hyperfine levels has parallel spins, and hydrogen atoms in the ISM get excited to this state via collisions with other particles. When an electron in a hydrogen atom flips its spin to anti-align with the nuclear spin, it emits a photon at a wavelength of 21.106 cm, giving rise to the observed 21 cm hydrogen emission (hereafter HI) in the radio regime. The transition probability is very small and thus only occurs approximately every 10 million years. But due to the cosmic abundance of hydrogen and its high column densities near galaxies, HI constitutes a remarkable tracer for studying several processes in the baryon cycle. It offers unique insights into the structure, kinematics, and dynamics of neutral gas, galaxies, and their environments.

Due to their limited spatial resolution of a few to tens of arcminutes at 21 cm, single-dish telescopes are unable to spatially resolve the HI gas in external galaxies, except for the nearest systems. Interferometers overcome this limitation of spatial resolution at the cost of reduced sensitivities compared to large single-dish telescopes (see chapter 2 for a detailed discussion). In preparation for the Square Kilometer Array (SKA), modern-day precursor facilities such as the MeerKAT (Jonas & MeerKAT Team 2016), ASKAP (Johnston et al. 2008; Hotan et al. 2021), uGMRT (Gupta et al. 2017), and Apertif/WSRT (Verheijen et al. 2008) have significantly advanced the state-of-the-art in their own ways. The precursor facilities have collectively initiated the era of wide-area, blind HI interferometric surveys, aimed at pushing HI detections to higher and higher redshifts through deeper observations and stacking. The Five-hundred-meter Aperture Spherical radio Telescope (FAST; Nan et al. 2011), which is the largest single-dish telescope to date, has recently become operational and has demonstrated its capability to supplement the resolved interferometric observations with observations of diffuse low column density HI. In the remainder of this section, we briefly review some results relevant to this thesis and for a detailed exploration we refer the reader to Saintonge & Catinella (2022).

The HI distribution in galaxies often extend to several times the radii of the optical disc and thus present the potential to directly study accretion, interactions, and other environmental effects (Sancisi et al. 2008). High sensitivity observations of lower column density HI make it possible to study the extended disc, disc-halo-interface, inner CGM, and even high-column-density cold gas in the extended environment. Resolved observations of the HI discs also provide rotation curves out to large radii and can probe the underlying dark matter (de Blok et al. 2008). However, the extended gas distribution is often far from a simple axisymmetric, thin, differentially rotating disc. The outer HI discs of spiral galaxies are known to be warped but the drivers and timescales of these warps have not yet been unambiguously established (Sancisi et al. 2008). Warps, lopsidedness in the morphology and kinematics of HI discs, as well as asymmetric global spectral profiles, in some cases, have been attributed to interactions. Furthermore, the neutral hydrogen is not confined to a thin disc, rather it extends to about $\sim 1 - 3$ kpc above the midplane. Unlike a thin disc, the vertical extent of this anomalous gas cannot be explained by

invoking vertical hydrostatic equilibrium, where the gravitational pull of the stellar disc and the Dark Matter (DM) is balanced by the gas turbulence. The HI disc is also expected to be flared in the outer parts, where the vertical force is lower. However, the flaring can only be directly observed in the Milky Way and highly inclined galaxies. In the literature, there are a plethora of examples of HI removed from galaxies and extending several kpc from the galaxy in the form of tails, plumes, bridges, envelopes, and cloud complexes (e.g., Hibbard et al. 2001; Sancisi et al. 2008; Taylor et al. 2016; Koribalski 2020). In many cases, the impressive HI features are understood to be results of gravitational interactions with companion galaxies. Hydrodynamical processes such as ram pressure stripping have also been studied extensively using HI in galaxies in clusters (e.g., "Jellyfish galaxies"; Vulcani et al. 2021; Hess et al. 2022b; Bacchini et al. 2023) and in groups (e.g., Rasmussen et al. 2008; Vulcani et al. 2018).

As discussed so far, the picture of the baryon cycle in disc galaxies is nuanced and multi-faceted. But as also discussed, so are our telescopes and methods. Going forward, the focus of our discussion will be limited to the application of HI to probe the baryon cycle. In the following section, we ask, what role do environments play in shaping galaxies?

1.3 Galaxy Environments

Environments play a crucial role in galaxy evolution as evidenced by the dependence of numerous galaxy properties on the environment. For instance, the morphology-density relation (Dressler 1980) highlights the observation of a higher fraction of morphologically elliptical galaxies in regions with higher density. But see Wijesinghe et al. (2012) and citations therein for the absence of a correlation between Star Formation Rate (SFR) and density for star-forming galaxies. Understanding the mechanisms responsible for driving the transition from gas-rich star-forming galaxies to gas-poor quenched galaxies with low star formation rates is a major challenge in galaxy evolution. The baryon cycle holds the signatures of the processes that give rise to the observed bimodality in the galaxy distribution (e.g., Strateva et al. 2001; Cortese et al. 2021; Brownson et al. 2022; Deb et al. 2023). To illustrate the effect of the environment on the baryon cycle, we consider two important questions below.

1.3.1 How do galaxies get cold gas?

Broadly, excluding interactions, galaxies at high redshift can accrete cold gas in two ways: cold mode and hot mode. In cold mode accretion, cool gas travels through the environment and CGM into the galaxy in the form of filaments often along with embedded satellite galaxies (Kereš et al. 2005; Kereš & Hernquist 2009). Whereas in hot mode, hot gas cools and gets accreted onto the disc either via instability-driven precipitation (Gronke & Oh 2020; Donahue & Voit 2022) or via radiative cooling (Stern et al. 2019, 2020; Hafen et al. 2022; Stern et al. 2023). While the former is expected to operate typically in lower-mass haloes at high redshift, the latter is expected to dominate in massive haloes (such as that of the Milky Way) at low redshift. Galaxies can also obtain cold gas necessary to fuel star formation through interactions with other galaxies. After accretion, feedback from ensuing episodes of star formation enriches the ISM and CGM. The gas then gets recycled between the disc and the CGM, forming the fuel for further episodes of star formation. At low-redshifts, most of the cold gas is obtained via galactic fountain flows,

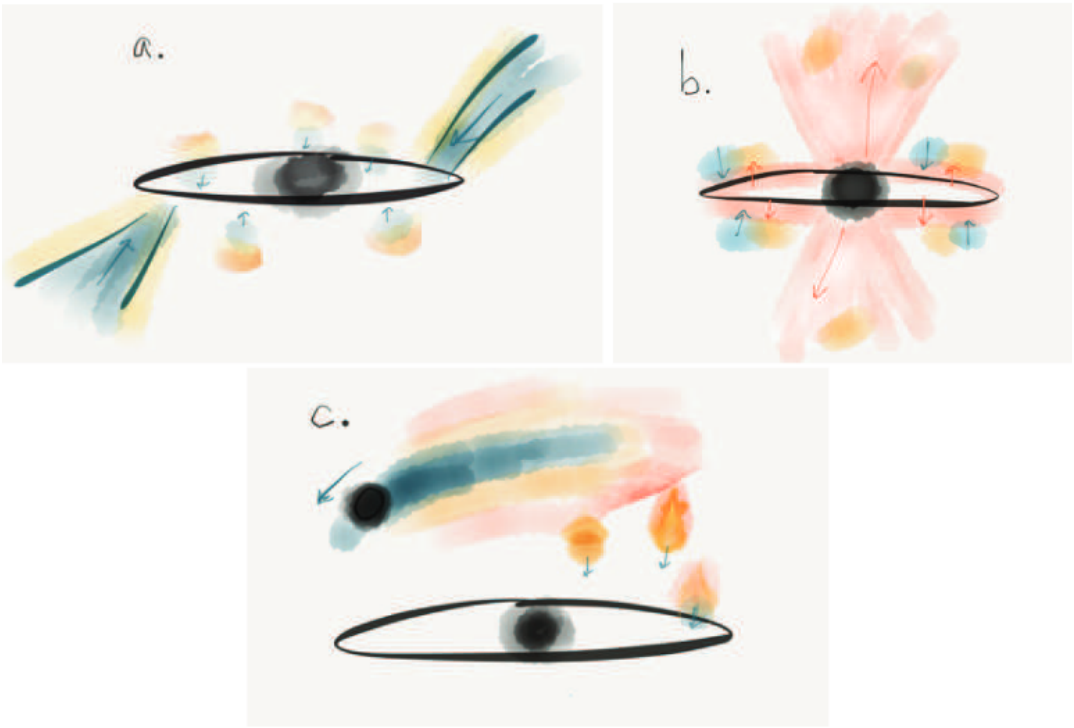

Figure 1.4: Image taken from Putman (2017) representing three expected sources of accretion. Red indicates hot gas and blue indicates cooler gas. (a) Cold-mode accretion from the IGM where filaments of cold gas surrounded by hotter gas are transported from the IGM to the disc. (b) Galactic fountain accretion, where feedback from the disc carries hot gas outside the disc which interacts with halo gas, cools and then falls back to the disc. (c) Gas from satellites passing through the halo medium of the host gets stripped and falls to the disc of the host.

the CGM, and the environment in which the galaxy resides (e.g., Putman 2017; Fraternali 2017; Afruni et al. 2021; Kamphuis et al. 2022; Zhang et al. 2023). In the local universe, different studies find contrasting results about the relative roles of different modes of accretion and sources of cold gas.

Afruni et al. (2021), using semi-analytical parametric models to describe the cold gas clouds detected in Lyα absorption in the CGM of 41 star-forming galaxies show that the observation cannot be reproduced using physically realistic galactic winds. Instead, they suggest accretion from the IGM as a likely origin for a significant part of the observed cold gas. A picture that is consistent with cold-mode accretion (e.g., Kereš et al. 2005) and the observation that a substantial part of cool gas absorbers around low-z galaxies have low metallicities (e.g., Wotta et al. 2019). However, HI observations attaining column density sensitivities of $\sim 10^{19}$ cm^{-2} fail to detect the filaments predicted by cold-mode accretion (e.g., Kamphuis et al. 2022). This could either imply the absence of direct cold-mode accretion filaments feeding galaxy discs or that the column density of such filaments is even lower. Afruni et al. (2021) disfavour the direct radiative cooling of the hot CGM, the so-called hot-mode accretion, due to the cooling times of the order of Hubble time implied by the low densities, especially in the outermost regions. However, thermal instabilities triggered by density perturbations in the hot corona driven by galactic feedback, can accelerate the cooling times and lead to a process known as condensation. While this is still debated (Binney et al. 2009), recent theoretical models and hydrodynamical simulations of massive elliptical galaxies predict that a fraction of cool gas in the CGM can originate from

condensation (see Donahue & Voit 2022 and citations therein). Afruni et al. (2021) also put forth satellite stripping as a potential source of cold gas in the CGM, citing evidence from recent simulations (e.g., Hafen et al. 2019) and observations of similar kinematics of dwarfs and cool ionized gas in M31 (Lehner et al. 2020). However, Teodoro & Fraternali (2014) find that minor mergers have an insignificant contribution to the overall gas accretion in nearby galaxies. In reality, it is probable that cold gas has contributions from most, if not all, of the aforementioned scenarios. Studying HI in galaxies with diverse properties residing in different environments, and experiencing various inflow processes at varied proportions, is crucial for understanding the relative contributions of the plausible gas accretion scenarios.

1.3.2 How do galaxies lose cold gas?

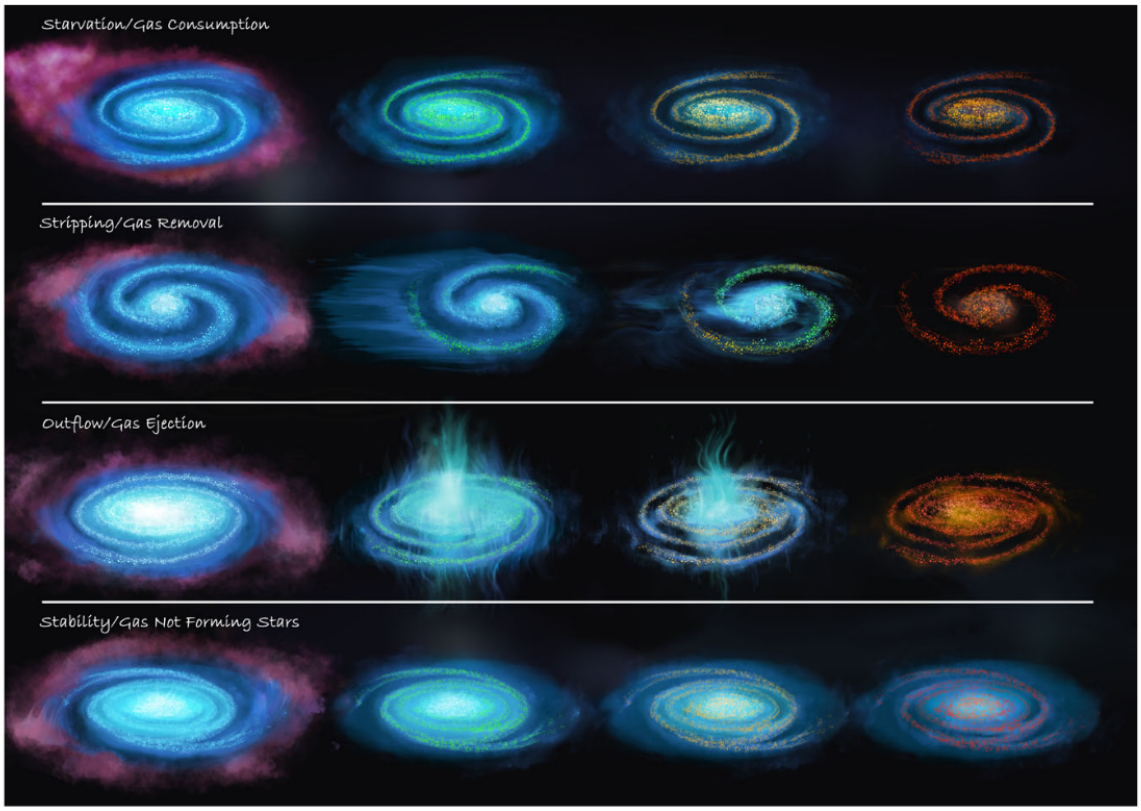

Figure 1.5: Illustration taken from Cortese et al. (2021) showing the impact of the various quenching pathways on the cold ISM (diffuse blue) and the stars (blue-young to red-old). The surrounding medium is represented in diffuse pink. For each of the four mechanisms shown, the evolution proceeds from left to right as indicated by the colour of the stellar disc (blue to red).

In the local universe, more than 50% galaxies reside in groups which are defined as gravitationally bound structures with at least two galaxies (Eke et al. 2005; Tempel et al. 2014). As a result, groups likely play a significant role in the evolution of galaxies, as also evidenced by pre-processing events observed in groups that are infalling towards clusters (e.g., Hess & Wilcots 2013; Kleiner et al. 2021). Identifying groups of galaxies is challenging compared to clusters, as demonstrated by Berlind et al. (2006) using mock catalogues. It is also hard to differentiate between gravitationally bound members and galaxies with similar projected line-of-sight velocities that are coincidentally superimposed. Within these limitations, groups can be classified based on various observed characteristics, such as loose or compact, gas-rich or gas-poor, small

or large, star-forming or fossilised, etc. In the hierarchical assembly model of the ΛCDM universe, these classes of groups can be placed in an evolutionary pathway that tends from young, gas-rich to old, fossil groups with stages from loose to compact (Verdes-Montenegro et al. 2001; Hess & Wilcots 2013; Zucker et al. 2016; Jones et al. 2019; Jones et al. 2023). Further assembly leads to the conglomeration of groups into clusters, the bright nodes of the cosmic web. As the groups evolve on this trajectory, the effects induced on the evolution of their members become significant. The groups are shaped by the evolution of the members and the evolution of the member galaxies are affected by the group properties.

Within the same group or cluster potential, the satellite and central galaxies can follow different evolutionary trajectories (e.g., Serra et al. 2012b; Hess & Wilcots 2013). The mechanisms for affecting the cold gas reservoirs of galaxies in various environments can be categorized into gravitational or hydrodynamical processes. If the dominant mechanism were gravitational in nature, cold gas from smaller galaxies will be tidally stripped and supplied to the larger galaxies. In groups, such gravitational encounters due to the proximity of companions, low-velocity dispersions, and the action of dynamical friction lead to frequent mergers. Whereas the high-velocity dispersion observed in massive groups and clusters leads to harassment (Moore et al. 1996). Hydrodynamical processes due to the hot ICM and IGrM also induce their imprint on the galaxies, whereby, the infalling satellites experience ram pressure stripping (Gunn & Gott 1972) and the centrals become increasingly HI deficient with time (Hess & Wilcots 2013). While some studies find increased SFR suppression events in group environments (e.g., Davies et al. 2015; Brown et al. 2017; Barsanti et al. 2018), several other studies report increased star formation in these environments due to gas supply from satellite galaxies, mergers, and accretion from the cosmic web (e.g., Wang et al. 2015; Janowiecki et al. 2017; Sotillo-Ramos et al. 2021). The dichotomy between gas-rich groups and gas-poor groups has been reasoned to be dependent on their stage in evolution with the former being in the early and the latter in late stages of assembly (e.g., Verdes-Montenegro et al. 2001; Hess & Wilcots 2013). Even though this seems plausible, the relative contribution of environmental (nurture) and intrinsic galactic processes (nature) still remain poorly understood (e.g., Di Matteo et al. 2005; Hopkins et al. 2006).

Over the last couple of decades, several works have contrasted galaxies residing in different environments with isolated galaxies to study the effect of environment on galaxy evolution. Such studies have identified several complex physical processes operating in group and cluster environments (See Cortese et al. (2021) for a review). Even though the diverse mechanisms can be categorized, in reality, a galaxy in its lifetime in an environment would have been affected by a combination of processes. For efficiently quenching the star formation in a galaxy, the internal and external mechanisms must be accompanied by the cessation of gas replenishment onto the disc. There are plenty of examples of HI removal in group environments and most of the evidence point towards gravitational interactions as the driving force (e.g., Verdes-Montenegro et al. 2001; Putman 2017; Leclercq et al. 2022). However, in recent years, hydrodynamical mechanisms have also been invoked to explain the HI structures observed in certain groups (e.g., Rasmussen et al. 2006; Sengupta et al. 2007; Rasmussen et al. 2008, 2012). The gravitational and hydrodynamical processes that operate in various environments to affect the cold gas can be further categorized as follows.

1. Internal feedback mechanisms such as stellar winds, feedback from Active Galactic Nuclei (AGN), Supernovae (SNe) feedback, etc. that either remove or heat the cold ISM (Hopkins et al. 2008). Based on the largest homogeneous kinematic sample drawn from MaNGA, Brownson et al. (2022), find that the average velocity dispersion ($\bar{\sigma}$) is the most crucial factor in distinguishing between star-forming and quenched populations among local high-mass galaxies. Their results favour preventive AGN feedback and disfavour SNe feedback and halo quenching.
2. Starvation or strangulation - lack of replenishment of the cold ISM leading to gas depletion by star formation (Larson et al. 1980) or the removal of only the hot gas component of the halo leading to the halting of accretion from the CGM.
3. Stripping the cold gas directly from the disc.
   (a) Hydrodynamical mechanisms - direct interaction between the ISM and the IGrM or ICM.
      i. Ram pressure stripping - removal of the ISM due to the pressure exerted by the ICM during the motion of a satellite through the host potential (Gunn & Gott 1972).
      ii. Viscous stripping - removal of the outer layer of the ISM due to the viscosity momentum transfer with the ICM (Nulsen 1982).
      iii. Thermal evaporation - the increase of temperature and subsequent evaporation of the cold ISM at the interface with the hot ICM (Cowie & Songaila 1977).
   (b) Gravitational mechanisms - removal of the ISM due to the gravitational pull acting on galaxies orbiting in groups and clusters (Binney & Tremaine 1987; Boselli & Gavazzi 2006). This can take the form of interactions, fly-bys, or collisions with companion galaxies. The combined effect of multiple high-speed interactions over time scales longer than typical crossing times is termed harassment (Moore et al. 1996) and is often seen in massive groups and clusters.
4. Stability of cold gas against fragmentation and star formation - all the processes listed above relate to the availability of cold gas to initiate star formation. Star formation could also be halted by affecting the second step of the star formation cycle by keeping the gas stable against collapse (Blitz & Rosolowsky 2006; Leroy et al. 2008; Bigiel et al. 2008). This phenomenon is seen in the outer regions of star-forming discs (Bigiel et al. 2010), low surface brightness galaxies (Wyder et al. 2009), early-type galaxies with significant HI reservoirs (Oosterloo et al. 2007b; Serra et al. 2012b), and HI-excess systems (Geréb et al. 2016, 2018)

So far, we have established that the cold gas reservoirs in and around galaxies likely have a combination of both internal and external origins. We also reasoned that environments, depending on their size enact varying levels of influence on their constituents. The environmental effects experienced by the galaxies depend on their position within the host potential. Furthermore, the gas in galaxies experience a combination of gravitational, hydrodynamical, and internal regulatory processes. Going forward, we restrict our discussion to low-intermediate mass group environments and focus our discussion on gravitational and internal processes of gas regulation. In the next subsection, we explore the role of gravitational encounters in shaping galaxies.

1.3.3 What role do galactic encounters play?

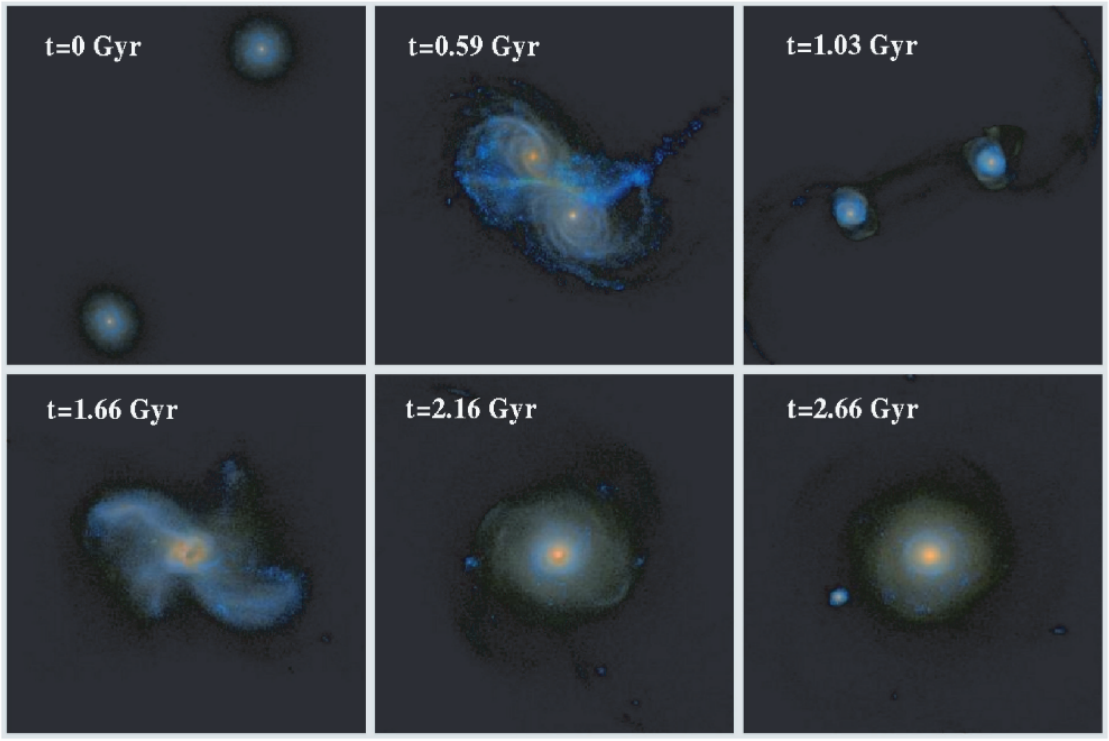

Figure 1.6: Image taken from Lotz et al. (2008), showing SDSS composite images (u-r-z) with dust extinction for a Sbc prograde-prograde simulation viewed face-on. Times since the start of the simulation are given in the upper left-hand corner of each image. Shown are the pre-merger galaxies, first pass, maximal separation, merger of the nuclei, post-merger at 0.5 Gyr, and the remnant at 1 Gyr after the merger. The initial galaxies and maximal separation have a field of view of 200 kpc, while the other images have a field of view of 100 kpc. Star-forming regions appear blue, while dust-enshrouded star-forming nuclei appear red.

Encounters between galaxies can take the form of collisions, fly-bys, or mergers, with varying geometries between galaxies of different shapes and sizes. The outcomes of these interactions are determined by the encounter geometry and the relative masses of the galaxies involved. Both factors can depend on the properties of the environment. Thus, the nature of interactions and the relative importance of gravitational encounters versus other evolutionary processes are heavily influenced by the environment. For instance, as previously mentioned, in clusters, multiple high-speed interactions can remove gas from galaxies via a process known as harassment (Moore et al. 1996). On the other hand, in groups, where the radial velocity dispersion between close companions is typically similar to their rotation velocities, the process of dynamical friction can cause encounters to evolve into mergers (see review by Struck 2006 and citations therein). Dynamical friction occurs when colliding galaxies interact gravitationally with the particles in the ISM of their companion galaxy, causing the galaxies to lose their orbital angular momentum (Chandrasekhar 1943; Tremaine & Weinberg 1984).

In its nascence, before galaxy collisional origins theory was established as a dominant mechanism for driving galaxy evolution, seminal numerical models by Toomre & Toomre (1972) showed that many of the peculiar bridges and tails catalogued in Arp (1966) can be explained as tidal relics resulting from various configurations of close encounters. Toomre (1977) through the addition of dynamical friction to their earlier models predicted that major mergers can dramatically alter

disc morphologies and transform them into elliptical galaxies. The paradigm-shifting detection of dark matter haloes later established a higher cross section for collisions due to galaxies being bound together in larger, invisible entities (see section 3.4 for a discussion on evidence of dark matter from rotation curve studies). Today within ΛCDM cosmology, we almost take for granted that galaxy interactions play an inevitable role in shaping galaxies. But if the Toomre (1977) prediction were accurate, how do we reconcile the observed abundance of disc galaxies?

One key indicator of the impact of a merger event is the mass ratio between the merging galaxies. From both observational and theoretical grounds, it is well established that minor mergers (mass ratio $\lesssim 1:10$) are ubiquitous (e.g., Walker et al. 1996; Stewart et al. 2008; Bournaud et al. 2007). Moreover, a large fraction of the $\sim L_*$ galaxy population is expected to have experienced a major merger (mass ratio $\lesssim 1:3$) since $z \sim 2-3$ (e.g., Hopkins et al. 2009; Lotz et al. 2008). Both major and minor mergers can drive transformations in the merger remnant (e.g., Walker et al. 1996; Hopkins et al. 2009). Since Toomre's early prediction which neglected crucial elements such as gas dynamics, it has now been established on stronger grounds that major mergers between spiral galaxies can indeed create remnants with properties consistent with that of local elliptical galaxies (e.g., Barnes & Hernquist 1996; Mihos & Hernquist 1996; Di Matteo et al. 2005). Hopkins et al. (2009) presented an analytical model to demonstrate that the complex behaviour of the gas and stellar components in mergers can be elegantly explained in terms of gravitational physics, regardless of gas physics, star formation, and feedback. They reason that gas in mergers primarily lose angular momentum to internal torques from induced asymmetries in the stellar disc. They find that hydrodynamic torques and the effect of direct torquing of the companion galaxy are second-order effects. Once the gas is stripped of its angular momentum, it likely falls to the centre of the galaxy to fuel starbursts and/or the AGN. Feedback alters the conditions of the merger by retaining higher gas content going into the merger and by blowing out the gas to larger radii (vertical and radial). For sufficiently high gas fractions and for gas at large radii, torquing by the smaller stellar disc proceeds inefficiently causing the gas to retain its angular momentum and survive largely intact. Thus explaining that gas-rich mergers can yield disc-dominated remnants.

The discovery of luminous far-infrared galaxies (LIRGs) and ultraluminous far-infrared galaxies (ULIRGs) provided an opportunity to test the predictions of numerical simulations, as they cover a range of merger stages from isolated systems to post-merger remnants. Several studies have sought to classify the observed melange of U/LIRGS into merger stages to study the impact of the mergers (e.g., Veilleux et al. 2002; Yuan et al. 2010; Rupke et al. 2010; Kewley et al. 2010; Rich et al. 2012). Early self-consistent merger models that included stellar disc, gas disc, and dark matter halo components, showed that during mergers, hot halo components merged more quickly than disc components (Barnes 1992). The models also demonstrated that in ULIRGs, a portion of the gas carried a significant amount of angular momentum into tidal tails, while the remaining gas fell into a small region at the centre of the remnant, fueling intense bursts of star formation. Such gravitational encounters can cause tidal distortions that result in distinct morphologies in HI. This is in part due to the fact that gas discs are usually more extended than stellar discs and are therefore more sensitive to perturbations. Hibbard et al. (2001) compiled the 'HI Rogues catalogue' to complement the Arp catalogue (Arp 1966) with 'peculiar' HI morphologies. Over twenty years later, we understand that such HI morphologies are not mere oddities but are

common phenomena connected to the evolution of galaxies.

Several theoretical and observational studies report strong anti-correlations between SFR enhancements and galaxy separations (e.g., Barton et al. 2000; Sol Alonso et al. 2006). At large separations, the less massive companion typically experiences tidal stripping (e.g., Putman 2017), while the more massive companion can experience an inflow of cold gas (e.g., Blumenthal & Barnes 2018). The influx of cold gas in the massive companion can lead to dilution of the metallicity gradient (Rupke et al. 2010; Kewley et al. 2010; Rich et al. 2012), nuclear star formation (Barnes & Hernquist 1996; Hopkins et al. 2009), and activation of the AGN (Mihos & Hernquist 1996; Barnes & Hernquist 1996). Imprints of galaxy encounters on the stellar disc can also take the form of enhanced star formation, nuclear bars, the formation of tidal dwarf galaxies in tidal tails, stellar streams, stellar bridges, extended spiral arms, and star-forming knots (e.g., Toomre & Toomre 1972; Barnes & Hernquist 1992; Struck 2006; De Mello et al. 2012). In the off-centre regions, starbursts could potentially be driven by tidal compression (e.g., Renaud et al. (2022) and citations therein) and direct shocks of the gas reservoirs (e.g., Jog & Solomon 1992; Barnes 2004). Conversely, Correa et al. (2018) discuss the role of hydrodynamic effects induced by overlapping hot haloes in suppressing SFR by cutting off the flow of cold gas. Observations of cold gas, such as HI, are essential for understanding the effects of gravitational encounters on galaxies as the effects induced on the stellar discs are innately linked to the cold gas.

In this section, we have established that mergers between galaxies of various masses are common and crucial for shaping galaxies. HI offers the potential to study unique morphologies and gas flows generated by the interactions, as well as the evolutionary trajectory of mergers, the impact of the environment, and the dynamics of the interactions.

1.4 Anomalous Gas

Studies of the HI disc of Milky Way as well as external edge-on and intermediately inclined galaxies have revealed the existence of gas at anomalous velocities, i.e. velocities that cannot be explained by rotation alone. Anomalous gas in the Milky Way has been observed in the form of high-velocity and intermediate-velocity clouds (HVCs and IVCs; Wakker & van Woerden 1997), in HI emission as well as absorption signatures on the spectra of background QSOs and halo stars (see Putman et al. 2012 for a review). The anomalous gas likely originates from a combination of numerous physical processes such as galaxy-galaxy interactions, galactic fountains, accretion from the environment, and cooling flows. One distinct type of anomalous gas is the lagging layer above the thin disc known as the Extra-planar gas (EPG) layer or thick HI disc or HI halo. EPG with radial motions, vertical motions, and lagging rotation has been observed directly in several edge-on galaxies (e.g., Matthews & Wood 2003; Zschaechner et al. 2011; Kamphuis et al. 2013) and kinematically in the Milky Way (e.g., Marasco & Fraternali 2011; Marasco et al. 2012), certain nearly face-on (e.g., Boomsma et al. 2008), and intermediately inclined galaxies (e.g., Marasco et al. 2019). The ionized counterpart ($T \sim 10^4$ K) of the EPG is termed the extraplanar Diffuse Ionized Gas (eDIG) and is found to have similar kinematic properties and vertical extent (1-2 kpc) as the EPG (e.g., Rossa & Dettmar 2003; Fraternali et al. 2004; Haffner et al. 2009; Boettcher et al. 2016, 2017b, 2019). The origin of both the EPG and the eDIG are still debated. A leading candidate model to explain the source of the neutral EPG is the

Galactic Fountain model (see below). One possible explanation for the origin of eDIG is the photoionization of the neutral EPG by the Lyman continuum photons from the disc and the extragalactic background radiation (See review by Haffner et al. 2009). The broad definition we adopt for anomalous gas represents gas that is not confined to the thin disc of a galaxy, this includes EPG, features resulting from interactions such as tails, filaments, and bridges, and also gas with non-circular motions (inflows and outflows along both vertical and radial directions).

1.4.1 Extraplanar gas

It has become clear that disc galaxies tend to store a fraction of their HI in a thicker disc extending to several kpc from the midplane. In the literature, the EPG, also known as the Disc-Halo-Interface (DHI) in the Milky Way, refers to neutral HI gas that resides above the stellar disc as a thick disc with a lagging rotation. Both terms have also been used to describe the eDIG layer. In this work, we adopt the term EPG to represent the thicker disc of HI which lags behind the HI disc (i.e. stellar disc, ISM, or thin disc). The kinematics of the EPG can be described by four parameters: gas velocity dispersion (σ), radial velocity (v_R), vertical velocity (v_z), and the vertical gradient in the rotational velocity (dv_ϕ/dz) (Schaap et al. 2000; Fraternali et al. 2005; Oosterloo et al. 2007a; Hess et al. 2009; Marasco et al. 2019).

Large vertical motions observed in several galaxies viewed close to face-on provide some of the initial evidence for the flow of HI gas between the disc and the halo (Dickey et al. 1990; Kamphuis & Sancisi 1993; Kamphuis 1993). The first detection of an EPG layer with distinct kinematics was reported for the edge-on galaxy NGC 891 (Swaters et al. 1997). Since then, observations of EPG in edge-on galaxies have played an integral part in aiding our understanding of the vertical extent of the thick HI layer (e.g., Fraternali et al. 2005; Zschaechner et al. 2011, 2012; Kamphuis et al. 2013; Zschaechner et al. 2015). Over the last couple of decades, we have gathered sufficient evidence of a lagging EPG and eDIG in galaxies with a range of inclinations. *But why is inclination an important consideration?* At high inclinations ($i \gtrsim 80$), projection effects become prominent and the spectral profiles are broadened because of the line-of-sight passing through a large number of projected velocities. This causes difficulties in extracting accurate measurements of rotation and dispersion velocities. At low inclinations ($i \lesssim 40$), the projected line-of-sight component of the rotation velocity decreases in amplitude as the rotation happens in a 2D disc whereas the 3D random motions which contribute to the dispersion remain the same. Both these extremes increase the uncertainty in the deprojected rotational velocity (de Blok et al. 2008). However, a close-to-face-on view allows us to study the motion of gas both perpendicular and parallel to the plane. It facilitates the detection of gas at anomalous velocities and the establishment of potential connections to structures in the disc such as HI holes and star-forming regions (Boomsma et al. 2008). In gaseous discs observed at intermediate inclinations, the measured line-of-sight velocities are a combination of rotational, radial, and vertical motions, and the column densities are integrated along an oblique line-of-sight. While this certainly adds complexities to the interpretation, it offers information on both the density structure and the kinematics along the vertical axis of the HI disc (Schaap et al. 2000).

The moderately inclined galaxy NGC 2403 ($i = 62\,^\circ$) and the edge-on galaxy NGC 891 are two of the most well-studied galaxies in terms of their anomalous gas. The EPG of NGC 2403

was first studied in depth by Schaap et al. (2000) and then later by Fraternali et al. (2002). The most recent characterisation of NGC 2403 by Marasco et al. (2019) has revealed an EPG fraction of 22% with a vertical lagging rotation gradient, $dv_\phi/dz \sim -12$ km s^{-1} kpc^{-1}, a global radial inflow velocity of -20 km s^{-1} and a vertical velocity of -10 km s^{-1}. The presence of an anomalous filamentary structure in NGC 2403 is discussed in Fraternali et al. (2001); de Blok et al. (2014) and Veronese et al. (2023). Marasco et al. (2019) carried out the first systematic investigation of EPG in a sample of intermediately inclined galaxies and concluded that EPG is ubiquitous in late-type galaxies. They report typical values for EPG mass fraction of $\sim 10-15$% of the total HI mass and scale height, h_z, in the range of 1-3 kpc. They also find an average vertical rotational lag dv_ϕ/dz of about ~ -10 km s^{-1} kpc^{-1} and global radial and vertical inflow motions with typical velocities of $\sim 20-30$ km s^{-1}. In the low-inclination galaxy NGC 6946 ($i = 38°$), several works have linked vertically extended gas structures to HI holes and star formation activity in the disc (Kamphuis & Sancisi 1993; Kamphuis 1993; Boomsma et al. 2008). Boomsma et al. (2008) report widespread, clumpy, high-velocity HI above the bright optical disc of NGC 6946 with a rotational component that lags behind the disc. They also associate the lopsided HI distribution and peculiar kinematics in the south-west to recent tidal encounters.

The Disc-Halo-Interface of the Milky Way which manifests observationally as HVCs and IVCs has been studied extensively using both HI and absorption line spectroscopy. Marasco & Fraternali (2011) applied a parametric thick disc model to the Galactic EPG observed in HI from the LAB survey (Kalberla et al. 2005). While their model successfully reproduced the IVCs and diffuse HI component, it failed to explain the HVCs which likely have a different origin. However, they found a global lagging rotation and an inflow velocity of $30-40$ km s^{-1}. Marasco et al. (2012) modelled the same data with a dynamic model of the Galactic Fountain and found an exceptional agreement. Their model on top of explaining the global inflow motion and the lagging rotation predicted a global accretion rate that is similar to the Galactic SFR. They employ both internal (stellar feedback) and external mechanisms (triggered condensation and accretion of halo gas) to explain the origin of the HVCs and IVCs. Marasco et al. (2022) attempted to model the kinematics of HVCs and IVCs observed in the absorption spectra of 55 Galactic halo stars. They found agreement in a double-component model consisting of a combination of inflows and outflows and characterised by both rotational and vertical motions.

1.4.2 Formation of the EPG

The mechanisms considered for explaining the formation of the EPG in disc galaxies can be broadly categorized into three. Below, we briefly summarize the different models and we point the reader to Fraternali (2017) for a deeper discussion.

1. Equilibrium models - these models attempt to enforce some form of hydrostatic or hydrodynamic equilibrium to the EPG.
   (a) The hydrodynamical baroclinic model investigated by Barnabè et al. (2006) predicts temperatures greater than 10^5 K which is incompatible with the neutral gas phase.
   (b) A dynamic model of the EPG with a large vertical anisotropic dispersion was examined by Marinacci et al. (2010) and they found good agreement with the data. However, such an anisotropy requires a driving force akin to galactic fountains.

2. Accretion or inflow models - these models explore the possibility that the EPG is produced exclusively by inflows. Fraternali (2017) makes the argument that such pure inflow models would give unrealistic infall rates.
   (a) Extragalactic accretion from the IGM, known as cold-mode accretion (Kereš et al. 2005; Afruni et al. 2021).
   (b) Thermal instabilities leading to condensation and inflows (Donahue & Voit 2022). However, there exists an argument of classical field instabilities in the corona being counteracted by buoyancy and suppressed by thermal conduction (Binney et al. 2009; Joung et al. 2012).
   (c) Cooling flows induced by the radiative cooling of the CGM (Stern et al. 2019, 2020; Hafen et al. 2022; Stern et al. 2023).
3. Galactic fountain models - the EPG is built up by gas that is pushed out of the disc plane due to stellar feedback but pulled back by gravity (Shapiro & Field 1976; Bregman 1980)
   (a) In its simplest form it is known as the ballistic model (Collins et al. 2002; Fraternali & Binney 2006) wherein fountain particles are treated as test particles shot up nearly vertically from the disc ignoring the hydrodynamical nature of the fountain gas. However, the prediction of the rotation of the EPG was found to be systematically higher than the observed rotation (Fraternali & Binney 2006). This is because of angular momentum conservation enforced throughout the trajectory of the ballistic particle.
   (b) Including hydrodynamical effects to the ballistic model introduces fountain-driven condensation and accretion of the coronal gas. Condensation and mass transfer take place in the turbulent mixing layer at the disc-corona interface. The transfer of momentum from the cold to the hot phase and the mass transfer from the hot to the cold phase has the effect of lowering the rotational velocity of the cold EPG. Thermal conduction then smooths the temperature gradients at the interface and makes the cloud more compact and resilient to destruction via Kelvin-Helmholtz instabilities. The combined effect of drag (ram pressure) and accretion (driven by condensation) (i) limits the maximum scale height attainable for the EPG, (ii) induces larger velocity lags, and (iii) imparts a negative radial velocity (move inward).

Evidence for the galactic fountain model comes from two main observations: the similarity between EPG and disc kinematics, and the fact that EPG in most cases is observed to be concentrated above the stellar disc (e.g., Oosterloo et al. 2007a; Boomsma et al. 2008). In this model, a large fraction ($\sim$ 80%) of the EPG is expected to originate from the stellar disc as galactic fountains and the remaining fraction consists of metal-poor coronal gas that condensed at the disc-corona interface. However, the presence of filaments and irregular gaseous structures in the halo of the Milky Way and nearby galaxies imply an extragalactic origin for at least a part of the EPG (e.g., Sancisi et al.

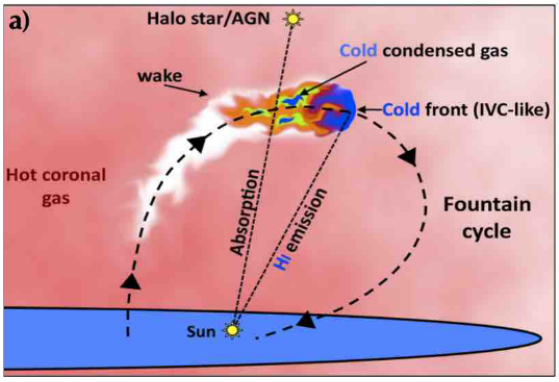

Figure 1.7: A sketch of a fountain cloud ejected from the disc and interacting with the hot corona. Image taken from Fraternali (2017).

2008; Kamphuis et al. 2013; Taylor et al. 2016; Koribalski 2020). These could be a result of minor mergers, tidal interactions, or accretion from the IGM. While the fountain model is the leading candidate to support the existence of EPGs, the relative contributions of the various phenomena as well as certain underlying physics still need to be better understood. In the galactic fountain flow framework, the gas leaves the disc in a hot phase and rains back to the disc after cooling. However, it is still unclear whether the observed eDIG is warm gas entrained in a hot outflow or if it is gas that condenses from the hot phase (Boettcher et al. 2017a). Li et al. (2023) presented the first full application of the current fountain accretion framework which has evolved considerably since Fraternali & Binney (2006, 2008) attempted to reproduce the properties of the EPG in NGC 891 and NGC 2403. While Li et al. (2023) successfully reproduce most of the EPG properties of NGC 2403, the model of the corona they adopt assumes an arbitrary value for the rotation of the gas in the ϕ direction. Aside from the uncertainty in the rotation, assuming bulk motion along only one of the cylindrical coordinates in a spherical potential (i.e. hydrostatic assumption along the radial (r) and θ directions) can also be questioned (Hafen et al. 2022; Stern et al. 2023).

Most of the EPG studies have focused on explaining the properties of the EPG without contributions from interactions. We instead attempt to study the effect of the interactions on the EPG and the disc. Resolved and sensitive observations of galaxies at a range of inclination angles experiencing varying levels of interactions and with different merger configurations will enable us to systematically investigate the roles played by the different processes in shaping the EPG.

1.4.3 Anomalous gas in groups

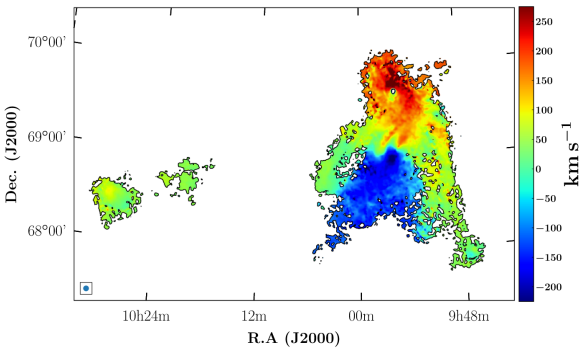

Figure 1.8: HI velocity field of M81 group observed using DRAO. Image taken from Sorgho et al. (2019).

As alluded to in section 1.3, gravitational and hydrodynamical interactions play a vital role in the supply and removal of cold gas from member galaxies. Gravitational interactions have the potential to enhance accretion by inducing cooling as well as prevent accretion by shock heating the cold gas (Ellison et al. 2013; Blumenthal & Barnes 2018; Wang et al. 2023). There have been some systematic studies of different samples of groups and galaxies to characterize anomalous gas seen as tidal tails, bridges, HVCs, etc. (e.g., Pisano et al. 2007; Taylor et al. 2016; Marasco et al. 2019; Koribalski 2020; Kamphuis et al. 2022; Jones et al. 2023; Eibensteiner et al. 2023). Within the Milky Way, the Magellanic streams and the HVCs/IVCs have been extensively studied through the lenses of tidal interactions (e.g., Putman et al. 2012; Pardy et al. 2018; Lucchini et al. 2021). Aside from the Magellanic clouds, the nearest well-characterised extragalactic tidal interaction is likely the M81 triplet (See figure 1.8) (de Blok et al. 2018; Sorgho et al. 2019, 2020). Interactions leading to anomalous HI features have been reported in various types of groups (e.g., Koopmann et al. 2008; Zhu et al. 2021; Wang et al. 2023; Liu et al. 2023). In particular, HI properties of compact groups have received considerable attention (Verdes-Montenegro et al. 2001; Borthakur et al. 2010; Serra et al.

2013; Hess et al. 2017; Jones et al. 2019; Jones et al. 2023. In contrast, Pisano et al. (2004, 2007) report an absence of HI detected compact HVCs in a sample of local group analogues (loose groups) and posit that most of the baryons could likely be in other phases. On the other side of the bimodal galaxy distribution, unsettled HI morphologies detected in Early Type Galaxies (ETGs) have been linked to past or ongoing mergers by Oosterloo et al. (2007b) and Serra et al. (2012b). Massive HI structures like the Leo ring have also raised some perplexing questions about the nature of multi-body interactions in dense group environments (e.g., Stierwalt et al. 2009; Michel-Dansac et al. 2010; Taylor et al. 2016; Sameer et al. 2022). Another key question about the long-lasting HI features seen in various environments is about their survival in the ambient medium. Due to their separation from the disc, the tails should be prone to thermal evaporation, ionization, shattering, and dispersal due to instabilities (Cowie & Songaila 1977; McCourt et al. 2018). Conversely, Gronke & Oh (2020) argue that in certain regimes cold gas not only survives but entrains many times its original mass through mixing layers with the hot medium.

The group evolutionary scenario put forth by Verdes-Montenegro et al. (2001) provides a plausible explanation for the observed range of HI fraction in compact groups. With galaxies in groups evolving from HI rich to galaxies with increasingly disturbed HI morphologies and subsequently to HI deficient galaxies. HI holds the key to understanding how galaxies obtain and lose cold gas in different environments. As discussed in section 1.3, a combination of gravitational and hydrodynamical processes likely operate within an environment to give rise to the observed HI morphologies (Cortese et al. 2021; Wang et al. 2023; Lin et al. 2023). With modern-day telescopes, we are beginning to see signatures of faint yet ubiquitous cold gas. Deep targeted observational programs such as the MHONGOOSE survey (de Blok et al. 2016) will deliver evidence (or lack thereof) for the accretion processes operating in isolated galaxies. Combining resolved interferometric observations with sensitive single-dish telescopes such as FAST further allows for the detection of even fainter emission (e.g., Zhu et al. 2021; Wang et al. 2023; Liu et al. 2023). Observational campaigns of galaxies across various environments can offer clues about the interplay between environment and galaxies for both fueling and quenching star formation (e.g., Hess et al. 2022b; Jones et al. 2023; Serra et al. 2023). In most cases, it has been difficult to isolate environmental mechanisms and diagnose the direct impact of a particular mechanism on the HI properties of individual galaxies. This has largely been due to technical limitations, underlying environmental effects, and the existence of multiple interactions (like in compact groups). In this work, we focus on late-type dominated low-mass groups showcasing varying levels of interactions to study in isolation, the gravitational mechanisms shaping the HI reservoirs in the groups.

1.5 MeerChoirs: Effects of Group Environment on Galaxy Evolution

MeerChoirs (PI: Moses Mogotsi, 2020 & 2022 Open Time Proposal) is a deep HI study of the Choirs group sample (Sweet et al. 2013) from the SINGG catalogue (Survey for Ionization in Neutral Gas Galaxies; Meurer et al. 2006). SINGG is an optical R-band and Hα imaging follow-up of HIPASS (HI Parkes All-Sky Survey; Meyer et al. 2004). The Choir sample consists of

15 nearby (< 151 Mpc) late-type dominated, gas-rich groups that are thought to be in their early stages of assembly. About half of the sample contains two large spirals and a number of dwarf galaxies making them morphological analogues of the local group that are in a more compact stage. The selection criteria for the Choir groups employed in Sweet et al. (2013) was constrained to a $\sim 15'$ field because of the field of view considerations of SINGG and the primary beam of the Parkes telescope. The unparalleled combination of high sensitivity, resolution, and large field of view offered by MeerKAT makes it the optimal instrument to study HI in nearby galaxies and groups out to large radii, down to low column densities, and with a high resolution (de Blok et al. 2016). MeerChoirs will be the deepest and highest resolution HI study of the Choir groups to date. The aim of the survey is to study the impact of the environment on galaxy evolution by mapping the cold gas in the group, investigating anomalous gas resulting from galaxy interactions, cataloguing the HI properties of known and unknown group members, and characterising the resolved HI-kinematics of the galaxies.

This study investigates the neutral hydrogen in two Choir groups, HIPASS SINGG J1403-06 (hereafter J1403-06) and HIPASS SINGG J1250-20 (hereafter J1250-20), where the largest members exhibit varying levels of interactions. The groups are understood to be isolated and the nearest filament of the cosmic web is at a distance greater than 4 Mpc (Džudžar et al. 2021). This allows us to focus on the effects solely induced by the group environment. Since hydrodynamic effects are expected to be sub-dominant in such low-mass groups, we can further isolate the gravitational effects that shape the cold gas in the environment. Both these groups showcasing tidal features can be categorized as phase 2 in the HI evolutionary sequence proposed by Verdes-Montenegro et al. (2001). The late-type-dominated Choir groups are more HI-rich than typical HCGs and are fated to result in gas-rich mergers. Studying interacting galaxies with different configurations and at different stages of the merger enables the exploration of the co-evolution of galaxies, the baryon cycle, and the group. We present a detailed look at the kinematics of the interacting galaxies in these groups and explore the impact of the group environment on the neutral gas properties of the galaxies.

1.5.1 Thesis objectives

The technical aspects of the thesis are mostly discussed in chapters 2 and 3, and the scientific explorations are documented in chapters 1, 5, and 4.

The technical objectives can be summarised as:

1. Image the pipeline calibrated visibilities and produce the best possible HI spectral cubes for the two groups.
2. Compare the resulting datacubes with existing observations.
3. Carry out a census of the HI in all the members of the groups and the extended fields covered by the primary beam.
4. Perform 3D tilted ring modelling on the biggest members in the groups and extract reliable kinematic and geometric properties.
5. Perform Gaussian decomposition and develop a method to separate the anomalous gas from the disc.

The scientific objectives can be summarised as:

1. What are the dominant mechanisms for cold gas accretion and removal in the galaxies in the groups? What are the impacts of the group environment on the member galaxies?
2. What gives rise to the anomalous gas (if any) in the galaxies and the groups? What can we learn from the distribution of the anomalous gas?
3. What are the properties of the EPG in the interacting galaxies? How does it differ from the EPG of isolated galaxies?
4. What can we infer about the interactions from the neutral gas kinematics? Do we detect gas exchange between the galaxies?

Throughout this work, we use the cosmological parameters from Planck Collaboration (2020): $H_0 = 67.7\ \mathrm{km\,s^{-1}\,Mpc^{-1}}$, $\Omega_m = 0.310$, and $\Omega_\Lambda = 0.69$.

2 | Observations and Data Reduction

2.1 Radio Interferometry 101

The low frequencies of radio signals imply low photon energies given by, $E = h\nu$. With relevance to this work, the radio window provides access to the extremely low-energy quantum level transition produced by the atomic hyperfine splitting of neutral hydrogen at $\nu \sim 1.420$ GHz ($\lambda \sim 21$ cm, see section 1.2.3). The low energies and long wavelengths make it difficult to employ conventional optical observational techniques to obtain photon counts and sub-arcsecond angular resolutions with reasonable-sized dishes. Two objects separated by angle θ can be resolved by a telescope of diameter D operating at a particular wavelength λ when the Rayleigh Criterion is satisfied.

$$\sin\theta \gtrsim 1.22\frac{\lambda}{D} \tag{2.1}$$

To get a $1''$ resolution at 21 cm, we would need an aperture of diameter ~ 52 km. To overcome this limitation, astronomers employ aperture-synthesis interferometers where several radio antennas are interlinked and an aperture is synthesized using Earth's rotation. Instead of counting the photons, the antenna response of the individual dishes to the target electromagnetic field is recorded and correlated across all available baselines. Interferometry offers several advantages such as accurate astrometry since it is based on measuring time delays between telescopes, unparalleled sensitivity owing to low quantum noise, and high angular resolution because of long baselines.

In this section, we provide a brief introduction to key concepts in interferometry. For detailed discussions of these concepts, we refer to: the CASA documentation[2], recordings of the 18th NRAO synthesis imaging school, 2022[3], CASA guides[4], and the learning resources referenced in the NRAO imaging school website. The source intensity distribution observed by an aperture-synthesis interferometer i.e. the antenna responses correlated across several baselines, is represented by a complex visibility function. The visibility, which is a two-point correlation function of the electromagnetic field, is the Fourier transform of the source intensity distribution. However, the observed electromagnetic field is corrupted by various effects induced by the atmosphere and the observational hardware. The set of equations representing the measured visibility values for a sky brightness distribution is referred to as the interferometer measurement equation. The measurement equation accounts for all the details of the locations and characteristics of individual antennas, effects of transmission through the atmosphere, the path of the incoming radiation, effects induced by the correlator, etc. Calibration is performed to correct for these effects and to arrive at corrected visibilities that resemble as closely as possible, the visibilities that would have been measured in a vacuum by a perfect interferometer. Observations are designed to alternate between science targets and strong astronomical point sources near the

[2] https://casadocs.readthedocs.io/
[3] https://tinyurl.com/5n8yy8jr
[4] https://casaguides.nrao.edu

science target at regular intervals to facilitate cross-calibration. Wherein, direction-independent calibration solutions are extracted from the calibration sources and then applied to the science observations. Another step of calibration known as self-calibration is also typically employed for high dynamic range continuum imaging, wherein a model of the sky brightness distribution is used to perform direction-dependent calibration.

Image reconstruction and deconvolution are processes that convert raw visibilities into an image of the sky brightness distribution by iteratively solving a set of linear equations.

$$V(u,v)S(u,v) \xrightarrow{\mathcal{F}} T^D(l,m) \tag{2.2}$$

In the equation, $V(u,v)$ represents the complex visibility function corrected for direction-independent effects, $S(u,v)$ represents the uv plane sampled at discrete points by the synthesized aperture, and $T^D(l,m)$ represents the dirty image, which is the true sky image as observed by the interferometer. Applying the convolution theorem gives:

$$T(l,m) * s(l,m) = T^D(l,m) \tag{2.3}$$

The dirty image in its simplest form is the true sky brightness $T(l,m)$, convolved with the Point Spread Function $s(l,m)$ (PSF or dirty beam). Where the PSF is the Fourier transform of the discretely sampled and weighted uv aperture. CASA performs image reconstruction in nested cycles: the major cycle implements transforms between the data (u,v) and image domains (l,m), and the minor cycles perform deconvolution in the image domain. Together, they implement an iterative weighted χ^2 minimization process that solves the measurement equation. Deconvolution in minor cycles is the process of iteratively building a model of the true sky by separating it from the PSF using an algorithm such as *CLEAN*. First, the locations and strengths of potential sources are identified by finding the peaks in the masked residual image. Then, a scaled PSF is subtracted from the residual image at the identified locations and the model of the sky brightness distribution is updated. This forms a step or an iteration in the minor cycle. The minor cycle is terminated when a stopping criteria, which is usually defined by the number of iterations or a threshold is reached. We set the number of iterations to a high value and specify a threshold as the stopping criteria.

The classical *CLEAN* algorithm assumes that the sky is comprised of point sources and therefore produces delta function models of the brightness distribution. However, this approach is often inadequate while dealing with extended sources. The Multi-Scale *CLEAN* algorithm (Cornwell 2008) on the other hand, assumes that the sky is composed of emission at different spatial scales and models the sky brightness distribution as a linear combination of inverted tapered paraboloids representing the flux components at different user-specified scale sizes. For continuum imaging, we employ a point source model, and for spectral cube imaging, we employ a multi-scale model. The *MS-CLEAN* deconvolution process is as follows:

1. The dirty image (residual) is convolved with each scale size to create a set of convolved images.

2. A matched-filtering technique is employed simultaneously on the convolved images to find the scale with the global peak. The position and flux of the dominant components and the scale size with the maximum total flux are recorded.

3. The set of components for each scale, convolved by the PSF (dirty beam) multiplied by some gain factor (~ 0.1), is subtracted from all the convolved images created in the first step. The model is then updated with the components and the residual is updated by subtracting the model components convolved with the PSF.

4. The above steps are repeated until a stopping criterion is reached.

At the end of each minor cycle, the model image is converted into a list of model visibilities using the measurement equation. This image-to-data transform is known as prediction and conversely, the data-to-image transform is known as imaging. After each minor cycle, the calculated model visibilities (prediction) are subtracted from the data visibilities and the result is re-gridded and transformed to produce a new residual image (imaging). Operating in the image domain with gridded visibilities (minor cycles) offers efficiency and returning to the un-gridded visibilities after every step (major cycles) ensures accuracy and avoids aliasing.

The instrumental PSF can be altered by utilizing different weighting schemes to obtain images with various angular resolutions, sensitivity, and noise. The PSF then represents the incomplete sampling of the spatial-frequency plane (uv-aperture) modulated by the weighting scheme employed during imaging. By down-weighting the long baselines, the sensitivity to extended emission can be increased at the cost of decreased angular resolution. This is achieved by using natural weighting and or applying a uv-tapering. Conversely, higher angular resolution at the cost of reduced sensitivity can be attained by using a uniform weighting scheme. The Robust Briggs weighting allows for the continuous variation between maximum point source sensitivity and resolution; robust $= -2$, equates to uniform weighting and robust $= 2$, equates to natural weighting. The choice of weighting also affects the synthesized beam of the reconstructed image, with natural weighting corresponding to the highest resolution and therefore the smallest beam. In the restoration step of imaging, the model is smoothed with a 2D elliptical Gaussian that matches the resolution of the main lobe of the PSF and then added back to the residual.

A note on the various "beams" in radio astronomy:

1. Dirty beam - interferometer response - this is the Point Spread Function which is a result of the discrete sampling and weighting of the uv-plane. The Fourier transform of the synthesised aperture in figure 2.5 will be the PSF for the J1250-20 MS.

2. Synthesized beam or restoring beam - smoothing applied to match the PSF resolution - this is the 2D elliptical Gaussian fit to the main lobe of the PSF to include residual flux that was not picked up by the model image. This is also typically done to compensate for the unphysical nature of the delta functions used in *CLEAN* algorithms.

3. Primary beam - antenna response - the antenna power pattern resulting from the time-varying direction-dependent complex gain induced by the aperture-illumination function of each antenna is called the primary beam.

2.2 MeerKAT Telescope

The MeerKAT radio interferometer (Jonas & MeerKAT Team 2016) is an array of 64 interlinked antennas each with a dish diameter of 13.5 m located in the arid Karoo region in South Africa. MeerKAT is a precursor for the Square Kilometre Array (SKA) mid-frequency telescope and is currently the most sensitive interferometer operating in the decimetre-wavelength regime. The 'core heavy' array layout of MeerKAT, containing 70% (48) of the dishes in the inner core, within 1 km in diameter, is optimal for studying extended emission. The shortest baselines span 29 m and the longest span 7.7 km. The telescope's wideband modes observe in the L band [900 to 1670 MHz] and UHF band [580 to 1015 MHz] with coarse (4K) and fine (32K) channelisation modes, offering about 209 kHz and 26 kHz channel resolutions respectively. Additionally, MeerKAT, currently also provides two narrowband modes in the L-band with 3.3 kHz and 1.633 kHz channel resolutions. The cryogenically cooled receivers and the Gregorian offset dishes provide exquisite sensitivity as envisioned in the design phase, where the goal was to optimise for point-source sensitivity.

Figure 2.1: The photo features a MeerKAT antenna and a section of the array in the background, captured during my visit to the MeerKAT site in Carnarvon during a SARAO open day in July 2022. I am also pictured in the foreground.

2.3 Observation and Calibration

The two Choir groups were observed with MeerKAT in L-band with the 32k correlator mode in two blocks, a rising block and a setting block as part of the 2020 Open Time Proposal, MKT-20172 (PI: Moses Mogotsi). The 32k channelization offers a spectral resolution of ~ 5.6 km s^{-1}, an angular resolution of $\sim 10''$ for robustness of 0, and a field-of-view of $1°$. The observation details are summarized in table 2.1. The whole track of 4.78 hours[5] was split into two to ensure efficient scheduling and better *uv* coverage. In this work, the output visibilities of these two tracks are labelled *P1* and *P2*, with the former being the first and the latter being the second block observed (refer figure 2.2).

The galaxy group, J1250-20, was previously studied in HI 21 cm with ATCA by Džudžar et al. (2019). We obtained the ATCA data from the authors for comparison. The MeerKAT observations were carried out in late February and April of 2021 (refer table 2.1 and figure 2.2). The radio bright QSO, *B1245-197*, $\sim 42'$ offset from the phase centre, contaminates the field by inducing artefacts and disproportionately increasing the noise (see figure 2.3). The observations are also affected by a strong RFI signal attributed to GPS L3. The channels affected by the RFI are ignored during imaging (see figure 2.6).

[5] about four hours and forty-six minutes

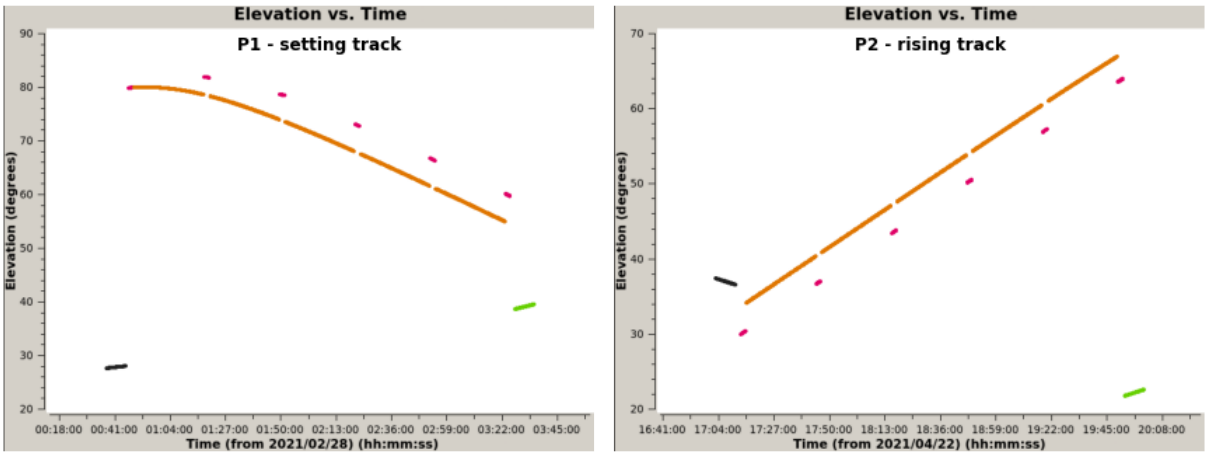

Figure 2.2: Elevation vs time plot to illustrate the rising and setting tracks. J1250-20 P1 is shown on the left and J1250-20 P2 is shown on the right. The orange lines denote the source and the pink lines are the bandpass calibrator. The green and black lines are the flux calibrators.

The galaxy group, J1403-06, was previously observed with VLA in 1996 by Clemens (1999). We obtained and imaged the historic VLA data in order to establish a benchmark for the MeerKAT data (see section 2.11). The central galaxies of the group (S1, S2) are continuum sources. So while modelling the continuum, it was crucial to specify line-free channels. This group was observed with MeerKAT in early March and June of 2021 (refer table 2.1). The P1 block, a setting track, was observed close to sunrise and the P2 block, a rising track, was observed close to sunset. Short baselines projected towards the Sun, particularly at sunrise and sunset, are expected to detect solar fringes. We see low-level artefacts close to the N and S edges of the primary beam in the P1 observation that can potentially be the result of minor-level solar interference. We make a note of this and proceed with the cleaning while ensuring that these signals are not detected by SoFiA2 as sources.

The two tracks observed for each target were taken at two different times and thus were calibrated individually. However, they must be combined before imaging. But, bright, off-phase centre, continuum sources in the field induce dissimilar contamination signatures due to the differences in the *uv* apertures of the two tracks (see figure 2.3). Therefore, the continuum must be subtracted separately before the two sets of visibilities (*GnP1.ms* & *GnP2.ms*) can be concatenated. The two visibility sets from the correlator were fed to the SARAO SDP calibration pipeline individually. The pipeline flags RFI signals, computes various cross-calibration solutions (delay, flux, phase, gain, bandpass), and applies the corrections to the data. The resulting gain-corrected, bandpass and flux-calibrated Measurement Sets (L1 visibility; hereafter MS) are used for imaging in the subsequent sections. The goal is to obtain a continuum subtracted and concatenated MS, and also spectral cubes of various resolutions. The following sections detail the methodology adopted to produce a full-track spectral cube from the two individual visibility datasets.

2.4 Imaging Philosophy

Imaging is a crucial step that needs great care and attention to ensure optimum results. The properties of the final cubes are sensitive to various parameters and methods employed during

Table 2.1: MeerKAT observation summary and imaging properties of MeerChoirs targets, HIPASS J1403-06 and HIPASS J1250-20. [a] indicates the cubes used for analysis in this work.

Observing Parameters	J1403-06	J1250-20
Observation dates	08 Mar, 12 Jun 2021	28 Feb, 22 Apr 2021
Flux/bandpass calibrator	J1939-6342, J0408-6545	J1939-6342, J1331+3030, J0408-6545
Phase/gain calibrator	J1337-1257	J1311-2216
Pointing Center	14:03:24.88, -06:04:09.20	12:50:52.84, -20:22:15.60
Total integration time	4.78h (2.39h × 2)	4.78h (2.39h × 2)
Number of antennas	59, 63	63, 62
Correlator mode	32k	32k
Band	L	L
Spectral resolution	26.123 kHz	26.123 kHz
Continuum imaging properties		
Imaged area	2.28×2.28 deg^2	2.28×2.28 deg^2
Frequency range	1399–1416 MHz	1375–1390 MHz
Robustness	-2.0	-2.0
Synthesised beam P1	7.6" × 6.4", 54.22 deg	6.63" × 5.50", 9.83 deg
Synthesised beam P2	8.22" × 6.47", -70.16 deg	7.92" × 5.64", -60.82 deg
HI imaging properties		
Imaged area	1.14×1.14 deg^2	1.14×1.14 deg^2
Synthesised beam (robust = 1.0)[a]	$17.39'' \times 16.81'', 1.22^\circ$	$16.11'' \times 14.95'', -21.66^\circ$
Synthesised beam (robust = 0.5)	$13.41'' \times 11.99'', -6.46^\circ$	$11.72'' \times 10.62'', -13.68^\circ$
channel width	~ 5.62 km s^{-1}	~ 5.81 km s^{-1}
RMS (robust = 1.0)	0.189 mJy/beam	0.189 mJy/beam

imaging. Scientific exploration, therefore, is intrinsically linked to the methods adopted for data reduction. Imaging is an iterative process with certain parameters being tweaked based on the inspection of outputs from previous runs.

First, at least a $\sim$ 15 MHz ($\sim$ 3000 kms^{-1}) chunk each of (*P1.ms* and *P2.ms*) centred at the redshifted 21 cm emission frequency, is extracted for continuum modelling. We utilize CASA v5.7.0 (Team et al. 2022) for imaging, SoFiA2 (Serra et al. 2015; Westmeier et al. 2021) for producing clean masks, and CARTA (Comrie et al. 2021), SIP (Hess et al. 2022a), and SlicerAstro (Punzo et al. 2017) for inspection. The flow of processes carried out to obtain the final cube is illustrated in the swim-lane flowchart 2.4. The diagram is divided into 3 columns or swim-lanes to distinguish the different major stages of the workflow. The first swim-lane illustrates the processes involved in continuum imaging of the $\sim$ 15 MHz L1 visibilities. The second swim-lane details the steps adopted to obtain a combined measurement set and subsequently, a spectral cube. The third swim-lane shows the operations performed on the spectral cube for preparing it for analysis. The diagram also shows inspection loops and handoffs between the lanes. In the third lane, the inspection loop is spread across multiple steps (see section 2.10). The next section details the steps involved in the continuum modelling of the $\sim$ 15 MHz MS of the individual passes (*GnP1-15MHz.ms* & *GnP2-15MHz.ms*). Where 'Gn' represents the group MS being reduced, G1 for J1403-06 and G2 for J1250-20. Since the steps are identical, the processes are illustrated on a single MS to avoid confusion (see figure 2.4).

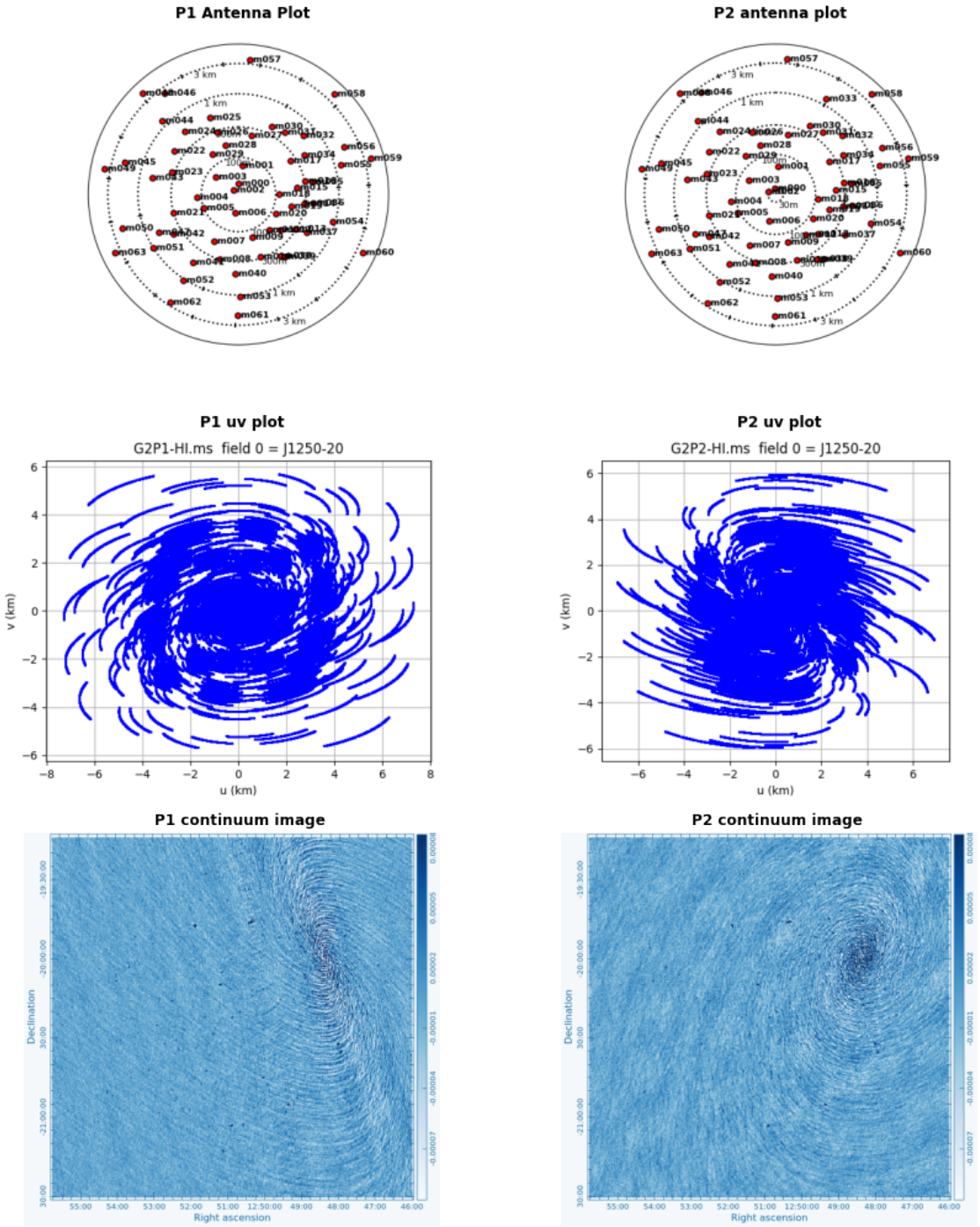

Figure 2.3: Image of the antenna layout (first row), *uv* aperture (second row), and the continuum image (third row). J1250-20 P1 (setting track) is shown on the left and J1250-20 P2 (rising track) is shown on the right.

2.5 Continuum Imaging

The Stokes I continuum of the MS is first blindly imaged using the Multi-Term Multi-Frequency Synthesis (*MT-MFS*) algorithm in the CASA task *tclean* (McMullin et al. 2007). The algorithm produces a continuum image of the broad-band sky brightness distribution by fitting a first-order Taylor polynomial (2 Taylor coefficients) to the data per flux component in the intensity-frequency space (I vs ν). To avoid the emission line from affecting the continuum model, only the

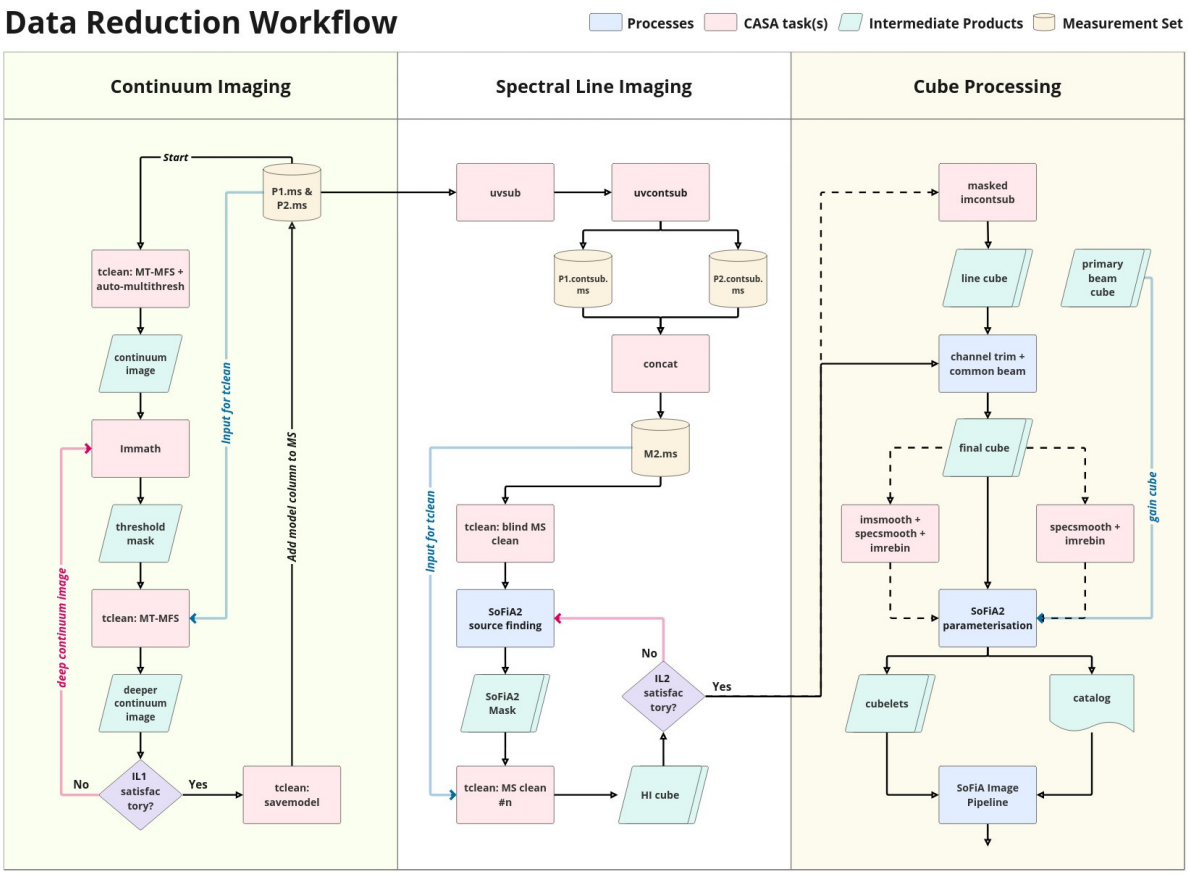

Figure 2.4: Swim-lane flowchart showing the data reduction workflow starting from cross-calibrated L1 visibilities to the final HI cube(s). The first column or swim-lane illustrates the steps involved in continuum imaging. The second swim-lane details the steps to merge measurement sets and obtain a spectral cube. The third swim-lane shows the operations done on the spectral cube for preparing it for analysis. The first swim-lane is repeated for both *P1.ms* and *P2.ms*. Each swim-lane has an inspection loop, ILn (n=1,2,3) for quality control. In the third swim-lane, IL3 is split across 3 stages. The black solid and dashed lines indicate the normal workflow, the red dotted lines denote the retrograde flow post rejection in IL, and the blue dotted lines denote additional inputs needed for the step. Black dashed lines denote optional trajectories that can be adopted based on inspection and or science. The blue rectangles denote processes or packages, the pink rectangles denote CASA tasks and processes, the green rhombuses (document) denote output images/cubes (catalogue), yellow cylinders denote Measurement Sets, and the purple diamonds denote ILs.

line-free channels are imaged. To image the full field observed by MeerKAT, we must account for the non-zero w-term caused by the sky curvature and non-coplanar baselines. For this, Gridding Convolution Functions (GCFs) for 128 w-planes were calculated and applied to the MS during gridding to limit artefacts around sources away from phase centre. The high number of w-planes comes at a computational cost, but this was alleviated to some extent by utilizing MPICASA to run *tclean* in parallel. For continuum imaging, only the major cycles are run in parallel whereas, for spectral cube imaging, even the minor cycles are parallelized. Clean masks for the blind cleans were produced automatically during deconvolution using the *auto-multithresh* algorithm in *tclean*. A Brigg's robust weight of -2.0 was used for continuum imaging to resolve the continuum sources and the induced artefacts.

The continuum image and the residual obtained from the blind clean are used to produce a simple threshold mask using CASA task *immath*, for the subsequent *MT-MFS* clean. The above steps

are repeated with deeper threshold masks produced from prior cleans until the continuum is modelled satisfactorily (IL1 in figure 2.4). The thresholds for cleaning and masking are chosen based on theoretical noise estimates obtained from the MeerKAT sensitivity calculator. The ideal outcome is a residual with a uniform noise distribution close to the theoretical value. But if there are strong artefacts, we find that there is a point of diminishing returns beyond which, cleaning introduces additional structure in the spectral cube. If the output HI cube, after spectral line imaging, contains residual continuum artefacts, the continuum of the individual passes is modelled again with deeper threshold masks. For some of the iterations where the imaged cube contained strong artefacts induced as a result of deep continuum imaging, we had to backtrack and model the continuum with shallower masks. A satisfactory continuum model must mostly contain the continuum sources with very few artefacts, the resulting continuum image and the residual image would appear relatively smooth in regions free of the strong artefacts. Once a satisfactory continuum model is produced, it is saved to the respective MS as a column by running tclean again in serial mode with *calcpsf = False, calcres = False* and *niter = 0*. At the time of the writing of this thesis, the 'savemodel' functionality in tclean has not been extended to parallel operations and a subsequent serial run is recommended to trigger a predict model step that obeys the 'savemodel' parameter.

2.6 Continuum Subtraction and Concatenation

The measurement sets of both tracks with the respective continuum models saved as columns are input into the CASA task *uvsub* individually. This task reads the model column and subtracts the saved model from the data. The continuum model subtracted MS is then fed to CASA task *uvcontsub* which fits a polynomial of specified order to the continuum in the *uv* domain and subtracts it from the data. The order of the polynomial is chosen based on the shape of the continuum in the baseline, scan, and time-averaged amplitude vs channel plot of the MS (refer figure 2.6). A zeroth-order polynomial applies an offset whereas a first-order polynomial applies an offset and a slope. We specify line-free channels for continuum fitting and we restrict the order to less than two. The respective outputs *P1.ms.contsub* and *P2.ms.contsub* are then concatenated using the CASA task *concat* to produce the final MS. The *uv* plot of the combined measurement set is shown in figure 2.5. Continuum subtraction can be done either in the *uv*-domain or in the image plane. The continuum fitted in the *uv*-domain is only a good representation of the continuum sources near the phase centre and residual signal may be visible for strong sources away from the phase centre. This is the case for J1250-20, wherein we see residual continuum emission in the spectral cube. To deal with this, we perform an iterative image plane continuum subtraction (see section 2.9).

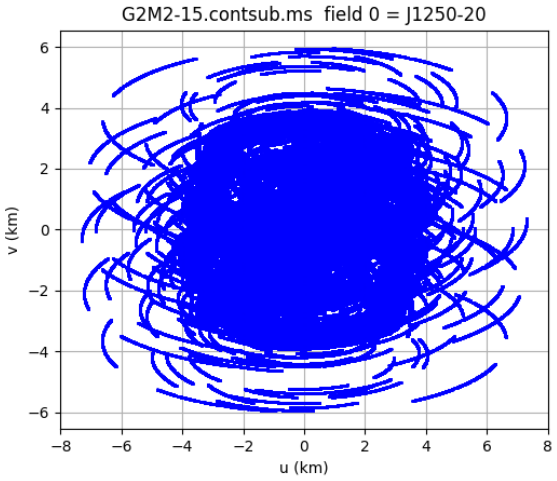

Figure 2.5: Combined *uv* plot illustrating how the rising and setting tracks maximise the *uv* aperture.

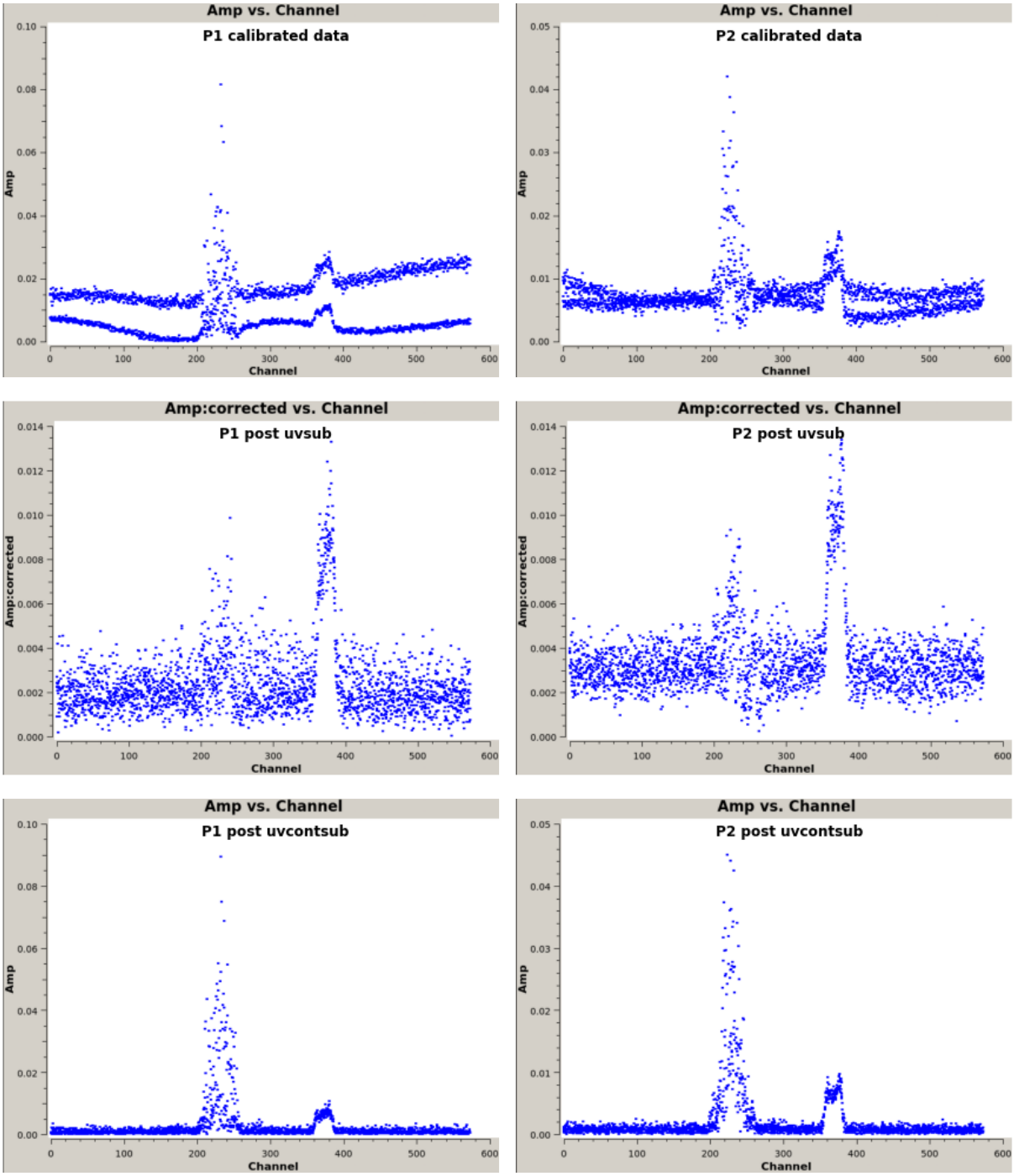

Figure 2.6: Baseline, scan, and time-averaged amplitude vs channel plot showing the evolution of the $\sim$ 15 MHz band from L1 visibilities to continuum subtracted measurement sets. J1250-20 P1 is shown on the left and J1250-20 P2 is shown on the right. The feature centred around channel 230 is the GPS L3 RFI.

2.7 HI Source Finding and Masking

Firstly, a shallow, blind *MS-CLEAN* is performed over $\sim$ 200 channels ($\sim$ 1000 kms^{-1}) of the continuum subtracted, concatenated MS centred at the redshifted HI 21 cm line. The blind cube is then input into the SoFiA2 pipeline (Serra et al. 2015; Westmeier et al. 2021), an HI Source-Finding Application for interferometric spectral-line data. SoFiA2 offers various preconditioning filters to deal with noise variations, low-level continuum emission, and artefacts (see figure 2.7).

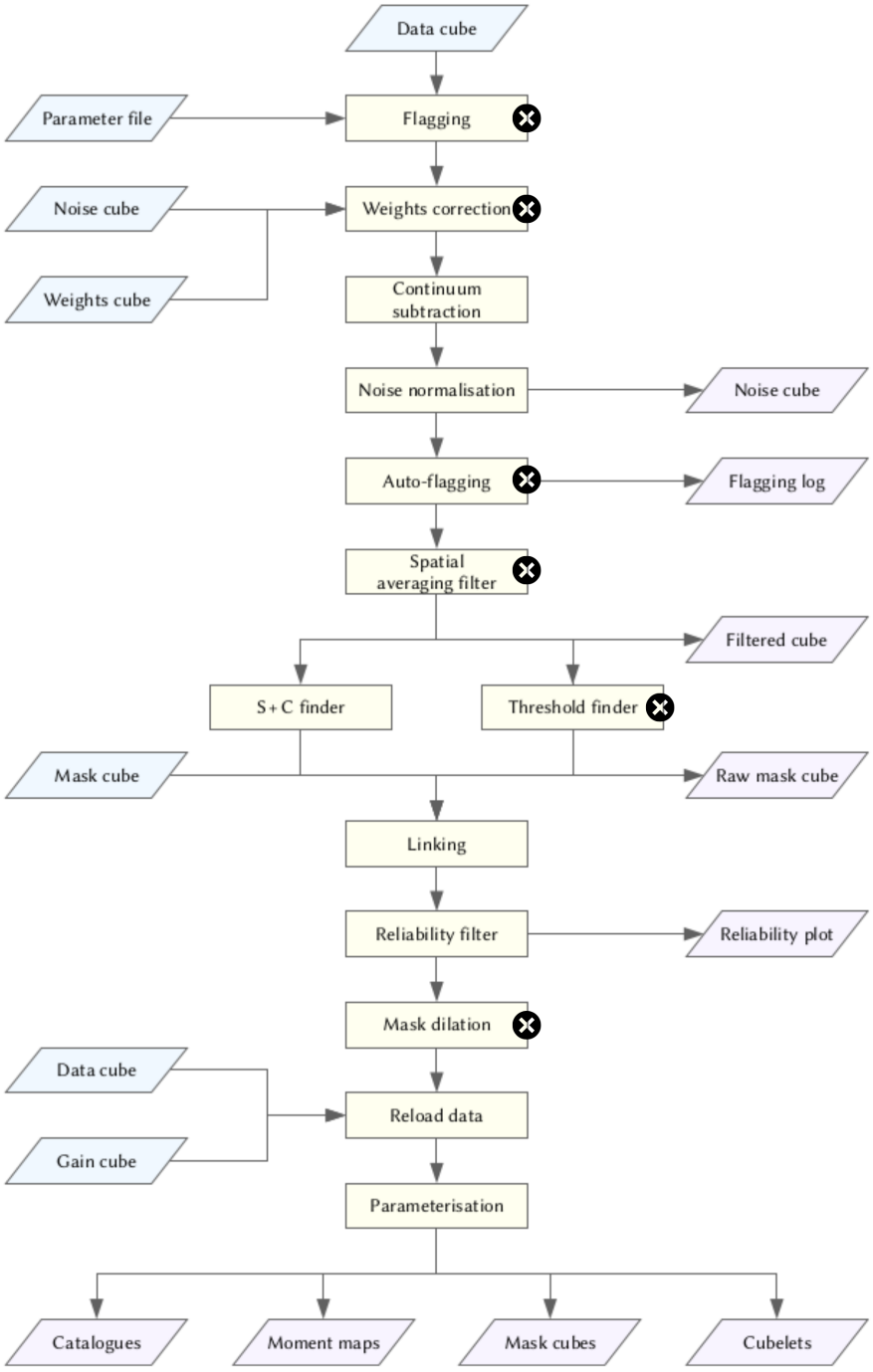

Figure 2.7: The flowchart of SoFiA2 taken from the documentation, shows the steps in the pipeline (yellow), input data cubes (blue), and the generated output files (purple). The steps that were not used for this work have been marked with a cross. We first run the pipeline for producing clean masks and after the final cube is obtained, we run it again for parameterisation. The primary beam is input as the gain cube during parameterisation.

In a typical cube that has not been primary beam corrected, the noise level is expected to vary only along the spectral axis. These noise level variations have to be normalized before a source-finding threshold can be applied to the data. We enable the noise normalization filter to measure and correct the noise fluctuations on a channel-by-channel basis. If the cube has low-level residual continuum emission, we also enable the continuum subtraction filter to fit and subtract a 0^{th} order polynomial from the spectrum of each spaxel prior to source finding.

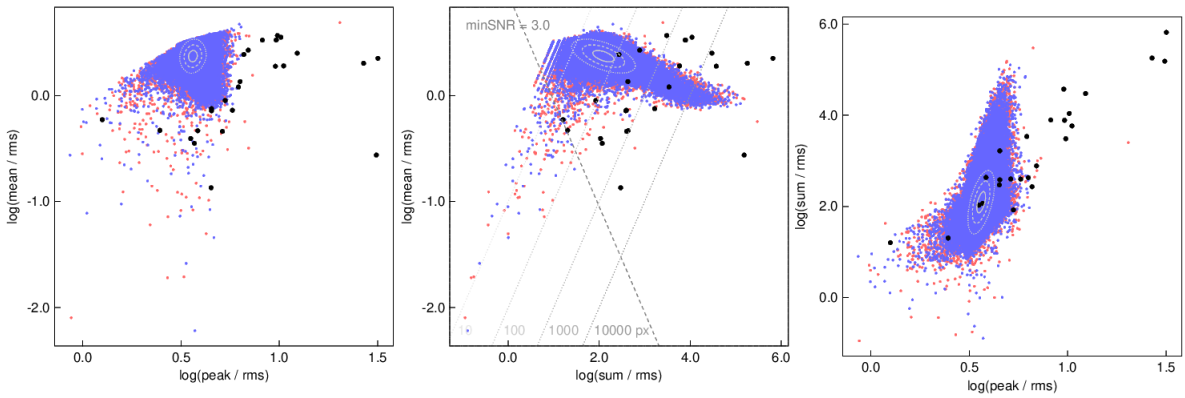

Figure 2.8: 2D projection of the distribution of positive (red) and negative (blue) detections in the 3D parameter space employed by SoFiA2 for reliability estimation in J1250-20. The black dots are positive sources with a reliability greater than 96%. The light-grey ellipses are 1σ, 2σ, and 3σ contours of the 3D Gaussian function used for Kernel Density Estimation (KDE). The dark grey, dashed line is the signal-to-noise limit below which sources are discarded.

For source finding, we make use of the 'smooth+clip' ($S+C$) algorithm (Serra et al. 2012a) in SoFiA2 with about six spatial Gaussian smoothing kernels with FWHM depending on the size of the beam and the 'cellsize' (e.g., 0, 4, 8, 12, 16, 24 pixels for a 'cellsize' of $2''$ and a $16''$ beam) and about four spectral boxcar smoothing kernels ($0, 3, 5, 7$ channels for a channel width of ~ 5.6 km s^{-1}). The smoothing functions are chosen to accommodate the fact that extragalactic HI sources have an exponential radial surface brightness profile and typically a double-horn spectral profile with steep flanks. The algorithm smooths the cube at the specified pixel levels, estimates the RMS of the smoothed cube, and applies a 4σ clip. Smoothing the data at various levels increases the signal-to-noise (SNR) ratio of sources with sizes comparable to the smoothing scales thereby enabling the detection of even faint, extended emission. The larger smoothing kernels are employed for increasing the column density sensitivity of the data. At the end of the $S+C$ algorithm, a source mask that contains all the pixels that exceed the source finding threshold on at least one of the smoothing scales is passed to a friends-of-friends grouping algorithm. The linker algorithm finds pixels marked as detections, but that are not yet associated with sources and labels them based on a search of the neighbouring pixels within the user-assigned merging lengths. SoFiA2 then estimates the reliability of the detections by statistically comparing the density of positive and negative detections in a three-dimensional logarithmic parameter space comprising of RMS normalized peak flux density, summed flux density, and mean flux density. Genuine detections are expected to populate a different region of the parameter space than false detections caused by noise peaks. When the positive detections are not accompanied by similar negative detections within the same volume, high reliability is assigned to the detection (Serra et al. 2012a; Westmeier et al. 2021; Healy et al. 2021). We adopt a 96% reliability threshold for the detection to be included in the clean mask (see figure 2.8).

2.8 Spectral Cube Imaging

The SoFiA2 masks produced using HI cubes from prior clean cycles are used as clean masks for subsequent deeper *MS-CLEAN* with at least four scales comparable to the kernels used for $S+C$. *MS-CLEAN* iteratively subtracts a scaled value of the PSF to construct a model confined

to the mask at each of the scales. As discussed extensively in Rich et al. (2008), neither the choice of the number of scales nor their distribution has any noticeable impact on the imaging. However, we have chosen comparable scales for both *S+C* and *MS-CLEAN* to stay consistent in our method and to ensure optimum sensitivity to structures corresponding to the specified scales. *MS-CLEAN* considers all scales together and model components are chosen in the order of decreasing integrated flux. In practice, this leads to the removal of extended emission before the removal of small-scale structures. Since our masks are extended, we ensure that the scales are reasonable to avoid noise getting added to the model.

For the total integration time, the target declinations, and a robustness of 0.5, the theoretical noise level for the spectral line is estimated to be typically around ~ 0.3 mJy/beam. In addition to updating the clean masks, the threshold, which is a stopping criterion, is also tweaked in an iterative fashion to facilitate deeper cleaning. During cleaning, the peak of the residual within the clean masks per channel is compared to the threshold parameter and the image gets cleaned until the residual flux becomes lower than the threshold. This procedure is repeated until satisfactory noise levels and residual flux levels are reached. We find that there is a trade-off between cleaning down to a low threshold to extract signals from low S/N regions and applying wider clean masks to recover diffuse emission signatures. Extended masks and low thresholds can result in over-cleaning, especially in low S/N regions. The SoFiA2 masks by design are extended to detect low column density gas and so we carefully ensure that the de-convolution threshold stays above the noise level. Over-cleaning will result in "spottiness" in the image and increased RMS due to the deconvolution operating into the noise. The residual cube is also inspected for negative bowls and other artefacts. A deeper clean is performed only when residual source emission is detected in the residual cube. We obtain optimum results with a cleaning threshold of $\sim 2.5\sigma \sim 0.45$mJy. We produce a high-resolution cube ($\sim$ 12") by imaging with a robustness of 0.5 and a medium-resolution cube ($\sim$ 16") by imaging with a robustness of 1.0. In this work, we only make use of the medium-resolution cube.

2.9 Cube Processing

Once a cube is obtained after spectral line imaging, we process it further based on a quality assessment and analysis strategy. If the cube suffers from residual continuum emission, we perform image plane continuum subtraction by following a strategy similar to that adopted by Gogate et al. (2020). Firstly, we clip the cube at the 2σ level to obtain an accurate representation of the residual continuum while avoiding the emission line. The clipping level is determined through iterative trial and error. Subsequently, we employ CASA task *imcontsub* to perform a zeroth order polynomial baseline fit to the spectrum of each spaxel in the clipped cube. The continuum file generated by *imcontsub* is then subtracted from the original cube. Next, we utilize SoFiA2 to create a source mask based on the continuum-subtracted cube and apply it to the original cube. Finally, we fit a zeroth-order continuum to the masked cube and subtract it from the original cube to obtain the final continuum-subtracted cube. This is a conditional step that is performed in cases where residual continuum is visible. The next step is mandatory wherein all cubes are trimmed along the spectral axis and spatially smoothed to a common beam.

Since the PSF changes as a function of frequency, the restoration step in *tclean* calculates a

synthesized beam per channel. Although the beam per channel does not vary much across narrow bandwidths, there can be bad channels with beams deviating from those of the rest of the channels (see CASA Memo 10). Before estimating the common beam for the cube, we export a smaller spectral slab spanning the emission and also remove any bad channels. Finding the smallest beam from a set of more than two beams is a complex convex optimisation problem. To further guarantee the accuracy of the common beam, we employ two different implementations of this calculation, the direct approach in CASA task *imsmooth* and the approximate method in the radio-beam[6] python package. The exact method in *imsmooth* iterates through the beams and compares each to the largest beam to find the overlapping area. The approximate method in radio-beam samples points at the boundaries of the beams in the set and finds the smallest common beam using the convex envelope. Using both these implementations is in line with our imaging philosophy of approaching from either end to arrive at an optimal solution. The final beam dimensions are compared and if no noticeable deviations are observed, the CASA implementation is adopted.

At this stage, from the medium-resolution $16''$ cube, we create two cubes: the kinematic cube and the low-resolution cube ($\sim 47''$). The kinematics cube is used for Gaussian decomposition and tilted ring modelling. The low-resolution cube is used for low-column-density gas detection. The low-resolution (high-sensitivity) cube is produced by degrading the spatial resolution of the medium-resolution cube by smoothing to a 2D Gaussian of $\sim 47''$ using CASA task *imsmooth*. This task performs a Fourier-based 2D convolution to smooth the direction plane of the cube. A deconvolved image, $\vec{\mathbf{I}}$, with a common restoring beam, $\mathbf{B}_{\rm com}$, can be smoothed to a target Gaussian beam, $\mathbf{B}_{\rm tar}$, through convolution with a correcting beam, $\mathbf{B}_{\rm cor}$.

$$\mathbf{B}_{\rm tar} * \vec{\mathbf{I}} = \mathbf{B}_{\rm cor} * (\mathbf{B}_{\rm com} * \vec{\mathbf{I}}) \tag{2.4}$$

The correcting beam, $\mathbf{B}_{\rm cor}$, can be obtained by finding the Fourier transform of equation 2.4 using the convolution theorem.

$$\begin{aligned} \mathbf{B}^f_{\rm tar}\vec{\mathbf{I}}^f &= \mathbf{B}^f_{\rm cor}(\mathbf{B}^f_{\rm com}\vec{\mathbf{I}}^f) \\ \mathbf{B}_{\rm cor} &= \mathcal{F}^{-1}\left(\frac{\mathbf{B}^f_{\rm tar}}{\mathbf{B}^f_{\rm com}}\right) \end{aligned} \tag{2.5}$$

For spectral line imaging, a $2''$ cellsize was adopted to ensure that the smallest restoring beam of $12''$ is sampled by at least 5 pixels across the major axis. This entails that the $16''$ and $47''$ beams are over-sampled by about 8 and 23 pixels across the beam major axes respectively. We use CASA task *imrebin* to rebin the data to sample the beam major axis by about 4-5 pixels. The output pixel after rebinning is the average of the input pixels specified by the binning factor. The rebinned med-resolution $16''$ cube is the kinematic cube (Beam $\sim 16''$, $\Delta v \sim 5.6\,\mathrm{km\,s^{-1}}$,

[6] https://radio-beam.readthedocs.io/en/latest/commonbeam.html

cellsize = 2″). The rebinned 47″ cube is then further convolved with a 1D boxcar kernel across 3 channels along the spectral axis using CASA task *specsmooth* to obtain the low-resolution cube.

$$z_i = \frac{\sum_{j=k}^{k+w-1} y_j}{w} \tag{2.6}$$

In the equation, z_i is the value at channel i on the smoothed cube, y_j is the value at channel k of the input cube, and w is the positive integer width of the boxcar kernel. If the input cube had L channels, then the output cube would contain L-(w+1) channels, as only every w_{th} channel is retained in the output cube. We re-sample the spectral resolution to ensure that the channel widths are representative of the inherent dispersion of HI. This produces the low-resolution cube (Beam $\sim$ 47″, $\Delta v \sim 17.4\,\mathrm{km\,s^{-1}}$, cellsize = 10″), which is used to plot the lowest contours in the HI column density overlay plots of the field.

All the cubes are exported as fits using CASA task *exportfits* with optical velocity along the spectral axis. The final cubes along with their correspondingly sampled primary beam cubes are passed through SoFiA2 for parameterisation and inspection. For parameterisation, we employ a higher reliability threshold than that adopted for generating clean masks. SoFiA2 produces a source catalogue and for each source in the catalogue, it outputs, a primary beam-corrected cubelet, a source mask, integrated 1D spectra, moment maps, an SNR map, a position-velocity map, and a map of the number of channels spanned by the emission in each pixel. The outputs are then fed to the SoFiA-Image-Pipeline (SIP; Hess et al. 2022a), which takes a SoFiA generated source catalog and produce images such as HI contours overlaid on multiwavelength images, HI moment maps, pixel-by-pixel SNR maps, pv-diagrams with SoFiA mask, and spectra with and without noise. These images are used for the final inspection (see an example figure 2.9).

2.10 Inspection & Quality Control

Initially, the outputs of the calibration pipeline are reviewed for residual calibration and flagging issues. In the workflow, there are three critical junctures (Inspection loops) where we perform a thorough inspection and if required, apply corrective measures to ensure the quality of the science products. The MS and files generated as the workflow progresses are tracked manually by rigorously following a naming and organizing convention. At each stage of reduction including the designated inspection loops, the images and cubes are examined using CARTA (Comrie et al. 2021). The three Inspection Loops (ILn; n = 1, 2, 3) are placed in each of the swim-lanes in the workflow figure 2.4. IL1 deals with threshold masking, continuum imaging, and producing two Measurement Sets with corresponding model columns; IL2 deals with source finding, and spectral line imaging; IL3 deals with cube processing, SoFiA2 parameterisation, and final inspection.

In IL1, since the task *uvsub* modifies the input MS, it is pertinent to ensure that the continuum subtraction is done on the original MS and not on a continuum subtracted MS. To avoid incorrect model subtraction, we ensure that a model column is added to the MS only after a satisfactory continuum model is obtained. In the cleaning inspection loops (IL1, IL2), the image/cube, residual, model, and mask are simultaneously inspected in CARTA. Firstly, the masks must be representative of the source signals. For clean masks produced for continuum imaging, the

emission lines must be avoided. Similarly, for clean masks produced for spectral line imaging, continuum signals must not be included in the mask. Secondly, the model of the sky brightness distribution should not contain artefacts. Finally, the residual must have the lowest possible emission levels at source locations and also uniform noise distribution across the cube. In IL2, the residual is carefully inspected for both residual emission and signs of over-cleaning such as negative bowls, spottiness, etc. As discussed in Walter et al. (2008) and in Rich et al. (2008), if there is uncleaned source emission in the residual, the restored image is an addition of two separate flux scales. A residual map with units of Jy per dirty beam and a cleaned map with units of Jy per clean beam. The extent of the dirty beam is always larger than the clean beam and thus the flux determined by using the clean beam will be an overestimate of the total source flux. Walter et al. (2008) addressed this issue by applying a correction factor to their masked signal cube. While this is no longer much of an issue with *MS-CLEAN*, the residuals still have to be carefully inspected to ensure that all the source emission has been recovered. In the cube processing swim-lane, the inspection loop IL3 is split across three steps. Firstly, the cube is examined for residual continuum emission and if found, image plane continuum subtraction as discussed in section 2.9 is performed. Secondly, noisy channels are removed before common beam estimation. Lastly, the outputs of the SoFiA2 parameterisation step are inspected using CARTA and the plots created by SIP. This is the final inspection of the final spectral cube and if the desired quality is not obtained, the preceding steps are scrutinized. The corrective measures adopted can range from tweaking SoFiA2 parameters to re-imaging the cube. The cubelets of the major members are also inspected in 3D using SlicerAstro (Punzo et al. 2017). In cases where the HI discs of member galaxies are interacting, additional separation is performed by slicing along planes identified from 3D examination.

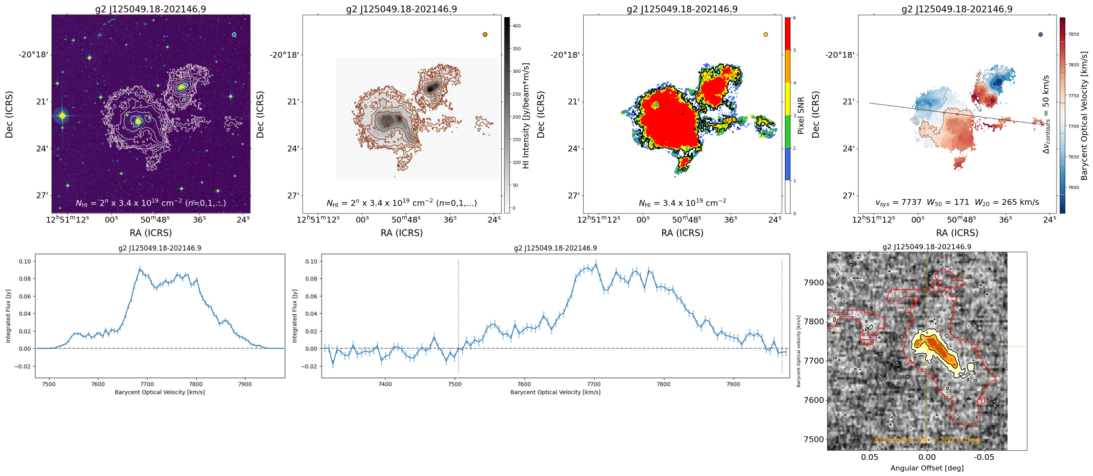

Figure 2.9: Example of a combined inspection plot of the cubelet of the central galaxies in J1250-20 produced by the SoFiA Image Pipeline (SIP). From left to right: HI column density contours overlaid on optical DSS2 image, HI column density map, SNR map, first-moment map, spectra without noose, spectra with noise, and position-velocity diagram.

2.11 VLA Data Reduction

J1403-06 was previously observed with VLA C and D configurations in March and July 1996 respectively as part of the program 'AA195' (Clemens 1999). The column density image of

the combined C+D cube is part of the HI rogues gallery (Hibbard et al. 2001). We procured the historical VLA data from the NRAO archive and imported them into CASA (v6.4.4.31; McMullin et al. 2007) using the *importvla* task. We then calculated and applied the calibration solutions using various tasks in CASA. We used a similar methodology as discussed above for imaging. The VLA D configuration being the most compact, offers maximum sensitivity but at a lower angular resolution ($\sim 46''$ for robust = 0.5). From the C configuration observation, we recover a synthesized beam of $\sim 14''$ with a weighting of robust = 0.5. The flags generated during observation were applied during data retrieval and additional flagging was not required. The flux density scale and bandpass calibrator, 3C286, labelled 1328+307 in the B1950 epoch, was observed at the beginning and end of the tracks. The complex gain calibrator, 1402-012, was observed for 140 seconds (2.2 min) for every 1140 seconds (19 min) on the target. The total on-source integration times are 2.35 hours (2 hours, 21 minutes) and 1.45 hours (1 hour, 27 minutes) for the C and D configurations respectively. We briefly discuss the procedures we adopted for cross-calibration. Initial flux density scaling was performed for the bandpass calibrator using the *setjy* task and Perley & Butler (2017) standard model, 3C286_L. The cross-calibration solutions were applied to both configurations individually.

1. **Antenna gain-elevation curve:** The effective collecting area and surface accuracy vary due to the effect of gravity on the surface of the antennas. To correct this, we create a calibration table based on standard gain curves from the VLA data repository using the *gencal* task.
2. **Bandpass calibration:** To correct for phase and amplitude variations across the spatial-frequency plane, we produce antenna-based solutions against a reference antenna (C - VA11; D - VA14) using the *bandpass* task.
3. **Complex gain calibration:** Using the *gaincal* task, the bandpass calibrator, and the complex gain calibrator, we produce antenna-based solutions to correct for phase and amplitude variations across time.
4. **Flux scale:** We compute the amplitude of the complex gain calibrator using the *fluxscale* task with the flux calibrator as a reference.

We apply the calibration solutions to the bandpass calibrator, the complex gain calibrator, and the target using the *applycal* task. This creates a 'corrected' data column in the MS. We further split the MS and extract the target field for continuum subtraction and imaging. We use the *uvcontsub* task to subtract the continuum by fitting the line-free channels with a first-order polynomial. After continuum subtraction, we combined the measurement sets of the two configurations using the *concat* task. The continuum subtracted and concatenated MS is then imaged using *tclean* with clean masks from SoFiA2 using a methodology similar to figure 2.4 (see section 2.8). Once the final cube is obtained, image plane primary beam correction is performed using the *impbcor* task. The cube is then re-projected from B1950 to J2000 using the *imregrid* task. We adopted a restoring beam of $35'' \times 27''$ to be comparable to the resolution of the column density image presented in Hibbard et al. (2001).

3 | Spectral Cube Analysis

Spectral-line cubes consist of observed specific intensities in units of Jy beam^{-1} spread across two spatial sky coordinate axes and one spectral axis. Techniques for spectral cube analysis often involve collapsing the cube (sum or mean) along one or more axes to extract information from the 3D data. This has given rise to several iconic diagrams that represent the motion of gas in galaxies such as the "double-horn" spectra, the "spider" diagram (see figure 3.1), the rotation curve, and the "butterfly" pattern in channel maps. This chapter begins with the cubelets of the sources and the corresponding data products obtained from the parameterisation step in the data reduction workflow discussed in the previous chapter. All the cubes have optical velocities in 'm s^{-1}' as the spectral axis and spatial axes based on ICRS coordinates in the J2000 epoch. The cubes have a $\sim 16''$ beam, a cellsize of $4''$, and a channel width of ~ 5.6 km s^{-1}. In the subsequent sections of the chapter, some general techniques and methods adopted for this work are introduced.

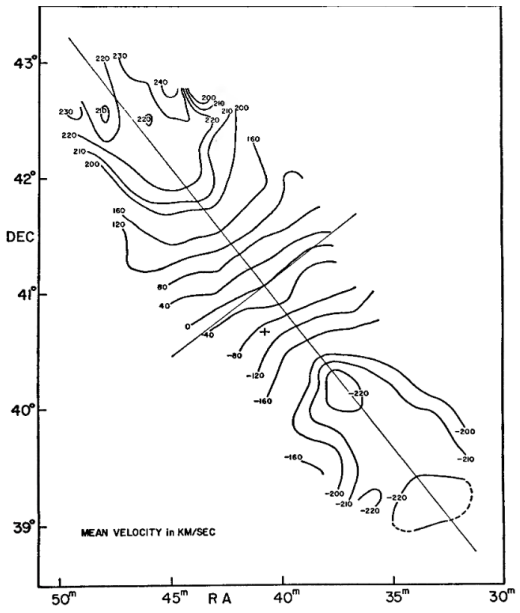

Figure 3.1: The first reported spider diagram taken from Argyle (1965) showing the iso-velocity contours of M31.

3.1 HI global profiles

The cube can be collapsed along the two spatial axes to obtain an integrated flux value per velocity channel. Since the cube contains spectra for each spatial pixel, one-dimensional spectra can be extracted by integrating across all pixels containing source emission. For a galaxy, such integration would produce a one-dimensional global spectral profile with a "double-horn" structure. The double-horn shape of the spectral profile is a result of the rotation of the emitting gas in the galaxy and the Doppler effect induced by the relative motion of the emitting gas with respect to the observer. The integrated HI spectra of large samples of galaxies have been employed to extract statistical information on parameters such as HI mass, asymmetry, rotation velocity, etc. and to study various well-known scaling relations (e.g., Bok et al. 2019, 2020, 2022; Yu et al. 2022; Watts et al. 2023). The global spectra are used consistently to perform 1D spectral stacking to search for low-intensity HI emission (e.g., Brown et al. 2017). In this work, we do not utilize the global spectral profile, this section is for the sake of completeness. We do however use 1D spectral profiles extracted from individual pixels (see section 3.6.2).

3.2 2D Moment Maps

A moment map can be produced by collapsing a cube along a single axis typically the spectral axis. It can be thought of as a linear combination of individual 2D planes or channels. For

each spaxel (spatial pixel), the third axis is collapsed to a pixel with a value computed from the data values along the moment axis. The moment maps are a two-dimensional representation of the total observed flux, velocity field, and dispersion of source emission. For observed specific intensity per pixel, I_i, velocity per channel, (v_i), and channel width, (Δv), the three most commonly used moments are:

Zeroth moment - Integrated intensity over the spectral line.

$$M_0 = \Delta v \ \Sigma I_i \tag{3.1}$$

First moment - Intensity weighted velocities of the spectral line.

$$M_1 = \frac{\Sigma I_i v_i}{\Sigma I_i} \tag{3.2}$$

Second moment - Intensity weighted variance of the spectral line[7]; The square root of Moment 2 gives the velocity dispersion.

$$\sigma = \sqrt{M_2} = \sqrt{\frac{\Sigma I_i (v_i - M_1)^2}{\Sigma I_i}} \tag{3.3}$$

To generate moment maps, we initially apply the 3D mask obtained from the parameterisation step in the previous chapter (Chapter 2) of the data reduction workflow. This mask ensures that only the emission from the source is integrated into the moments. To calculate the zeroth moment, we sum all the masked flux, but for the first and second moments, we sum across only the channels with positive flux. The zeroth moments or total intensity maps display the integrated flux of the HI gas along the line of sight. In this work, total intensity maps of data cubes are used for defining column density contours and for calculating the HI mass. The colorbar associated with the zeroth moment shows the intensity distribution of the emission. The first moments (velocity fields or "spider" diagrams) are used to represent the rest frame line-of-sight component of the velocity vector of the motion of HI in the gravitational potential of the galaxy. The rest frame velocities are obtained by subtracting the systemic heliocentric recession velocity (cz) from the projected line-of-sight velocities. Iso-velocity contours deviating from the expected spider pattern have been interpreted as signs of non-circular motion.

3.3 2D Position-Velocity Diagram

A position-velocity diagram (PVD) is a two-dimensional map that shows the distribution of the emission in position and velocity space. To create a PVD, first, a line or polygon slice is defined through a region of interest in the sky. In this work, we utilize line slices typically along, or parallel to, the major and minor axes of the galaxies. A line slice is defined by central coordinates, length, position angle, and width. A PV slice along the line is given by the mean of the observed specific intensity within the width as a function of velocity. The result is a

[7] https://spectral-cube.readthedocs.io/en/latest/moments.html

two-dimensional representation of the three-dimensional observed specific intensity (Jy beam^{-1}) distribution along the slice. The ordinate (y-axis) of a PVD contains velocity and the abscissa (x-axis) contains offset from the centre of the slice. Thus the resulting PVD is a map of mean intensity within the width along the slice represented in position-velocity space. In this work, unless specified, the major axis of the beam ($\sim 16''$) is adopted as the width of the slices.

PVDs serve as valuable tools for investigating the kinematics of a gas distribution, as they capture information about both circular and non-circular motions within the slice. Figure 3.2 displays the major axis PVD of NGC 2403, revealing the presence of lagging gas, commonly referred to as 'beard gas,' below the emission from the disc. In their study, Fraternali et al. (2001) also identify anomalous gas in the forbidden quadrants (upper right and lower left), indicating non-circular motion. Similarly, Marasco et al. (2019) demonstrate the ability to identify signatures of various anomalous gas motions through PVDs extracted along both the major and minor axes. Furthermore, Di Teodoro & Peek (2021) showcase how PVDs extracted along the major and minor axes can unveil signatures of radial motions and warps in position angle and inclination. In this study, we extensively employ PVDs to show the rotating disc and the anomalous gas. The occurrence of Extended Planar Gas (EPG) as 'beard' gas is discussed in detail in section 1.4.1. Chapters 4 and 5 feature numerous PVDs that demonstrate the effectiveness of this representation in practice.

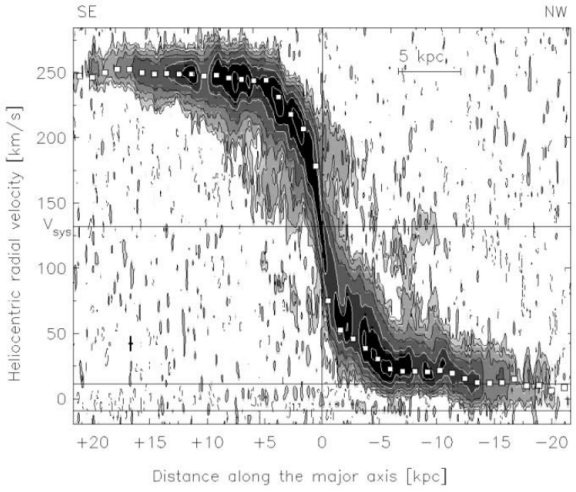

Figure 3.2: Major axis position-velocity diagram of NGC 2403 taken from Fraternali et al. (2001). The white squares show the projected rotation curve. Beard gas and kinematically anomalous "forbidden gas" can also be seen in the PVD.

3.4 Rotation Curves and 2D Tilted Ring Modelling

Kinematic analysis is one of the most powerful techniques at our disposal to deduce the dynamics of a galaxy and the distribution of dark matter (Sofue & Rubin 2001). Spectroscopy is an important tool for extracting kinematics, as the Doppler shift of spectral lines traces the motion of matter in the disc. The rotation of galaxies was discovered by Slipher (1914) using inclined absorption lines in the spectra of M31 (Andromeda galaxy) and M104 (Sombrero galaxy). The spectral signatures of various species and their transitions probe the motions of different kinematic tracers in the disc such as gas, stars, star clusters, and planetary nebulae. Among these tracers, HI 21 cm typically has a higher filling factor and extends much farther than the luminous stellar disc, allowing us to probe further out into the galactic halo. As an aside to the point of HI typically being more extended than luminous counterparts, we note that recent advances in telescopes, instrumentation, and photometric data processing have led to the detection of low surface brightness light in the outskirts of nearby galaxies, groups, and clusters (See Mihos (2019) for a review).

To illustrate the rotation of a galaxy, the rotation velocities are plotted as a function of distance from the centre. The first 'rotation curve' to be extracted was of the 'Andromeda nebula' by Pease (1918). Traditionally, rotation curves for nearby galaxies have been extracted from long-slit spectroscopic observations along the major axis (e.g., Pease 1918; Burbidge et al. 1959; Rubin et al. 1980) and single-dish observations of neutral Hydrogen and CO (e.g., Argyle 1965; Sofue 1996). Modern-day Integral Field Spectrographs and sensitive Interferometers enable us to extract the 3D gas distribution of galaxies and derive rotation curves for several emission lines in large samples of galaxies, such as: Hα (e.g., Bershady et al. 2010; Epinat et al. 2012; Di Teodoro et al. 2016; Förster Schreiber et al. 2018; Bizyaev et al. 2022; Olivares et al. 2022), HI 21 cm (e.g., de Blok et al. 2008; Iorio et al. 2017; Marasco et al. 2019; Murugeshan et al. 2020; Ponomareva et al. 2021; Piña et al. 2022; Deg et al. 2022), and CO (e.g., Lang et al. 2020; Su et al. 2022).

A technique known as tilted-ring modelling (bending model as first introduced by Rogstad et al. 1974) is commonly adopted to determine rotation curves from 2D velocity fields extracted from the 3D spectral-line data. Assuming that the emitting material is confined to a thin disc and that the kinematics is dominated by rotation, the disc can be divided into concentric rings (or annuli) having constant circular velocities. These rings are assigned certain intrinsic properties in the plane of the galaxy, such as thickness, surface density, etc. and also certain geometric properties induced by the galaxy's projection to the plane of the sky, such as the position angle and inclination. The rotation velocities of the rings are recovered from the observed line-of-sight velocities by solving the analytic fitting expression given by:

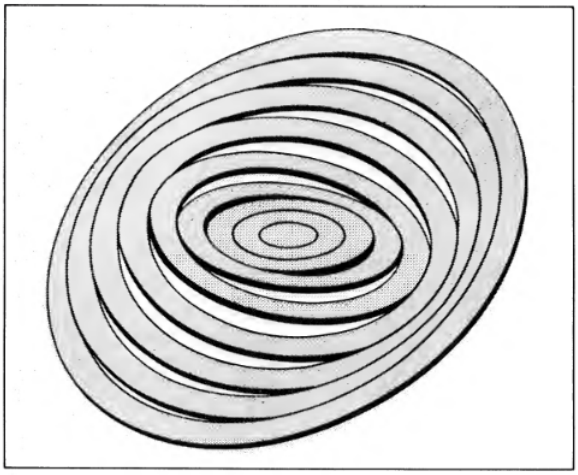

Figure 3.3: An illustration of a tilted ring model taken from Rogstad et al. (1974).

$$V_{los}(r) = V_{sys} + [V_{rot}(r)\ \cos(\theta) + V_{rad}(r)\ \sin(\theta)]\ \sin(i) \tag{3.4}$$

In equation 3.4 (Rogstad et al. 1974; Begeman 1987; de Blok et al. 2008; Di Teodoro & Peek 2021), $V_{los}(r)$, V_{sys}, $V_{rot}(r)$, and $V_{rad}(r)$ are the observed line-of-sight velocities, systemic velocity, rotational velocities, and radial expansion velocities respectively. Additionally, a fourth velocity component, $V_z(r)\cos i$, can be added to describe vertical motions perpendicular to the disc as discussed in Urrejola-Mora et al. (2022). However, compared to V_{sys} and V_{rot}, the contributions from V_{rad} and V_z to V_{los} are small. The azimuthal angle measured counter-clockwise from the major axis in the plane of the galaxy, θ, is related to the inclination, i, and the position angle, ϕ (angle measured counter-clockwise from North to the receding major axis), measured in the plane of the sky as follows.

$$\cos(\theta) = \frac{-(x - x_0)\sin(\phi) + (y - y_0)\cos(\phi)}{r}$$
$$\sin(\theta) = \frac{-(x - x_0)\cos(\phi) - (y - y_0)\sin(\phi)}{r\cos(i)} \tag{3.5}$$

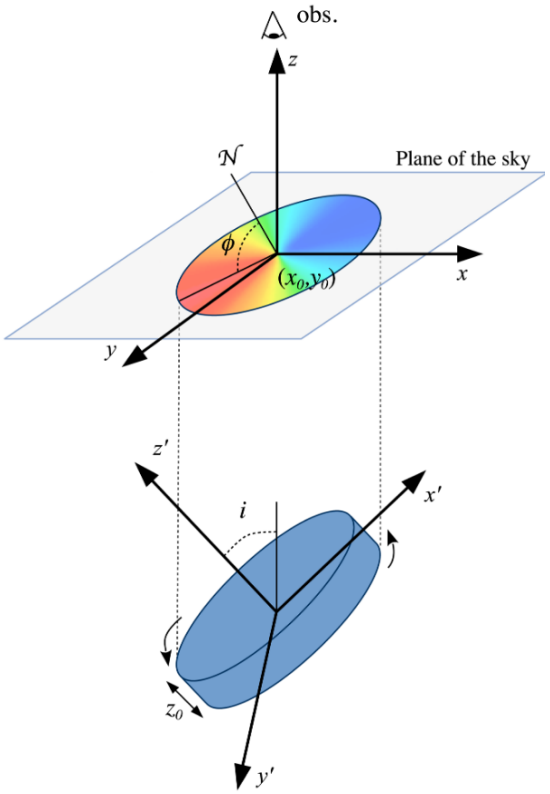

Figure 3.4: The model geometric parameters in the plane of the sky and in 3D (taken from Di Teodoro & Fraternali 2015).

Equation 3.5 (Begeman 1987) converts the sky position (x, y) measured in a rectangular coordinate system to a polar coordinate system (r, θ), where r is the radial distance from the centre (x_0, y_0). The observed line-of-sight velocity of the gas in the disc is a superposition of several projected velocities such as the systemic velocity, rotation velocity, radial motions (if any) and vertical motions (if any) (Di Teodoro & Peek 2021). The effect induced by all of these velocities is to shift the centroid of the spectrum. The velocity dispersion determines the width of the profile. Several different mathematical functions have been employed in the past to extract velocities from spectral-line data. These include intensity weighted mean along the velocity axis (Moment 1; Rogstad & Shostak 1971), single or multiple Gaussian functions (Begeman 1987; Oh et al. 2008), and Gauss-hermite polynomials (van der Marel & Franx 1993; de Blok et al. 2008) which incorporates an additional term for skewness.

There are several algorithms and packages that have been developed to perform 2D tilted-ring modelling. The most common is ROTCUR (van Albada et al. 1985), which fits a simpler form of the analytical function in 3.4 without the radial velocity component, using a Levenberg-Marquardt solver. Over the last three decades, several other 2D fitting algorithms have been developed to take into account non-circular motions and complex disc geometries. These include include RESWRI (Schoenmakers 1999), RINGFIT (Simon et al. 2003), KINEMETRY (Krajnović et al. 2006), DISKFIT (Spekkens & Sellwood 2007; Sellwood & Sánchez 2010; Sellwood et al. 2021), GBKFIT (Bekiaris et al. 2016), XOOKSUUT (López-Cobá et al. 2021), and 2DBAT (Oh et al. 2018). However, all these packages fit rotation curves to 2D velocity fields extracted from emission line data. The results of 2D tilted ring modelling can vary depending on the method adopted for velocity field extraction (de Blok et al. 2008). Further limitations are induced by the fact that the observed velocity profiles are subject to several systematic effects which can either be induced by the source geometry or the observations. Firstly, physical processes within the galaxy such as the presence of a bar, mergers, interactions, etc., can cause non-circular motions which are challenging to account for, even with

$V_{rad}(r)$ and $V_z(r)$ terms in equation 3.4 (Sellwood et al. 2021). Secondly, additional limitations are induced due to the fact that the derivation of an unambiguous velocity is difficult when the line-of-sight intersects multiple components of the galaxy such as thin disc, EPG, flares, etc. or when there are other projection effects introduced by the source geometry such as the case of edge-on systems wherein the line-of-sight intersects the disc twice or more (Di Teodoro & Fraternali 2015). Thirdly, instrumental and observational effects such as the finite size of the telescope beam can induce asymmetry and broaden line profiles in the central regions, leading to a slowly-rising rotation curve. This effect known as 'beam smearing', is more pronounced as the spatial resolution of the observation becomes poorer and the inclination angle of the galaxy increases (Begeman 1987). Lastly, tilted-ring modelling in general operates on a largely degenerate parameter space with well-known degeneracies between: rotation velocity and inclination; rotation velocity and dispersion; radial velocity and warps in position angle; and inclination and disc thickness (Begeman 1987; Józsa et al. 2007; Di Teodoro & Fraternali 2015; Kamphuis et al. 2015; Oh et al. 2018; Di Teodoro & Peek 2021). These degeneracies are particularly noticeable at lower resolutions due to beam smearing, as well as for irregular galaxies and dwarfs, and also for inclinations where $i \leq 40\,^\circ$ or $i \geq 70\,^\circ$. Moreover, tilted-ring modelling does not typically provide statistically meaningful uncertainties for the derived parameters and is highly sensitive to initial guess parameters. Some recent developments in 2D tilted ring modelling attempt to address some of these issues. These are, statistically valid uncertainty calculations put forth by Sellwood & Sánchez (2010), and MCMC-based automated tilted-ring analysis that is less affected by initial guesses and local minima of the model parameters developed by Oh et al. (2018).

3.5 3D Tilted Ring Modelling

A 3D tilted-ring modelling approach naturally solves most of the drawbacks of 2D modelling, while also removing the intermediate step of velocity field extraction. Careful implementations of the 3D approach for typical galaxies break some of the known degeneracies by fitting the radial surface brightness distribution alongside kinematic and geometric modelling (Józsa et al. 2007). Furthermore, the 3D approach allows for modelling complicated morphologies and kinematics across a wide range of disc geometries. However, unlike the 2D tilted-ring model, an analytic form for the fitting function in 3D does not exist. The package used in this work ^{3D}BAROLO (3D-Based Analysis of Rotating Objects from Line Observations; Di Teodoro & Fraternali 2015), constructs the model using a Monte Carlo extraction. The flexibility and the larger number of free parameters in the 3D approach come with a higher computational cost and a greater chance of the model converging to a local minimum of the function that is being minimized. Furthermore, 3D tilted-ring modelling is bound by some of the same limitations associated with tilted-ring analysis in general, such as the lack of statistically meaningful uncertainties (Sellwood et al. 2021) and sensitivity to initial parameters. ^{3D}BAROLO estimates the uncertainties for certain parameters through a Monte Carlo approach, where models are varied around the best fit until the residuals increase by some factor (typically 5%). While this remains a frequentist method based on ad hoc variations, the returned errors have been found to be consistent with the conventional methods of error reporting in tilted-ring analysis (Di Teodoro & Fraternali 2015). In our implementation, we take extra precautions by employing an iterative multistep approach to optimize the geometric and kinematic parameters sequentially (see section 3.5.1).

For completeness, other tools for 3D modelling that currently exist are: KinMS, which is used for creating mock interferometric data cubes with a realistic treatment of source brightness distribution, geometry, kinematics, projection effects, and observational effects (Davies et al. 2015); GALPAK3D, which is targeted towards high-redshift galaxies (Bouché et al. 2015); FAT/PYFAT, (Kamphuis et al. 2015) which is based on TIRIFIC (Józsa et al. 2007); GALACTUS, which includes a treatment for the self-absorption of HI gas (Peters et al. 2017); and QUBEFIT, which offers the flexibility to model high-z targets with non-thin-disc morphologies (Neeleman et al. 2021). While TIRIFIC has been developed for sophisticated modelling of local galaxies, ^{3D}BAROLO was designed to handle low-resolution data.

3.5.1 ^{3D}BAROLO

^{3D}BAROLO builds a number of artificial 3D models and compares them with the input cube until it obtains a set of geometrical and kinematic parameters that best describe the data. An artificial gaseous disc is constructed with a 3D tilted-ring model by using a stochastic function that randomly populates the space with emitting gas clouds. The disc is then divided into a set of concentric rings or annuli with a width conventionally given by $W = beam/2$. (Józsa et al. 2007; Di Teodoro & Fraternali 2015; Deg et al. 2022) The gas in each ring is defined in three spatial dimensions and with three components of the velocity. For data of sufficient quality and resolution, an additional fourth velocity component can be added to estimate the radial motions in the rings. Each ring of radius, R, and width, W, is described by the following geometrical and kinematic parameters, all of which are allowed to vary from ring to ring:

1. Spatial coordinates of the centre, (x_0, y_0)
2. Inclination angle, i, with respect to the observer (90° for edge-on)
3. Position angle, ϕ, of the major axis on the receding half of the galaxy, measured anticlockwise from the North direction on the sky
4. Systemic velocity, V_{sys}
5. Rotational velocity, V_{rot}
6. Velocity dispersion, σ_{gas}
7. Face-on gas column density, Σ
8. Scale-height of the gas layer, z_0

^{3D}BAROLO also comes with a source finder based on DUCHAMP (Whiting 2012), which can perform smoothing and masking before initializing the models. ^{3D}BAROLO can also automatically estimate the initial parameters for the fit. But since the model is sensitive to the initial parameters, we provide these separately. Where sources are sufficiently detected by SoFiA2 during the parameterisation step at the end of cube processing (section 2.9), we input initial values for $(x_0, y_0), V_{sys}$, and ϕ from the SoFiA2 catalogue (Kamphuis et al. 2015). SoFiA2 also performs ellipse fitting on the moment maps of the detected sources and we use the semi-major axis (a) and semi-minor axis (b) to obtain initial guesses for the inclination using $i = \cos^{-1}(b/a)$. In cases where the sources had to be manually separated, we obtain these initial guess values from either HyperLeda[8] or NED[9]. We assume a constant scale height and that the disc follows a sech^2

[8]https://leda.univ-lyon1.fr/
[9]The NASA/IPAC Extragalactic Database: ned.ipac.caltech.edu

profile along the vertical direction.

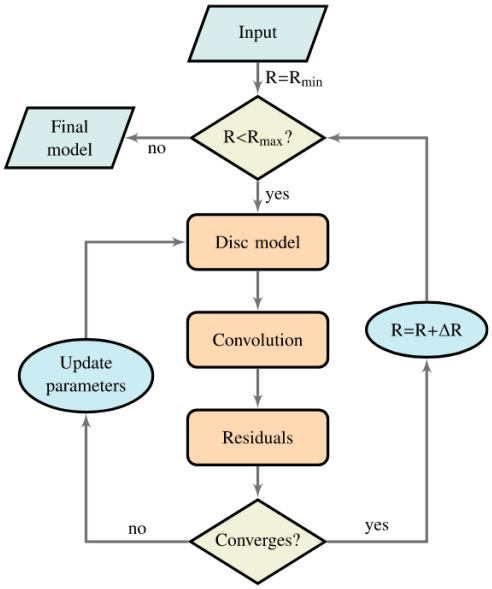

Figure 3.5: Flow chart taken from Di Teodoro & Fraternali (2015) showing the χ^2 minimisation implementation in ^{3D}BAROLO .

After a model has been created, it is further degraded to the same spatial resolution as the data by convolution with a 2D Gaussian representing the observed Point Spread Function (PSF). The degraded model is then projected into a 3D cube which contains two spatial dimensions and one spectral dimension. The model can also be normalized to either the zeroth-moment map of the observations pixel by pixel (local) or azimuthally (azim) to exclude the surface density parameter Σ of the gas from the fit. Residuals are then calculated by performing pixel-by-pixel comparisons between the model and the data. The averaged sum of the residuals over each pixel, F, given by equation 3.6, is then passed to the minimization algorithm, and this quantity is used to determine whether a model is suitable or not.

$$F = \frac{1}{n} \sum_{1=1}^{n} \Delta r_i w(\theta_i) \tag{3.6}$$

In equation 3.6, n is the number of pixels, Δr_i is the residual per pixel, and $w(\theta_i)$ is a weighting function. From the three residuals that ^{3D}BAROLO provides, we adopt the intermediate, $\Delta r = |M - D|$, where M and D are flux values of the model and data, respectively.

Dynamical structures in the disc including lopsidedness, bars, spiral arms, warps, and non-circular motions can often lead to drastic variations in ϕ and i from ring to ring (Di Teodoro & Fraternali 2015; Oh et al. 2018). Fitting the geometrical and kinematic parameters simultaneously can lead to unphysical discontinuities in the derived rotation curve. After deriving a first model by fitting all the free parameters together, ^{3D}BAROLO automatically performs parameter regularization, wherein the geometrical parameters are fixed to a functional form, before proceeding to the second fitting step where only the dispersion velocity and the rotation velocity remain as free parameters. The functional form for interpolation and regularization during the second step is automatically chosen by the algorithm as a median value, a polynomial, or a Bezier function. A key consideration here is the adopted ring width which affects the choice of the functional form by shaping the interpolation intervals. The conventional choice of $W = beam/2$ implies that the rings are not independent because of the spatial coherence induced by the beam. But sampling the disc with more points allows for smaller intervals and thus smoother interpolation functions. The alternative is to choose a width, $W \sim beam$, which provides independent rings but reduces the number of rings and thus broadens the interpolation intervals. Although the models produced with both ring widths are similar, the conventional choice provides smoother functional forms. Hence, we adopt the conventional choice of having two rings per beam.

Aside from the two-step fitting in ^{3D}BAROLO , we employ a three-stage modelling approach

similar to Di Teodoro & Peek (2021), wherein the first stage is the geometric stage, the second is the kinematic stage, and the third is the radial velocity stage. Although not trivial, it is possible to disentangle the relative contributions of radial motions and warps to the observed line-of-sight velocity V_{los} through kinematic modelling, as these effects have different impacts on various regions of the disc. As shown in figure 1 of Di Teodoro & Peek (2021), a warp produces bending of the kinematical major and minor axes while radial motions only introduce an offset between the systemic velocity (V_{sys}) and V_{los} along the minor axis. During the first stage, the inclination (i), position angle (ϕ), centre of the rings ($(x_0, y_0), V_{sys}$), rotation velocity (V_{rot}), and velocity dispersion (σ_{gas}) are fitted as free parameters in each ring. In this stage, the model is normalised to the azimuthally averaged flux in each ring to accurately determine the functional forms of the inclination and the position angle. In the second stage, only the rotation velocity and velocity dispersion are fitted as free parameters and all the other parameters are fixed to their respective functions recovered in the first stage. In this stage, a pixel-by-pixel normalisation is adopted to allow for a non-axisymmetric model in density. In the third and final stage, all the parameters except V_{rad} are fixed to their previously fitted functional forms and only the radial velocity is fitted as a free parameter. In all the stages we maintain a constant scale height (z_0) of a few hundred pc ($\sim 400 - 500$ pc). In the first two stages, we adopt $w(\theta_i) = |\cos\theta|^2$ as the weighting function in equation 3.6, to give more weight to the pixels near the major axis, where most of the information about rotation velocity and warps resides (Di Teodoro & Peek 2021). In the third stage, we adopt $w(\theta_i) = |\sin\theta|^2$, to give more weight to the pixels near the minor axis, where radial motions are expected to have a stronger effect. In ^{3D}BAROLO positive and negative v_{rad} in a disc rotating in the anti-clockwise direction implies inflow and outflow motions respectively. The signs reverse for discs rotating in the clockwise direction. Furthermore, we also model the approaching side and receding side separately to study the asymmetries potentially induced by interactions with neighbouring galaxies. In the end, we obtain 3 model cubes - 'R', 'A', and 'B' for receding, approaching and both side models respectively.

3.6 Gaussian Decomposition

A spectral cube holds a wealth of information about the kinematics of the gas. Most of the analysis techniques introduced in the previous sections, in their simplest forms, are based on an inherent assumption that the entire volumetric gas distribution can be represented as a single coherently rotating structure. However, the gas distribution is a superposition of several clouds with distinct kinematics filtered through various observational and systematic effects. There are several factors to be considered before attempting to recover the individual kinematic components from the observed gas distribution. The projection effects can be minimized by selecting targets with a low-intermediate inclination. The systematic effects introduced by the observation and method can be alleviated to some extent by sufficiently sampling ($\gtrsim 10$ beams across the major axis) a gas distribution with an optimum spatial and spectral resolution. Even then, the spatial coherence introduced by the beam must be considered carefully to limit the systematics.

Each spatial pixel in a cube, known as a spaxel has an associated spectrum which can typically be modelled with either a single component or multiple components defined by some mathematical function. For such models, the most commonly adopted mathematical function is the Gaussian

function for its simplicity and compatibility with the observed emission spectra. The assumption of the model shape is further supported by the fact that the random thermal and non-thermal motions in the gas lead to Doppler motions with a Gaussian distribution. A spaxel can be decomposed into Gaussian components given by:

$$G(z; A_i, \mu_i, \sigma_i) = \sum_{i=1}^{n} \frac{A_i}{\sqrt{2\pi}\sigma_i} \, e^{\left(\frac{-(z-\mu_i)^2}{2\sigma_i^2}\right)} \tag{3.7}$$

Where n is the total number of components with each i^{th} component defined by amplitude A_i, mean or velocity centroid μ_i, and dispersion σ_i. The Full Width at Half Maximum (FWHM) can be calculated from the dispersion as FWHM $= 2\sqrt{2\ln(2)}\sigma_i$.

However, modern-day spectral cubes contain thousands of spectra, which introduce challenges in terms of computation and interpretation. To model the emission as a superposition of n independent Gaussian components, a non-linear optimization problem with $3n$ parameters must be solved in a non-convex parameter space (Lindner et al. 2015). That is, the multi-dimensional parameter space contains local optima instead of a single, global optimum which introduces a dependency on the initial guesses (n, A_i, σ_i, μ_i). Radio astronomical packages such as CASA, AIPS, and GIPSY offer the functionality to perform non-linear, least squares, multi-component profile decomposition using the Levenberg-Marquardt algorithm. But providing initial guesses manually for thousands of spectra is time-consuming and subjective. Several tools have been developed for semi-automatic (PySpecKit: Ginsburg & Mirocha 2011; Ginsburg et al. 2022b; ScousePy: Henshaw et al. 2016, 2019) and automatic spectral decomposition (Procedural algorithms: Haud 2000; Nidever et al. 2008; Bayesian approaches: Allison et al. 2012, BAYGAUD - Oh et al. 2019; Topology based algorithms: Whiting 2012; Machine learning based approaches: GaussPy - Lindner et al. 2015, GaussPy+ - Riener et al. 2019; Algorithms with conditions for spatial coherence: Miville-Deschênes et al. 2017, ROHSA - Marchal et al. 2019; Algorithm based on derivative spectroscopy: BTS - Clarke et al. 2018).

From reviewing the existing packages for Gaussian decomposition, we highlight some important considerations for an ideal workflow for decomposing an HI 21 cm spectral cube.

1. χ^2 minimization requires initial guesses to avoid converging to local optima.
   (a) Automate initial guesses by employing derivative spectroscopy.
   (b) Enforce conditions for ensuring spatial coherence.
   (c) Use a Bayesian approach for parameter estimation.
2. How to discern between multiple models?
   (a) Use corrected Akaike Information Criterion (AICc) or Bayesian Information Criterion (BIC) for model selection.
   (b) Use Bayesian evidence and Bayes factor for model selection.
3. Dealing with deviations from the description of the emission as a sum of Gaussian components: PPV (position-position-velocity) is not the same as PPP (position-position-position), velocity blending, ambiguities in the number of components, non-Gaussianity, noise peaks, plurality of solutions.
   (a) Perform simultaneous fitting and favour solutions that account for spatial coherence.

   (b) Employ smoothing and derivative spectroscopy to identify the number of components and avoid noise peaks.
   (c) Employ tests for quality control.
4. Optimal use of computing resources
   (a) The package has to be optimized to simultaneously fit all the spaxels with sufficient SNR within a reasonable time and using the lowest possible computing power.

In the following subsections, we describe two fully automated approaches for Gaussian decomposition, BAYGAUD and GAUSSPY+ . We place more emphasis on the latter as it fits our use case better and the output products are easier to handle. Our goal is to decompose the profiles of a spectral cube above $2.5\bar{\sigma}_{rms}$ into an optimum number of Gaussian components. We impose certain constraints to ensure the decomposition's physical validity and prevent over-fitting of the spectra. Both methods are constrained to a maximum of three components but GAUSSPY+ allows for imposing additional physically motivated constraints.

3.6.1 BAYGAUD

BAYGAUD is an automated Gaussian decomposition tool based on the Bayesian nested sampling framework (Oh et al. 2019, 2022; Kim & Oh 2022; Wang et al. 2023). The Bayesian approach is more efficient than a least squares algorithm in sampling a high-dimensional parameter space and is less likely to converge to a local minimum. The broad range of priors adopted in BAYGAUD for each parameter eliminates the need for initial guesses. BAYGAUD utilizes nested sampling to simultaneously estimate both the evidence and the posterior to perform parameter estimation and Bayesian inference. For each spectrum, BAYGAUD generates a set of live points to sample the $4N$-dimensional parameter space (where N is the number of components) defined by the priors. For every spectrum that meets the SNR threshold, the package fits Gaussians starting from a single component to models with the maximum number of components, N, assigned by the user. The optimal model is then selected based on the Bayes factor which is calculated as the ratio of the likelihoods of the data given each model, after integrating all possible values of the parameters. Even though the results of BAYGAUD are likely more reliable than that of a least squares method, BAYGAUD is computationally expensive. We tested two versions of the package BAYGAUD: the original version written in FORTRAN/C, which uses MULTINEST for nested sampling, and a recent PYTHON package that uses DYNESTY for nested sampling. We attest to the potential of BAYGAUD but note that at the time of the writing of this thesis, the package is still in its early stages of development.

3.6.2 GAUSSPY+

GAUSSPY+ (Riener et al. 2019) is an automated decomposition package based on the GAUSSPY algorithm (Lindner et al. 2015) but with additional physically-motivated considerations for fitting the gas distribution observed by an interferometer. The GAUSSPY algorithm performs machine learning-assisted per-pixel spectral decomposition by automatically determining initial guesses for the Gaussian components using derivative spectroscopy (see figure 1 in Lindner et al. 2015). This technique smooths the spectrum and finds the functional maxima and minima of the smoothed spectrum to distinguish real emission features from noise peaks. We employ the two-phase decomposition procedure where two Gaussian kernels (α_1 and α_2) are utilized to filter the

noise (denoising) before calculating higher order derivatives for each of the smoothed spectrum. Such a two-phased approach to denoising is useful for the decomposition of datasets that show a mix of both narrow and broad line widths. The success of derivative spectroscopy is related to the optimal choice of the smoothing kernels for the original spectra. To limit subjectivity and avoid iterations of trial-and-error, the GaussPy algorithm implements a supervised machine learning approach. The algorithm employs a momentum-driven gradient descent technique on a user-supplied training set of a couple of hundred well-fit spectra to find values for α_1 and α_2 that yield the most accurate decomposition on the training set.

GaussPy+ improves upon the GaussPy algorithm (see figure 3.6) by including (i) automated preparatory steps for noise calculation and for training set creation from the input data; (ii) automated quality checks for the decomposition results; and (iii) automated routines that check the spatial coherence of the decomposition and in case of conflicts, attempts to refit the spectrum based on the models of the neighbouring spaxels. The two phases of spatially coherent refitting incorporate the information from neighbouring spectra for refitting. In the first phase which checks for local spatial coherence to account for the beam, fits that differ from their immediate neighbours are flagged and attempted to be refit. In the second phase, a weighting scheme is used to enforce a global form of spatial coherence, wherein, the entire data set is checked for consistency between the centroid velocities of components in neighbouring spectra. Refitting iterations are performed for all the flagged spectra. In cases where multiple models can be used to describe a spectrum, $\chi^2_{\rm red}$ cannot be used to discern between the models, as the degrees of freedom cannot be reliably estimated in such cases of non-linear models (Andrae et al. 2010; Riener et al. 2019). GaussPy+ utilizes the corrected Akaike Information Criterion (AICc) for model selection, as it penalises the use of a large number of fit components that do not contribute to a significant increase in fit quality. Along with the flow chart in figure 3.6, we provide here a brief description of the workflow in the appendix section A. For an in-depth explanation of the functionality, discussion, and assumptions involved, see Riener et al. (2019).

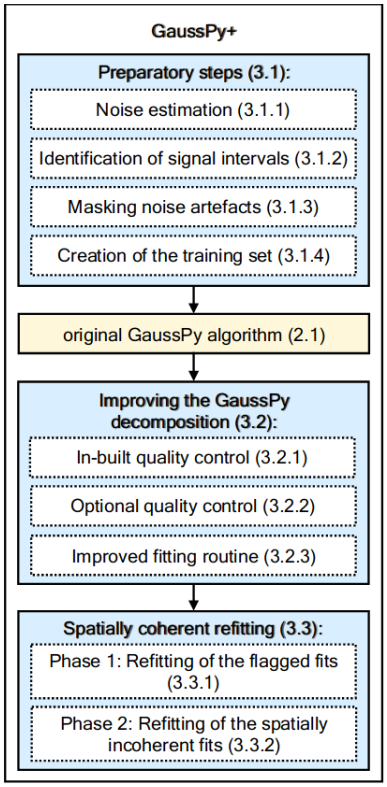

Figure 3.6: Flow chart taken from Riener et al. (2019) showing the enhancements in GaussPy+ .

3.7 Kinematic Separation

The Gaussian decomposition produces either a single or multiple component model for the spaxels with an SNR above $2.5\bar{\sigma}_{rms}$. This section deals with the classification of these components into disc and anomalous components. We review three methods for classification and discuss our custom approach in depth.

3.7.1 Fitting the peak

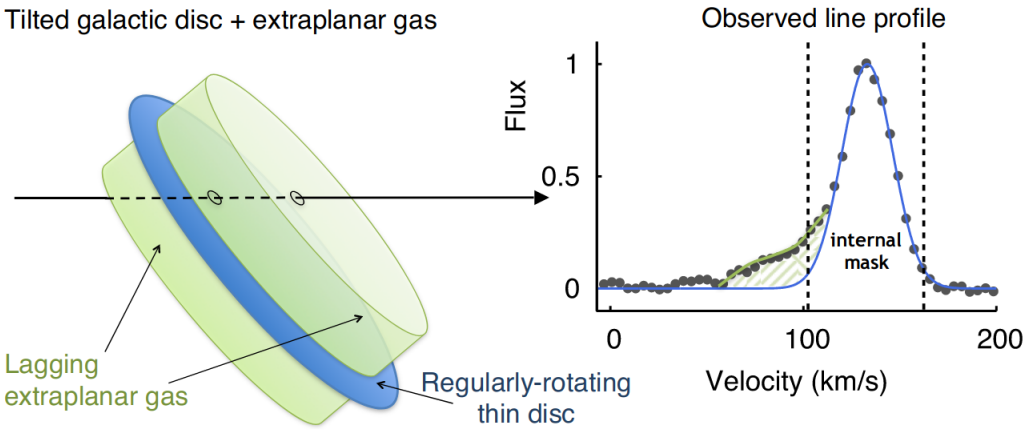

Figure 3.7: Sketch taken from Marasco et al. (2019) showing the observation of extraplanar gas in a moderately inclined galaxy. The blue solid line shows the Gaussian fit to the 40% of the peak of the profile. The green hatched region shows the asymmetric tail identified as EPG.

The technique for separating anomalous gas from the disc pioneered by Schaap et al. (2000) and Fraternali et al. (2002) involves fitting a single Gaussian to the peak of the HI profiles in the spectral cube to isolate emission from the disc. The technique relies on the assumption that the kinematics of the anomalous gas differs from that of the regularly rotating disc and thus occupies distinct locations within the galaxy. For a thin disc with a moderate inclination observed with sufficient resolution, a slowly rotating extraplanar gas (EPG) layer is seen as an asymmetric tail extending towards the systemic velocity (see figure 3.7). The asymmetric tail typically vanishes around the minor axis unless non-circular motions are also present. For the assumption to hold, it is paramount to ensure that beam smearing and projection effects do not influence the shape of the line profile. This technique of fitting a fraction of the peak with a single Gaussian representing the emission from the disc has been adopted to separate disc and EPG in various works (e.g., Fraternali et al. 2002; Hess et al. 2009; Marasco et al. 2019; Randriamiarinarivo et al. 2022; Veronese et al. 2023). While the recipe and assumptions remain more or less the same in all of these works, they often differ in the fraction of the peak fitted. Marasco et al. (2019) apply this technique to study the EPG in a sample of 15 moderately inclined galaxies. They fit the upper 40% of the peak with a Gaussian component and develop an internal mask to mask out all emission from the fitted channels above a 2σ threshold. They further convolve the non-parametric, approximate, disc model cube with the data beam to account for beam smearing. Beam smearing typically becomes prominent in the inner regions of the disc where the rotation curve has a steep gradient. The techniques discussed in Marasco et al. (2019) were adopted to avoid contamination from the disc emission in order to recover reliable EPG parameters within their assumptions. Recently, Randriamiarinarivo et al. (2022) implemented a similar technique for isolating anomalous gas, but with values for identifying peak emission determined via experimenting on a sample of noise-free, simulated model cubes without a beam.

The model obtained from fitting just the peak can often be an inaccurate representation of the complete profile. This would result in unphysical artefacts in the EPG cube due to improper subtraction of the disc component. Further, convolving the non-parametric disc model cube with the data beam broadens the profile in the central regions. While this sounds reasonable,

the total flux in the fitted profile is redistributed and the peak of the disc component is lowered. Subtracting this smeared disc model from the data cube will result in residual flux at peak velocities, thus artificially introducing a rotation in the EPG layer, albeit with a lower 'lag'. Furthermore, while modelling the EPG, it is paramount to avoid contamination from the disc (Marasco et al. 2019). Therefore, convolving with the beam to smear the fitted disc component only makes sense if the internal mask approach implemented in Marasco et al. (2019) is adopted. However, this conservative approach of masking all the emission in the fitted channels above a threshold overestimates the contribution of the disc component and therefore only accounts for a fraction of the anomalous gas. Moreover, when dealing with interacting systems, the anomalous gas is unlikely to just be a low-intensity asymmetric tail in the spectra expected for a lagging EPG. An ideal anomalous gas separation method must be sensitive to all possible spectral features that can be introduced by the interactions.

3.7.2 BAYGAUD

BAYGAUD classifies the components in two ways: (i) according to the bulk kinematics and (ii) according to the dispersion (Oh et al. 2018). The latter approach assumes the dispersion of the components as a proxy for the kinematic temperature of the associated gas clouds. The former classification based on bulk kinematics compares the components with a reference velocity map and identifies rotating and non-rotating components. We utilize the first-moment map of the ^{3D}BAROLO model of the disc as the reference velocity map. The classification routine iterates through the fitted spaxels and identifies all the components with a velocity centroid, μ_i, that falls within a range centred on the reference velocity at the spaxel as 'bulk'. The range is determined by a dispersion value which can be supplied as a 2D map. We supply the second-moment map from the ^{3D}BAROLO model. If no dispersion map is supplied, the routine utilizes the dispersion values from the single component fits. All the components with a centroid value that is outside this broad range are classified as 'non-bulk'.

The classification criteria for each spaxel is as follows:

Bulk: $\mu_{ref} - f\sigma_{ref} < \mu_{component} < \mu_{ref} + f\sigma_{ref}$

Non-bulk: $\mu_{component} < \mu_{ref} - f\sigma_{ref}$ or $\mu_{component} > \mu_{ref} + f\sigma_{ref}$

Where f is a constant factor to adjust the range considered as bulk and σ_{ref} is defined by either the user supplied dispersion map or the dispersion of the single component models.

The bulk classification technique implemented in BAYGAUD has the following drawbacks:

1. The reference velocity field, which is often the first-moment map of a disc model, is different from the peak velocity field. That is, the μ_{ref} for a spaxel is offset from the velocity centroid of the peak, μ_{peak}.
2. While the above drawback can be mitigated to an extent by adopting a broad range for the bulk classification, this approach adds an additional level of arbitrariness.
3. The classification scheme does not differentiate between EPG and the thin disc.
4. Each spaxel is treated independently and the spatial coherence in the data is not considered.

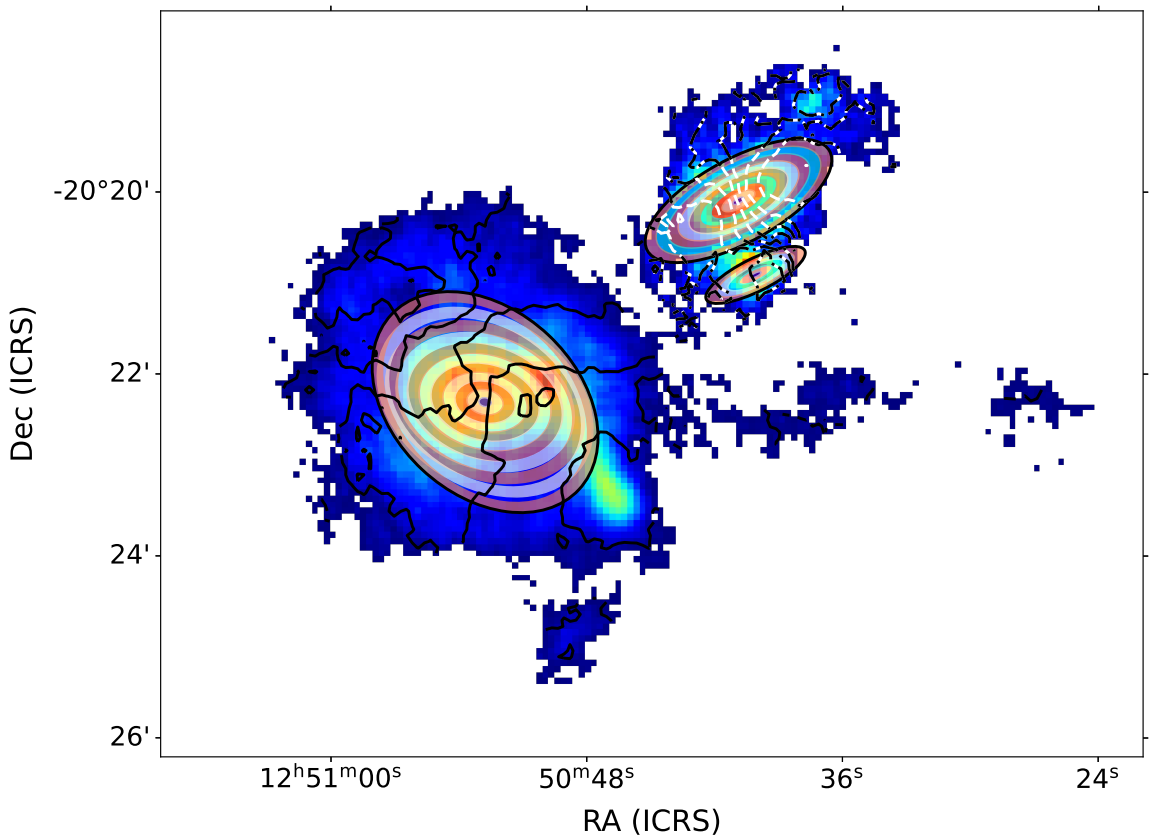

Figure 3.8: Plot illustrating the rings defined for the ring by ring tagging on S1 in J1250-20 (see chapter 4). In S1 The first 3 rings are treated as the rising rings and the rest as flat rings. Whereas in S2, due to beam smearing, all the rings are treated as rising rings and no AG components are tagged within the rings. The final ellipse defined by the last ring is used as a mask to separate the tail and the disc. All the fitted components outside this mask are tagged as 'NDAG'.

3.7.3 Ring by ring tagging

We developed a method to classify the components from Gaussian decomposition using the 3D ^{3D}BAROLO model cube as reference (see section 3.5.1). In this work, we adopt the 'B' model without radial velocities for the tagging step. The component tagging happens ring by ring, where rings are defined by the annuli defined for fitting the ^{3D}BAROLO model (see annuli plotted in figure 3.8). This allows the user to tailor the tagging approach to each ring and makes it possible to account for beam smearing in the rising rings. One possible customisation is for tagging intruder components, such as that of a dwarf within the HI envelope of the galaxy. The tagging happens in two phases, in the first phase the disc component(s) are identified by comparison with the ^{3D}BAROLO model. In the second phase, the anomalous components are identified by comparison with the disc component. All the fitted components are classified into one of 4 categories: '**disc**', '**EPG**' (lagging component), '**FC**' (fast/leading component) and '**NDAG**' (non-disc anomalous gas). In phase I, the main assumption for tagging the disc component in the rings tracing the flat part of the rotation curve is that the disc emission can be represented by a single component. The component with the maximum amplitude and minimum velocity separation from the ^{3D}BAROLO model's peak is tagged as the disc component. Multiple components can be tagged as disc in the rings with rising rotational velocities to account for beam smearing. All the spaxels that do not have a corresponding ^{3D}BAROLO model are tagged

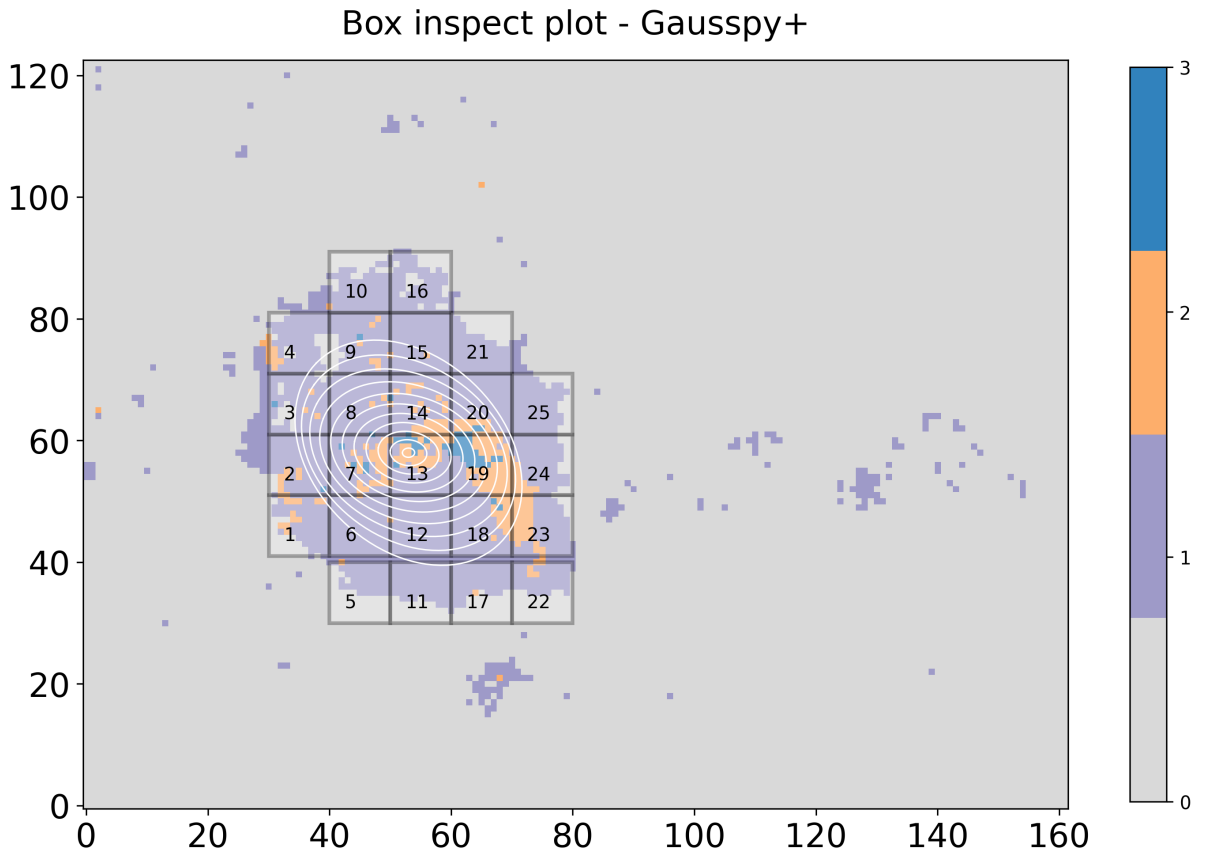

Figure 3.9: Plot illustrating the map of the fitted components of J1250-20 S1. Each numbered box contains 120 spectra most of which are fitted. Each box represents a document of all the spectra within the box. The documents containing the spectra are used for inspection. The colorbar shows the number of components fitted to a spectrum.

as '**NDAG**'. In phase II, the components with velocity centroids lower (closer to V_{sys}) than that of the disc component are tagged as '**EPG**' and the components with velocity centroids greater (farther from V_{sys}) than that of the disc component are tagged as '**FC**'. The condition is different for approaching and receding sides to account for lagging and leading motion projected along the line of sight.

The algorithm for identifying '**disc**', '**EPG**', and '**FC**' components is as follows:

Phase 1: **disc** component identification in each fitted spectra in all the rings.

The data spectral cube and ^{3D}BAROLO model cube are given as input. If a channel range is not specified, it is adopted as the model FWHM at the spaxel, which is calculated from the dispersion map of the ^{3D}BAROLO model. The variables important for the classification are as follows. v_{ref}^{peak} - velocity of the peak of the ^{3D}BAROLO model spectrum of a spaxel, μ_i - velocity centroid of the component, A_i - amplitude of the component, $\bar{\mu}_{nb}$ - mean velocity centroid calculated from the neighbouring disc components, and $\bar{A}_{nb}$ - mean amplitude calculated from the neighbouring disc components.

1. Case 1: Spectra that are fitted with a single component and that also have a corresponding ^{3D}BAROLO model with a peak intensity higher than the RMS are classified as **disc**.
2. Case 2: Spectra that are fitted with single or multiple components but **do not** have an

associated ^{3D}BAROLO model with a peak intensity higher than the RMS are classified as **NDAG**.

3. Case 3: Spectra that are fitted with multiple components and also have a ^{3D}BAROLO model with a peak intensity higher than the RMS are tagged as follows.
   (a) Check 1: Check the number of components within v_{ref}^{peak} − channel limit and v_{ref}^{peak} + channel limit.
      i. If there is only one component within the range and it is both the closest component to v_{ref}^{peak} and also the component with maximum amplitude in the decomposed spectra, it is labelled as **disc**.
      ii. If there are multiple components within the range or if the component closest to v_{ref}^{peak} does not also have the maximum amplitude then the component with maximum A_i is tagged as the **disc**. But the next check is also performed.
      iii. If the spectrum is in the rising rings then all the components with an amplitude, A_i, greater than 60% of the maximum amplitude are tagged as the '**disc**'.
   (b) Check 2: If there are multiple components with an A_i value that is above 75% of the maximum A_i, then spatially coherent tagging is performed.
      i. From the 8 immediate neighbouring spectra, the ones with an unambiguous disc component are selected and the following are calculated: (1) mean centroid of the local disc components, $\bar{\mu}_{nb}$, and (2) mean amplitude of the local disc components, $\bar{A}_{nb}$. The number of components within $\bar{\mu}_{nb}$ − channel limit and $\bar{\mu}_{nb}$ + channel limit are also calculated.
      ii. If there is only 1 component within the range and if it is both the closest component from $\bar{\mu}_{nb}$ and the component with the maximum amplitude in the decomposed spectra, it is tagged as the **disc**.
      iii. If there are multiple components within the range or if the component nearest to $\bar{\mu}_{nb}$ does not also have the maximum amplitude, then the next check is performed.
      iv. Check 3: Check if the component with the minimum difference with the mean local amplitude ($\Delta A_i = |A_i - \bar{A}_{nb}|$) is the same as the component nearest to $\bar{\mu}_{nb}$. If true, the component is tagged as the **disc**.
      v. If there are multiple components with an A_i value that is above 75% of $\bar{A}_{nb}$, then flag the spaxel but assign the component with the smallest value for ΔA_i as the **disc** component.

Phase 2: **EPG** and **FC** component tagging is performed for fitted spectra with at least one disc component. The tagging is based on expectations obtained from transferring the rest-frame velocities to projected line-of-sight velocities. When referring to a lagging EPG or a faster velocity component, we do so within the context of an inertial frame centred at the galaxy, where the primary motion is rotation around the centre of the frame. The rotation can be roughly measured as the difference between the observed line-of-side velocity (V_{los}) and systemic recession velocity (V_{sys} in equation 3.4). In the approaching side, since the rotation is towards the observer, the observed line-of-sight velocities will be less than the systemic recession velocity. Thus resulting in the negative velocities obtained in the galactic frame. Similarly, since the projected rotation component along the line-of-sight in the receding side is directed away from the observer, the observed line-of-sight velocities will be higher than V_{sys}, leading to positive velocities in the

galaxy's frame. A lagging EPG would manifest in a similar fashion but with a lower rotation velocity with reference to the disc's rotation velocity and a faster component will have a higher velocity with respect to the disc's rotation. In the line-of-sight frame, EPG components tend towards systemic velocity and the FC tend away from the systemic velocity. This means that in the receding side, the EPG component's line of sight velocity will be lower than the disc's V_{los} but greater than V_{sys} and the FC's line of sight velocity will be greater than the disc's V_{los} but less than V_{sys}. In the approaching side, the EPG component's V_{los} will be greater than the disc's V_{los} but less than V_{sys} and the FC's V_{los} will be lower than the disc's V_{los} but greater than V_{sys}.

In the end, we save all the Gaussian components into their respective cubes and treat them similarly to the data cube to produce PVDs, moment maps, etc.

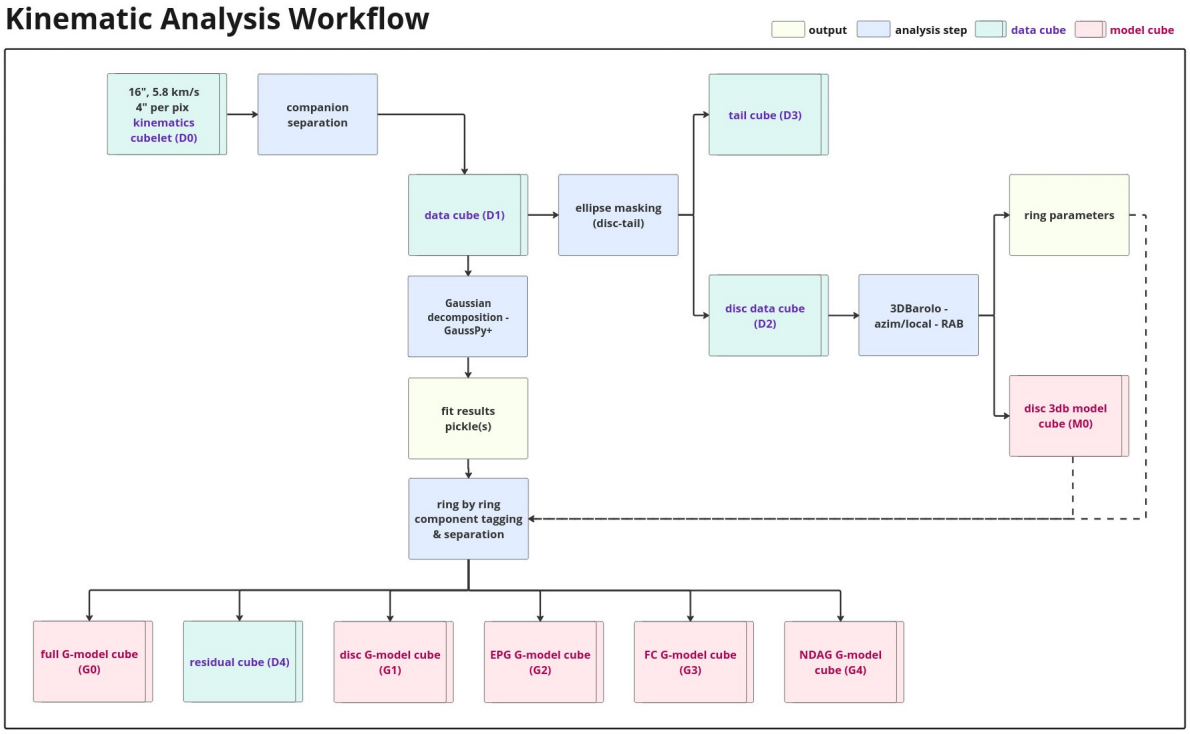

Figure 3.10: Flow chart depicting the kinematic analysis workflow adopted in this work. Pink cuboids indicate model cubes (G0-G4, M0), green cuboids indicate data cubes (D0-D3), blue rectangles indicate operations and yellow rectangles indicate output files that are used in the workflow. The end result of ring-by-ring tagging and separation is the Gaussian model cubes obtained for each component. ^{3D}BAROLO models are also obtained for the Receding side (R), Approaching side (A), and Both sides (B).

3.8 Physical Parameters

The observed specific intensity, I_v, in units of Jy beam^{-1} when divided by the beam area, $\Omega_{\rm beam}$, (equation 3.8) and integrated across the spatial extent of the source gives flux density, S_v, in Jy per pixel as given by equation 3.9.

$$\Omega_{\rm beam} = \frac{\pi B_{\rm maj} B_{\rm min}}{4ln(2)\Delta x \Delta y} \tag{3.8}$$

Where Δx and Δy are the 'cellsizes' (solid angle of the sky contained in a single pixel) of the

cube and $B_{\rm maj}$ and $B_{\rm min}$ are the major and minor axes of the beam respectively.

$$\left(\frac{S_v}{\rm Jy}\right) = \frac{1}{\Omega_{\rm beam}} \int_{\Omega_{\rm src}} I_v(\theta, \phi) d\Omega \tag{3.9}$$

Flux in units of Jy $\rm km\,s^{-1}$ is obtained when the cube with flux density, S_v, is collapsed to create a total intensity image (zeroth moment). The flux measurement encompasses the full volume of the source by integrating across the velocity axis (see equation 3.1 and 3.10).

$$\left(\frac{S}{\rm Jy\ km\ s^{-1}}\right) = \int S_v dv \tag{3.10}$$

In equations 3.11 and 3.12, we use observed flux, $S_{\rm obs} = S \times \Omega_{\rm beam}$, in units of Jy $\rm beam^{-1} kms^{-1}$.

3.8.1 Column density

HI column density ($N_{\rm HI}$) is defined as the number of atoms per unit area along the line of sight through an optically thin emitting cloud (Hibbard et al. 2001; Meyer et al. 2017). The sensitivity of an observation is determined by the telescope properties, observational setup, target declination, applied weighting etc. and it represents the lowest column density gas cloud that an observation can detect, assuming the cloud fills the entire synthesized beam. If the cloud does not fill the entire beam then we detect it at lower than its peak column density due to beam dilution. If a low-resolution (bigger beam) observation detects the same cloud as a high-resolution (smaller beam) observation but at a lower column density, it implies that the low-resolution observation cannot differentiate between a low-density cloud and a high-density clump within the beam. In this section, we discuss the considerations required for the estimation of the lowest column density contour in the column density map, which differs from the sensitivity of the observation.

$$\left(\frac{N_{\rm HI}}{\rm cm^{-2}}\right) = 1.104 \times 10^{24} \times \left(\frac{S_{\rm obs}}{\rm Jy\ beam^{-1}\ km\ s^{-1}}\right) \left(\frac{B_{maj} \times B_{min}}{arcsec^2}\right)^{-1} \tag{3.11}$$

The above relation converts the total intensity image introduced in 3.2 to a map of the gas columns along the line of sight. Column density maps can offer insights into the spatial extent of a radially declining gas distribution and also indirectly serve as a rough illustration of the sensitivity of the observation. There are various ways of defining the lowest column density in the literature and a rigorous estimation must consider certain important caveats.

The RMS noise, σ_{rms}, in the cube provides a representative baseline for comparing emission across cubes as much like the signal, it also varies across cubes depending on the data processing techniques. But when a cube is collapsed into a total intensity map, the RMS per pixel in the 2D map becomes non-uniform (e.g., Healy et al. 2021). The conventional 3σ definition overestimates the lowest column density level (i.e. lower column densities than actual) as it does not account for the number of channels summed over. Upon incorporating the number of channels integrated into the intensity map, the actual 3σ level becomes $3\sigma_{rms}\sqrt{N_{channels}}$. However, when a 3D mask is employed to account for the variable number of channels in each pixel, the summation

of channels to create a 2D map differs for each pixel. The challenge is to recover a reliable limit from the column density map by accounting for the non-uniform noise distribution. In this work, we use the term "column density limit" to refer to the lowest column density contour defined in the column density map.

The approach adopted in SIP estimates the column density limit by calculating the median of the observed flux in pixels with an SNR within a specified range (default is [2,3]; see Healy et al. (2021) for a similar implementation). The signal-to-noise ratio (SNR) in each pixel in the total intensity map is calculated as SNR = $\Sigma S_i/(\sigma_{rms}\sqrt{N_{channels}})$. Where ΣS_i is the total observed flux density across ($N_{channels}$) per pixel and the noise in each pixel is given by $\sigma_{rms}\sqrt{N_{channels}}$. However, since the SNR is different for each pixel, the proportion of high-SNR and low-SNR pixels will affect the median calculation. A higher fraction of high-SNR pixels will skew the median towards a column density limit that is higher than the conventional 3σ level and a higher fraction of low-SNR pixels will skew the median towards a lower column density limit. A choice of a narrow SNR range, like what we adopt in this work, will reduce the magnitude of the skew of the column density limit. But we nonetheless provide an exploration of this behaviour for future users to make informed decisions. The proportion of the high and low SNR pixels is dependent on (i) the beam and the imaging weight adopted, (ii) the binning factor (or cellsize), (iii) the channel width, and (iv) the smoothing kernels used in SoFiA2 for source finding.

1. Spatial smoothing decreases the noise by the ratio of the beam areas. Thus, bigger beams lead to a greater number of low-SNR pixels, which skews the median towards lower column density levels. However, the larger beam dimensions cause a decrease in the calculated N_{HI} value according to equation 3.11. The weighting adopted during imaging affects both the beam dimensions and the noise distribution.

2. The binning factor or 'cellsize' used for producing the cube will further dictate the number of available pixels within a specified SNR range. An over-sampled cube would have a higher fraction of low-SNR pixels than a reasonably sampled cube and lead to a lower column density limit.

3. The cube's channel width must represent the emission line's inherent dispersion. Spectrally smoothing the data decreases the noise by the square root of the number of channels smoothed over. This further increases the number of high-SNR pixels within a specified SNR range and leads to a higher column density limit.

4. The smoothing scales used for SoFiA2 S+C will determine the size of the mask and therefore the amount of masked emission. If large smoothing kernels are employed to detect extended signals, then a larger fraction of low-SNR pixels will be incorporated into the column density image. However, the kernels are bound by physical limitations, as one cannot expect to detect gas beyond a particular spatial extent, which is often subjective. Conversely, if the smoothing kernels are chosen conservatively, then the column density image would contain a higher fraction of high-SNR pixels and could miss some extended low-column density emission.

We also find that if a threshold mask were applied to the cube before it is collapsed, $3\sigma_{chan}$ can be a reasonable contour level. In this work, we followed the SoFiA2 convention and integrated

all the flux within the mask. While it is clear that column density images generated using different channel widths or beam sizes cannot be directly compared, the SNR approach further complicates the assessment of emission levels across different cubes. We adopt the SNR approach but take certain precautions to ensure the consistency of our detection limits. Firstly, we ensure that the cubes are not over-sampled ($\sim 3-4$ pixels across the major axis) and that the beam sizes and S+C kernel sizes are reasonable. Secondly, we constrain the SNR range to a narrow range of 2.8 and 3. Finally, we adopt the column density limit estimated with the SNR map of the data to characterise both the data and the Gaussian models. We consider the precise determination of the column density limit as a crucial step in our parameterisation process, as it ensures that the mass calculation remains within this limit. While we acknowledge that the error in the HI mass would be dominated by the distance to the source, small discrepancies in the observed flux can affect the calculated mass as these values get multiplied by the square of the distance. Moreover, due to the extended kernels we chose in our SoFiA2 parametrisation step, we opt to stay consistent with the column density limit we carefully estimated.

3.8.2 HI mass

The mass of the HI gas enclosed in a volume can be calculated by measuring the observed flux, $S(v)$, in the volume. In practice, this can be achieved by constraining the volume of integration for the intensity map within a 3D mask. In addition to the mask, the integration is also constrained within the column density limit as discussed in the prior section (see section 3.8.1).

The HI mass can be obtained by using the equation derived by Roberts (1962).

$$\left(\frac{M_{HI}}{M_{\odot}}\right) = 2.35 \times 10^5 \left(\frac{D_L}{Mpc}\right)^2 \left(\frac{S_{\rm obs}}{\rm Jy\ beam^{-1}\ km\ s^{-1}}\right) \left(\frac{1}{\Omega_{beam}}\right) \tag{3.12}$$

Where, the luminosity distance, D_L, is calculated from the systemic velocity of the gas disc obtained from 3D tilted ring modelling and using cosmological parameters from Planck Collaboration (2020) ($\rm H_o = 67.7\ km\,s^{-1}\,Mpc^{-1}$, $\Omega_m = 0.310$, & $\Omega_\Lambda = 0.69$). Ω_{beam} is the area of the beam in pixels given by equation 3.8. We report the HI masses in logarithm, $\log \rm M_{HI}$ (Meyer et al. 2017). To estimate the uncertainty in the mass, first, we estimate the uncertainty in flux as:

$$\sigma_S = \sqrt{\frac{N_{pix}}{\Omega_{beam}}} \Delta v \sigma_{rms} \tag{3.13}$$

Where, Δv is the channel width, N_{pix} is the number of pixels spanned by the source, and σ_{rms} is the mean RMS per channel near the source. To get the uncertainty in D_L, we propagate the maximum uncertainty in V_{sys} estimated by ^{3D}BAROLO to distance using:

$$\sigma_{D_L} = D_L \frac{\sigma_{V_{sys}}}{V_{sys}} \tag{3.14}$$

The error in $\rm M_{HI}$ is calculated by taking the quadrature sum of the ratio between the respective

uncertainties and the measured values for distance and flux. This is followed by a logarithmic transformation of the base from linear to log.

$$\sigma_{M_{HI}} = \frac{\log_{10}(M_{HI})}{\ln(10)} \sqrt{\left(\frac{\sigma_{D_L}}{D_L}\right)^2 + \left(\frac{\sigma_S}{S}\right)^2} \tag{3.15}$$

We note that differences in the distances adopted dominate the error budget. If emission outside the column density limit were to be integrated into the calculated HI mass, the difference in the value would likely be minor. We adopt to do this extra step to be consistent in our methods. Additionally, the estimation of mass from the adopted approach of integrating all the masked flux can potentially be impacted by several factors such as residual continuum structure, cleaning artefacts, non-Gaussian noise, and uncleaned emission. Specifically, the mass of any residual emission below the adopted cleaning threshold (2.5σ) may be slightly overestimated due to the reasons discussed in section 2.8 and Walter et al. (2008). While a thresholded summation of the flux in the cube alleviates some of these issues, we find that the approach we adopt produces similar total integrated flux across dissimilar datasets. This is an intriguing observation as it informs us that even with distinct noise profiles, the integration across the extended mask recovers comparable amounts of low-level emission in data from different instruments processed using varied techniques. Thus the additional flux we report is likely physical and is not caused by artefacts incorrectly integrated into the total intensity image.

In this work, we report the HI masses of the galaxies detected within MeerKAT's primary beam and compare the masses of the central regions with masses recovered in a similar fashion from archival data. We also report the HI masses of the Gaussian component models and their fractions with respect to the HI mass measured from the data.

4 | HIPASS J1250-20

In this chapter, the spectral cubes for J1250-20 obtained from the data reduction pipeline elaborated in chapter 2 are analysed using techniques detailed in chapter 3. For our analysis, we make use of the medium resolution cubes with a spatial resolution of $16.11'' \times 14.95''$, ($\sim 8.6 \times 8$ kpc), channel width of 5.8 kms^{-1}, and pixel size of 4 arcsec (~ 2 kpc). The luminosity distance to the group is ~ 116 Mpc and the scale at this distance is 0.54 kpc/$''$.

4.1 Overview

The HIPASS J1250-20 (J1250-20) Choir group, within a projected radius of ~ 250 kpc, hosts two large spiral galaxies (ESO575-G006 or S1 and ESO575-G004 or S2), three dwarf galaxies (S3, S4, and S5), and two compact Hα emitters (S6 and S7; Sweet et al. 2013; Džudžar et al. 2019). The selection criteria for the Choir groups employed in Sweet et al. (2013) was constrained to a $15.5'$ field. Džudžar et al. (2021) (hereafter D21) investigated the wider field of the choir groups by querying NASA/IPAC Extragalactic Database (NED) for sources in a $\sim 4°$ field around each Choir group. They then cross-matched the obtained catalogue with the 2MASS Extended Source Image Server to create a magnitude-limited sample. They also utilize a catalogue of filaments in the local universe curated by Kleiner et al. (2017) to estimate distances to the nearest filament for the Choir Groups. The catalogue of filaments was compiled by running the Discrete Persistent Structures Extractor (DisPerSe) on data from the 6-degree Field Galaxy Survey (6dFGS). From both these explorations, D21 conclude that J1250-20 is embedded in a low-density environment and that its distance to the nearest filament is about $\sim$ 4Mpc. Subsequently, they classify J1250-20 as an isolated group (See panel (c) and (d) of appendix figure B.1). D21 also report the star formation rates, stellar mass, and mid-infrared colour properties of the Choir galaxies derived from integrated mid-infrared photometry in the four WISE bands (see table 4.1). The literature on this group is sparse. This work will be the first to perform a resolved kinematic analysis for the major members and provide spectroscopic information for many of the dwarfs in this field.

Table 4.1: The table lists some basic properties of the galaxies in the J1250-20 group and the extended field. The table contains their name, optical identification, Right Ascension (RA), declination (Dec.), stellar mass and SFR values from D21, and morphology taken from Sweet et al. (2013). Only sources labelled with * have been previously detected in HI. [a] - 6dFGS gJ124846.1-202334

Name	Optical ID	RA (h:m:s)	Dec. (d:m:s)	$M_\star$ ($M_\odot$)	SFR ($M_\odot$ yr^{-1})	Morphology
S1*	ESO 575-G006	12:50:52.84	−20:22:15.65	10.45 ± 0.1	6.54 ± 2.27	SA(s)bc pec HII
S2*	ESO 575-G004	12:50:40.91	−20:20:06.22	10.44 ± 0.10	4.67 ± 1.62	S
S3*	ESO-LV 575-0061	12:50:49.77	−20:22:03.44	9.30 ± 0.19	0.35 ± 0.13	[Irr]
S4	LEDA 842984	12:50:39.92	−20:20:52.87	9.57 ± 0.27	0.05 ± 0.02	Irrs
S5	-	12:50:59.16	−20:28:14.80	8.63 ± 0.68	0.07 ± 0.03	[cD]
S6	-	12:50:45.87	−20:23:30.10	-	-	[D]
S7	-	12:50:46.92	−20:23:12.40	-	-	[D]
Mkt8	-	12:50:30.08	−20:40:36.57	-	-	-
Mkt9	LEDA 840758	12:52:40.41	−20:30:30.19	-	-	-
Mkt10	-	12:48:50.56	−20:24:24.97	-	-	-
Mkt11	6dFGS[a]	12:48:46.12	−20:23:33.28	-	-	-
Mkt12	-	12:53:08.82	−20:26:24.26	-	-	-

4.2 HI in the group

The neutral hydrogen content of the central region of the group was mapped with ATCA and was presented in Džudžar et al. (2019) (hereafter D19). The total integration time across all the configurations of the ATCA observation was $\sim$ 13 hours. The two large spiral galaxies in J1250-20 (S1 and S2) have comparable stellar masses and are both labelled as central galaxies by D19 but they have vastly different HI masses. Both S1 and S2 have ongoing minor mergers with dwarfs S3 and S4 respectively. D19 report a possible interaction between the HI-rich galaxy, S1 and the HI-poor galaxy, S2. The dwarf galaxy S3 and the compact Hα emitters, S6 and S7 were found to be within the HI envelope of S1. The HI associated with S2 was found to be offset in the direction of S1 and the gas content of the dwarf galaxy S4 was reported to be associated with S2. Within their resolution, they were unable to detect HI in S4 and thus classify the dwarf as HI deficient. They conclude that the ongoing minor merger in S1 and the tidal interaction between S1 and S2 could be responsible for the increased HI content of S1 and the decreased HI content of S2. They report an HI mass of log $M_{HI}[M_\odot] = 10.53 \pm 0.2$ for a group distance of 114 Mpc, comparable to the mass of log $M_{HI}[M_\odot] = 10.39 \pm 0.11$ quoted in the HIPASS catalogue for a group distance of 110 Mpc (Meyer et al. 2004). Due to the target's declination ($\sim -20°$), the synthesized beam for their observation is elongated in the North-South direction ($102.8'' \times 30.79''$). This elongation causes spurious emission features due to beam smearing. (See figure 4.1). Their observations, although smeared, have been reported to probe HI down to a column density of $\sim 3.5 \times 10^{19}$ cm^{-2} with a channel width of 15 km s^{-1}. In sub-section 4.2.1, we discuss the comparison between our MeerKAT data and the ATCA data that we obtained from the authors of D19.

4.2.1 Comparison with ATCA cube

HIPASS measured an integrated flux of 10.5 Jy km s^{-1} for J1250-20 within the $15'$ primary beam of the Parkes telescope. Using equation 3.12 and a distance of $\sim$ 116 Mpc, this translates to an HI mass of, log $M_{HI} = 10.52$ $M_\odot$. For the HI distribution in the group shown in figure 4.1, in both the $\sim 100''$ ATCA cube and the $\sim 16''$ MeerKAT cube, we measure a log HI mass of ~ 10.72 $M_\odot$. The HI mass is 0.2 dex higher than that observed by HIPASS. The higher mass we recover from the same ATCA cube as D19 is still within their reported error (± 0.2). The difference between our mass measurement and theirs can be attributed to several factors. Firstly, to obtain the total intensity we integrate all the masked emission whereas D19 only integrate signal above a 3σ threshold (see section 3.8 for a detailed discussion). Additionally, we considered a $\sim$ 3 Mpc higher D_L and utilized extended SoFiA2 masks to calculate the total flux. We recover similar masses from the ATCA and MeerKAT cubes through consistent characterisation of the cubes, employing identical procedures for masking, defining column density limits, and extracting column density images without imposing threshold limits. Despite the cubes exhibiting distinct noise properties and being imaged using different techniques, the concurrence in the recovered mass implies that the 'additional' integrated flux obtained from including all the emission within the source mask is likely real.

D19 report a column density limit of 3.5×10^{19} cm^{-2} over a channel width of 15 km s^{-1} corres-

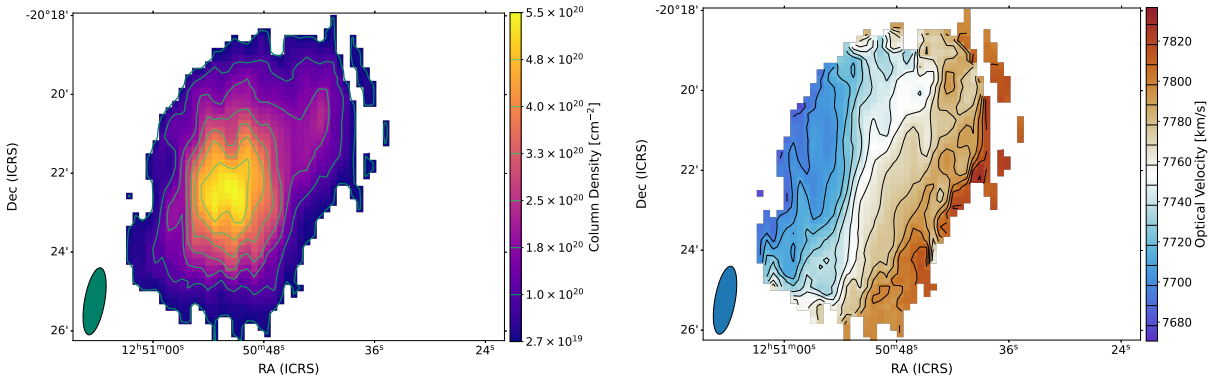

Figure 4.1: The column density image (left) and the velocity field (right) extracted from the ATCA cube with a $102.8'' \times 30.79''$ elliptical beam.

ponding to a 3σ level for a σ[10] of 2 mJy beam^{-1}. For the ATCA dataset with $5\,\mathrm{km\,s^{-1}}$ resolution, using our parameterisation approach (see section 3.8.1), we recover an RMS of ~ 2.5 mJy beam^{-1} and a column density limit of 2.72×10^{19} cm^{-2}. For the MeerKAT cube, we recover an RMS of ~ 0.19 mJy beam^{-1}, which is ~ 13 times lower than the RMS in the ATCA cube. In the MeerKAT cube, we determine a column density limit of $3.3 \times 10^{19}\,\mathrm{cm^{-2}}$. Even though both datasets have comparable channel widths of ~ 5.8 km s^{-1}, the high noise, low spatial resolution, and asymmetric beam of the ATCA cube render it difficult to extract reliable gas kinematics. The 6 times higher spatial resolution of the MeerKAT data, for the first time, allows us to properly separate the HI in the interacting galaxies and study the gas kinematics of the group. The 4.78-hour MeerKAT data probes gas down to similar sensitivities as the 12.9-hour ATCA data but with a significantly better resolution, enabling us to resolve the members and perform detailed kinematic modelling. The improvement is evident from the column density image and the velocity field shown in figure 4.2.

Furthermore, within MeerKAT's $\sim 1^\circ$ primary beam (~ 1.9 Mpc), we detect HI in 5 other dwarf galaxies with optical counterparts in the deep DECam images (see figure 4.3). Only Mkt11 has a catalogued redshift (6dFGS gJ124846.1-202334). Mkt9 (LEDA 840758) does not have a redshift in the literature and the other three (Mkt8, Mkt10, Mkt12) have not yet been identified as sources in any catalogue. The galaxies in the field are annotated in figure 4.3 and their HI properties are summarised in table 4.2. As discussed in section 1.3, due to difficulty in determining group membership owing to projection effects, we label the new detections as sources in the field. Additionally, from looking at a simple caustic curve of the group potential, the galaxies we detect in the field seem unlikely to be part of the group (see appendix figure B.13). The structure near Mkt11 is likely a result of the increased noise near the edge of the primary beam and residual continuum artefacts. The presence of a bright continuum source away from the phase centre introduces extensive artefacts across the field. While most of this was subtracted in three stages, low-level artefacts are still present near the edges. Furthermore, the strong RFI close to the source emission also likely introduces artefacts such as Gibbs ringing to the continuum. We fit and subtract a zeroth-order polynomial to the continuum in the image plane but we note that a higher-order polynomial is required in certain parts of the cube.

[10]It is unclear if the quoted RMS corresponds to the $5\,\mathrm{km\,s^{-1}}$ cube or the $15\,\mathrm{km\,s^{-1}}$ cube.

While this does not affect our analysis, properly handling the continuum could strengthen our conclusions about the observed tail in S1.

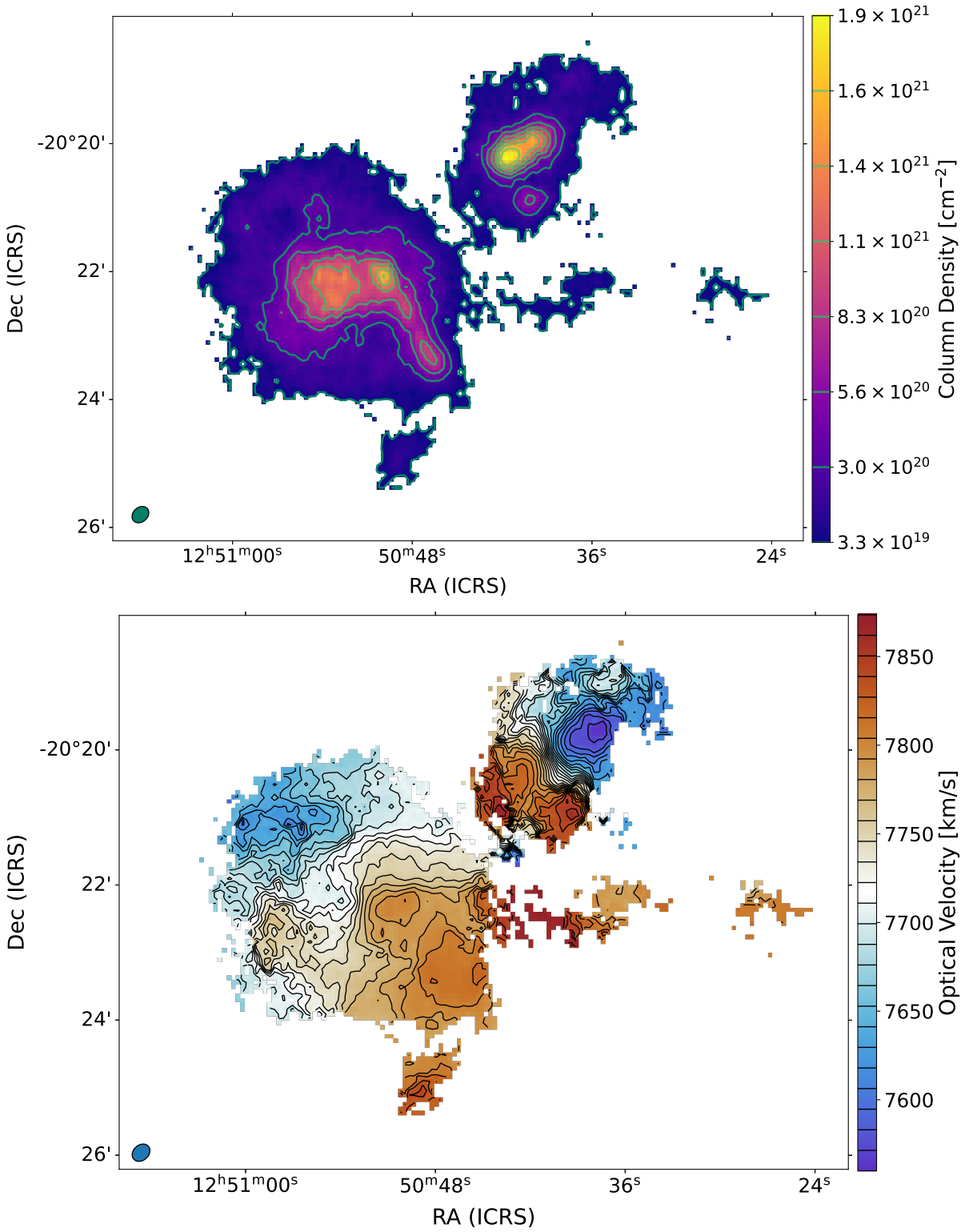

Figure 4.2: The column density image (top) and velocity field (bottom) extracted from the MeerKAT cube with a $\sim 16''$ beam.

Table 4.2: The table displays the HI properties of the galaxies in the field. The systemic velocity values (V_{HI}) marked with ^{a} are from tilted ring modelling and the rest are from SoFiA2 parameterisation. The RMS values are from the SoFiA2 generated source catalogue. We measure the total flux (S_v) and the HI mass (M_{HI}) within the column density limit (N_{HI}). * possible contamination due to artefacts in the edges of the primary beam.

Name	V_{HI} (km s^{-1})	D_L (Mpc)	RMS (mJy beam^{-1})	log M_{HI} ($M_\odot$)	S_v (Jy km s^{-1})	N_{HI} (10^{19} cm^{-2})
S1+S3	$7733.14^{+3.177\,a}_{-3.115}$	116.53	0.19	10.60 ± 0.05	12.47 ± 0.13	3.27
S2	$7697.77^{+10.83\,a}_{-10.715}$	115.99	0.19	10.05 ± 0.09	3.56 ± 0.08	3.27
S4	$7851.21^{+12.581\,a}_{-9.310}$	118.34	0.19	8.96 ± 0.01	0.28 ± 0.08	3.27
S5	7662.74 ± 1.64	115.45	0.21	8.69 ± 0.31	0.16 ± 0.02	1.54
Mkt8	7591.63 ± 1.15	114.36	0.23	9.02 ± 0.25	0.34 ± 0.03	2.48
Mkt9	7573.88 ± 1.67	114.09	0.29	9.60 ± 0.19	1.31 ± 0.06	3.15
Mkt11+10*	7767.76 ± 1.29	117.06	0.35	9.89 ± 0.17	2.41 ± 0.10	5.82
Mkt12	7569.59 ± 1.44	114.02	0.38	9.33 ± 0.29	0.69 ± 0.05	7.17

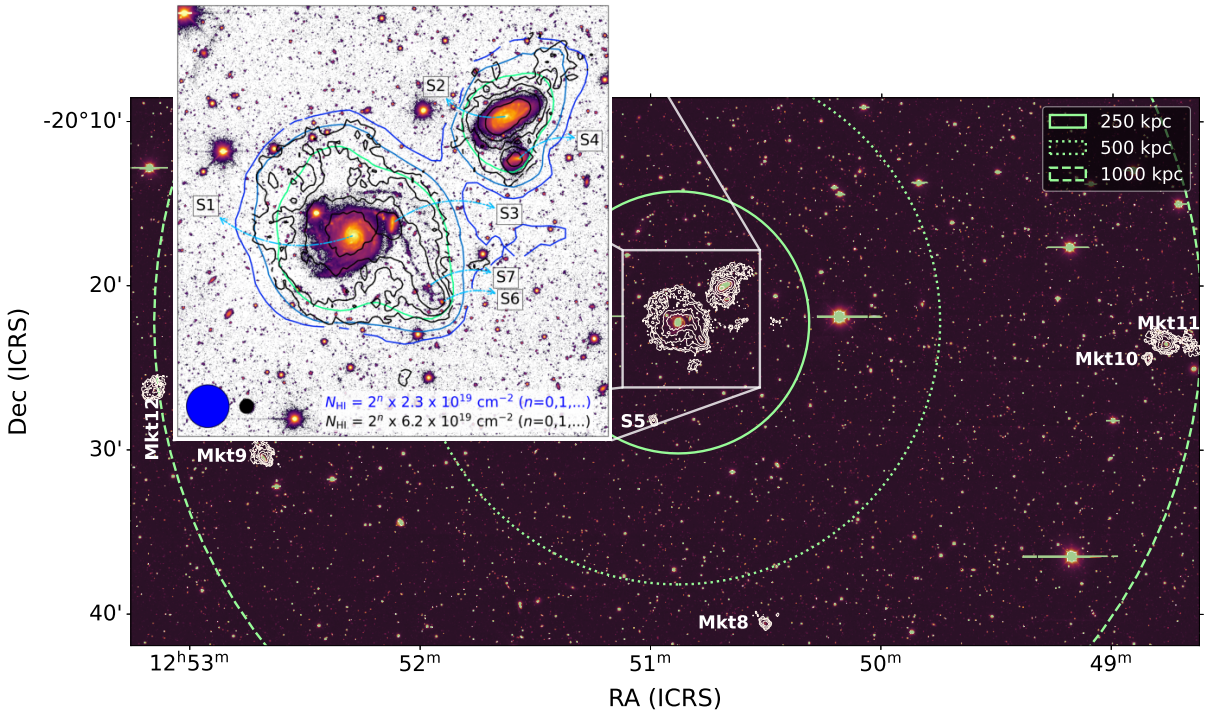

Figure 4.3: HI column density contours overlaid on DECam g-band image of the extended field of J1250-20. The dashed green circles denote the projected separation from the centre at 250 kpc, 500 kpc and 1 Mpc respectively. The blue-green and black contours in the inset image represent the 47″ cube and the 16″cube, respectively, both having a channel width of approximately 17 km s^{-1}. The positions of dwarf galaxies which are interacting with S1 & S2 are indicated in the inset plot.

4.3 Interacting galaxies

S1 is one of the largest central galaxies in the Choirs sample in terms of the HI diameter measured at a surface density of 1 $M_\odot$ pc^{-2}. D21 measured an HI radius at their column density limit and found it to be about 20 times the effective r-band radius (5.5 kpc) estimated in Meurer et al. (2006). At the column density limit, we measure the diameter for the HI envelope in the $\sim$ 16″ and $\sim$ 47″ MeerKAT cubes to be about 150 kpc, extended along the NE-SW direction. For the first time, we detect and separate the HI associated with S4. The projected distance

from the optical centre of S1 to those of S3, S4, and S2 is $\sim$ 24 kpc, $\sim$ 107 kpc, and $\sim$ 114 kpc respectively. The projected distance from the optical centre of S2 to that of S4 is $\sim$ 26 kpc. We do not find a significant deviation between the optical and HI centres of S2. However, in the case of S1 and S4, we observe a slight offset of about $\sim$ 1.6 kpc, which is smaller than our pixel scale and thus is likely unphysical. The line-of-sight velocity separation between S1 and S2 is $\sim$ 35 km s^{-1}, S1 and S3 is $\sim$ 20 km s^{-1}, and S2 and S4 is 150 km s^{-1}. Part of S3's disc appears to have kinematically merged with S1's disc. S4 is closer to the receding side of S2 which has velocities comparable to the systemic velocity of S4. Both S3 and S4 have a rotation velocity of $\sim 30 - 40$ km s^{-1}.

4.3.1 S1 & S3

The HI disc of S1 is extended ($D_{HI} \sim 150$ kpc), warped, lopsided, and shows signs of disturbance (see figure 4.2). The ongoing minor merger with the dwarf galaxy S3 is at an advanced stage and is likely fueling the star formation in the central region of S1. The extended HI envelope also engulfs the SW stellar stream and the two tidal dwarf candidates S6 and S7. The long straight stellar stream extends from the SW of S3 to about 60-80 kpc. We observe anomalous gas along S3 and the stellar stream, potentially indicating a shared origin for the stream and the anomalous gas as material stripped from S3. There is a bridge of neutral gas from the S2+S4

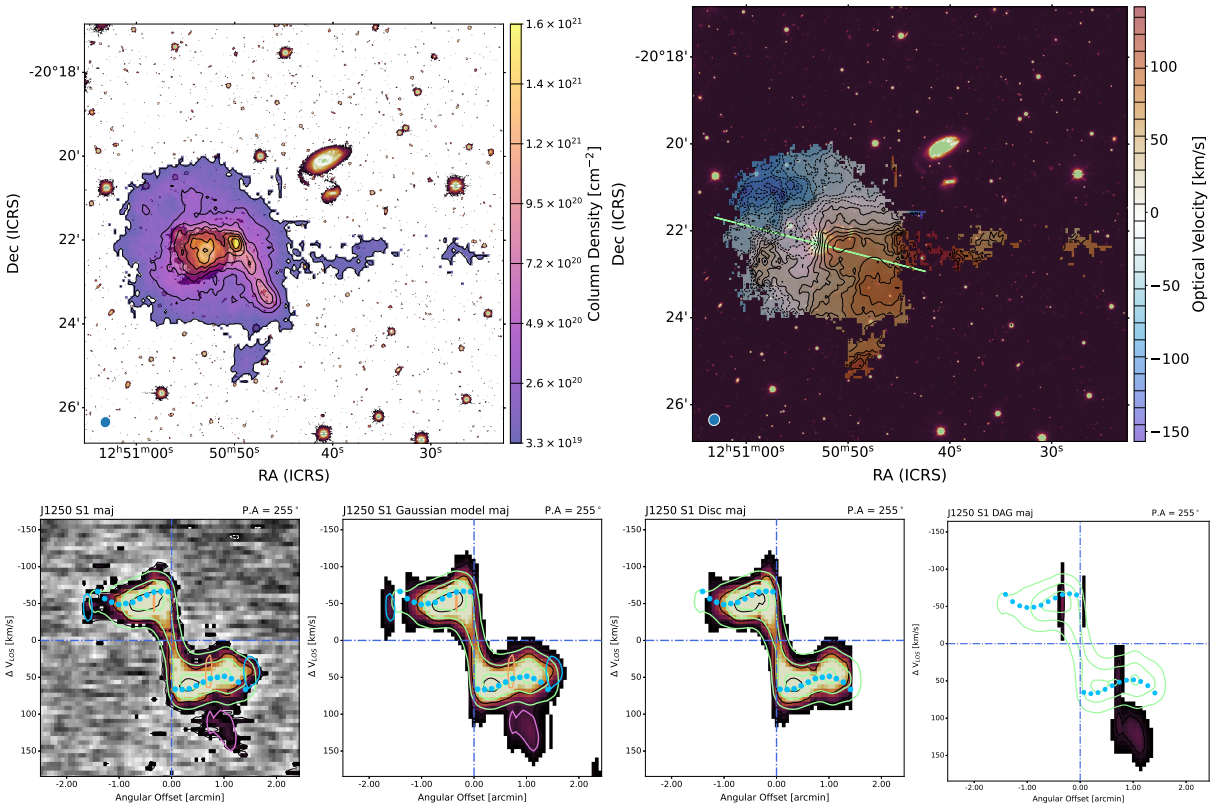

Figure 4.4: **Top row:** Column density image (panel 1) and velocity field map (panel 2) of S1 overlaid on DECam g-band image. The major axis (median P.A.) along which the subsequent PV slices were extracted is represented by the pale green line in the velocity field map. **Bottom row:** Panels 3-6 (left to right) show PV slices with ^{3D}BAROLO contours of the corresponding model slice overlaid. PV slices of the data cube, multi-component Gaussian model cube, disc Gaussian model cube, and the disc anomalous gas Gaussian model cube. In panels 3 and 4, the violet contour corresponds to FC, sky blue represents NDAG, and orange represents EPG.

system at velocities similar to that of S3. We also detect an HI plume to the south of the stellar stream and a tail extending to the west. We note a possible extension of this tail to the east and a link to the twisted contours in the approaching side of S1 (see the eastern side of S1 in panel 2 of figure 4.2). We measure a log M_{HI} of 10.60 $M_{\odot}$ for the HI distribution of S1+S3, 0.12 dex higher than the mass reported in D19. This places S1 (including S3) among the most HI-rich systems in H IX (Lutz et al. 2017, 2018). It is evident that the gas disc has contributions from S3 and S2. In addition to the observed bridge, the HI associated with S4 appears to be offset towards S1 indicating a potential tidal interaction between S1 and S4.

Firstly, we apply a 2D elliptical mask to all channels to isolate the disc and the Non-Disc Anomalous Gas (NDAG). We then use the disc data cube for tilted ring modelling and the full data cube for Gaussian decomposition. We perform tilted ring modelling on the disc data cube of S1 using ^{3D}BAROLO as discussed in section 3.5.1 with a constant vertical thickness of 1.0″ which corresponds to $\sim$ 560 pc at the systemic recession velocity, V_{sys} = 7733 km s^{-1}. We recover a median inclination, $i \sim 45^{\circ} \pm 4^{\circ}$ and median P.A., $\phi \sim 256^{+4^{\circ}}_{-40}$. The fitted parameters of the models are shown in figure 4.6 and the rings defined for the tilted ring modelling are shown in figure 3.8. The extended disc of S1 is significantly warped and ^{3D}BAROLO is only able to recover reasonable values for the geometric and kinematic parameters out to a radius of $\sim$ 50 kpc. Even within this radius, the warp is evident from $\sim$ 25 kpc, which is the projected distance to S3 (see panels 1 and 2 of figure 4.6). At this radius, we observe a decrease of approximately $\sim$ 25 km s^{-1} in the rotation curve, which might be connected to the dwarf galaxy in the envelope. We employ our Gaussian decomposition and kinematic tagging method to separate the gas associated with S3 from the disc of S1. We take advantage of the fact that some of the gas associated with S3 is seen distinctly in the emission line profiles (see figure 4.7). All along the stellar stream and S3, we note the presence of a leading anomalous component with velocities similar to S4 and the receding side of S2. This anomalous leading component is also seen in the PV slices shown in figure 4.4 between 100 - 150 km s^{-1}. The anomalous gas component could be gas infalling from the S2+S4 system but its morphology is puzzling. Unlike the next chapter, we do not distinguish between lagging and leading anomalous gas components. The disc anomalous gas in S1 consists of EPG, leading gas, and also gas associated with S3. While it is possible to separate S3 from the anomalous gas, it remains beyond the scope of this work due to the complexities involved in disentangling the component structure. However, we managed to separate most of the gas associated with S3 from S1's disc. But we note that the disc likely extends further into what we label as NDAG. In future work, we will employ a more sophisticated approach to identify the disc emission.

Nonetheless, our multi-component Gaussian model shown in the second panel in the bottom row of figure 4.4 reasonably reproduces the data PV shown in the first panel. The third and fourth panels in the bottom row respectively show the separated disc and anomalous gas components. We also performed tilted ring modelling on the disc Gaussian model to eliminate the possibility of the warp and falling rotation being artefacts induced by the anomalous gas on the χ^2-minimisation implemented in ^{3D}BAROLO. Notably, we obtain comparable outcomes from models of both sides, separate sides, and the Gaussian disc component, indicating that the observed fall in rotation and the warp are genuine. The rotation of the disc increases beyond 30 kpc and we suspect plausible indications of radial inflows in the receding side outer rings (see

panel 6 of figure 4.6). In the appendix, we include supplementary figures showcasing different PV slices, intensity maps, and velocity fields of the data, Gaussian disc model, multi-component Gaussian model, as well as the anomalous gas after disc subtraction (see appendix section B). Additionally, in appendix figure B.11, we show the 2D residuals obtained by subtracting the intensity, velocity field, and dispersion maps of the models from that of the data.

4.3.2 S2 & S4

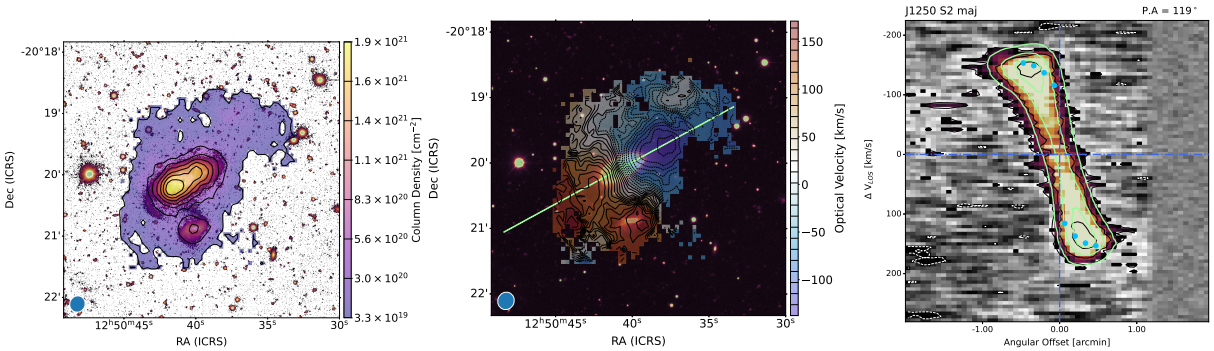

Figure 4.5: The column density image (first panel) and velocity field (second panel) of S2 overlaid on DECam g-band image. The major axis (median P.A.) along which the subsequent PV slice was extracted is represented by the pale green line in the velocity field map. Panel 3 shows the major axis PV slice with ^{3D}BAROLO contours of the corresponding model slice overlaid.

The S2+S4 system has a total HI mass, log $M_{HI} \sim 10.09$ $M_\odot$, which is 0.5 dex higher than the mass reported in D19. We recover log$M_{HI} \sim 8.95$ $M_\odot$ for S4, which is comparable to the theoretical limit estimated by D21. Thus, we measure an HI deficiency of ~ 0.7 dex as predicted for S4 in D21. The stellar disc of S2 appears to be lopsided towards the direction of S1 (see inset plot in figure 4.3). S4 also appears to have a star-forming ring-like structure extended towards SE. Although, the HI disc of S2 seems to be more extended in the approaching side (NW) and we also observe a greater proportion of gas with lagging velocities in the NW (see figure 4.5). We create two elliptical masks extruded along the line-of-sight to isolate S2's disc and S4's disc. We perform tilted ring modelling on the masked disc data cubes of S2 and S4 using ^{3D}BAROLO as discussed in section 3.5.1. For S2, we adopt a constant vertical thickness of $1.0''$ which corresponds to ~ 560 pc at the systemic recession velocity, $V_{sys} = 7698$ km s^{-1} and we model S4 as a thin disc with no vertical thickness. For S2, we recover a median inclination, $i \sim 66° \pm 5°$, a median P.A., $\phi \sim 118° \pm 4°$, and a maximum rotation velocity of ~ 170 km s^{-1}. The fitted parameters of the models are shown in figure 4.8 and the rings defined for the tilted ring modelling are shown in figure 3.8. For S4, we retain a median inclination of $\sim 72° \pm 2°$, a median P.A., $\phi \sim 297° \pm 2°$, and a maximum rotation velocity of ~ 35 km s^{-1}. We expect radial flows out of the discs onto the bridge to S1 but on the contrary, the radial profiles shown in panel 6 of figure 4.8 suggest inflows towards S2. However, the effect of degeneracy in the parameter space amplified by the resolution of the data and the inclination of S2, cast significant doubt on the radial profiles. Moreover, due to the galaxy's inclination, distance, and resolution, the major axis is only sparsely sampled by approximately 4-5 beams, which can cause the data to blend together and broaden the emission line profiles. We perform Gaussian decomposition but we do not attempt to separate anomalous gas from the disc as the prominent components will likely be smeared disc components. A rigorous tagging approach can potentially extract non-smeared

components such as the component around -90 km s^{-1} in the spectra on the top left in figure 4.9, but such an exploration is beyond the scope of this work.

4.4 Discussion

The intriguing case of J1250-20 encompasses several crucial processes important for understanding galaxy evolution. The group hosts two interacting spirals, namely S1 and S2, each with its own dwarf companions, S3 and S4, respectively. While S1, S3, and S4 rotate in the anti-clockwise direction, S2 rotates clockwise. The rings defined for modelling the discs of S1, S2, and S4 are shown in figure 3.8. By leveraging the resolved and sensitive MeerKAT HI data, we are able to examine the different stages of the mergers involving these galaxies. Specifically, we are able to study the advanced stage of

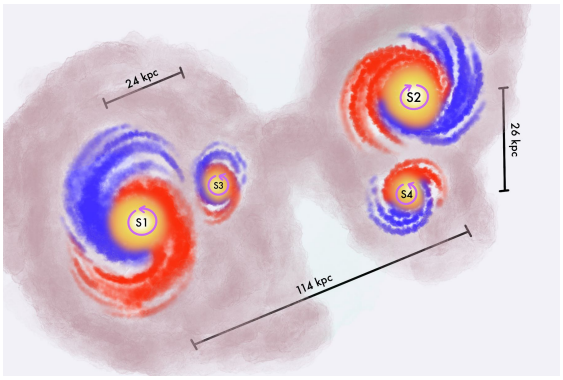

Figure 4.10: Illustration of the rotation and the projected separations of the interacting galaxies by Aiswarya Arun (Univ. Chile). The sketch is not to scale.

Table 4.3: The two sections presents the logarithmic HI masses of the data and models for S1 and S2. The third column shows the fraction of the component with respect to the full data and the fourth column shows the fraction of the model with respect to the data in the 'sub-table'. First two rows: full data and full Gaussian model. The subsequent four rows: disc data, ^{3D}BAROLO model of the disc, Gaussian component model of the disc, and Disc Anomalous Gas (DAG) model. The next two rows: Non-Disc Anomalous Gas (NDAG) data and NDAG Gaussian model.

Label	log M_{HI} ($M_\odot$)	fraction of component	fraction of data modelled
		S1+S3	
S1+S3 Data	10.60 ± 0.05	100%	
Full Model	10.51 ± 0.01	81.61%	
S1+S3 Disc Data	10.50 ± 0.01	78.18%	100%
S1 ^{3D}BAROLO Model	10.44 ± 0.04	68.87%	88.11%
S1 Disc Model	10.35 ± 0.01	56.19%	71.78%
S1+S3 DAG Model	9.27 ± 0.01	4.69%	5.98%
S1 NDAG Data	9.94 ± 0.01	21.82%	100%
S1 NDAG Model	9.92 ± 0.01	20.74%	95.06%
		S2+S4	
S2+S4 Data	10.09 ± 0.09	100%	
Full Model	9.97 ± 0.01	77.29%	
S2 Data	10.05 ± 0.09	92.74%	
S2 Disc Data	9.93 ± 0.01	70.49%	100%
S2 ^{3D}BAROLO Model	9.85 ± 0.08	57.51%	81.66%
S2 Disc Model	9.90 ± 0.01	65.47%	92.90%
S2 NDAG Data	9.43 ± 0.01	22.25%	100%
S2 NDAG Model	8.84 ± 0.01	5.61%	25.24%
S4 Data	8.95 ± 0.01	7.26%	100%
S4 Barolo Model	8.80 ± 0.20	5.22%	71.94%
S4 Model	8.88 ± 0.01	6.21%	85.51%

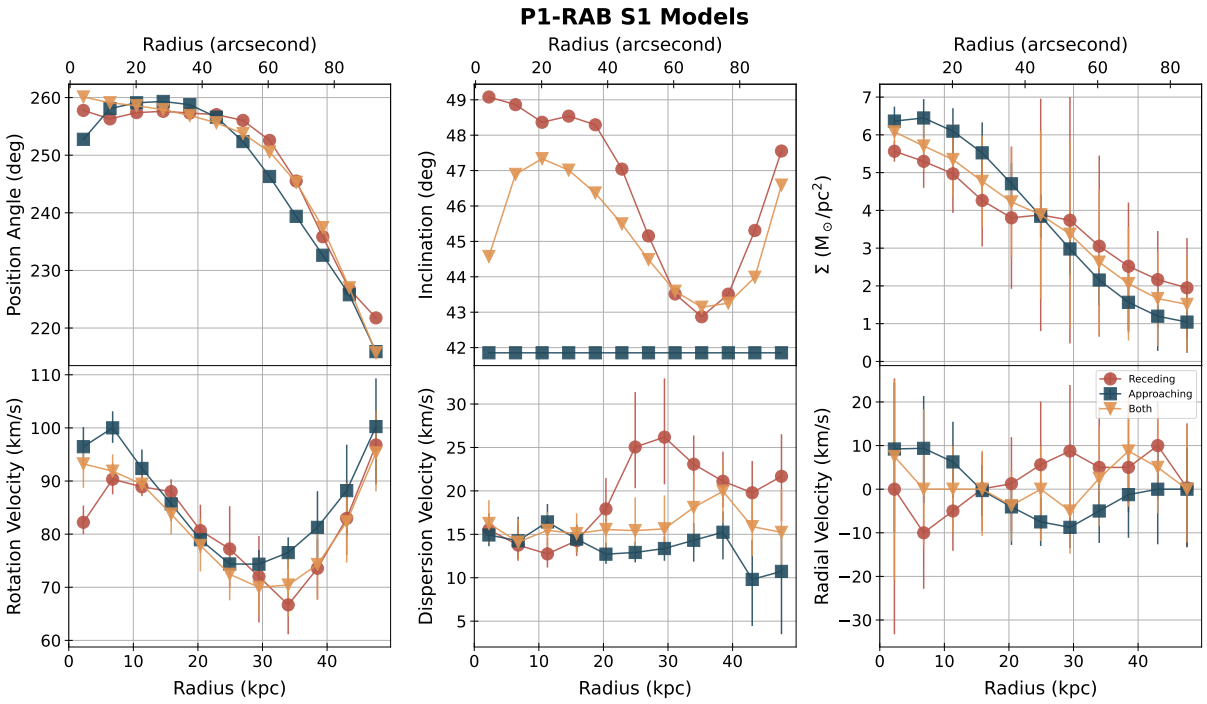

Figure 4.6: ^{3D}BAROLO tilted ring model parameters for S1. The triangle, square, and circle symbols denote the parameters for the model of both sides, the approaching side, and the receding side respectively. The modelling was performed in three steps as delineated in section 3.5.1.

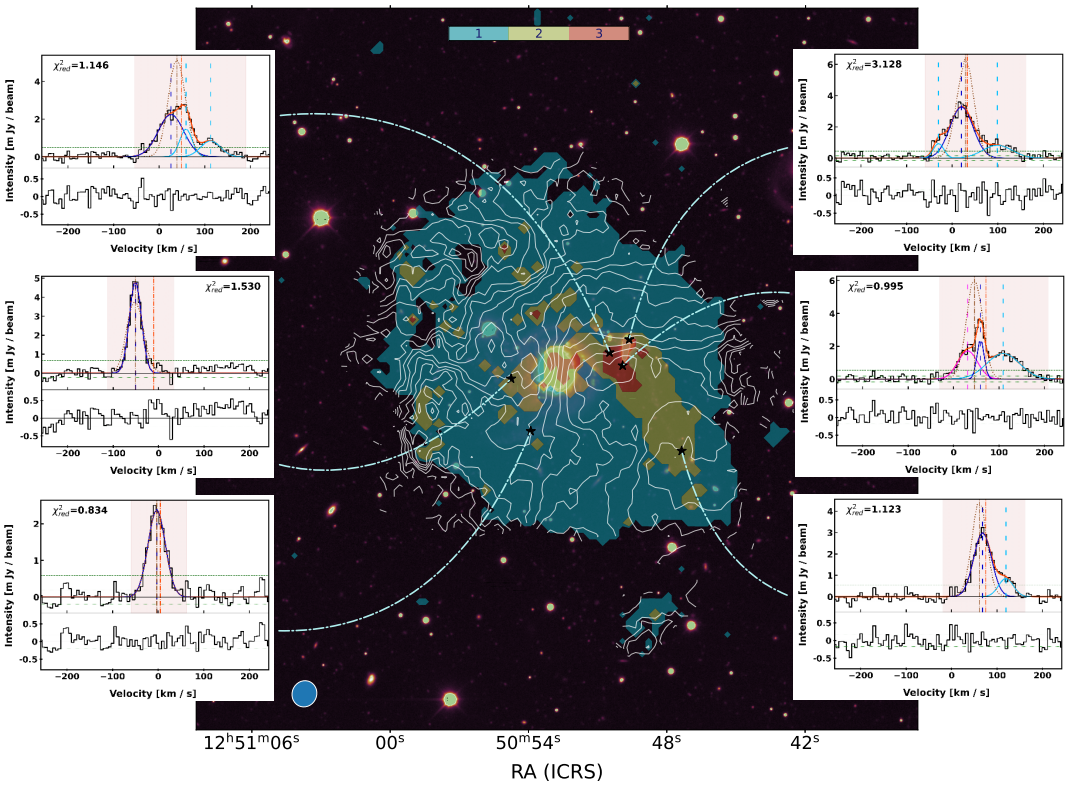

Figure 4.7: Component map and illustrative spectral profiles of S1. First-moment contours and a map of the number of fitted Gaussian components overlaid on DECam g-band image. The colour bar shows the number of fitted components. The inset plots show the spectra extracted at the annotated spaxels and Gaussian components fitted to the corresponding spectra for illustration. The blue-coloured Gaussian is tagged as the disc component, the magenta Gaussian is tagged as the EPG component, and the sky-blue Gaussian is tagged as the anomalous gas component. The ^{3D}BAROLO model spectra extracted at the annotated spaxels are plotted as brown dotted lines in the inset plots for comparison.

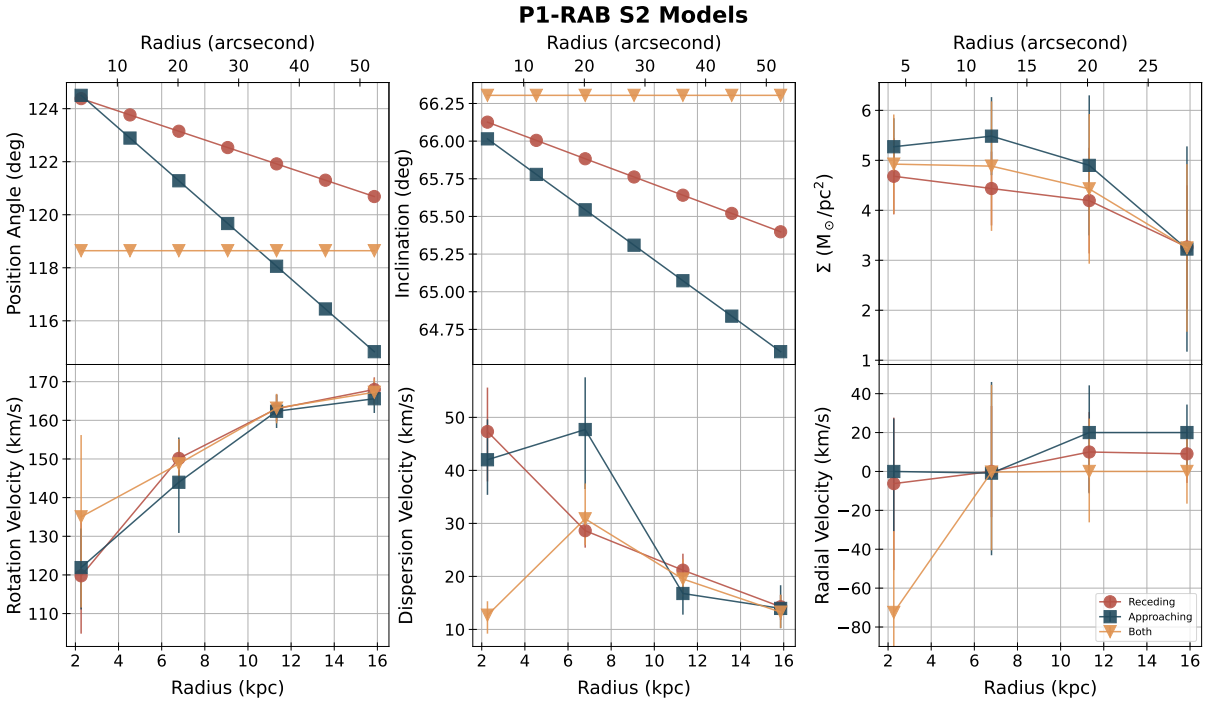

Figure 4.8: ^{3D}BAROLO tilted ring model parameters for S2. The triangle, square, and circle symbols denote the parameters for the model of both sides, the approaching side, and the receding side respectively. The modelling was performed in three steps as delineated in section 3.5.1.

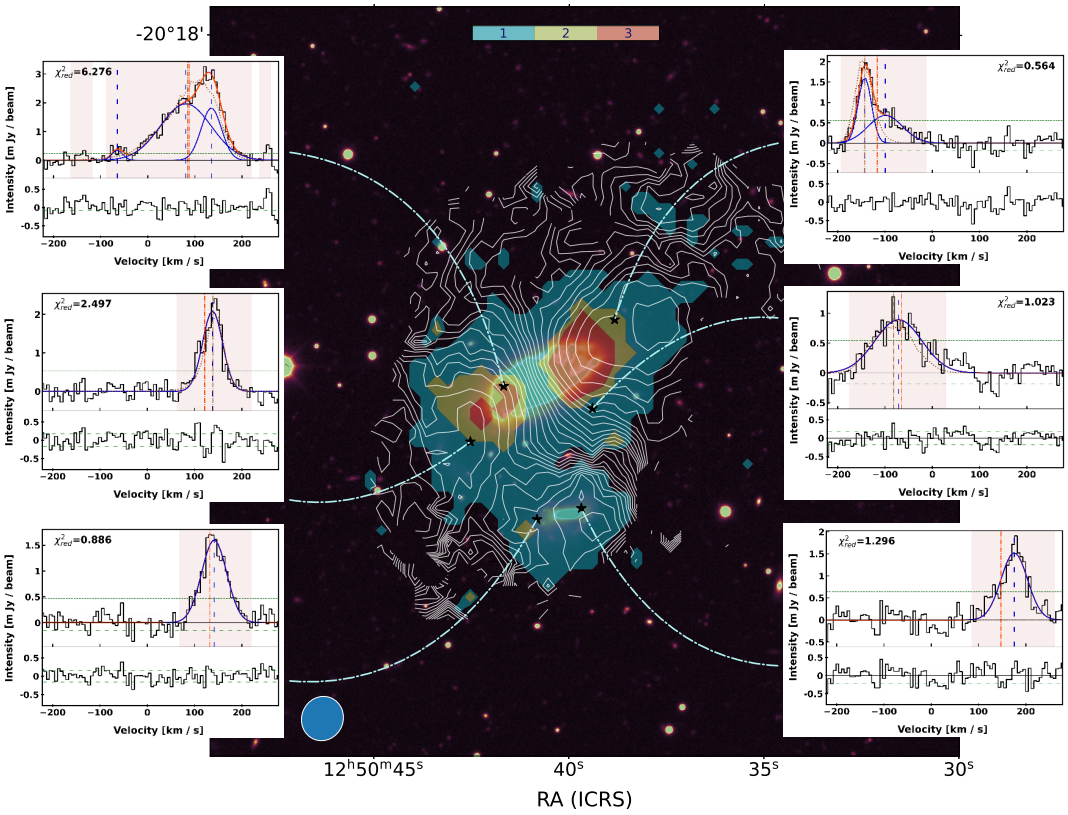

Figure 4.9: Component map and illustrative spectral profiles of S2. First-moment contours and a map of the number of fitted Gaussian components overlaid on DECam g-band image. The colour bar shows the number of fitted components. The inset plots show the spectra extracted at the annotated spaxels and Gaussian components fitted to the corresponding spectra for illustration. The blue-coloured Gaussian is tagged as the disc component, the magenta Gaussian is tagged as the EPG component, and the sky-blue Gaussian is tagged as the anomalous gas component. The ^{3D}BAROLO model spectra extracted at the annotated spaxels are plotted as brown dotted lines in the inset plots for comparison.

the S1+S3 minor merger, the intermediate stage of the S2+S4 minor merger, and the intermediate stage of the major merger of the S1+S3 system and the S2+S4 system. The interactions have given rise to peculiar morphologies in both the stellar and HI discs. The HI disc of S1 (including S3) is 5-6 times greater in extent than the optical disc and is among the most HI-rich galaxies in the local universe with a log $M_{HI} \sim 10.6$ $M_{\odot}$. Moreover, the extended HI disc is significantly warped and features peculiar kinematics. The envelope spanning a diameter of ~ 150 kpc contains a substantial reservoir of anomalous gas and a $\sim 60 - 80$ kpc long stellar stream which hosts two tidal dwarf candidates S6 and S7. While we managed to separate most of the gas associated with S3 from S1's disc, we had to limit the disc component to about 50 kpc due to the significant warp in the outer discs. In this work, we label the outer disc as NDAG and treat it as a separate component. In fact, the NDAG mass quoted in 4.3 is an upper limit as the disc and Disc Anomalous Gas (DAG) likely extend into NDAG. Nonetheless, the lower limit of HI mass of DAG ($\log M_{HI} \gtrsim 9.27$) is still higher than the combined mass of the Magellanic clouds ($\log M_{HI} \sim 9$). Additionally, we detect a low column density bridge connecting the S2+S4 system to the S1+S3 HI envelope. The stellar and HI discs of both S2 and S4 are lopsided towards the direction of S1. S2 appears to be rotating faster than S1 with a $V_{rot} \sim 170$ kms^{-1}. S1's rotation in the inner disc ($\lesssim 30$ kpc) falls from ~ 90 km s^{-1} to $\sim$ 70 kms^{-1} and rises again in the warped outer disc. What is the reason behind the peculiar rotation curve of S1? What is the cause of the outer warp? How are the minor and major interactions shaping the galaxies? How does S1 have such a massive HI reservoir?

The falling rotation in the inner disc is likely due to the accretion of lower angular momentum gas stripped from S3, which has a projected separation of ~ 25 kpc from the centre of S1. Lagos et al. (2018), using EAGLE simulations, find that in the case of minor mergers, stars that belonged to the secondary end up in preferentially more extended structures such as streams or shells. We detect anomalous gas components near S3 consistent with such a hypothesis (see figure 4.7). The stellar stream and the associated anomalous gas point to an origin connected to S3. But interestingly, we also observe another anomalous gas component tracing the stellar stream with velocities similar to S4 and the receding side of S2. This leading component is more prevalent in the outer rings and is likely connected to the rising rotation observed beyond 30 kpc. However, the localized alignment of this component along the stellar stream is perplexing.

Warps can result from various mechanisms such as minor mergers, misaligned gas accretion, torques resulting from interaction with sub-haloes, etc. (e.g., Józsa et al. 2007; Sancisi et al. 2008). The faster-rotating, warped, and extended outer disc of S1 could possibly be a result of gas accreted along the bridge from the S2+S4 system. The relative orientation and mutual orbits of S1 and S2 are likely conducive to the growth of the extended envelope around S1. The faster rotation in the warped outer rings of S1 could potentially be due to a combination of factors such as the inefficient dissipation of the angular momentum of the accreted gas, counter-rotation in the pair, and misaligned accretion. As discussed in section 1.3.3 and in Hopkins et al. (2009), gas in mergers primarily lose angular momentum to internal gravitational torques driven by asymmetries in the stellar disc induced by the merger. In the outskirts where the effect of the stellar disc is diminished, the torquing would be inefficient and thus the gas is less likely to lose sufficient angular momentum to feed inflows to the host nucleus or to the companion. However, the radial inflows seen in the inner rings of S2 (panel 6 of figure 4.8), if true, could

be a result of the torques produced by the triggered asymmetries in S2's stellar disc. Such an inflow can also explain the enhancement in the SFR of S2. Furthermore, a similar argument can be made for the existence of anomalous gas along the stellar stream. Wherein, torques produced by the stellar stream drive inflows of the accreting gas (from S2+S4) into the plane of the stellar stream. However, it is difficult to differentiate between radial and vertical motions since both introduce offsets along the line-of-sight velocities of the components (but see Marasco et al. 2019). Moreover, an outflow towards the observer in the side facing the observer and an inflow towards the observer in the side facing away, or vice versa (an inflow in the side facing us and an outflow away from us in the side facing away), can produce offsets in the same direction along the line-of-sight. Therefore, the leading anomalous gas along the stellar stream can either be an inflow in the side facing us or an outflow driven by the star formation in the side facing away.

The HI disc of S1 is more massive than the 'Bluedisk' sample of HI-rich galaxies in the local universe mapped with the WSRT (Wang et al. 2013). From the similarity of the HI discs in their sample, Wang et al. (2013), infer that the excess gas must come in with a broad range of angular momentum in a well-ordered way. Lutz et al. (2018), in their investigation of the kinematics of a sample of HI-rich galaxies (H IX), find that HI at large galactocentric radii cannot flow to the central parts of the galaxy due to its high specific angular momentum. By comparing with semi-analytic models they suggest that H IX galaxies might reside in high-spin dark matter haloes and that their specific angular momentum could be inherited from the halo. Using cosmological zoom-in simulation, Stewart et al. (2011, 2013, 2017), suggest that cold filamentary accretion can form 'cold flow discs' that co-rotate with the galaxy disc and increase the angular momentum. A similar scenario can also be obtained in the cooling flow solution (Stern et al. 2023). One of the consequences of the gas at high galactocentric radii is to increase the specific baryonic angular momentum which has been shown to be a primary regulator of HI disc size and mass (Obreschkow et al. 2016; Lagos 2018). Interestingly, Lagos et al. (2018) find that the specific angular momentum of galaxies can be increased by gas-rich mergers especially mergers between co-rotating galaxies. In contrast, they find that counter-rotating dry mergers are the most efficient mechanism for reducing the specific angular momentum of galaxies.

From these proposed mechanisms, we take away that gas in extended HI discs likely have contributions from multiple pathways. In the case of J1250-20:S1, the extended HI envelope likely has contributions from the interactions with S3, S2, and S4. While the inner disc is predominantly supplied by gas from S3, the extended warped envelope is likely built up of gas accreted from the interaction with the S2+S4 system in a fashion similar to the cold flow discs proposed by Stewart et al. (2013). The two discs (inner disc and misaligned outer disc) will eventually settle into one as the outer accreting disc gains sufficient mass to effectively 'bend' the inner disc. Conducting comprehensive dynamical modelling of the counter-rotating gas-rich major merger involving S1 and S2, as well as the minor mergers involving S3 and S4, although challenging, will provide valuable insights into the formation and evolutionary trajectory of such extended structures. Such an exploration will also enable the study of the role of misaligned accretion of cold gas in shaping the properties (e.g., warp, angular momentum) of galactic discs.

5 | HIPASS J1403-06

In this chapter, the spectral cubes for J1403-06 obtained from the data reduction pipeline described in chapter 2 are analysed using techniques detailed in chapter 3. For our analysis, we make use of the medium resolution cubes with a spatial resolution of $17.39'' \times 16.81''$ ($\sim 3 \times 3$ kpc), channel width of 5.6 kms^{-1}, and pixel size of 4 arcsec ($\sim$ 760 pc). The luminosity distance to the group is $\sim$ 40 Mpc and the scale at this distance is $\sim$ 0.19 kpc/$''$.

5.1 Overview

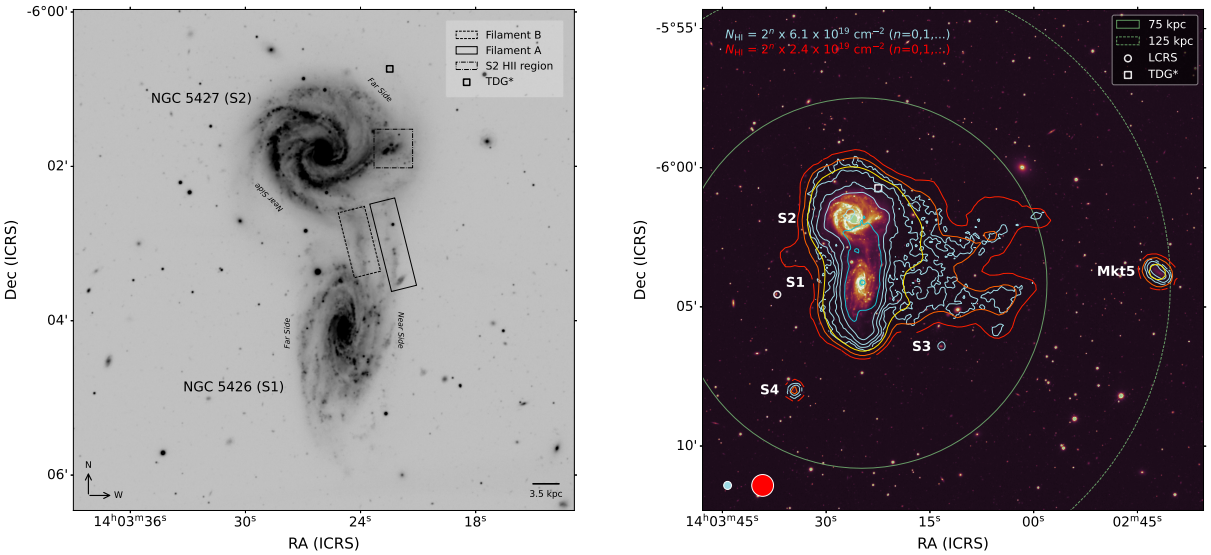

Figure 5.1: **Left panel:** B band image of the interacting pair Arp 271 observed using VIMOS/VLT. The annotations highlight the near and far sides as well as the eastern and western spiral arms of both S1 and S2. The filaments of the bridge are also annotated. **Right panel:** Column density contours of HI observed with MeerKAT are overlaid on the DECam g-band image of the group. The orange contours correspond to the $\sim$ 47$''$ resolution and the blue contours correspond to the $\sim$ 17$''$ resolution. Both contours were extracted from cubes smoothed to a channel width of $\sim$ 17 kms^{-1}.

HIPASS J1403-06 (J1403-06), one of the groups with the highest Hα luminosity in the Choirs sample, consists of the interacting pair, Arp 271 (Arp 1966), and 3 dwarf members (S3, S4, Mkt5). Additionally, Kourkchi & Tully (2017), in their catalogue of groups, report an LCRS object named LCRS B140059.8-055011 (LEDA 1037046) located to the east of the pair. While this object is likely a part of the group, it is not detected in HI or Hα. The faint dwarf companion to the west of the interacting central galaxies, Mkt5, is a catalogued APMUKS object, B140004.67-054920.9. Sweet et al. (2014) performed a study of the dwarf galaxies in Choir groups including S3 and S4 and they found that both dwarfs are metal-poor ($12 + \log(\mathrm{O/H}) < 8.0$) akin to gas-rich cluster dwarf galaxies (e.g., Hydra: Duc et al. 2001). They suggest that one plausible explanation for the low metalicity could be the inflow of neutral gas resulting from interactions with nearby galaxies (e.g., Kannappan et al. 2013; Skillman et al. 2013). In their later work, Sweet et al. (2016) identify a Tidal Dwarf Galaxy (TDG) candidate with a disturbed rotation curve above S2 (see square marker in figure 5.1). In terms of the environment of J1403-06, Džudžar et al. (2021) find that the closest filament is located approximately 6.6 Mpc from the group. The nearest neighbours to the group are farther than $\sim$ 0.8 Mpc in projection. Džudžar et al. (2021), assuming that the

neighbouring galaxies are moving towards the group, predict J1403-06 to evolve into an HCG-like compact group in the future.

Table 5.1: The table lists some basic properties of the member galaxies of the J1403-06 group, including their name, optical identification, Right Ascension (RA), declination (Dec.), heliocentric velocity (V_{hel}), Hα luminosity ($L_{H\alpha}$) from WiFeS spectra, stellar mass, and the star formation rate.
'*' Sources previously detected in HI.
[1] TDG candidate identified in Sweet et al. (2016).
[2] APMUKS(BJ) B140004.67-054920.9
[3] LCRS B140059.8-055011.
[a] Values taken from Sweet et al. (2014) and Sweet et al. (2016).
[b] Values taken from NED.
[c] $M_\star$ calculated using WISE W1 band by Mosenkov et al. (2019).
[d] SFR calculated using an SED model of UV, optical, and FIR by Misiriotis et al. (2004).

Name	Optical ID	RA (h:m:s)	Dec. (d:m:s)	V_{hel} ($km\,s^{-1}$)	$L_{H\alpha}$ (10^{-20} erg cm^{-2} s^{-1})	log $M_\star$ $M_\odot$	SFR $M_\odot$ yr^{-1}
S1*	NGC 5426	14:03:24.88	−06:04:09.14	2498[a]	31.100 ± 0.210[a]	10.64[c]	4.17[d]
S2*	NGC 5427	14:03:26.09	−06:01:51.20	2727[a]	48.200 ± 0.460[a]	10.68[c]	8.91[d]
S3	APMUKS	14:03:13.48	−06:06:24.17	2753[a]	0.099 ± 0.001[a]	-	-
S4*	APMUKS	14:03:34.62	−06:07:59.27	2671[a]	0.024 ± 0.001[a]	-	-
g1[1]	-	14:03:22.48	−06:00:44.24	2692[a]	0.215 ± 0.002[a]	-	-
Mkt5*	APMUKS[2]	14:02:42.01	−06:03:44.19	-	-	-	-
LCRS	LCRS[3]	14:03:37.06	−06:04:33.30	2609[b]	-	-	-

The interacting pair, Arp 271, consists of two spiral galaxies, NGC 5426 (southern member; hereafter S1) and NGC 5427 (northern member; hereafter S2). Due to their similar morphology types, internal structures, and comparable sizes, Yamagata et al. (1989) categorize S1 and S2 as 'twin galaxies' that formed under the same initial conditions. S1 has been classified as SA(s)c pec with luminosity class II and S2 as SB(s)c pec, Seyfert 2 with luminosity class I by Blackman (1982) and de Vaucouleurs et al. (1991). S2 has been variably classified as barred and unbarred in the literature (e.g., Fuentes-Carrera et al. 2004; Comerón et al. 2010). The interacting pair has been studied photometrically as part of various surveys in: near-, mid-, and far-infrared (Spitzer: Smith et al. 2007; Zaragoza-Cardiel et al. 2018, WISE: Mosenkov et al. 2019, Hershel Space Observatory: Mosenkov et al. 2019), FUV and NUV (Galex: Smith et al. 2010), optical (Smith et al. 2016; Sweet et al. 2013). The bridge between S1 and S2 is seen in UV (Smith et al. 2010), IR (Smith et al. 2007), and optical (Fuentes-Carrera et al. 2004; Smith et al. 2010; Font et al. 2011; Sweet et al. 2013; Smith et al. 2016). The bridge of stars can be divided into two filaments (see left panel of figure 5.1). Filament A can be interpreted as the extension of the western arm of S1 while filament B seems likely to have originated from in-situ star formation resulting from the interaction (Fuentes-Carrera et al. 2004). The star formation in the pair is knotty as indicated by the discernible clusters of HII regions. In S1, the HII regions are predominantly located in the western half (near-side), whereas in S2, they are mostly concentrated in the north-eastern half. Interestingly, at the end of the unusual straight-arm segment of the eastern spiral arm of S2, there is a bright star-forming region that does not follow the logarithmic spiral-arm pattern. Using the Nobeyama single dish telescope, Sorai et al. (2019), report a total Molecular gas mass, log M_{mol} of 9.683 and 10.033 respectively for S1 and S2. From Misiriotis et al. (2004); Sorai et al. (2019); Mosenkov et al. (2019), we take away that compared to S1, S2 seems to have a higher SFR, stellar mass, and molecular gas mass.

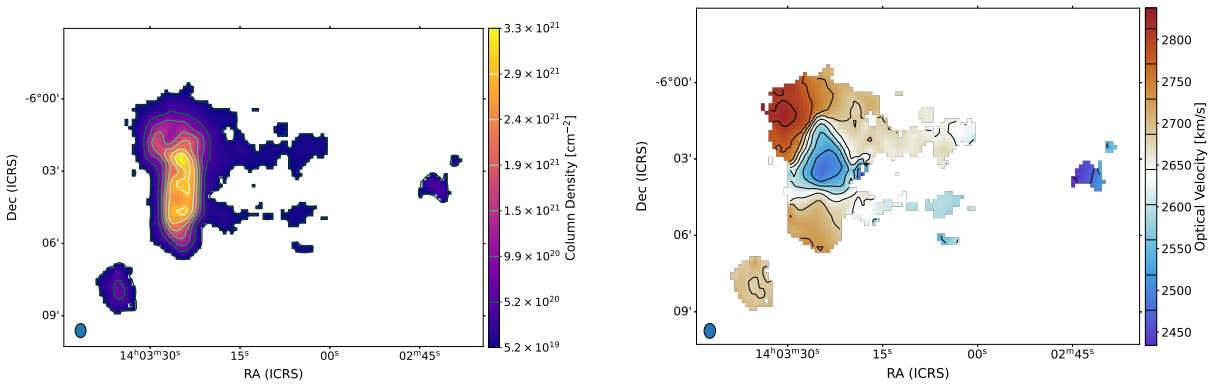

Figure 5.2: The column density image (left) and the velocity field (right) extracted from the VLA cube with a $\sim 35''$ beam. HI in S1 and S2 is seen as a single structure. Dwarfs S4 and Mkt5 are also detected.

The kinematics of Hα in Arp 271 was studied by Fuentes-Carrera et al. (2004) and Font et al. (2011) using Fabry-Perot spectroscopy (FP). From the iso-velocity contours, Fuentes-Carrera et al. (2004) posit the existence of a $\sim 6''$ incipient bar in S1 and a $\sim 32''$ bar in S2. They further find that most of the HII regions in the bridge have line-of-sight velocities corresponding to the approaching side velocities of S1 and therefore are likely a part of S1. Font et al. (2011) detect anomalous gas behind the disc of S2 with velocities comparable to S1. They find that the anomalous emission mainly comes from the regions between spiral arms and off the disc edge of S2. Furthermore, the pattern in the anomalous gas reflects the distribution of the HII regions of S2 as the brightness of an emitter depends on its distance from the source of Lyc photons. They conclude that the anomalous emission from behind the disc of S2 gets modulated by the dust in the disc before reaching the observer. To explain the anomalous emission, they draw a parallel to the High-Velocity Clouds (HVCs) in the Milky Way and propose that the emission originates from ionized gas from S1 falling towards S2. Font et al. (2011), using the mass of the anomalous ionized hydrogen gas detected behind S2 and certain simplistic assumptions, infer a mass inflow of 10 $M_\odot$ yr^{-1} distributed across the disc. The rotation of Arp 271 was also studied as part of Mogotsi (2016), who employed DiskFit and ROTCUR to fit the velocity field of H_α observed with the SparsePak IFU on the WIYN telescope.

5.2 HI in the group

The neutral hydrogen in the group, prior to this work, has been observed as part of HIPASS (Meyer et al. 2004) and with the VLA as part of Clemens (1999), but a detailed examination of the HI does not exist in the literature. Due to the unique HI distribution in Arp 271, it has been added to the HI rogues gallery (Hibbard et al. 2001). Even though we were unable to access the Clemens (1999) doctoral dissertation containing the data reduction and analysis of the VLA observation, we obtained the data from the archive and performed the data reduction steps outlined in section 2.11. In sub-section 5.2.1, we compare our data against the archival VLA data and in sub-section 5.3, we discuss the neutral gas properties of the interacting galaxies in the group.

5.2.1 Comparison with VLA data

The column density image and the velocity field of the group observed with the C and D configurations of the VLA for a total integration time of 3.8 hours are displayed in figure 5.2. The HI gas linked to S1 and S2 appears as a unified structure and two elongated tails stretching towards the west are also seen. Two of the four dwarf members, S4 and Mkt5, are detected. Due to the low-velocity resolution, the kinematics of the individual galaxies cannot be extracted. We observed J1403-06 with the MeerKAT telescope for a total integration time of 4.78 hours. We show the column density image and the velocity field in figure 5.3. Our observation resolves the complex HI morphology of the interaction both spatially and spectrally, allowing us to perform detailed kinematic analysis of the individual galaxies. Our observation reveals apparently normally rotating HI discs alongside two distinct tails emerging in the western direction. The approaching side of S1 appears to be in front of S2 in projection. The smooth gradient observed for the two long tails originating from S1 and S2 seen in the velocity map (bottom panel of figure 5.3) and their extensions to about ~ 90 kpc from the discs, hint at a potential tidal origin. The group members are annotated in figure 5.1 and their HI properties are summarised in table 5.2.

Table 5.2: The table displays the HI properties of the galaxies in the group. The systemic velocity values (V_{HI}) marked with ^{a} are from tilted ring modelling, while those marked with ^{b} are from SoFiA2 parameterisation. The luminosity distance (D_L) was calculated from the systemic velocities using cosmological parameters from Planck Collaboration (2020). The RMS values are from the SoFiA2 generated source catalogue. We measure the total flux (S_v) and the HI mass (M_{HI}) within the column density limit (N_{HI}), which is obtained as the median of the observed flux at an SNR between 2 and 3.

Name	V_{HI} ($km\,s^{-1}$)	D_L (Mpc)	RMS ($mJy\,beam^{-1}$)	log M_{HI} ($M_\odot$)	S_v (Jy km s^{-1})	N_{HI} ($10^{19}\,cm^{-2}$)
S1	$2582.228^{+2.843}_{-2.701}$	38.42	0.19	10.07 ± 0.03	33.39 ± 0.22	4.29
S2	$2736.21^{+3.256}_{-3.473}$	40.72	0.19	9.97 ± 0.03	19.92 ± 0.22	4.29
S3	2767.93 ± 1.72	41.20	0.33	7.31 ± 0.48	0.05 ± 0.01	4.11
S4	2687.2 ± 0.54	39.99	0.26	7.88 ± 0.18	0.20 ± 0.01	2.29
Mkt5	$2480.907^{+0.353}_{-0.321}$	36.86	0.24	8.34 ± 0.11	0.68 ± 0.019	2.2

HIPASS measured an integrated flux of 50 Jy km s^{-1}, which using equation 3.12 and a distance of 40 Mpc, translates to an HI mass of, log $M_{HI} = 10.27\ M_\odot$. For the HI distribution shown in figures 5.2 and 5.3, in both the $\sim 35''$ VLA cube and the $\sim 17''$ MeerKAT cube, we measure a log HI mass of $\sim 10.34\ M_\odot$, which is 0.07 dex higher than that measured by HIPASS. The fact that we recover the same mass from two different datasets attests to the validity of our parameterisation methods. While the VLA data has a channel width of ~ 21 $km\,s^{-1}$ an RMS of ~ 0.5 mJy $beam^{-1}$, and a column density limit of 5.2×10^{19} cm^{-2}, the MeerKAT data has a channel width of ~ 5.6 $km\,s^{-1}$ an RMS of ~ 0.19 mJy $beam^{-1}$ and a column density limit of 4.3×10^{19} cm^{-2}. Compared to the VLA data, the MeerKAT data has a 4 times higher velocity resolution, 2.5 times lower noise, and twice the spatial resolution. The improvement is evident from the column density image and the velocity field shown in figure 5.3. The sensitive and resolved MeerKAT observation enables us to perform detailed kinematic modelling to study the complex motions in the interaction. In the following sections, we discuss the structure and kinematics of S1, S2, and Mkt5. We also attempt to explain the origin of the western tails and anomalous gas emission seen in S1 and S2. For the first time, we detect the neutral gas in S3, rotation in Mkt5, isolate the neutral hydrogen in the interacting galaxies and retrieve the

complex structure of the two western tails.

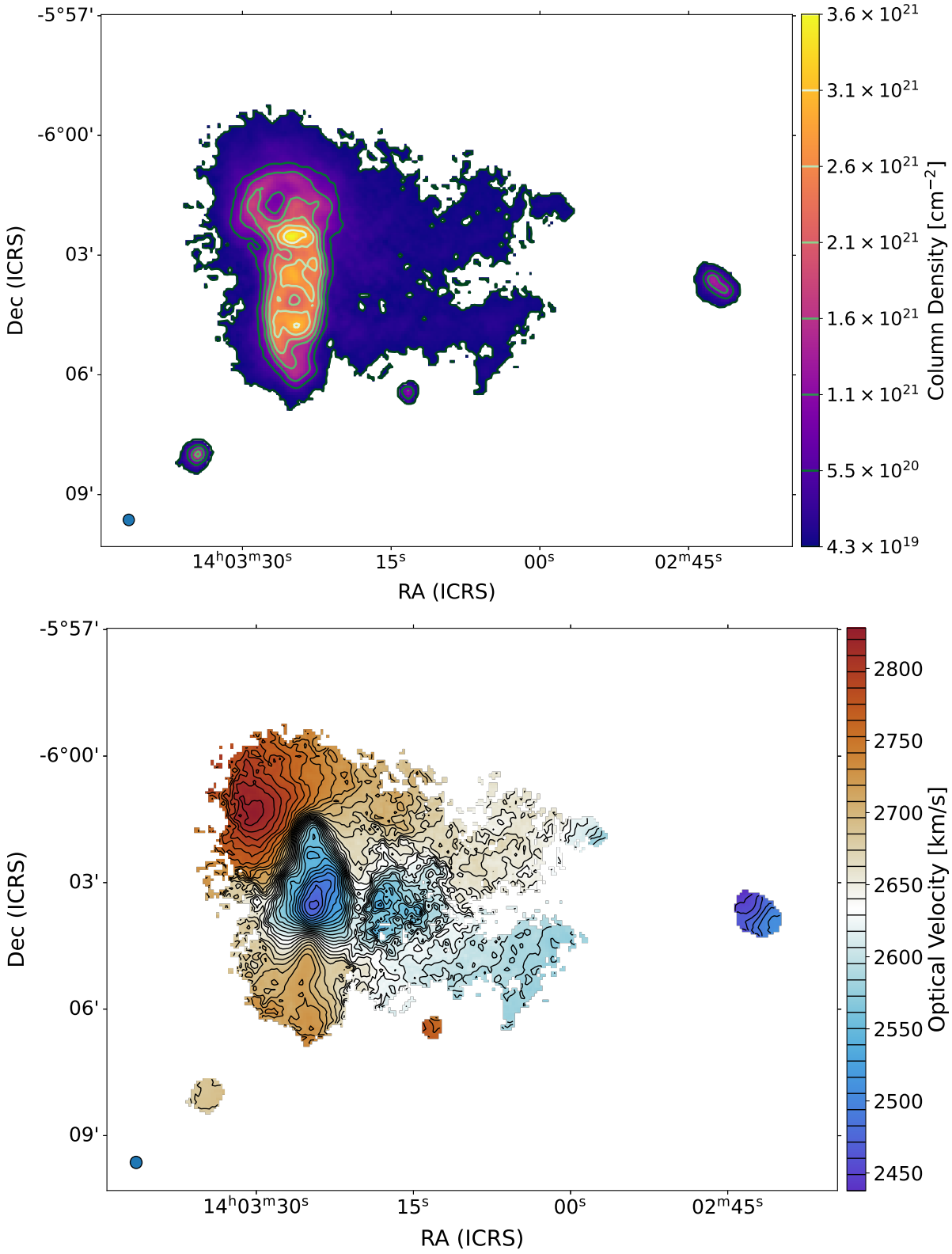

Figure 5.3: The column density image (top) and the velocity field (bottom) extracted from the MeerKAT $\sim 17''$ cube. HI in S1, S2, S3, S4, and Mkt5 can be clearly seen along with the three western tails.

5.3 The interacting pair

Due to the proximity and nature of the interaction between S1 and S2, as seen in the spectra in figure 5.4 and the channel maps in figure 5.5, we inspected the data in 3D using AstroSlicer (Punzo et al. 2017) to identify 2D planes at the intersection of the pair without emission above a few times the noise ($\sim 2\sigma_{chan}$). We then separate the two galaxies at the identified planes. The spectra extracted at certain illustrative spaxels shown as insets in figure 5.4 highlight that the gas associated with the two galaxies can be identified distinctly by their spectral profiles. The projected spatial separation between the centres of S1 and S2 is $\sim$ 26 kpc. The PV diagrams extracted parallel to the major and minor axes of S1 shown in the appendix figure C.15 emphasize the difficulty of the task of separation. The companion Mkt5 is at a projected distance of $\sim$ 120 kpc and $\sim$ 125 kpc respectively from the centres of S1 and S2. The optical and HI centres of S1, S2, and Mkt5 are consistent within our pixel scale. Along the line of sight, the velocity separation between S1 and S2 is ~ 150 km s^{-1} and that between S1 and Mkt5 is ~ 100 km s^{-1} (S2 & Mkt5 is 250 km s^{-1}). By following the assumption of trailing spiral arms, we infer that both S1 and S2 are co-rotating in the clockwise direction.

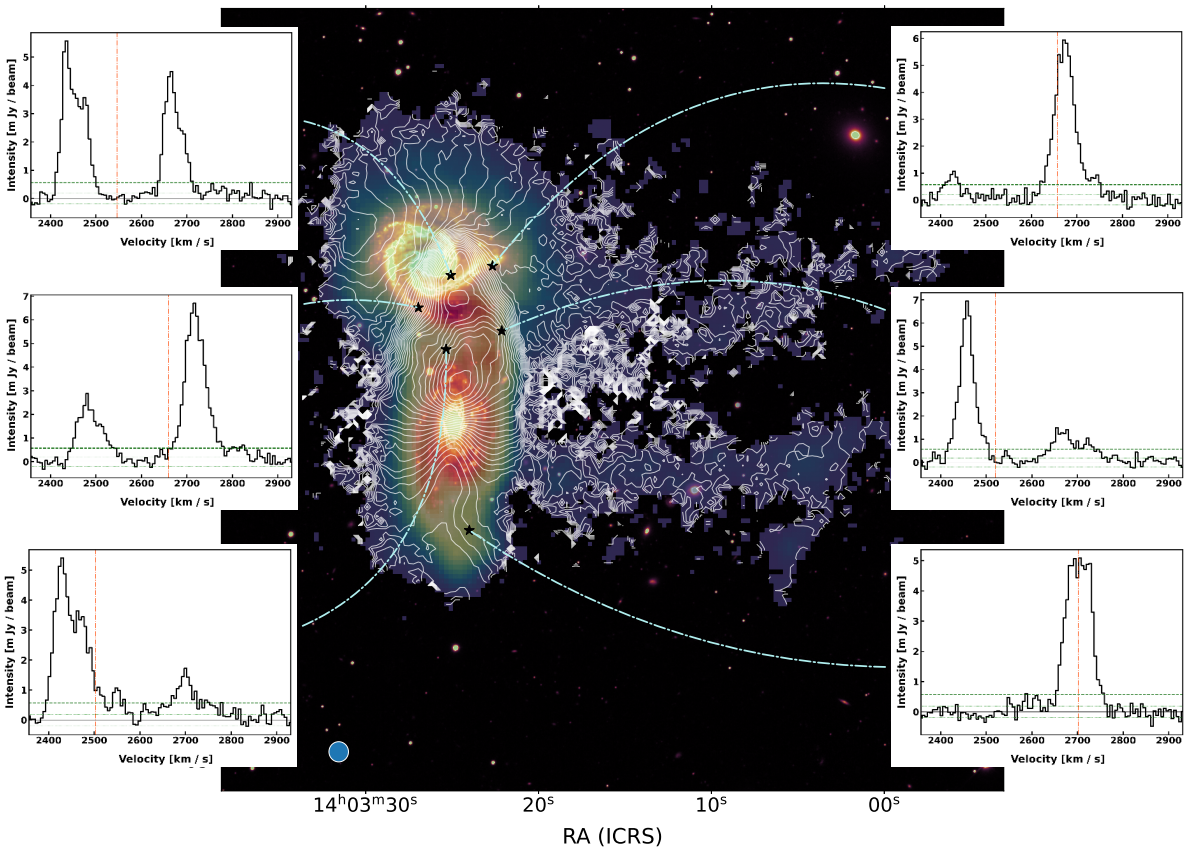

Figure 5.4: Column density image of the combined gas distribution of S1 and S2 overlaid on DECam g-band image. The white contours correspond to the velocity field of the total gas distribution. The inset plots show spectra extracted at the annotated spaxels for illustration. In the inset plots, the red vertical line corresponds to the value on the first moment at the respective spaxel.

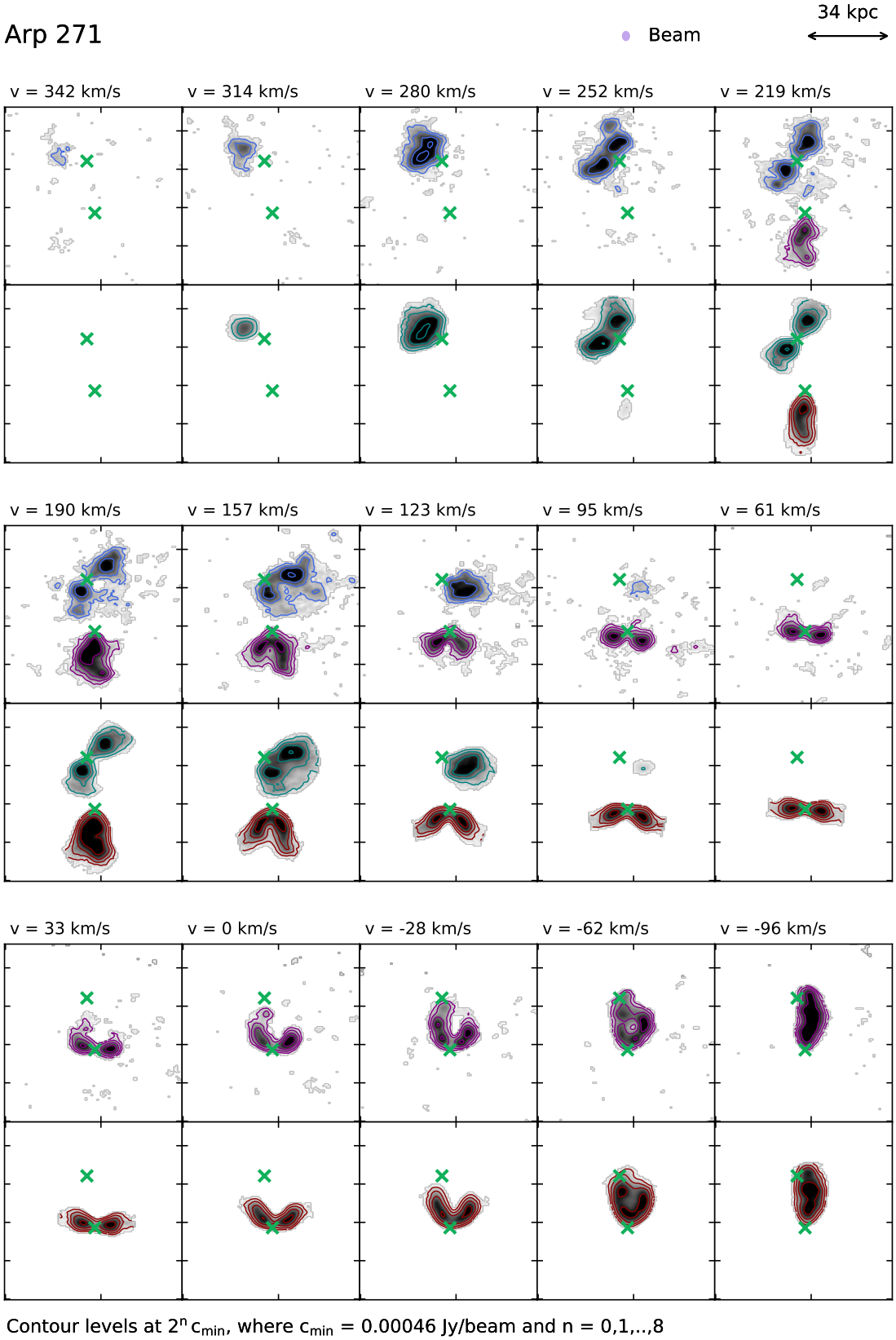

Figure 5.5: Channel maps showing the structure of the neutral gas in Arp 271. The bottom panel in each channel show the ^{3D}BAROLO model of the respective discs. The anomalous gas emission in the data can be seen clearly in regions not modelled as a disc.

5.3.1 J1403-06 S1

NGC 5426 (S1) is a two-armed grand design spiral with an intermediate inclination, $i \sim 60°$. Based on the relative position of the receding and approaching sides and the convention of trailing spiral arms, it can be inferred that the galaxy is rotating clockwise and that the western side is closer to the observer (near side) than the eastern side (far side). From the MeerKAT HI data of S1 we measure a total mass of log $M_{HI} = 10.11 \pm 0.03$, above the column density limit (minimum column density contour shown in panel 1 of figure 5.6). Aside from the two western tails which have a combined mass of log $M_{HI} = 9.09 \pm 0.03$, the HI morphology of S1 is that of a rotating disc featuring a prominent warp in the outer regions. The VIMOS B band image in the left panel of figure 5.1 shows a higher fraction of star-forming regions in the near side of S1 compared to the far side. The HI column density maps shown in figure 5.6 hint at a potential link between the locally enhanced star formation and the western tails. We also note that the iso-velocity contours seem more disturbed in the receding side. The position velocity diagram extracted along the major axis (median P.A.) demarcated in the second panel of figure 5.6 is shown in the subsequent panels of the same figure. The approaching side exhibits a slightly greater extension compared to the receding side, while the latter appears to be truncated. The ^{3D}BAROLO model of the disc is plotted as pale green contours to distinguish the anomalous gas in the disc. Closer inspection of the HI reveals the existence of 'beard' gas or EPG and also an asymmetric gas distribution. While gas at velocities lower than the rotation velocity is expected in disc galaxies (EPG), here, we also detect gas with velocities greater than the rotation velocities in the disc (see PV slices in the appendix figure C.15).

We create an elliptical mask of the disc in 2D and extrude it along the line of sight to isolate the disc data and the tails. We use the disc data cube for tilted ring modelling and the full data cube for Gaussian decomposition. We perform tilted ring modelling on the disc data cube of S1 using ^{3D}BAROLO as discussed in section 3.5.1 with a constant vertical thickness of 2.5″ which corresponds to $\sim$ 485 pc at the systemic recession velocity, $V_{sys} = 2582$ km s^{-1}. We find a median inclination, $i \sim 62° \pm 6°$ and median P.A., $\phi \sim 173° \pm 6°$. The fitted parameters of the models are shown in figure 5.7 and the rings defined for the tilted ring modelling are shown in figure 5.8. Interestingly, in the approaching side, the rotation curve peaks around $\sim$ 10 kpc and drops by about $\sim$ 20 km s^{-1} at $\sim$ 15 kpc with a gradient of ~ -4 km s^{-1} kpc^{-1}. We find a rotation velocity, $v_{rot} \sim 170$ km s^{-1} similar to Mogotsi (2016). Although, our v_{rot} is lower than the $v_{rot} \sim 200$ km s^{-1} obtained by Fuentes-Carrera et al. (2004) with an inclination of 59° using FP observations of Hα and Bottinelli et al. (1984) using 1D HI spectra. The discrepancy in v_{rot} can be attributed to the differences in the adopted inclination, as there is a well-known degeneracy between inclination and rotation velocity. They also estimate the total dynamical mass of both galaxies within $D_{25}/2$ to be between $6.72-11.2\times10^{10}$ $M_\odot$ for S1 and $4.5-7.5\times10^{10}$ $M_\odot$ for S2. The uncertainty in the adopted inclination greatly affects their mass models based on which they conclude that S1 is the more massive galaxy of the pair within the optical radius.

Additionally, as shown in figure 5.7, in our three-step approach to tilted ring modelling, we allow for the variation in i and P.A. in contrast to the constant values adopted in Fuentes-Carrera et al. (2004). In doing so, we find that the receding side is more warped than the approaching side. Notably, in projection, although the approaching side of S1 may seem closer to S2, the

receding side of S1 is closer to S2 along the line of sight. In the third step, where we solely fit the radial velocities, we measure positive radial velocities ($v_{rad} \sim 20$ km s^{-1}) in the outer rings ($\gtrsim 15$

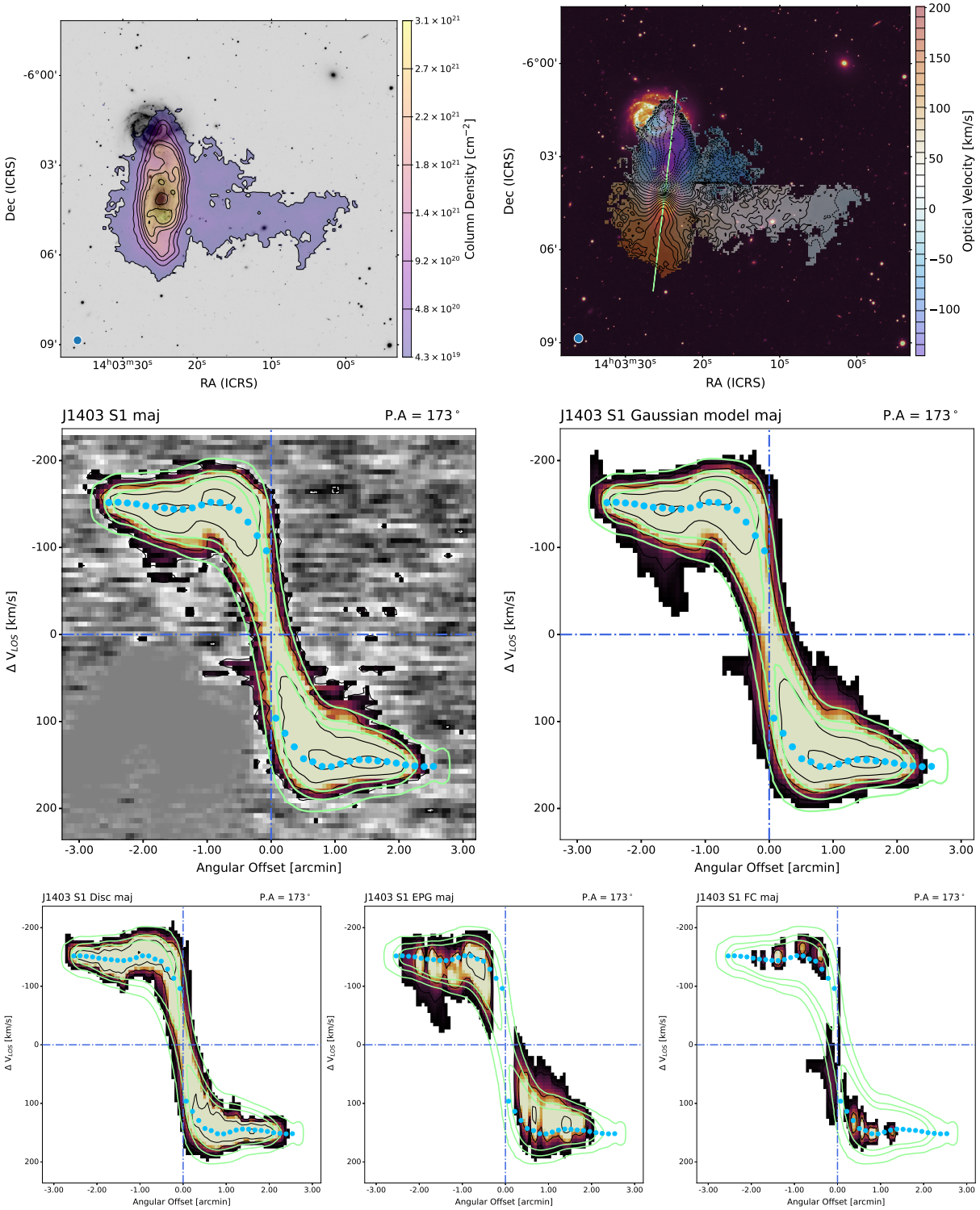

Figure 5.6: **Top row:** Moment maps of S1 overlaid on DECam g-band image. Panel 1 (left) shows the column density image. Panel 2 (right) shows the velocity field. The major axis (median P.A.) along which the subsequent PV slices were extracted is represented by the pale green line in the velocity field map. Panels 3-7 (left to right) show PV slices with ^{3D}BAROLO contours of the corresponding model slice overlaid. **Middle row:** PV slices of the data cube and the multi-component Gaussian model cube. **Bottom row:** PV slices of the disc Gaussian model cube, EPG Gaussian model cube and the fast component (FC) Gaussian model cube.

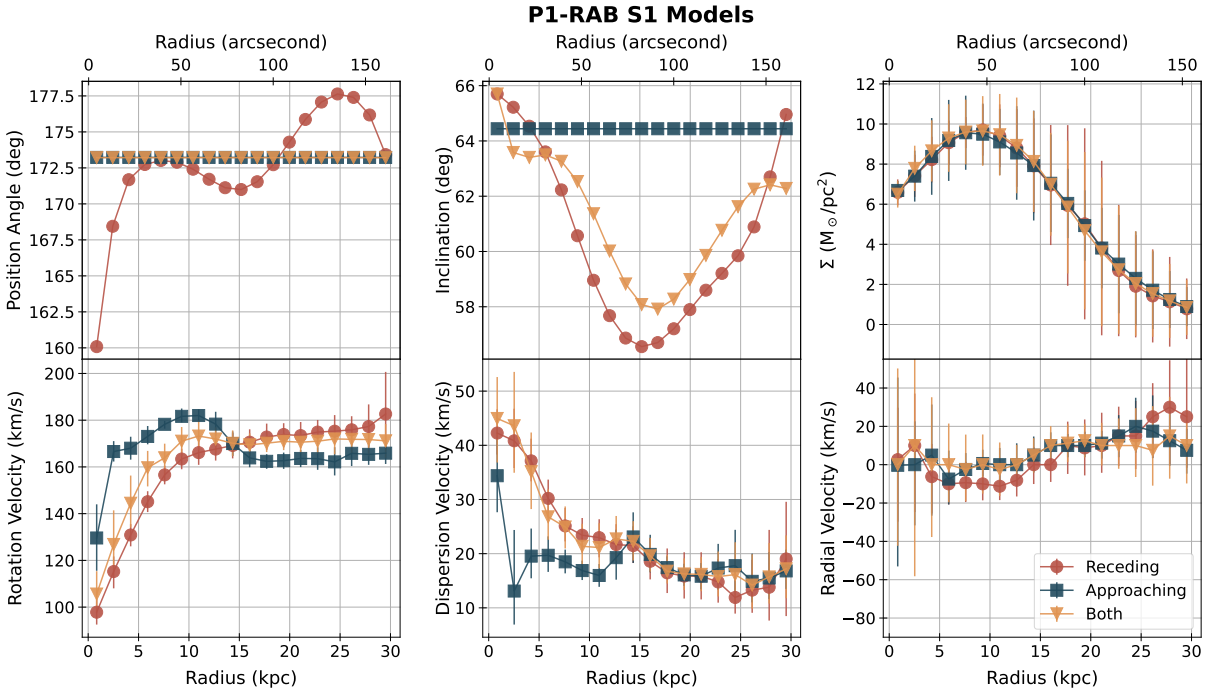

Figure 5.7: ^{3D}BAROLO tilted ring model parameters for S1 plotted as a function of radius. From left to right, P.A., inclination, surface density, rotation velocity, dispersion velocity, and radial velocity. The orange triangle, blue square, and red circle symbols denote the parameters for the model of both sides, the approaching side, and the receding side respectively. The modelling was performed in three steps as delineated in section 3.5.1.

kpc), particularly in the receding side. As discussed in Di Teodoro & Peek (2021), in ^{3D}BAROLO positive v_{rad} in discs rotating clockwise suggests an outflow. However, we do note that if the warp is not well-constrained, changes in P.A. can often be misinterpreted as radial velocities. If true, this could either be a sign of an outflow potentially due to the pull from S2 or due to the mechanism(s) causing the tails or a combination of both. In the inner rings ($\lesssim$ 15 kpc), we see negative V_{rad} in the receding side which could imply an inflow triggered by the interaction. An inflow of low angular momentum cold gas can also explain the observed negative velocity gradient at $\sim$ 10 kpc in the approaching side. It seems likely that we are observing an amalgam of different processes leading to an inflow at $\sim$ 10 kpc in the inner rings and an outflow beyond $\sim$ 15 kpc in the outer rings. Conversely, if there were an inflow in the outer rings caused by the re-accretion of the tail gas, it could potentially explain the locally enhanced star formation observed in the near side of S1. The latter phenomenon has been observed in several galaxy interactions and the ensuing star-forming regions are known as hinge clumps (e.g., Smith et al. 2014, 2016).

To separate the anomalous gas from the disc, we perform Gaussian decomposition on the full data cube using GaussPy+ (see section 3.6.2) followed by our kinematic tagging technique introduced in section 3.7.3. The PV slices extracted along the major axis of the data and Gaussian model cubes are shown in figure 5.6. The major axis PV slice of the total multi-component Gaussian model of the data shown in panel 4 of figure 5.6 adequately reproduces the major axis PV of the data shown in panel 3 of the same figure. In figure 5.9 we show an illustration of the Gaussian decomposition and kinematic tagging performed on S1. The component map overlaid on the DECam g-band image shows the extensive presence of multiple components across the disc

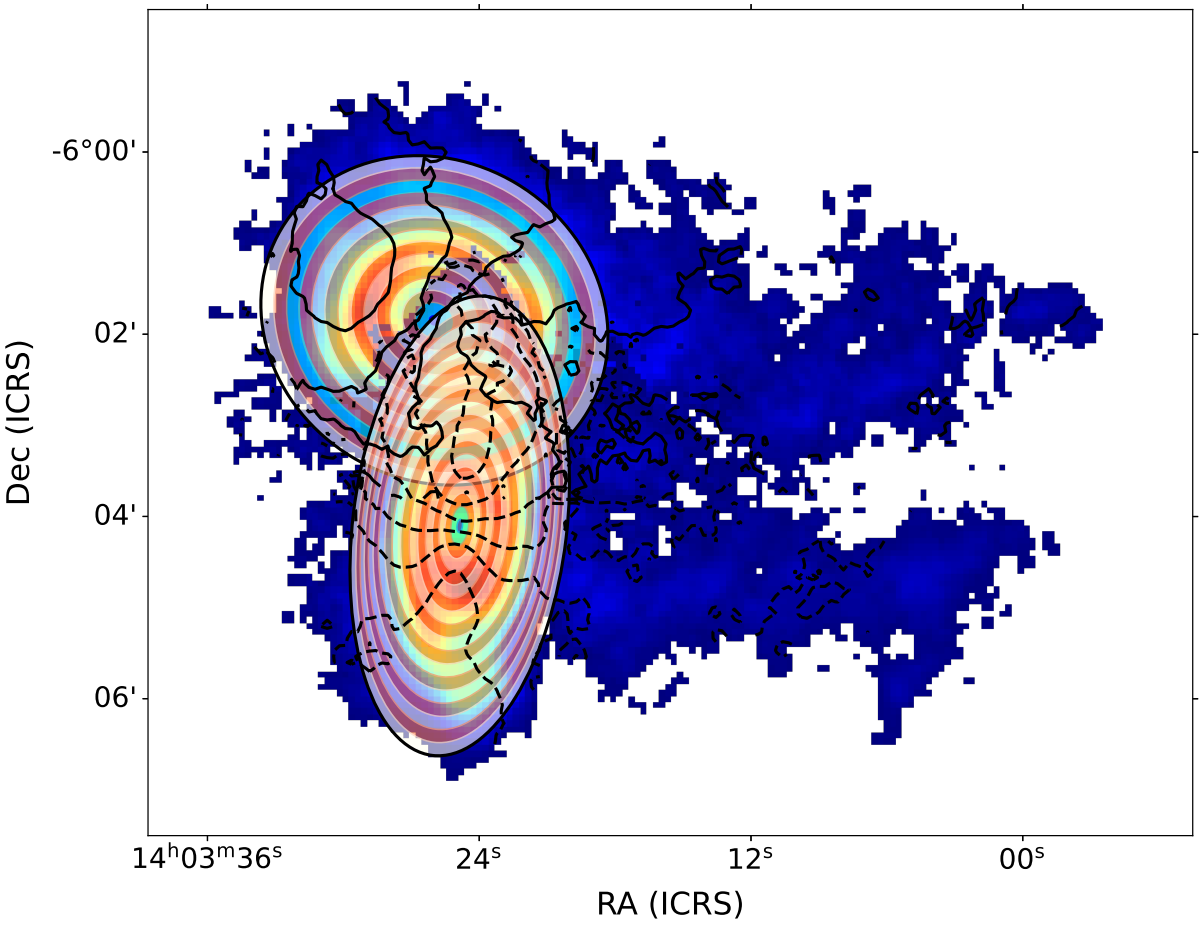

Figure 5.8: The rings defined for deriving the kinematic parameters of S1 and S2 and overlaid on a column density image to show the geometry. The image also serves to represent the overlap of the discs of the two galaxies in the projected sky plane.

which suggests the presence of anomalous gas clouds. In the inset plots of the spectra extracted from the annotated spaxels, we also plot the corresponding spectra extracted from the tilted ring model fitted to S1 using ^{3D}BAROLO . Our tagging algorithm utilizes the ^{3D}BAROLO model to identify the disc component (blue Gaussian in figure 5.9) and it tags the lagging component with respect to the disc as EPG (magenta Gaussian in figure 5.9) and the component with velocities faster than the disc component as FC (sky-blue Gaussian in figure 5.9). We then save all the Gaussian models obtained per spaxel into respective cubes for each of the components. The column density image, velocity field, and PV slices of the Gaussian model cubes for disc, EPG, and FC can be found respectively in appendix figures C.16-C.17, C.18-C.19, and C.20-C.21. The figures of the disc component show a successful separation of the bulk of the anomalous gas albeit with some residual in the outer rings of the disc model (panel 5 of figure 5.6 and appendix figures C.16 and C.17). The major axis PV slices of EPG and FC (panels 6 and 7 of figure 5.6) show a concentration of EPG on the approaching side and a concentration of FC on the receding side. This asymmetry is seen more clearly in slices of the anomalous components extracted parallel to the major axis in the near and far side (top row, panels 1 and 3 of appendix figures C.19 and C.21). The same can also be seen qualitatively in the moment maps (appendix figures C.18 and C.20), the approaching side slice parallel to the minor axis in the EPG PV diagrams (bottom row, panel 6 in appendix figure C.19), and the receding side slice parallel to the minor axis in

the FC PV diagrams (bottom row, panel 4 in appendix figure C.21). Additionally, to illustrate the effectiveness of the models in reproducing the data, we show the 2D residuals obtained by subtracting the intensity, velocity field, and dispersion maps of the models from that of the data in appendix figure C.22. In summary, the Gaussian decomposition and kinematic tagging performed on S1 qualitatively indicate a higher fraction of lagging gas in the approaching side and a higher fraction of leading gas in the receding side.

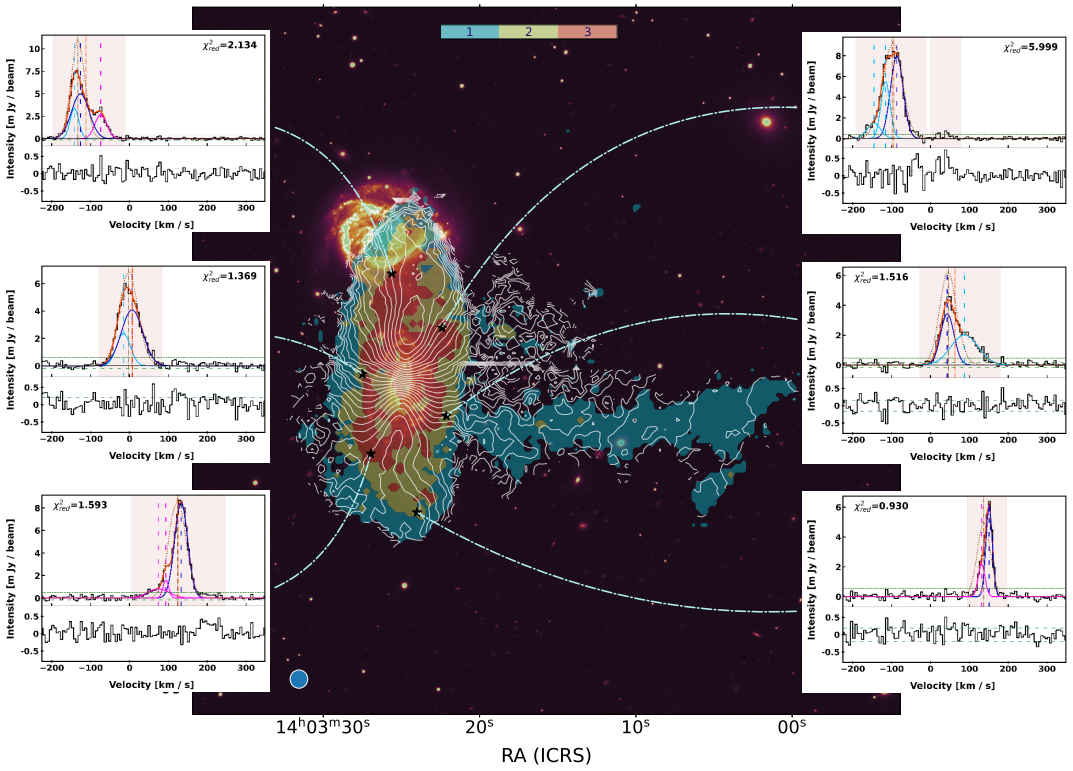

Figure 5.9: Component map and illustrative spectral profiles of S1. Velocity field contours and a map of the number of fitted Gaussian components overlaid on DECam g-band image. The colour bar shows the number of fitted components. The inset plots show the spectra extracted at the annotated spaxels and Gaussian components fitted to the corresponding spectra for illustration. The blue-coloured Gaussian is tagged as the disc component, the magenta Gaussian is tagged as the EPG component, and the sky-blue Gaussian is tagged as the anomalous gas component. The ^{3D}BAROLO model spectra extracted at the annotated spaxels are plotted as brown dotted lines in the inset plots for comparison.

5.3.2 J1403-06 S2

NGC 5427 (S2) is an Sc-type spiral seen at a low-inclination, $i \sim 30°$ and hosting a Seyfert 2 nucleus. S2 has a clockwise rotation with the approaching side in the south-west, being closer to S1 along the line-of-sight. The near side is in the south-east and the far side is in the north-west (see annotations in figure 5.1). While Fuentes-Carrera et al. (2004) report signs of a bar in S2, Comerón et al. (2010) classify S2 as unbarred. Comerón et al. (2010) and Buta & Crocker (1993) report a circumnuclear feature that is ambiguous between nuclear rings and pseudo-rings. They also note that parts of the feature appear to be missing in the north and south. In the inner 700 pc, Martini et al. (2003) report four or five nuclear dust spirals. The circumnuclear ring structure of HII regions can be seen to extend up to about 1 kpc from the nucleus in Hα images and emission line maps (Evans et al. 1996; González Delgado et al. 1997; Dopita et al. 2014). Furthermore,

Dopita et al. (2014) find that the Extended Narrow-Line region (ENLR) of the Seyfert 2 galaxy is extended more in the north-west and south-east directions which is roughly perpendicular to the nuclear ring of star formation and thus potentially a sign of a classical "ionisation cone". Dopita et al. (2014), in their investigation of a range of emission lines observed with WiFeS IFU (Hα, Hβ, N[II], O[III]), detect a clear global radial abundance gradient in S2 which according to Rich et al. (2012) is typical of galaxies in Stage 1 of their merging process. The nuclear metallicity that they measure, $\sim 12 + \log(\mathrm{O/H}) \sim 9.2$, indicates that S2 is among the most metal-rich star-forming galaxies in the local mass-metallicity relation (cf. Lara-López et al. 2013). Although, the high abundance is comparable to several other observational and theoretical studies that suggest high metallicities in Seyfert galaxies (e.g., Nagao et al. 2002; Ballero et al. 2008). In their Hα FP data analysis, Font et al. (2011) report the presence of a galactic wind with a velocity of around $400\,\mathrm{km\,s^{-1}}$ and they propose that the wind may have originated from the increased SFR of S2, particularly near the galaxy's nucleus. The enhancement in He and N required by the best-fitting model adopted in Dopita et al. (2014) implies that massive fast-rotating stars form within the accretion flow near the black hole and enrich the ENLR. The circumnuclear star formation, nuclear activity, and the metallicity gradient suggest a plausible link to the ongoing interaction with S1 Kennicutt & Keel 1984; Comerón et al. 2010; Font et al. 2011; Dopita et al. 2014). But until this work, a direct relationship between the star formation in S2 and the cold gas in the interaction has not yet been established.

From the MeerKAT HI data of S2 we determine a total mass of $\log \mathrm{M_{HI}} = 9.97 \pm 0.03$, above the column density limit (minimum contour shown in panel 1 of figure 5.10). The column density image and the surface brightness profile show a drop in emission in the central regions (< 10 kpc) which could potentially be due to ionization by the nuclear and circumnuclear activity. The western HI tail seems to extend from the approaching side of the disc and has a mass of $\log \mathrm{M_{HI}} = 9.18 \pm 0.03$. The eastern boundary of the receding side appears to be truncated. The VIMOS B band image in the left panel of figure 5.1 shows a star-forming region in the east, potentially linked to the HI tail seen in the column density image. The position velocity diagram extracted from the datacube along the major axis (median P.A.) demarcated in the second panel of figure 5.10 is shown in the third panel of the same figure. Similar to S1, the PV slices reveal the existence of EPG, asymmetric gas distribution and also leading gas.

Similar to S1, we create a 2D elliptical mask of the disc and extrude it along the line-of-sight to isolate the disc data and the tails. We use the disc data cube for 3D tilted ring modelling and the full data cube for the Gaussian decomposition. We perform tilted ring modelling on the disc data cube of S2 using ^{3D}BAROLO as discussed in section 3.5.1 with a constant vertical thickness of $2.5''$ which corresponds to ~ 485 pc at the systemic recession velocity, $\mathrm{V}_{sys} = 2736$ km s^{-1}. We recover a median inclination, $i \sim 27^\circ \pm 3^\circ$ and median P.A., $\phi \sim 60^\circ \pm 6^\circ$. The fitted parameters of the models shown in figure 5.11 reveal several interesting features. Firstly, the rotation and the warp appear to be different for the approaching and the receding sides. Secondly, focusing just on the 'both sides' model (yellow triangles), the rotation and radial velocity curves within $\lesssim 5$ kpc indicate an outflow with $v_{rad} \sim 20$ $\mathrm{km\,s^{-1}}$ qualitatively consistent with the galactic wind argument by Font et al. (2011). Thirdly, the approaching side model in the outer rings ($\gtrsim 10$ kpc) indicates a radial outflow with $v_{rad} \sim 10$ $\mathrm{km\,s^{-1}}$ which could plausibly be linked to the western tail. As discussed in Di Teodoro & Peek (2021), in ^{3D}BAROLO , positive v_{rad} in discs

rotating clockwise suggests an outflow. Lastly, the rotation peaks around $\sim$ 12 kpc and drops by about $\sim$ 20 $\mathrm{km\,s^{-1}}$ at $\sim$ 20 kpc with a gradient of ~ -4 $\mathrm{km\,s^{-1}\,kpc^{-1}}$. Similar features

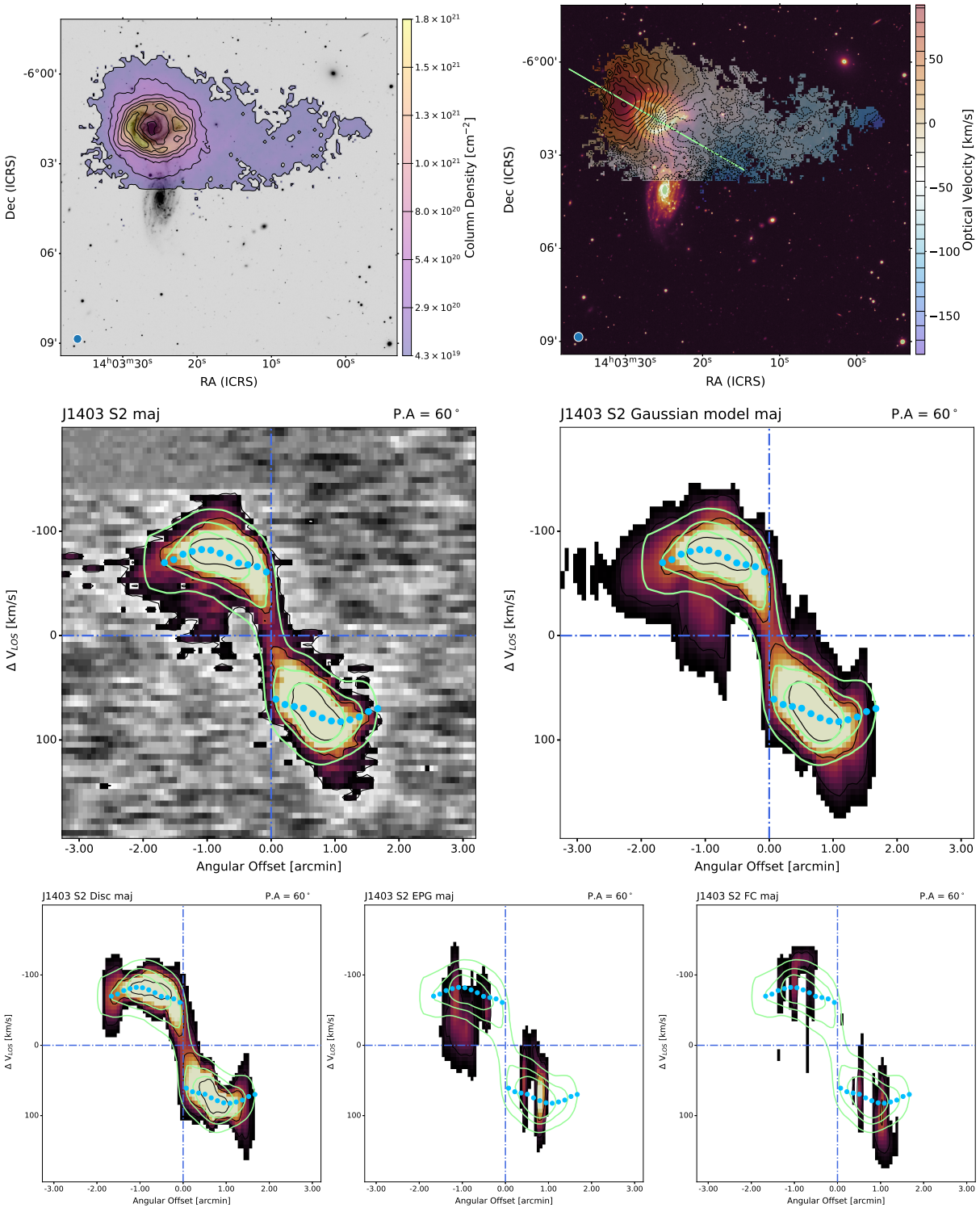

Figure 5.10: **Top row:** Moment maps of S2 overlaid on DECam g-band image. Panel 1 (left) shows the column density image. Panel 2 (right) shows the velocity field. The major axis (median P.A.) along which the subsequent PV slices were extracted is represented by the pale green line in the velocity field map. Panels 3-7 (left to right) show PV slices with ^{3D}BAROLO contours of the corresponding model slice overlaid. **Middle row:** PV slices of the data cube and the multi-component Gaussian model cube. **Bottom row:** PV slices of the disc Gaussian model cube, EPG Gaussian model cube and the fast component (FC) Gaussian model cube.

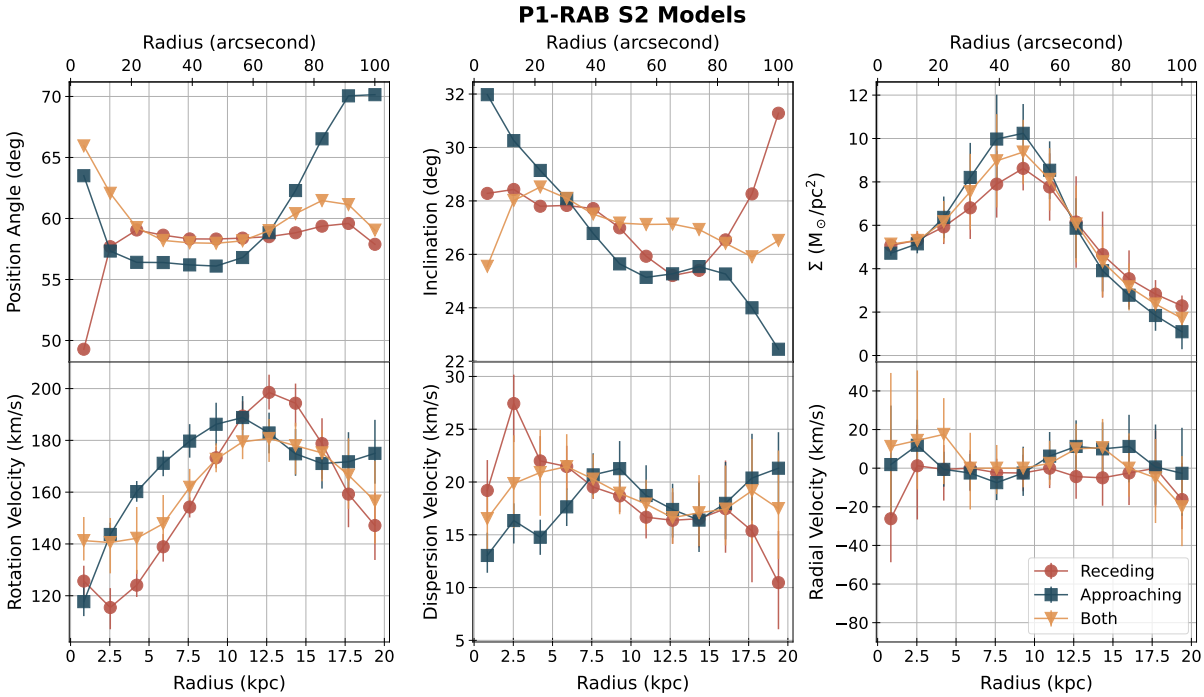

Figure 5.11: ^{3D}BAROLO tilted ring model parameters for S2 plotted as a function of radius. From left to right, P.A., inclination, surface density, rotation velocity, dispersion velocity, and radial velocity. The orange triangle, blue square, and red circle symbols denote the parameters for the model of both sides, the approaching side, and the receding side respectively. The modelling was performed in three steps as delineated in section 3.5.1.

can also be seen in the Hα rotation curve reported in Mogotsi (2016) and therefore are likely real. Although, while we determine a rotation velocity, $v_{rot} \sim 180$ km s^{-1}, they obtain a lower rotation ($v_{rot} \sim 150$ km s^{-1}) due to the higher inclination adopted in their work. Like in S1, we qualify our observations of radial velocities by acknowledging that if the warp is not well-constrained, changes in P.A. can often be misinterpreted as radial motions. Furthermore, unlike S1, the low inclination of S2 adds additional uncertainties to the recovered kinematic parameters. Nonetheless, the drop in rotation in the outer rings could either be a sign of an inflow potentially from S1 or the re-accretion of the tail gas or a combination of both. An inflow of low angular momentum cold gas could explain the observed negative velocity gradient around ~ 15 kpc and the re-accretion of the tail gas can potentially clarify if the western HII region observed in S2 is a hinge clump (annotated in the left panel of figure 5.1). In this case, it is likely a combination of both scenarios, but due to the low inclination and uncertainties associated with the radial velocity curve, we are unable to arrive at an unequivocal conclusion. Additionally, in appendix figure C.31, we show the 2D residuals obtained by subtracting the intensity, velocity field, and dispersion maps of the models from that of the data.

Similar to S1, we perform Gaussian decomposition on the full data cube using GaussPy+ (see section 3.6.2) and apply our kinematic tagging technique introduced in section 3.7.3 to separate the anomalous gas from the disc. In figure 5.12, we show an illustration of the Gaussian decomposition and kinematic tagging performed on S2. The component map overlaid on the DECam g-band image shows the extensive presence of multiple components across the gas disc which suggests the presence of anomalous gas clouds (lagging and leading components). In the inset plots of the spectra extracted from the annotated spaxels, we also plot the corresponding

spectra extracted from the tilted ring model fitted to S2 using ^{3D}BAROLO (see section 3.5.1). Our tagging algorithm utilizes the ^{3D}BAROLO model to identify the disc component (blue Gaussian in figure 5.12) and tags the lagging component with respect to the disc as EPG (magenta Gaussian in figure 5.12) and the component with velocities faster than the disc component (leading) as FC (sky-blue Gaussian in figure 5.12). We then save all the Gaussian models obtained per spaxel into respective cubes for each of the components.

The PV slices extracted along the major axis from the Gaussian model cubes are shown in figure 5.10. The major axis PV slice of the total multi-component Gaussian model of the data shown in panel 4 of figure 5.10 adequately reproduces the major axis PV of the data shown in panel 3 of the same figure. The column density image, velocity field, and PV slices of the Gaussian model cubes for disc, EPG, and FC can be found respectively in appendix figures C.25-C.26, C.27-C.28, and C.29-C.30. The figures of the disc component show a successful separation of the bulk of the anomalous gas albeit with some residual in the outer rings of the disc model (panel 5 of figure 5.10 and appendix figures C.25 and C.26). The major axis PV slices of EPG and FC (panels 6 and 7 of figure 5.10) show a concentration of EPG on the approaching side and a concentration of FC on the receding side. This asymmetry is seen more clearly in slices of the anomalous components extracted parallel to the major axis in the near and far side (top row in appendix figures C.28 and C.30). The same can be seen qualitatively in the moment maps (appendix figures

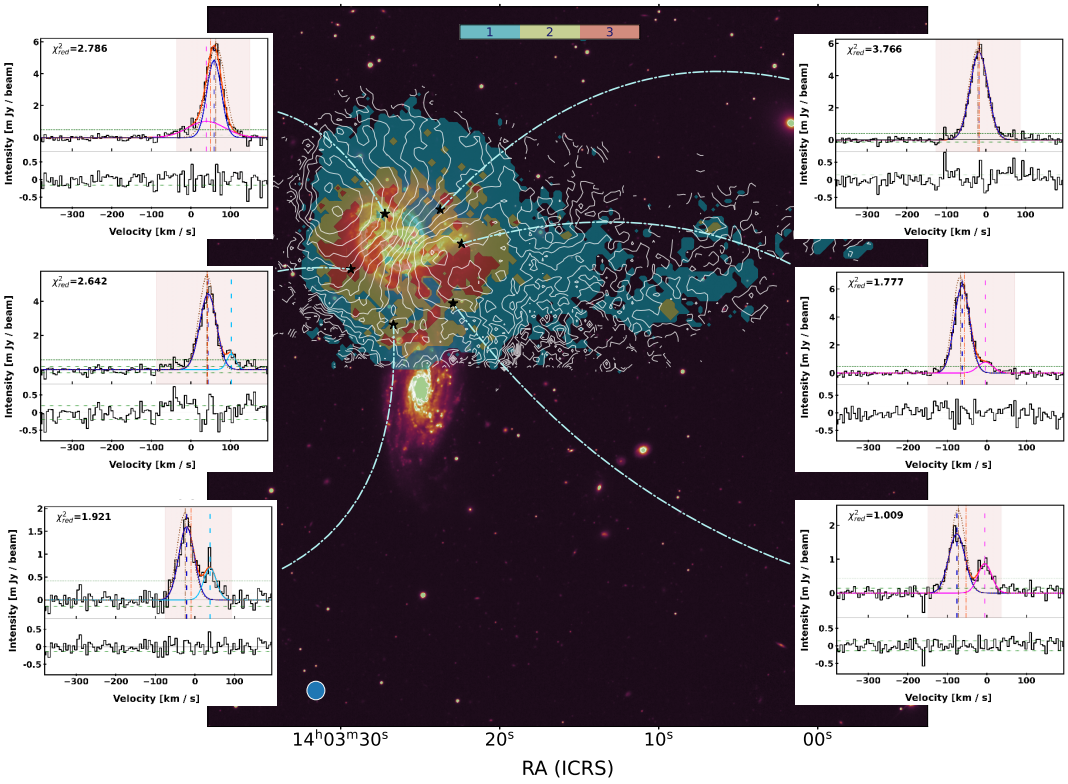

Figure 5.12: Component map and illustrative spectral profiles of S2. First-moment contours and a map of the number of fitted Gaussian components overlaid on DECam g-band image. The colour bar shows the number of fitted components. The inset plots show the spectra extracted at the annotated spaxels and Gaussian components fitted to the corresponding spectra for illustration. The blue-coloured Gaussian is tagged as the disc component, the magenta Gaussian is tagged as the EPG component, and the sky-blue Gaussian is tagged as the anomalous gas component. The ^{3D}BAROLO model spectra extracted at the annotated spaxels are plotted as brown dotted lines in the inset plots for comparison.

C.27 and C.29), the approaching side slice parallel to the minor axis in the EPG PV diagrams (bottom row, panel 6 in appendix figure C.28), and the receding side slice parallel to the minor axis in the FC PV diagrams (bottom row, panel 4 in appendix figure C.30). Interestingly, in the approaching side (south) of the moment maps of FC (see right panel of appendix figure C.29), we see a bridge of gas above filament B of the stellar bridge (see annotation in the left panel of figure 5.1) at velocities ranging from systemic to the receding side velocities. This is surprising because the expectation would be to detect components consistent with approaching side velocities but, instead, we identify seemingly counter-rotating clouds. In summary, in a similar fashion to S1, the Gaussian decomposition and kinematic tagging performed on S2 qualitatively indicate a higher fraction of lagging gas in the approaching side and a higher fraction of leading gas in the receding side. We also detect plausible signs of gas exchange between S1 and S2.

5.3.3 Mkt5

The dwarf galaxy, Mkt5 has an HI mass, $M_{HI} \sim 8.34\ M_{\odot}$, an inclination, $i \sim 52°$, and a maximum rotation velocity, $v_{rot} \sim 45$ kms^{-1} at a radius of ~ 6 kpc. The column density image and velocity field shown in figure 5.13 indicates an offset in the optical centre and HI centre. However, we were unable to obtain an optical centre from the literature to quantify the offset. The HI appears to be somewhat extended towards the southeast and there are hints of a plausible enhancement in star formation in the northern region. The seemingly low surface brightness dwarf could potentially be experiencing a cold inflow from the east. The gradients of the tails from the interacting pair in the east of Mkt5 also support this hypothesis (see bottom row of figure 5.14). However, within the sensitivity of our observation, we do not detect a connection between the tails and Mkt5 (see 47″ contours in figure 5.1). A deeper observation will allow for an investigation into the presence or absence of gas supply from the tails to the dwarf.

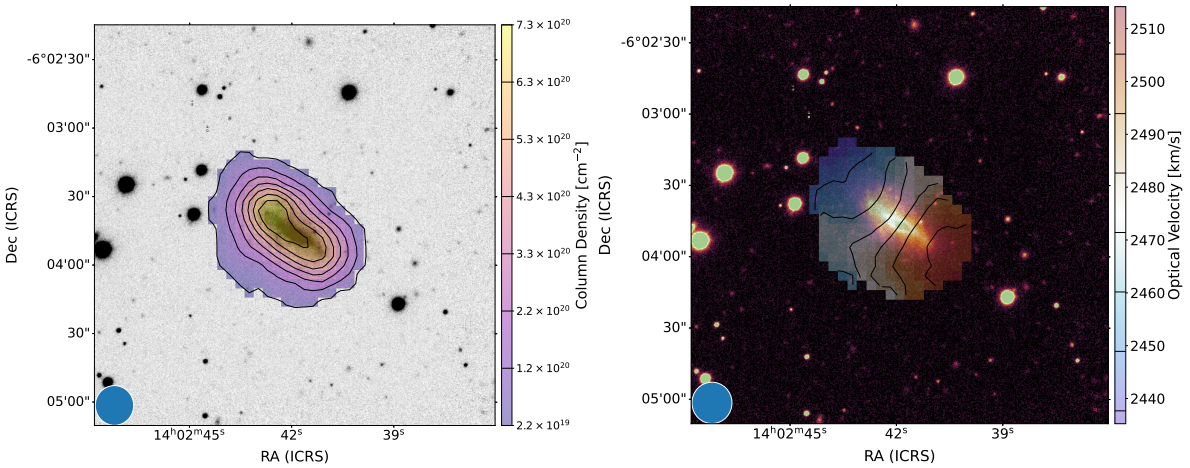

Figure 5.13: The column density image (left) and velocity field map (right) of Mkt5 overlaid on optical DECam g-band image.

5.4 Discussion

Using high-sensitivity MeerKAT observations of the group J1403-06, we attempt to unravel the gas kinematics and galaxy dynamics of the co-rotating pair Arp 271. We remind that the receding side of S1 (NGC 5426) is closer to S2 (NGC 5427) along the line of sight even though the

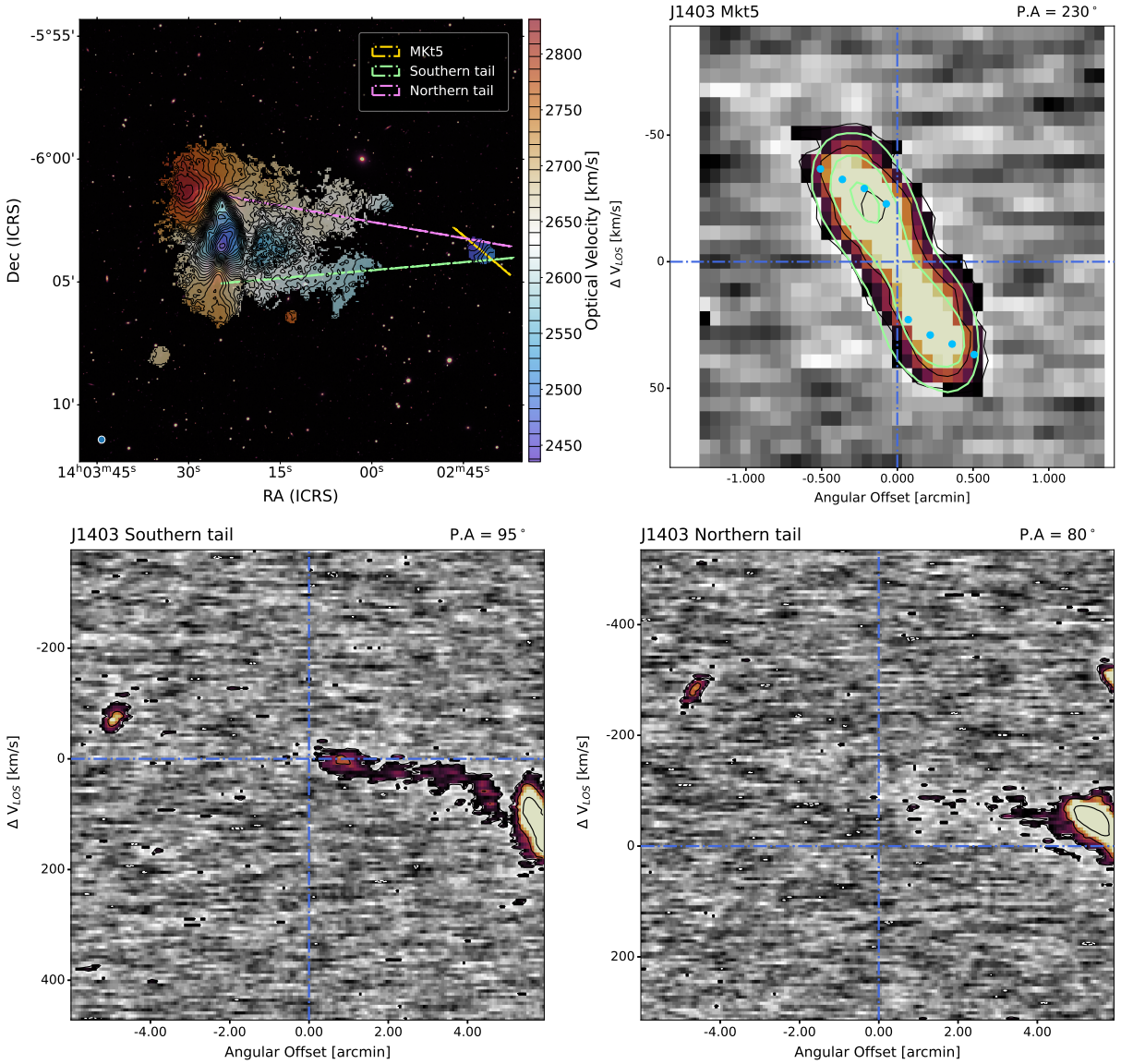

Figure 5.14: *First panel:* Velocity field of J1403-06 overlaid on DECam g-band image. The lines along which the subsequent PV slices were extracted are also annotated. *Second panel:* The major axis PV of Mkt5 with ^{3D}BAROLO model contours and rings defined for tilted ring modelling overlaid. *Panels 3-4:* PV slices along the southern and northern tails respectively.

approaching side appears closer in projection. We performed tilted ring modelling and Gaussian decomposition on the HI gas distribution of both S1 and S2. The rotation curve of S2 rises until $\sim$ 12 kpc and falls with a gradient of -4 km s^{-1} kpc^{-1} until 20 kpc, potentially indicating an inflow at these radii. The approaching side rotation curve of S1 also exhibits a similar drop between 10-15 kpc. Based on qualitative observations of the Gaussian model components, we find that both galaxies have a higher concentration of EPG in the approaching side and FC in the receding side. We could potentially be observing evidence of an inflow into S2 from S1 through the bridge. We also suspect indications of the re-accretion of the tidal tails and subsequent formation of hinge clumps at the bases of the western tails in both S1 and S2. We further posit plausible formation scenarios for the tidal tails and compare their peculiar morphology with other structures in the literature and simulations.

5.4.1 Considerations for separating anomalous gas from the disc

Past investigations of the neutral extraplanar gas (EPG) have predominantly focused on undisturbed galaxies at distances of $\lesssim 20$ Mpc while intentionally avoiding galaxies showcasing signs of interactions. This selection is motivated by the goal of understanding the intrinsic origin of EPG, such as Galactic fountains and/or cooling halo gas, through the study of kinematics of the lagging layer. However, emerging evidence from sensitive observations suggests that the EPG could also have external contributions from galaxy interactions. In fact, deep observations often reveal that even galaxies thought to be isolated can have dwarf companions in the field (e.g., Sancisi et al. 2008; Marasco et al. 2019; de Blok et al. 2018; Veronese et al. 2023; but see Zhu & Putman 2023). In contrast, our approach focuses on studying anomalous gas, including EPG, in interacting galaxies and is designed to detect any possible enhancement due to interactions. Typically conservative methods have been adopted for separating EPG from the disc to ensure that the EPG kinematics are not influenced by contamination from the disc kinematics (Fraternali et al. 2002; Marasco et al. 2019). We developed a tagging algorithm that first identifies the disc component by comparison with a model of the disc and then tags velocity components that have line-of-sight velocities that are either faster or slower than the disc rotation. The algorithm tags the faster components as FC and the slower components as EPG. We summarise the results of the Gaussian decomposition and kinematic tagging of S1 and S2 in tables 5.3 and 5.4; and figures 5.15 and 5.16. Our fitted Gaussian component models recover $\sim 92\%$ and $\sim 86\%$ of the total HI masses of S1 and S2 respectively. We create three model cubes representing the disc, leading gas, and EPG, from the tail-masked disc data of both S1 and S2, which together respectively encompass approximately 96% and 91% of the corresponding disc data. These percentages convey the effectiveness of the Gaussian decomposition and add the caveat that we fail to model a small percentage ($< 10\%$) of low SNR pixels. While the missing flux increases the uncertainty of the recovered component fractions that are evaluated against the disc data cube, it is unlikely to affect the kinematic analysis.

What is the impact of plausible contamination in the anomalous gas models?
In the rising part of the rotation curve, to prevent associating smeared disc emission as anomalous gas, we designate as disc, all the components falling within 3 $fwhm$ from the velocity of the peak of the ^{3D}BAROLO model spectra (for more information see 3.7.3). There is also a possibility of inaccurate profile decomposition resulting in disc emission being split across multiple components, which can then be mischaracterized as EPG or FC. Even though GaussPy+ employs several quality control checks to prevent such an outcome, there could still be some outliers. An inadvertent consequence of the spatially coherent refitting is to amplify this outlier, at least locally. This could leave visible signs in the component maps and fitted profiles. Our visual inspection does not reveal any drastic effects that can affect our conclusions. We expect some low levels of contaminating disc emission in the anomalous gas models but it is unlikely to be significant. While the isolation of the EPG aids in avoiding contamination from gas rotating at varying velocities or in different directions, as well as non-circular components, there remains a potential for the EPG to be affected by anomalous lagging components, such as a filament that lags behind the rotation (e.g., Fraternali et al. 2001; Veronese et al. 2023). However, we consider such components as part of the EPG in our approach, as we anticipate additional contributions to the EPG beyond those originating from intrinsic processes.

What is the impact of plausible contamination in the disc model?

We identify two scenarios where anomalous gas can seep into the disc model. Firstly, if the spectra are fitted with single components and also have corresponding spectra in the ^{3D}BAROLO model cube, we associate the component with the disc. In the outer rings where the SNR is not high enough for the profiles to be decomposed into multiple components, the component that is tagged as the disc could potentially be anomalous gas. Conversely, due to the elliptical masking we employ to isolate the disc and the Non-Disc Anomalous Gas (NDAG), some of the faint emission in the outer discs that cannot be modelled by ^{3D}BAROLO gets tagged as NDAG. Secondly, when the number of components is not correctly identified, the profile can be fitted

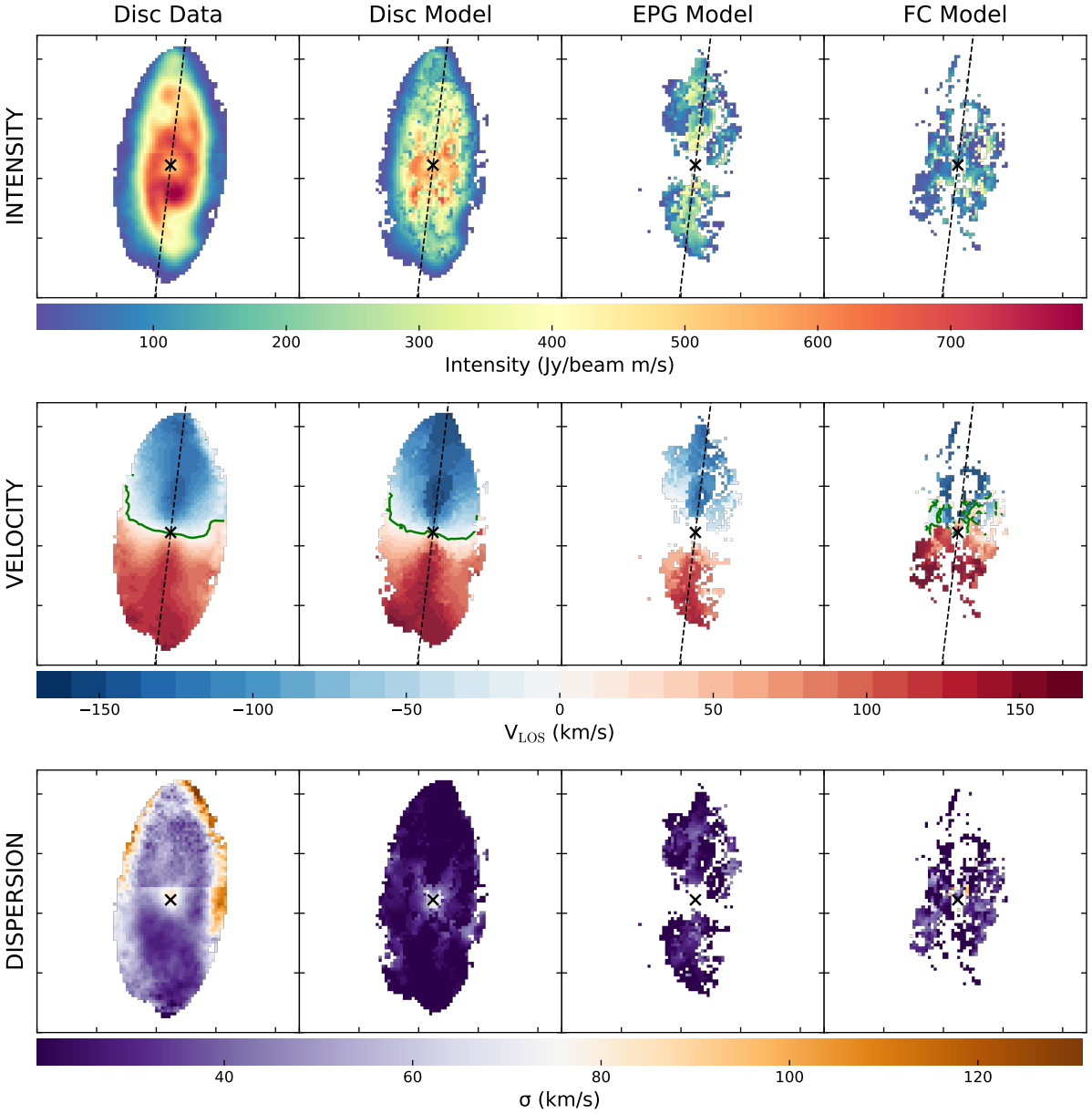

Figure 5.15: Maps of the intensity, velocity field, and dispersion of the components listed in table 5.4 for S1 are shown. The data for the disc, disc model, EPG model, and FC model are displayed in the first, second, third, and fourth columns, respectively. All the moment maps were extracted above the column density limit obtained from the SNR map of the data. The 'x' denotes the centre and the dashed line denotes the P.A. obtained from tilted ring modelling with ^{3D}BAROLO . The green contour in the first moment demarcates the 0 km s^{-1} line at the systemic recession velocity.

with a broad single component instead of multiple Gaussians. Both these scenarios can introduce anomalous gas into the disc model as seen in the disc model PV slices (panel 5 in figures 5.6 and 5.10). While this is unlikely to impact the kinematics inferred from the disc model, it affects the masses calculated for both the disc and the anomalous gas components. On top of this, the residual ($\sim$ 4% for S1 and $\sim$ 9% for S2) is also expected to contain low SNR anomalous gas components which are not accounted for by the quoted masses. The main consequence of both these effects is the underestimation of the anomalous gas masses.

As previously discussed in the introduction to EPG (see section 1.4.1), recovering accurate rota-

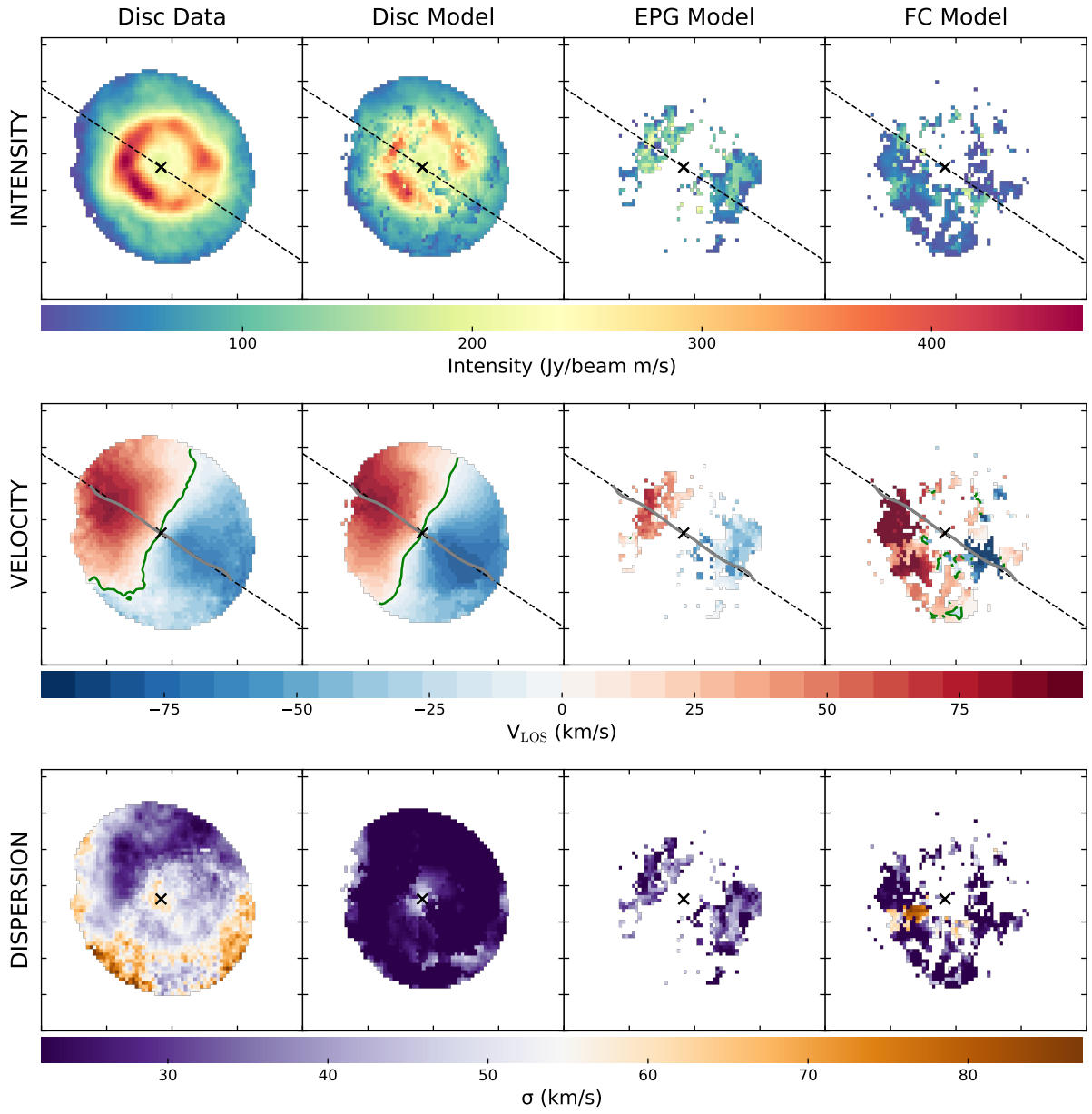

Figure 5.16: Maps of the intensity, velocity field, and dispersion of the components listed in table 5.4 for S2 are shown. The data for the disc, disc model, EPG model, and FC model are displayed in the first, second, third, and fourth columns, respectively. All the moment maps were extracted above the column density limit obtained from the SNR map of the data. The 'x' denotes the centre and the dashed line denotes the P.A. obtained from tilted ring modelling with ^{3D}BAROLO . The green contour in the first moment demarcates the 0 km s^{-1} line at the systemic recession velocity.

tional velocities for galaxies with inclinations close to face-on ($\lesssim 40$ as defined by de Blok et al. 2008) can be challenging due to the damping of the projected line-of-sight component of rotation. Moreover, there are fundamental constraints that apply to the anomalous gas we recover from galaxies of all inclinations. For instance, the lagging EPG component will disappear close to the minor axis where no signature of rotation is visible (Marasco et al. 2019; Veronese et al. 2023). Additionally, both radial and vertical motions can introduce an offset along the line-of-sight velocities of the components, making it difficult to differentiate between the two (but see Marasco et al. 2019). Moreover, an outflow towards the observer in the side facing the observer and an inflow towards the observer in the side facing away, or vice versa (an inflow in the side facing us and an outflow away from us in the side facing away), can produce an offset in the same direction along the line-of-sight. We do not rely solely on line-of-sight velocities to distinguish between radial and vertical motions or inflows and outflows. Instead, we consider additional factors and ancillary evidence that suggest possible non-circular motions in the gas. Given that our primary focus is on investigating interacting galaxies, where non-circular motions are expected, our approach is appropriate. Finally, while we acknowledge the possibility of systematic effects due to improper profile decomposition and component misidentification (as discussed above), we believe their impact to be negligible compared to the fundamental limitations.

5.4.2 Gas exchange between S1 and S2

Table 5.3: The two sections presents the logarithmic HI masses of the data and models for S1 and S2. The third column shows the fraction of the component with respect to the full data and the fourth column shows the fraction of the model with respect to the data in the 'sub-table'. First two rows: full data and full Gaussian model. The subsequent four rows: disc data, ^{3D}BAROLO model of the disc, Gaussian component model of the disc, and Disc Anomalous Gas (DAG) model. The next two rows: Non-Disc Anomalous Gas (NDAG) data and NDAG Gaussian model.

Label	log M_{HI} ($M_\odot$)	fraction	fraction of data modelled
	S1		
Full data	10.11 ± 0.03	100%	
Full model	10.07 ± 0.03	91.58%	
Disc data	10.07 ± 0.03	90.42%	100%
^{3D}BAROLO Model	10.09 ± 0.03	95.85%	105.93%
Disc model	9.89 ± 0.03	60.96%	67.30%
DAG model	9.52 ± 0.03	25.78%	28.51%
NDAG data	9.09 ± 0.03	9.58%	100%
NDAD model	8.79 ± 0.03	4.84%	50.47%
	S2		
Full data	9.97 ± 0.03	100%	
Full model	9.90 ± 0.03	86.08%	
Disc data	9.89 ± 0.03	82.91%	100%
^{3D}BAROLO model	9.84 ± 0.03	74.27%	89.54%
Disc model	9.74 ± 0.03	59.87%	72.11%
DAG model	9.15 ± 0.03	15.14%	18.24%
NDAG data	9.20 ± 0.03	17.10%	100%
NDAG model	9.01 ± 0.03	11.06%	73.79%

In the intermediately inclined galaxy, S1, we find that the gas distribution in the disc is divided into $\sim 68\%$ thin disc, $\sim 18\%$ lagging EPG, and $\sim 10\%$ leading gas (FC). Similarly, in the close-

Table 5.4: HI masses and their fractions for different components and sides of galaxies S1 and S2. The table presents the logarithmic HI masses (in $M_\odot$) along with the corresponding fractions of side (approaching and receding) and component for each component and subsequent sides of the galaxies. The four components separated by horizontal lines include the Data disc, Data model, EPG model, and FC model. The side fractions are calculated as the ratio of the HI mass of the side and the total mass for each component M_{HI}(A or R)/M_{HI}(Both). The component fractions are calculated as the ratio of the total mass of the model component and the total mass of the disc data (M_{HI}(component)/M_{HI}(disc data)). The final row is a summation of all the total masses of the model components and the fraction is with respect to the total mass of the data disc in the first row. The moment maps of the respective components are plotted in figures 5.15 for S1 and 5.16 for S2.

Component	Side	S1			S2		
		log M_{HI} ($M_\odot$)	f_{side}	$f_{component}$	log M_{HI} ($M_\odot$)	f_{side}	$f_{component}$
Data disc	Both	10.07 ± 0.03		100%	9.89 ± 0.03		100%
	Approaching	9.77 ± 0.03	50.20%		9.61 ± 0.03	52.40%	
	Receding	9.76 ± 0.03	49.80%		9.56 ± 0.03	47.60%	
Disc model	Both	9.89 ± 0.03		67.42%	9.74 ± 0.03		72.21%
	Approaching	9.60 ± 0.03	50.94%		9.46 ± 0.03	52.08%	
	Receding	9.58 ± 0.03	49.06%		9.43 ± 0.03	47.92%	
EPG model	Both	9.32 ± 0.03		18.14%	8.88 ± 0.03		9.90%
	Approaching	9.08 ± 0.03	56.78%		8.60 ± 0.03	52.06%	
	Receding	8.96 ± 0.03	43.22%		8.56 ± 0.02	47.94%	
FC model	Both	9.08 ± 0.03		10.36%	8.81 ± 0.03		8.36%
	Approaching	8.69 ± 0.03	40.23%		8.22 ± 0.02	25.68%	
	Receding	8.86 ± 0.03	59.77%		8.68 ± 0.02	74.32%	
Total model	Both	10.05 ± 0.05		95.93%	9.84 ± 0.04		90.47%

to-face-on galaxy, S2, the gas distribution in the disc is divided into $\sim$ 72% thin disc, $\sim$ 10% EPG, and $\sim$ 8% FC. The fraction of EPG we recover using our new approach is consistent with the values typically measured in intermediately inclined galaxies (see table 4 in Marasco et al. 2019). While typical EPG fractions are measured to be around $\sim$ 14%, the most well-studied EPG of NGC 891 has a log HI mass of $\sim$ 9.08 which amounts to a fraction of 28% of the edge-on galaxy's total HI mass (Oosterloo et al. 2007a). Marinacci et al. (2010) find that a part of the anomalous gas of NGC 891 could result from an interaction with its companion, UGC 1807. Similarly in NGC 2403 which is the best-studied case of EPG in intermediately inclined galaxies, Marasco et al. (2019) report an EPG fraction of $\sim$ 22% and Veronese et al. (2023) report the presence of a 20 kpc long filament plausibly resulting from an interaction with a companion. Although it is worth noting that in the cases of NGC 0672 and NGC 0925, which are identified as interacting systems, Marasco et al. (2019) recover an EPG fraction of $\sim$ 14%. In our case, the EPG of S1 with a mass of log $M_{HI} = 9.324$, is among the most massive EPG reservoirs detected to date. Moreover, these are also the farthest EPG to be studied in detail ($\sim$ 40 Mpc). Table 5.3 displays the total masses of S1 and S2, with log M_{HI} values of 10.11 ± 0.03 and 9.97 ± 0.03, respectively. In addition to having a bigger gas reservoir, S1 also has more mass stored in its disc, EPG, and FC, compared respectively to the reservoirs of S2 (see table 5.4). But interestingly, S2 displays enhanced star formation activity throughout its disc, despite having a smaller gas reservoir than S1. Marasco et al. (2019) only find a mild co-relation between SFR and mass of the EPG (see figure 11 and the subsequent discussion in their work). This indicates that the kinematics of the EPG (e.g., outflow vs inflow) is important for studying the impact of the lagging gas reservoir on star formation. Furthermore, a fraction of the EPG could likely be photoionized

due to the AGN and star formation activity in S2. Nonetheless, the question of the lower SFR seen in S1 despite the larger HI reservoir remains intriguing. As discussed in section 1.3.3 and in Hopkins et al. (2009), the inflow towards the nucleus in S2 is likely due to the gas losing angular momentum to internal torques generated by asymmetries in S2's stellar disc which are induced by the interaction with S1.

Next, we investigate how the gas distribution in the companion galaxy is affected by its counterpart. From the HI masses and the dynamical mass from Fuentes-Carrera et al. (2004), it seems likely that S1 is the bigger galaxy of the pair. This would suggest that in a simple gravitational tug of war for the accretion of loosely bound gas, S1 would emerge victorious. However, the higher SFR, larger stellar mass, anomalous Hα clouds, and nuclear activity could potentially suggest that S2 is likely experiencing an inflow. We are possibly seeing the indications of such an inflow in the FC layer of S2 (appendix figure C.29). We also see a bridge of gas extending to the NE side (receding) of S2, which also seems to be experiencing a higher amount of star formation activity compared to other quadrants of the galaxy. Since FC has a higher V_{los}, if we were to attempt to model it using equation 3.4, we would have to introduce a third term $v_z \cos i$ to allow for motion perpendicular to the disc plane. The v_{rad} term in the receding side might also be positive suggesting a radial inflow towards the centre. While this is speculative without having performed the act of modelling the observed anomalous velocity field, it is still a didactic tool to visualize how a positive v_z could imply an inflow in the side facing us or an outflow in the side facing away. From the observed gradient emanating from the bridge in the velocity field of FC, the anomalous gas is unlikely to be an outflow in the side facing away. The evidence likely suggests that FC could be an inflow in the side facing us and potentially originating from gas previously associated with S1.

To test such a scenario of an inflow without resorting to advanced multi-disc tilted ring modelling, we put forth a hypothesis and examine the decomposed components for evidence that either supports or rejects the hypothesis. If we are perceiving the aftermath of gas being pulled from S1 by S2, we would expect to see a trace of this perturbation in the anomalous gas distribution in either galaxy. The challenge is in decoding this information from the projected line-of-sight velocities. As we reminded at the start of this section, S2 is behind S1 along the line-of-sight and thus the "pull" should induce a perturbation that results in the anomalous gas distribution getting skewed in a direction that goes away from the observer. Revisiting the discussion in section 3.7.3, when referring to a lagging EPG or a leading component, we are discussing them in the context of an inertial frame centred at the galaxy where the dominant motion is rotation about the centre of the frame. This produces negative velocities in the approaching side and positive velocities in the receding side. The best way to illustrate the hypothesis is in the frame defined by the line-of-sight velocity. The rotation can be roughly approximated as the difference between the systemic recession velocity (V_{sys} in equation 3.4) and observed line-of-side velocity (V_{los}) on either the approaching side or the receding side. In the approaching side, since the rotation is towards the observer, the observed line-of-sight velocities would be less than the systemic recession velocity. Thus resulting in the negative velocities obtained in the inertial frame of the galaxy. Similarly, since the projected rotation component along the line-of-sight in the receding side is directed away from the observer, the observed line-of-sight velocities will be higher than V_{sys}. Thus resulting in positive velocities in the galaxy's inertial frame. A lagging

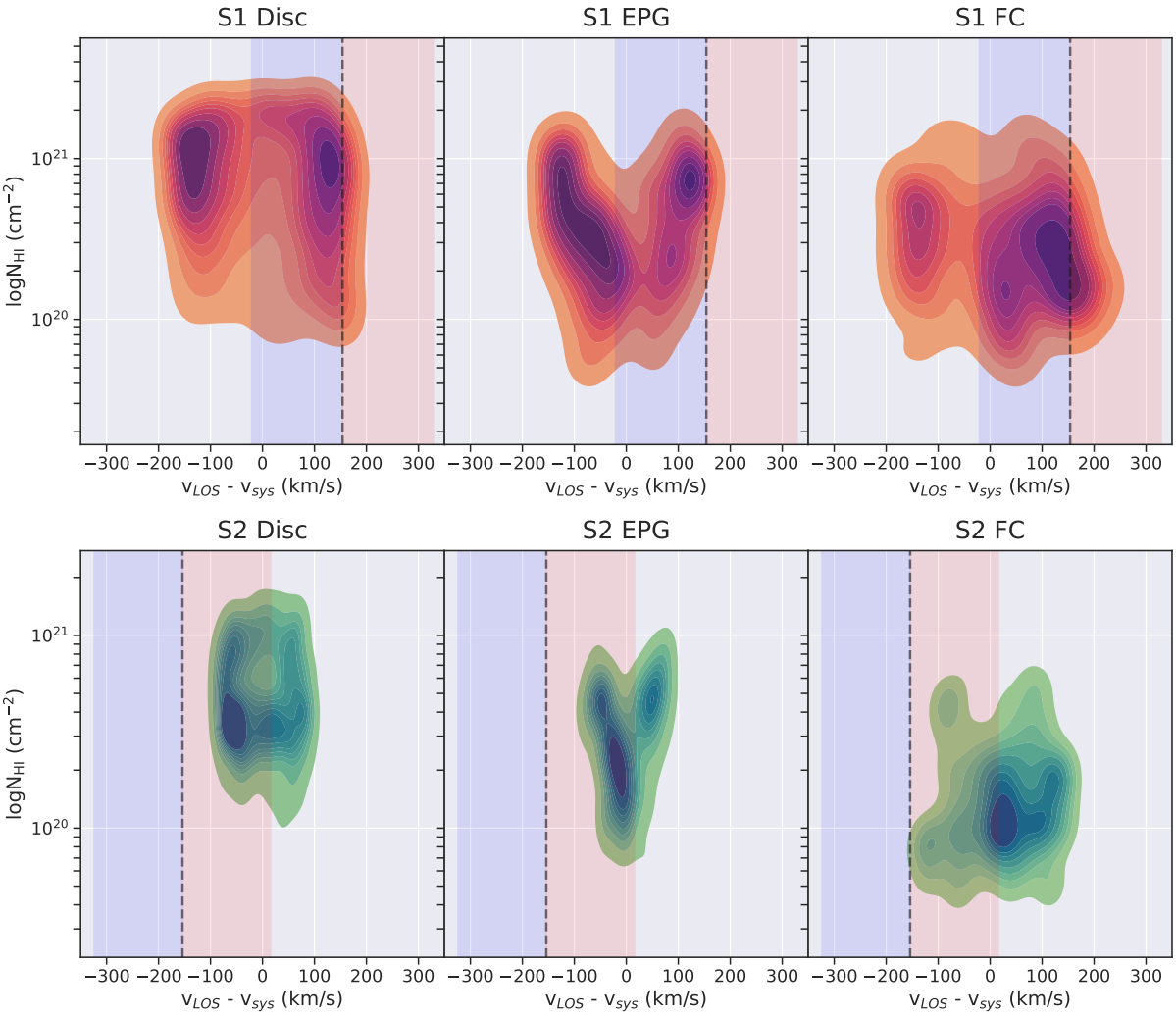

Figure 5.17: Figure shows a KDE (Kernel Density Estimation) plot of parameter space spanned by the column density of the Gaussian profile (NHI) and ΔV ($V_{los} - V_{sys}$) for the disc, EPG, and FC model components of both S1 (top row) and S2 (bottom row). ΔV is calculated with respect to the respective V_{sys} of S1 and S2. The red and blue shaded regions depict the rotation velocity of the companion galaxy with respect to the systemic velocity of the galaxy i.e in S1 it denotes the rotation of S2 and vice versa. The dashed line represents the systemic velocity of the counterpart with respect to the V_{sys} of the galaxy.

EPG would manifest in a similar fashion but with a lower rotation velocity with reference to the disc's rotation velocity. Similarly, a leading component will show up with a higher velocity with respect to the disc's rotation. In the line-of-sight frame, the EPG components tend towards the systemic velocity and FC tend away from the systemic velocity. This means that at the receding side, the EPG will have a lower V_{los} and the FC will have a higher V_{los} than that of the disc component. Conversely, at the approaching side, the EPG will have a higher V_{los} and the FC will have a lower V_{los} than that of the disc component.

The expectation based on the hypothesis in the case of S1 which has a lower V_{los} than the perturber, S2, would be a concentration of leading components (FC) in the receding side (pull is away from V_{sys}) and a concentration of EPG components in the approaching side (pull is towards V_{sys}). Since the difference between the V_{sys} of S1 and S2 is comparable to the rotation in both S1 and S2 ($\sim$ 150 km s^{-1}), the EPG pulled from S1 will likely manifest mostly as lagging gas in the approaching side of S2. The FC pulled from the outer rings of the receding side of S1 will

have V_{los} comparable to the V_{los} of the receding side of S2 and thus will likely result in clumping up in the receding side. This can be seen in the KDE plot of the Δv - N_{HI} parameter space shown for each component in both S1 and S2 in figure 5.17. Here, $\Delta V = V_{los} - V_{sys}$ km s^{-1} and N_{HI} is the neutral gas column density along the line of sight in units of cm^{-2}. As predicted, in S1, there is a higher concentration of EPG in the approaching side and FC in the receding side (top row second and third panels in figure 5.17). In S2, also as expected we see a higher concentration of EPG in the approaching side and FC in the receding side. In table 5.4, this observation is also presented in terms of the fraction of HI mass measured for the receding side and the approaching side for each component of the two galaxies. For S1, as per the prediction, we see a higher fraction of HI in the approaching side of the EPG model ($\sim$ 57%) and the receding side of the FC model ($\sim$ 60%). For S2, the fraction of HI in the receding side of the FC model ($\sim$ 74%) is more than twice as that of the approaching side ($\sim$ 27%) which is consistent with the hypothesis. Also as predicted by the hypothesis, the fraction of HI in the approaching side of S2's EPG model ($\sim$ 52%) is higher than the receding side ($\sim$ 48%). Hence, our data and methodologies potentially reveal clues to test the validity of the hypothesis regarding the exchange of neutral gas between S1 to S2. We indeed might be detecting signs of an inflow in the low-inclination companion, S2.

5.4.3 What about the tails?

We detect three tails to the west of the interacting pair, extending to about 90 kpc from the discs (see figure 5.14). The tails together account for $\sim$ 13% (log $M_{HI} \sim 9.45$ $M_\odot$) of the total HI in the group. The tails individually correspond to $\sim$ 10% (log $M_{HI} \sim 9.09$ $M_\odot$) and $\sim$ 17% (log $M_{HI} \sim 9.20$ $M_\odot$) of the total HI masses of S1 and S2 respectively. For context, the log HI mass of the Large Magellanic Cloud (LMC) is $\sim 8.6 - 8.9$ $M_\odot$ (Brüns et al. 2005; Smart et al. 2019) and the Small Magellanic Cloud (SMC) is ~ 8.6 $M_\odot$ (Brüns et al. 2005; Di Teodoro et al. 2019). The NDAG masses we recover for S1 and S2 are individually greater than the combined mass of the Magellanic Clouds (MC). We expect the tails to extend beyond our current detection, and we anticipate that future, more sensitive observations will reveal their full extent. In this subsection, we provide a brief overview of similar features in the literature and briefly examine certain plausible scenarios that may have contributed to the tails.

Building on the HI Rogues Gallery by Hibbard et al. (2001), Koribalski (2020) provide a succinct review of some of the largest HI structures such as tidal tails, plumes, bridges to companions, and cloud complexes in the Local Universe. Such structures have been found in the vicinity of both spiral galaxies and Early-type galaxies (ETGs) typically in groups and clusters (e.g., Koribalski et al. 2004; Koribalski & Dickey 2004; Oosterloo et al. 2007b; Serra et al. 2012b, 2013; Taylor et al. 2016). A catalogue of well-characterised HI structures with a wide range of morphologies and kinematics, all seen in projection at a single snapshot in time will enable the study of various gas removal and accretion mechanisms operating in different environments. However, this is no easy task due to the complexities and nuances to be considered for each system observed with different instruments. The nearest HI structure, the Magellanic stream has been reported to have a mass, log $M_{HI} \sim 8.43$ $M_\odot$ and an extent of at least 180 kpc (Brüns et al. 2005; Koribalski 2020). But we note that the uncertainty in the distance adopted to the stream can cause a discrepancy in the mass by a factor of 5 (Lucchini et al. 2021). Recently, there have been several

reports of long filaments observed with the sensitive Five-Hundred-meter Aperture Spherical radio Telescope (FAST). Zhu et al. (2021) detect a 130 kpc long stream of accretion onto the disc of M106 with log $M_{HI} \sim 8.23$ $M_{\odot}$. Liu et al. (2023) detect an extended envelope and a 100 kpc tidal tail in NGC 4085/90, an isolated dwarf-dwarf interaction analogue to MC (for the mechanisms and implications for dwarf-dwarf interactions, see Pearson et al. 2016, 2018). To highlight the fact that the tails we detect in Arp 271 are significant HI reservoirs, we contrast it with the 200 kpc Leo ring, a well-known peculiar HI structure. The mass of the southern tails (S1's tails) is similar to that of the Leo ring, whereas the northern tail (S2's tail) is more massive (Stierwalt et al. 2009).

The interaction between the co-rotating pair is the most probable explanation for the formation of the tails. However, even though a large amount of neutral gas has been removed from the galaxies, the stellar and gaseous discs do not seem to be significantly disturbed. An interaction between the pair is evident from the observed bridge between S1 and S2 which could either be a swing bridge or a splash bridge. While the former is a tidal tail captured by a companion, the latter is a feature resulting from an inelastic collision between two gas discs (Yeager & Struck 2019, 2020). The swing bridge offers the simplest explanation for the observed gas exchange in the pair and the seemingly undisturbed optical morphology. Struck & Smith (2012), by extending the classical impulse approximation, offer an analytical explanation for long tidal tails resulting from an increase in the angular momentum in certain regions caused by prolonged prograde encounters. But, the fact that the two prominent tails from S1 and S2 have similar morphology is puzzling.

On the other hand, an offset slicing collision and an intermediate merger stage can be invoked to support a splash origin for the bridge and the tails. In collisions between discs that are nearly orthogonal, each disc slices through a small part of the other and the gas from the sliced disc is accreted onto the other, with little splashed into the bridge (Yeager & Struck 2019). According to Lotz et al. (2008), for equal mass gas-rich mergers, merging galaxies observed between their first pass and final merger may not show disturbed morphologies. Moreover, Yeager & Struck (2020) find that inclination effects and the offset of disc centres at impact can lead to various morphological features, including unidirectional transverse gas filaments. When an offset is introduced, the majority of the gas is displaced in a single direction as the collision predominantly occurs on one side of the galaxy. In their models with 10 kpc offset and inclinations $20°, 45°$, & $90°$, a substantial amount of gas can be seen far from the discs in the direction of the offset. The difference in inclination between S1 and S2 in Arp 271 is $\sim 30°$ and the current projected offset between the centres is $\lesssim 10$ kpc. The $20°$, 10 kpc offset model of Yeager & Struck (2020) shown in this linked movie [11] at $\tau_{age} > 100$ Myr in 'XY' space appears qualitatively similar to the column density image of Arp 271 shown in figure 5.8. The observed morphology is likely comprised of both tidal and splash features. However, detailed dynamical modelling of Arp 271 is required to establish the formation of the HI morphology.

The tails could also be attributed to an interaction with Mkt5, a gas-rich low surface brightness companion located to the west of the pair. However, for the scenario of LSB stripping to be

[11] https://www.youtube.com/watch?v=-Tdnwvm8u1U

valid, Mkt5 would need to have been three times more gas-rich prior to the interaction (but see Bekki et al. 2005). This would raise further questions about the inefficient star formation in Mkt5. It would take about $\sim$ 1.2 Gyr for Mkt5 to traverse a distance of 120 kpc with a velocity of 100 kms^{-1}. Moreover, within the sensitivity of our observation, we do not detect any signs of interaction in the HI distribution of Mkt5 or a link between the tails and Mkt5. Nonetheless, a detailed dynamical modelling of the interactions coupled with the star formation histories of the galaxies will enable us to compare timescales of interactions and tail formation. Another conceivable scenario for the formation of the tails involves a combination of outflows (e.g., starburst-driven outflows, stellar winds, AGN, etc.), ram pressure stripping, and an eastward motion. However, such a motion cannot be justified without the influence of a bigger potential, such as a cluster. Additionally, we do not observe compressed HI contours in the east that would support the occurrence of ram pressure stripping. Furthermore, the similar morphology of the tails and the different star formation and AGN activity observed in S1 and S2 raise doubts about the validity of an outflow argument. Nonetheless, it is likely that these scenarios collectively contribute to at least a small portion of the observed morphology. Additionally, we detect 3-4 galaxies outside MeerKAT's 1° primary beam which roughly corresponds to 700 kpc. Assuming that these galaxies are falling towards Arp 271 with a velocity of 100 kms^{-1}, we recover a timescale of $\sim$ 6.8 Gyr. From Lotz et al. (2008), typical merger timescales are about 2-3 Gyr. Thus it is unlikely that the galaxies in the extended field played a role in the formation of the tails. Although, as concluded by Džudžar et al. (2021), J1403-06 could possibly evolve into an HCG-like group.

6 | Summary and Conclusion

We present a comprehensive kinematic analysis of the HI distribution of the interacting galaxies in two groups from the Choirs sample, observed with MeerKAT. The two groups that are the focus of this study, J1403-06 and J1250-20, each contain two late-type central galaxies that showcase varying levels of interactions and unique HI morphologies. The central pairs in the two groups have projected spatial separations of 114 kpc and 26 kpc respectively and line-of-sight velocity separations of 35 $\mathrm{km\,s^{-1}}$ and 150 $\mathrm{km\,s^{-1}}$ respectively. In the literature, both spatial separation and line-of-sight separation have been employed to categorize merger stages, but these methods in the case of these two interacting pairs would give conflicting classifications.

As introduced in chapters 2 and 3, we utilized state-of-the-art packages and methodologies for data processing and analysis. Employing 3D tilted ring modelling, we extract the kinematic and geometric parameters of the discs of the galaxies. Through physically motivated Gaussian decomposition and kinematic tagging, we identify and characterize the anomalous gas largely arising from the interactions. We see signatures of inflows in the rotation curve, radial velocity profile, and anomalous gas distribution in both groups. The high sensitivity of our observations enables the detection of anomalous gas outside the galaxy discs, manifesting as extended envelopes, tails, plumes, and bridges. We posit plausible scenarios for the formation of the peculiar HI morphologies and the anomalous gas in the groups. Anomalous gas can offer insights into how galaxies attain and lose cold gas. This work looks at the role of gravitational interactions in shaping the gas distribution and thus the evolution of galaxies in group potentials. Additionally, we also report the HI masses of dwarf galaxies observed within the groups and extended fields. We list some of our key results below.

1. We imaged the high-sensitivity & resolution MeerKAT observations of two low-mass gas-rich late-type dominated groups with varying levels of interaction between the central galaxies. We use state-of-the-art tools in HI interferometry (e.g., CASA, SoFiA2, SIP, GaussPy+, ^{3D}BAROLO, etc.) to perform imaging and systematic parameterisation of the HI distribution in terms of mass, column density, geometry, and kinematics. We developed methods based on 3D tilted ring modelling, physically motivated Gaussian decomposition and kinematic tagging to detect and characterize the kinematics of the peculiar HI morphologies and pervasive anomalous gas within and around the centrals in both groups. We separate and distinguish some of the diverse contributions to the HI discs arising from interactions with companion galaxies. The tools developed can be applied to galaxies observed in HI with sufficient spatial and spectral resolutions. This work demonstrates the power of Gaussian decomposition for characterising anomalous gas in the era of SKA.

2. In **J1250-20**, at a distance of 116 Mpc, we study the impacts of two co-rotating minor mergers (J1250-20:S1 + J1250-20:S3; J1250-20:S2 + J1250-20:S4) and a counter-rotating major merger (J1250-20:S1 + J1250-20:S2).

   (a) Our MeerKAT data is a significant improvement on the existing ATCA data (Džudžar et al. 2019) in terms of resolution and sensitivity. We are able to resolve the spatial and kinematic structure of the peculiar HI morphology. For the first time, we detect

and separate gas associated with J1250-20:S4. We also isolate gas associated with J1250-20:S1's disc by removing contributions from J1250-20:S3 and anomalous gas.

(b) J1250-20:S1 is among the most HI-rich galaxies in the local universe with a log $M_{HI} \sim 10.6$ $M_{\odot}$ and an HI envelope extending to about ~ 150 kpc in diameter.

(c) In the warped, lopsided, and extended disc of J1250-20:S1, in addition to the gas inflow due to the minor merger with J1250-20:S3, we detect potentially misaligned accretion from J1250-20:S2+S4 through an HI bridge, in a fashion similar to 'cold-flow' discs predicted by Stewart et al. (2013).

(d) We observe significant quantities of anomalous gas along the stellar stream in J1250-20:S1, likely originating from the minor merger with J1250-20:S3. The lower limit for the HI mass of the anomalous gas in the disc that we report in table 4.3 exceeds the combined mass of the Magellanic clouds.

(e) We see indications of a low column-density tail extending westward, but the non-uniform noise in the data prevents us from establishing the feature as a tidal tail.

(f) We suspect an inflow in J1250-20:S2 driven by torques produced by asymmetries induced in the stellar disc due to the tidal interactions with companions (Hopkins et al. 2009).

3. In **J1403-06**, at a distance of 40 Mpc, we study the impact of an intermediate-stage co-rotating major merger between NGC 5426 (J1403-06:S1) and NGC 5427 (J1403-06:S2).

(a) Our MeerKAT data is a significant improvement on the archival VLA observation of the source in terms of resolution and sensitivity.

(b) For the first time, we observe: (i) exchange of neutral gas between the pair; (ii) HI associated with S3; and (iii) rotation in Mkt5.

(c) We identify two HI tails extending out to ~ 90 kpc to the west of the pair, for which we suspect a combination of tidal and collisional origin.

(d) We detect and characterize substantial reservoirs of neutral gas in the lagging (EPG) and leading (FC) anomalous gas layers of both J1403-06:S1 and J1403-06:S2.

(e) We present the characterisation of the farthest (40 Mpc) neutral EPG to date. The EPG in J1403-06:S1 is also among the most massive EPG reservoirs studied to date.

(f) J1403-06:S1, despite having a bigger HI reservoir, has a lower SFR and stellar mass compared to J1403:06:S2. We attribute the enhanced star formation in J1403-06:S2 to the efficient removal of angular momentum from the neutral gas driven by asymmetries triggered in the stellar disc of J1403-06:S2 due to the tidal interaction with J1403-06:S1 (Hopkins et al. 2009). The unique HI morphology and peculiar kinematics is likely a combination of feedback, splash and tidal interactions.

4. The companion galaxies in the pairs have comparable stellar masses but drastically different HI masses. Surprisingly, while in J1250-20, the companion with higher SFR also has the bigger HI reservoir, in J1403-06, the companion with higher SFR has the smaller HI reservoir. We attribute this to differences in the interaction geometries and the ongoing minor mergers in J1250-20. In both groups, the primary (S1), in addition to the disc, has a massive HI reservoir either above the plane (EPG) or in the extended disc.

5. J1250-20 and J1403-06 have a total log HI mass of ~ 10.72 and ~ 10.33 respectively.

J1250-20 has 2.5 times more HI than J1403-06 and most of the mass in the former is stored in J1250-20:S1. Therefore, J1250-20 could potentially be at a more advanced stage in the evolutionary sequence proposed by Verdes-Montenegro et al. (2001). However, we do note that an examination of HI morphology and HI deficiency is required to determine the evolutionary stage of the groups.

6. The HI mass ratio between J1403-06:S1 and J1403-06:S2 is 1.25 and that between J1250-20:S1+S3 and J1250-20:S2+S4 is 3.28. While the former is a co-rotating major merger and the latter is a counter-rotating major merger. In terms of stellar mass, both are 1:1 mergers. According to Hopkins et al. (2009), these gas-rich mergers can yield disc-dominated remnants.

We are on the precipice of the era of sensitive wide-field HI surveys with large single-dish telescopes and powerful interferometers capable of producing resolved observations. As this era unveils, we can anticipate a significant increase in the number of catalogued peculiar galaxies and HI structures. Sensitive observations such as this by precursor telescopes like MeerKAT serve as harbingers to the next generation of galaxy evolution studies seeking to understand various gas accretion and removal mechanisms that shape galaxies and their environments.

6.1 Future Work

This section provides a concise overview of the potential areas of investigation in the near future for both groups examined in this study and the broader MeerChoirs survey.

1. **Data reduction:** The data reduction approaches adopted in this work utilized the L1 visibilities provided by the SARAO pipeline. While the default flagging and calibration produce data of sufficient quality, a more rigorous approach employing CARACAL to deal with RFI and continuum artefacts can potentially improve the noise properties of the spectral cubes. If successful, this could enable the detection of fainter gas and provide confirmation of the tidal tail suspected in J1250-20.
2. **Gaussian decomposition and kinematic tagging:** The Bayesian decomposition package, BAYGAUD, can be extended to incorporate certain physically motivated features implemented in GaussPy+. Applying BAYGAUD will enable the independent confirmation of the decomposition we performed in this work. The kinematic tagging can also be extended to be applied to the output products of BAYGAUD. The two independent approaches to Gaussian decomposition in tandem with physically motivated kinematic tagging can then be applied to the larger MeerChoirs sample and other resolved observations.
3. **Dynamical modelling:** Performing dynamical modelling of the interactions will facilitate understanding of the timescales, orbits, and impacts on the neutral gas in the groups. Beginning with the two groups discussed in this work, the modelling can be performed for the entire sample to understand the processes operating in gas-rich low-mass groups.
4. **Multi-wavelength observations:** Follow-up observations in optical and IR will provide valuable information on the star formation and ionized gas in the groups. This will enable explorations such as stellar population modelling, DIG/eDIG characterisation, etc., providing a holistic picture of the co-evolution of the galaxies and the group environment.

Bibliography

Afruni A., Fraternali F., Pezzulli G., 2021, Monthly Notices of the Royal Astronomical Society, 501, 5575

Afruni A., Pezzulli G., Fraternali F., 2022, Monthly Notices of the Royal Astronomical Society, 509, 4849

Allison J. R., Sadler E. M., Whiting M. T., 2012, Publications of the Astronomical Society of Australia, 29, 221

Anderson M. E., Bregman J. N., 2011, The Astrophysical Journal, 737, 22

Anderson M. E., Bregman J. N., Dai X., 2013, The Astrophysical Journal, 762, 106

Anderson M. E., Churazov E., Bregman J. N., 2016, Monthly Notices of the Royal Astronomical Society, 455, 227

Andrae R., Schulze-Hartung T., Melchior P., 2010, Dos and Don'ts of Reduced Chi-Squared, doi:10.48550/arXiv.1012.3754

Argyle E., 1965, The Astrophysical Journal, 141, 750

Arp H., 1966, The Astrophysical Journal Supplement Series, 14, 1

Astropy Collaboration et al., 2022, The Astrophysical Journal, 935, 167

Bacchini C., et al., 2023, 3D Modeling of the Molecular Gas Kinematics in Optically-Selected Jellyfish Galaxies (arXiv:2301.03090)

Ballero S. K., Matteucci F., Ciotti L., Calura F., Padovani P., 2008, Astronomy and Astrophysics, 478, 335

Barnabè M., Ciotti L., Fraternali F., Sancisi R., 2006, Astronomy and Astrophysics, Volume 446, Issue 1, January IV 2006, pp.61-69, 446, 61

Barnes J. E., 1992, The Astrophysical Journal, 393, 484

Barnes J. E., 2004, Monthly Notices of the Royal Astronomical Society, 350, 798

Barnes J. E., Hernquist L., 1992, Annual Review of Astronomy and Astrophysics, 30, 705

Barnes J. E., Hernquist L., 1996, The Astrophysical Journal, 471, 115

Barsanti S., et al., 2018, ApJ, 857, 71

Barton E. J., Geller M. J., Kenyon S. J., 2000, The Astrophysical Journal, 530, 660

Begeman K. G., 1987, PhD thesis

Bekiaris G., Glazebrook K., Fluke C. J., Abraham R., 2016, Monthly Notices of the Royal Astronomical Society, 455, 754

Bekki K., Koribalski B. S., Ryder S. D., Couch W. J., 2005, Monthly Notices of the Royal Astronomical Society, 357, L21

Berlind A. A., et al., 2006, The Astrophysical Journal Supplement Series, 167, 1

Bershady M. A., Verheijen M. A. W., Swaters R. A., Andersen D. R., Westfall K. B., Martinsson T., 2010, The Astrophysical Journal, 716, 198

Bigiel F., Leroy A., Walter F., Brinks E., de Blok W. J. G., Madore B., Thornley M. D., 2008, The Astronomical Journal, 136, 2846

Bigiel F., Leroy A., Walter F., Blitz L., Brinks E., de Blok W. J. G., Madore B., 2010, The Astronomical Journal, 140, 1194

Binney J., Tremaine S., 1987, Galactic Dynamics

Binney J., Nipoti C., Fraternali F., 2009, Monthly Notices of the Royal Astronomical Society, 397, 1804

Bizyaev D., Walterbos R. A. M., Chen Y.-M., Drory N., Lane R. R., Brownstein J. R., Riffel R. A., 2022, Monthly Notices of the Royal Astronomical Society, 515, 1598

Blackman C. P., 1982, Monthly Notices of the Royal Astronomical Society, 200, 407

Blitz L., Rosolowsky E., 2006, The Astrophysical Journal, Volume 650, Issue 2, pp. 933-944., 650, 933

Blumenthal K. A., Barnes J. E., 2018, Monthly Notices of the Royal Astronomical Society, 479, 3952

Boettcher E., Zweibel E. G., Gallagher J. S. I., Benjamin R. A., 2016, ApJ, 832, 118

Boettcher E., Gallagher III J. S., Zweibel E. G., 2017a, The Astrophysical Journal, 845, 155

Boettcher E., Gallagher J. S. I., Zweibel E. G., 2017b, ApJ, 845, 155

Boettcher E., Gallagher J. S. I., Zweibel E. G., 2019, ApJ, 885, 160

Bok J., Blyth S. L., Gilbank D. G., Elson E. C., 2019, Monthly Notices of the Royal Astronomical Society, 484, 582

Bok J., Skelton R. E., Cluver M. E., Jarrett T. H., Jones M. G., Verdes-Montenegro L., 2020, Monthly Notices of the Royal Astronomical Society, 499, 3193

Bok J., Cluver M. E., Jarrett T. H., Skelton R. E., Jones M. G., Verdes-Montenegro L., 2022, Monthly Notices of the Royal Astronomical Society, 513, 2581

Boomsma R., Oosterloo T. A., Fraternali F., van der Hulst J. M., Sancisi R., 2008, Astronomy and Astrophysics, Volume 490, Issue 2, 2008, pp.555-570, 490, 555

Borthakur S., Yun M. S., Verdes-Montenegro L., 2010, The Astrophysical Journal, 710, 385

Boselli A., Gavazzi G., 2006, Publications of the Astronomical Society of the Pacific, 118, 517

Bottinelli L., Gouguenheim L., Paturel G., de Vaucouleurs G., 1984, Astronomy and Astrophysics Supplement Series, 56, 381

Bouché N., Carfantan H., Schroetter I., Michel-Dansac L., Contini T., 2015, The Astronomical Journal, 150, 92

Bournaud F., Jog C. J., Combes F., 2007, Astronomy and Astrophysics, 476, 1179

Bregman J. N., 1980, The Astrophysical Journal, 236, 577

Brown T., et al., 2017, Monthly Notices of the Royal Astronomical Society, 466, 1275

Brownson S., Bluck A. F. L., Maiolino R., Jones G. C., 2022, Monthly Notices of the Royal Astronomical Society, 511, 1913

Brüns C., et al., 2005, Astronomy and Astrophysics, 432, 45

Burbidge E. M., Burbidge G. R., Prendergast K. H., 1959, The Astrophysical Journal, 130, 739

Buta R., Crocker D. A., 1993, The Astronomical Journal, 105, 1344

Chandrasekhar S., 1943, The Astrophysical Journal, 97, 255

Clarke S. D., Whitworth A. P., Spowage R. L., Duarte-Cabral A., Suri S. T., Jaffa S. E., Walch S., Clark P. C., 2018, Monthly Notices of the Royal Astronomical Society, 479, 1722

Clemens M. S., 1999, The interstellar medium and star formation in interacting galaxies.. Ph.D. Dissertation, University of Cambridge

Collins J. A., Benjamin R. A., Rand R. J., 2002, The Astrophysical Journal, 578, 98

Comerón S., Knapen J. H., Beckman J. E., Laurikainen E., Salo H., Martínez-Valpuesta I., Buta R. J., 2010, Monthly Notices of the Royal Astronomical Society, 402, 2462

Comrie A., et al., 2021, CARTA: The Cube Analysis and Rendering Tool for Astronomy, Zenodo, doi:10.5281/zenodo.4905459

Cornwell T. J., 2008, IEEE Journal of Selected Topics in Signal Processing, 2, 793

Correa C. A., Schaye J., van de Voort F., Duffy A. R., Wyithe J. S. B., 2018, Monthly Notices of the Royal Astronomical Society, 478, 255

Cortese L., Catinella B., Smith R., 2021, Publications of the Astronomical Society of Australia, 38, e035

Cowie L. L., Songaila A., 1977, Nature, 266, 501

Davies L. J. M., et al., 2015, MNRAS, 452, 616

De Mello D. F., Urrutia-Viscarra F., Mendes De Oliveira C., Torres-Flores S., Carrasco E. R., Cypriano E., 2012, Monthly Notices of the Royal Astronomical Society, 426, 2441

Deb T., Verheijen M. A. W., van der Hulst J. M., 2023, An HI Story of Galaxies in Abell 2626 and Beyond (arXiv:2303.10141)

Deg N., et al., 2022, WALLABY Pilot Survey: Public Release of HI Kinematic Models for More than 100 Galaxies from Phase 1 of ASKAP Pilot Observations (arXiv:2211.07333), doi:10.1017/pasa.2022.43

Di Matteo T., Springel V., Hernquist L., 2005, Nature, 433, 604

Di Teodoro E. M., Fraternali F., 2015, Monthly Notices of the Royal Astronomical Society, 451, 3021

Di Teodoro E. M., Peek J. E. G., 2021, The Astrophysical Journal, 923, 220

Di Teodoro E. M., Fraternali F., Miller S. H., 2016, Astronomy & Astrophysics, 594, A77

Di Teodoro E. M., et al., 2019, Monthly Notices of the Royal Astronomical Society, 483, 392

Dickey J. M., Hanson M. M., Helou G., 1990, The Astrophysical Journal, 352, 522

Donahue M., Voit G. M., 2022, Physics Reports, 973, 1

Dopita M. A., et al., 2014, Astronomy & Astrophysics, Volume 566, id.A41, 14 pp., 566, A41

Dressler A., 1980, ApJ, 236, 351

Duc P. A., Cayatte V., Balkowski C., Thuan T. X., Papaderos P., van Driel W., 2001, Astronomy and Astrophysics, 369, 763

Džudžar R., et al., 2019, MNRAS, 483, 5409

Džudžar R., Kilborn V., Sweet S. M., Meurer G., Jarrett T. H., Kleiner D., 2021, MNRAS, 500, 3689

Eibensteiner C., et al., 2023, Kinematic Analysis of the Super-Extended HI Disk of the Nearby Spiral Galaxy M83 (arXiv:2304.02037)

Eke V. R., Baugh C. M., Cole S., Frenk C. S., King H. M., Peacock J. A., 2005, Monthly Notices of the Royal Astronomical Society, 362, 1233

Ellison S. L., Mendel J. T., Scudder J. M., Patton D. R., Palmer M. J. D., 2013, Monthly Notices of the Royal Astronomical Society, 430, 3128

Epinat B., et al., 2012, Astronomy & Astrophysics, 539, A92

Evans I. N., Koratkar A. P., Storchi-Bergmann T., Kirkpatrick H., Heckman T. M., Wilson A. S., 1996, The Astrophysical Journal Supplement Series, 105, 93

Font J., et al., 2011, ApJ, 740, L1

Förster Schreiber N. M., et al., 2018, The Astrophysical Journal Supplement Series, 238, 21

Fraternali F., 2017,] 10.1007/978-3-319-52512-9-14, 430, 323

Fraternali F., Binney J. J., 2006, Monthly Notices of the Royal Astronomical Society, 366, 449

Fraternali F., Binney J. J., 2008, Monthly Notices of the Royal Astronomical Society, 386, 935

Fraternali F., Oosterloo T., Sancisi R., van Moorsel G., 2001, The Astrophysical Journal, 562, L47

Fraternali F., van Moorsel G., Sancisi R., Oosterloo T., 2002, The Astronomical Journal, 123, 3124

Fraternali F., Oosterloo T., Sancisi R., 2004, Astronomy and Astrophysics, v.424, p.485-495 (2004), 424, 485

Fraternali F., Oosterloo T. A., Sancisi R., Swaters R., 2005, 331, 239

Fuentes-Carrera I., et al., 2004, Astronomy and Astrophysics, 415, 451

Geréb K., Catinella B., Cortese L., Bekki K., Moran S. M., Schiminovich D., 2016, Monthly Notices of the Royal Astronomical Society, 462, 382

Geréb K., Janowiecki S., Catinella B., Cortese L., Kilborn V., 2018, Monthly Notices of the Royal Astronomical Society, 476, 896

Ginsburg A., Mirocha J., 2011, Astrophysics Source Code Library, p. ascl:1109.001

Ginsburg A., et al., 2022a, Zenodo

Ginsburg A., Sokolov V., de Val-Borro M., Rosolowsky E., Pineda J. E., Sipőcz B. M., Henshaw J. D., 2022b, The Astronomical Journal, 163, 291

Gogate A., Verheijen M., Deshev B., Montero-Castaño M., van Gorkom J., van der Hulst T., Jaffé Y., Poggianti B., 2020, Monthly Notices of the Royal Astronomical Society, 496, 3531

González Delgado R. M., Pérez E., Tadhunter C., Vilchez J. M., José Miguel Rodríguez-Espinosa a., 1997, The Astrophysical Journal Supplement Series, 108, 155

Gronke M., Oh S. P., 2020, Monthly Notices of the Royal Astronomical Society, 492, 1970

Gunn J. E., Gott III J. R., 1972, The Astrophysical Journal, 176, 1

Gupta Y., et al., 2017, Current Science, 113, 707

Hafen Z., et al., 2019, Monthly Notices of the Royal Astronomical Society, 488, 1248

Hafen Z., et al., 2022, Monthly Notices of the Royal Astronomical Society, 514, 5056

Haffner L. M., et al., 2009, Reviews of Modern Physics, 81, 969

Haud U., 2000, Astronomy and Astrophysics, v.364, p.83-101 (2000), 364, 83

Healy J., Deb T., Verheijen M. A. W., Blyth S. L., Serra P., Ramatsoku M., Vulcani B., 2021, A&A, 654, A173

Henshaw J. D., et al., 2016, Monthly Notices of the Royal Astronomical Society, 457, 2675

Henshaw J. D., et al., 2019, Monthly Notices of the Royal Astronomical Society, 485, 2457

Hess K. M., Wilcots E. M., 2013, The Astronomical Journal, 146, 124

Hess K. M., Pisano D. J., Wilcots E. M., Chengalur J. N., 2009, The Astrophysical Journal, 699, 76

Hess K. M., Cluver M. E., Yahya S., Leisman L., Serra P., Lucero D. M., Passmoor S. S., Carignan C., 2017, Monthly Notices of the Royal Astronomical Society, 464, 957

Hess K. M., paoloserra Boschman L., Shen A., H J., 2022a, Kmhess/SoFiA-image-pipeline: SoFiA Image Pipeline v1.2.0, Zenodo, doi:10.5281/zenodo.6821586

Hess K. M., Kotulla R., Chen H., Carignan C., Gallagher J. S., Jarrett T. H., Kraan-Korteweg R. C., 2022b, Astronomy and Astrophysics, 668, A184

Hibbard J. E., van Gorkom J. H., Rupen M. P., Schiminovich D., 2001, An HI Rogues Gallery (arXiv:astro-ph/0110667)

Hopkins P. F., Hernquist L., Cox T. J., Di Matteo T., Robertson B., Springel V., 2006, The Astrophysical Journal Supplement Series, 163, 1

Hopkins P. F., Cox T. J., Kereš D., Hernquist L., 2008, The Astrophysical Journal Supplement Series, 175, 390

Hopkins P. F., Cox T. J., Younger J. D., Hernquist L., 2009, The Astrophysical Journal, 691, 1168

Hotan A. W., et al., 2021, Publications of the Astronomical Society of Australia, 38, e009

Hummels C. B., et al., 2019, The Astrophysical Journal, 882, 156

Hunter J. D., 2007, Computing in Science & Engineering, 9, 90

Iorio G., Fraternali F., Nipoti C., Di Teodoro E., Read J. I., Battaglia G., 2017, Monthly Notices of the Royal Astronomical Society, 466, 4159

Janowiecki S., Catinella B., Cortese L., Saintonge A., Brown T., Wang J., 2017, MNRAS, 466, 4795

Jog C. J., Solomon P. M., 1992, The Astrophysical Journal, 387, 152

Johnston S., et al., 2008, Experimental Astronomy, 22, 151

Jonas J., MeerKAT Team 2016, The MeerKAT Radio Telescope, doi:10.22323/1.277.0001.

Jones M. G., et al., 2019, A&A, 632, A78

Jones M. G., et al., 2023, Astronomy and Astrophysics, 670, A21

Joung M. R., Bryan G. L., Putman M. E., 2012, The Astrophysical Journal, 745, 148

Józsa G. I. G., Kenn F., Klein U., Oosterloo T. A., 2007, Astronomy and Astrophysics, 468, 731

Kalberla P. M. W., Burton W. B., Hartmann D., Arnal E. M., Bajaja E., Morras R., Pöppel W. G. L., 2005, Astronomy and Astrophysics, Volume 440, Issue 2, September III 2005, pp.775-782, 440, 775

Kamphuis J. J., 1993, PhD thesis

Kamphuis J., Sancisi R., 1993, Astronomy and Astrophysics, Vol. 273, p. L31-L34 (1993), 273, L31

Kamphuis P., et al., 2013, Monthly Notices of the Royal Astronomical Society, 434, 2069

Kamphuis P., Józsa G. I. G., Oh S. . H., Spekkens K., Urbancic N., Serra P., Koribalski B. S., Dettmar R. J., 2015, Monthly Notices of the Royal Astronomical Society, 452, 3139

Kamphuis P., et al., 2022, Astronomy and Astrophysics, 668, A182

Kannappan S. J., et al., 2013, The Astrophysical Journal, 777, 42

Keeney B. A., Stocke J. T., Rosenberg J. L., Danforth C. W., Ryan-Weber E. V., Shull J. M., Savage B. D., Green J. C., 2013, The Astrophysical Journal, 765, 27

Kennicutt Jr. R. C., Keel W. C., 1984, The Astrophysical Journal, 279, L5

Kereš D., Hernquist L., 2009, The Astrophysical Journal, 700, L1

Kereš D., Katz N., Weinberg D. H., Davé R., 2005, Monthly Notices of the Royal Astronomical Society, 363, 2

Kewley L. J., Rupke D., Zahid H. J., Geller M. J., Barton E. J., 2010, The Astrophysical Journal, 721, L48

Kewley L. J., Nicholls D. C., Sutherland R. S., 2019, ARA&A, 57, 511

Kim M., Oh S.-H., 2022, Journal of Korean Astronomical Society, 55, 149

Kleiner D., Pimbblet K. A., Jones D. H., Koribalski B. S., Serra P., 2017, MNRAS, 466, 4692

Kleiner D., et al., 2021, Astronomy and Astrophysics, 648, A32

Koopmann R. A., et al., 2008, The Astrophysical Journal, 682, L85

Koribalski B. S., 2020, Hydrogen Tails, Plumes, Clouds and Filaments, doi:10.48550/arXiv.2002.07312

Koribalski B., Dickey J. M., 2004, Monthly Notices of the Royal Astronomical Society, 348, 1255

Koribalski B. S., et al., 2004, The Astronomical Journal, 128, 16

Kourkchi E., Tully R. B., 2017, The Astrophysical Journal, 843, 16

Krajnović D., Cappellari M., de Zeeuw P. T., Copin Y., 2006, Monthly Notices of the Royal Astronomical Society, 366, 787

Lagos C. d. P., 2018, Angular Momentum Evolution of Galaxies: The Perspective of Hydrodynamical Simulations, doi:10.48550/arXiv.1810.13074

Lagos C. d. P., et al., 2018, Monthly Notices of the Royal Astronomical Society, 473, 4956

Lang P., et al., 2020, The Astrophysical Journal, 897, 122

Lara-López M. A., et al., 2013, Monthly Notices of the Royal Astronomical Society, 434, 451

Larson R. B., Tinsley B. M., Caldwell C. N., 1980, The Astrophysical Journal, 237, 692

Leclercq F., et al., 2022, Astronomy & Astrophysics, Volume 663, id.A11, 20 pp., 663, A11

Lehner N., et al., 2020, arXiv e-prints, 2002, arXiv:2002.07818

Leroy A. K., Walter F., Brinks E., Bigiel F., de Blok W. J. G., Madore B., Thornley M. D., 2008, The Astronomical Journal, 136, 2782

Li A., Fraternali F., Marasco A., Trager S. C., Pezzulli G., Piña P. E. M., Verheijen M. A. W., 2023, Fountain-Driven Gas Accretion Feeding Star Formation over the Disc of NGC 2403 (arXiv:2301.03614)

Lin X., et al., 2023, FAST-ASKAP Synergy: Quantifying Coexistent Tidal and Ram-Pressure Strippings in the NGC 4636 Group (arxiv:2304.09795)

Lindner R. R., et al., 2015, The Astronomical Journal, 149, 138

Liu Y., Zhu M., Yu H., Ai1 M., Jiang P., Liu S., Yuan L., 2023, FAST Discovery of Long Tidal Tails in NGC 4490/85 (arxiv:2304.13964)

López-Cobá C., Lin L., Sánchez S. F., 2021, XookSuut a Code for Modeling Circular and Non–Circular Flows on 2D Velocity Maps

Lotz J. M., Jonsson P., Cox T. J., Primack J. R., 2008, Monthly Notices of the Royal Astronomical Society, 391, 1137

Lucchini S., D'Onghia E., Fox A. J., 2021, The Astrophysical Journal, 921, L36

Lutz K. A., et al., 2017, Monthly Notices of the Royal Astronomical Society, 467, 1083

Lutz K. A., et al., 2018, Monthly Notices of the Royal Astronomical Society, 476, 3744

Macquart J.-P., et al., 2020, Nature, 581, 391

Marasco A., Fraternali F., 2011, Astronomy and Astrophysics, 525, A134

Marasco A., Fraternali F., Binney J. J., 2012, Monthly Notices of the Royal Astronomical Society, 419, 1107

Marasco A., et al., 2019, Astronomy & Astrophysics, Volume 631, id.A50, 27 pp., 631, A50

Marasco A., Fraternali F., Lehner N., Howk J. C., 2022, Monthly Notices of the Royal Astronomical Society, 515, 4176

Marchal A., Miville-Deschênes M.-A., Orieux F., Gac N., Soussen C., Lesot M.-J., d'Allonnes A. R., Salomé Q., 2019, Astronomy & Astrophysics, Volume 626, id.A101, 19 pp., 626, A101

Marinacci F., Fraternali F., Ciotti L., Nipoti C., 2010, Monthly Notices of the Royal Astronomical Society, 401, 2451

Martin C. L., Ho S. H., Kacprzak G. G., Churchill C. W., 2019, The Astrophysical Journal, 878, 84

Martini P., Regan M. W., Mulchaey J. S., Pogge R. W., 2003, The Astrophysical Journal Supplement Series, 146, 353

Matthews L. D., Wood K., 2003, The Astrophysical Journal, 593, 721

McCourt M., Oh S. P., O'Leary R., Madigan A.-M., 2018, Monthly Notices of the Royal Astronomical Society, 473, 5407

McMullin J. P., Waters B., Schiebel D., Young W., Golap K., 2007, Conference Name: Astronomical Data Analysis Software and Systems XVI Bibcode: 2007ASPC..376..127M, 376, 127

Meiksin A. A., 2009, Reviews of Modern Physics, 81, 1405

Meurer G. R., et al., 2006, ApJS, 165, 307

Meyer M. J., et al., 2004, MNRAS, 350, 1195

Meyer M., Robotham A., Obreschkow D., Westmeier T., Duffy A. R., Staveley-Smith L., 2017, Publ. Astron. Soc. Australia, 34, 52

Michel-Dansac L., et al., 2010, The Astrophysical Journal, 717, L143

Mihos J. C., 2019, Deep Imaging of Diffuse Light Around Galaxies and Clusters: Progress and Challenges

Mihos J. C., Hernquist L., 1996, The Astrophysical Journal, 464, 641

Misiriotis A., Papadakis I. E., Kylafis N. D., Papamastorakis J., 2004, Astronomy and Astrophysics, 417, 39

Miville-Deschênes M.-A., Murray N., Lee E. J., 2017, The Astrophysical Journal, 834, 57

Mogotsi M. K. M., 2016, PhD thesis

Moore B., Katz N., Lake G., Dressler A., Oemler A., 1996, Nature, 379, 613

Mosenkov A. V., et al., 2019, Astronomy & Astrophysics, 622, A132

Murugeshan C., Kilborn V., Jarrett T., Wong O. I., Obreschkow D., Glazebrook K., Cluver M. E., Fluke C. J., 2020, Monthly Notices of the Royal Astronomical Society, 496, 2516

Nagao T., Murayama T., Shioya Y., Taniguchi Y., 2002, The Astrophysical Journal, 575, 721

Nan R., et al., 2011, International Journal of Modern Physics D, 20, 989

Neeleman M., et al., 2021, The Astrophysical Journal, 911, 141

Nidever D. L., Majewski S. R., Butler Burton W., 2008, The Astrophysical Journal, 679, 432

Nielsen N. M., Kacprzak G. G., Sameer Murphy M. T., Nateghi H., Charlton J. C., Churchill C. W., 2022, Monthly Notices of the Royal Astronomical Society, 514, 6074

Nulsen P. E. J., 1982, Monthly Notices of the Royal Astronomical Society, 198, 1007

Obreschkow D., Glazebrook K., Kilborn V., Lutz K., 2016, The Astrophysical Journal, 824, L26

Oh S.-H., de Blok W. J. G., Walter F., Brinks E., Kennicutt Jr. R. C., 2008, The Astronomical Journal, 136, 2761

Oh S.-H., Staveley-Smith L., Spekkens K., Kamphuis P., Koribalski B. S., 2018, Monthly Notices of the Royal Astronomical Society, 473, 3256

Oh S.-H., Staveley-Smith L., For B.-Q., 2019, Monthly Notices of the Royal Astronomical Society, 485, 5021

Oh S.-H., Kim S., For B.-Q., Staveley-Smith L., 2022, The Astrophysical Journal, 928, 177

Olivares V., et al., 2022, Astronomy & Astrophysics, 666, A94

Oosterloo T., Fraternali F., Sancisi R., 2007a, The Astronomical Journal, 134, 1019

Oosterloo T. A., Morganti R., Sadler E. M., van der Hulst T., Serra P., 2007b, Astronomy and Astrophysics, 465, 787

Pardy S. A., D'Onghia E., Fox A. J., 2018, The Astrophysical Journal, 857, 101

Pearson S., et al., 2016, Monthly Notices of the Royal Astronomical Society, 459, 1827

Pearson S., et al., 2018, Monthly Notices of the Royal Astronomical Society, 480, 3069

Pease F. G., 1918, Proceedings of the National Academy of Science, 4, 21

Peeples M. S., et al., 2019, The Astrophysical Journal, 873, 129

Perley R. A., Butler B. J., 2017, The Astrophysical Journal Supplement Series, 230, 7

Péroux C., Howk J. C., 2020, Annual Review of Astronomy and Astrophysics, 58, 363

Péroux C., Rahmani H., Arrigoni Battaia F., Augustin R., 2018, Monthly Notices of the Royal Astronomical Society, 479, L50

Peters S. P. C., van der Kruit P. C., Allen R. J., Freeman K. C., 2017, Monthly Notices of the Royal Astronomical Society, 464, 21

Piña P. E. M., Fraternali F., Oosterloo T., Adams E. A. K., di Teodoro E., Bacchini C., Iorio G., 2022, The Impact of Gas Disc Flaring on Rotation Curve Decomposition and Revisiting Baryonic and Dark-Matter Relations for Nearby Galaxies (arXiv:2205.12977)

Pisano D. J., Barnes D. G., Gibson B. K., Staveley-Smith L., Freeman K. C., Kilborn V. A., 2004, The Astrophysical Journal, 610, L17

Pisano D. J., Barnes D. G., Gibson B. K., Staveley-Smith L., Freeman K. C., Kilborn V. A., 2007, The Astrophysical Journal, 662, 959

Planck Collaboration 2020, A&A, 641, A6

Ponomareva A. A., et al., 2021, Monthly Notices of the Royal Astronomical Society, 508, 1195

Pradeep J., Sankar S., Umasree T. M., Narayanan A., Khaire V., Gebhardt M., Sameer Charlton J. C., 2020, Monthly Notices of the Royal Astronomical Society, 493, 250

Punzo D., van der Hulst J. M., Roerdink J. B. T. M., Fillion-Robin J. C., Yu L., 2017, Astronomy and Computing, 19, 45

Putman M. E., 2017,] 10.1007/978-3-319-52512-9$_1$, 430, 1

Putman M. E., Peek J. E. G., Joung M. R., 2012, Annual Review of Astronomy and Astrophysics, 50, 491

Putman M. E., Zheng Y., Price-Whelan A. M., Grcevich J., Johnson A. C., Tollerud E., Peek J. E. G., 2021, The Astrophysical Journal, 913, 53

Randriamiarinarivo N., Elson E., Baker A., 2022, A New Technique to Isolate Kinematically Anomalous Gas in HI Data Cubes (arXiv:2211.12306)

Rasmussen J., Ponman T. J., Mulchaey J. S., 2006, Monthly Notices of the Royal Astronomical Society, 370, 453

Rasmussen J., Ponman T. J., Verdes-Montenegro L., Yun M. S., Borthakur S., 2008, Monthly Notices of the Royal Astronomical Society, 388, 1245

Rasmussen J., Mulchaey J. S., Bai L., Ponman T. J., Raychaudhury S., Dariush A., 2012, The Astrophysical Journal, 757, 122

Ravi V., et al., 2019, Nature, 572, 352

Renaud F., Segovia Otero Á., Agertz O., 2022, Monthly Notices of the Royal Astronomical Society, 516, 4922

Rich J. W., de Blok W. J. G., Cornwell T. J., Brinks E., Walter F., Bagetakos I., Kennicutt R. C., 2008, The Astronomical Journal, 136, 2897

Rich J. A., Torrey P., Kewley L. J., Dopita M. A., Rupke D. S. N., 2012, The Astrophysical Journal, 753, 5

Riener M., Kainulainen J., Henshaw J. D., Orkisz J. H., Murray C. E., Beuther H., 2019, Astronomy & Astrophysics, 628, A78

Roberts M. S., 1962, The Astronomical Journal, 67, 437

Rogstad D. H., Shostak G. S., 1971, Astronomy and Astrophysics, Vol. 13, p. 99-107 (1971), 13, 99

Rogstad D. H., Lockhart I. A., Wright M. C. H., 1974, The Astrophysical Journal, 193, 309

Rossa J., Dettmar R.-J., 2003, Astronomy and Astrophysics, 406, 505

Rubin V. C., Ford Jr. W. K., Thonnard N., 1980, The Astrophysical Journal, 238, 471

Rudie G. C., Steidel C. C., Pettini M., Trainor R. F., Strom A. L., Hummels C. B., Reddy N. A., Shapley A. E., 2019, The Astrophysical Journal, 885, 61

Rupke D. S. N., Kewley L. J., Chien L. H., 2010, The Astrophysical Journal, 723, 1255

Saintonge A., Catinella B., 2022, The Cold Interstellar Medium of Galaxies in the Local Universe

Sameer et al., 2022, Monthly Notices of the Royal Astronomical Society, 510, 5796

Sancisi R., Fraternali F., Oosterloo T., van der Hulst T., 2008, The Astronomy and Astrophysics Review, Volume 15, Issue 3, pp.189-223, 15, 189

Sankar S., Narayanan A., Savage B. D., Khaire V., Rosenwasser B. E., Charlton J., Wakker B. P., 2020, Monthly Notices of the Royal Astronomical Society, 498, 4864

Schaap W. E., Sancisi R., Swaters R. A., 2000, Astronomy and Astrophysics, 356, L49

Schoenmakers R. H. M., 1999, PhD thesis

Sellwood J. A., Sánchez R. Z., 2010, Monthly Notices of the Royal Astronomical Society, 404, 1733

Sellwood J. A., Spekkens K., Eckel C. S., 2021, Monthly Notices of the Royal Astronomical Society, 502, 3843

Sengupta C., Balasubramanyam R., Dwarakanath K. S., 2007, Monthly Notices of the Royal Astronomical Society, 378, 137

Serra P., Jurek R., Flöer L., 2012a, Publ. Astron. Soc. Australia, 29, 296

Serra P., et al., 2012b, Monthly Notices of the Royal Astronomical Society, 422, 1835

Serra P., et al., 2013, Monthly Notices of the Royal Astronomical Society, 428, 370

Serra P., et al., 2015, MNRAS, 448, 1922

Serra P., et al., 2023, The MeerKAT Fornax Survey – I. Survey Description and First Evidence of Ram Pressure in the Fornax Galaxy Cluster (arXiv:2302.11895)

Shapiro P. R., Field G. B., 1976, The Astrophysical Journal, 205, 762

Simon J. D., Bolatto A. D., Leroy A., Blitz L., 2003, The Astrophysical Journal, 596, 957

Skillman E. D., et al., 2013, The Astronomical Journal, 146, 3

Slipher V. M., 1914, Lowell Observatory Bulletin, 2, 66

Smart B. M., Haffner L. M., Barger K. A., Hill A., Madsen G., 2019, The Astrophysical Journal, 887, 16

Smith B. J., Struck C., Hancock M., Appleton P. N., Charmandaris V., Reach W. T., 2007, AJ, 133, 791

Smith B. J., Giroux M. L., Struck C., Hancock M., 2010, AJ, 139, 1212

Smith B. J., Soria R., Struck C., Giroux M. L., Swartz D. A., Yukita M., 2014, The Astronomical Journal, 147, 60

Smith B. J., Zaragoza-Cardiel J., Struck C., Olmsted S., Jones K., 2016, The Astronomical Journal, 151, 63

Sofue Y., 1996, The Astrophysical Journal, 458, 120

Sofue Y., Rubin V., 2001, Annual Review of Astronomy and Astrophysics, 39, 137

Sol Alonso M., Lambas D. G., Tissera P., Coldwell G., 2006, Monthly Notices of the Royal Astronomical Society, 367, 1029

Sorai K., et al., 2019, Publications of the Astronomical Society of Japan, 71, S14

Sorgho A., Foster T., Carignan C., Chemin L., 2019, Monthly Notices of the Royal Astronomical Society, 486, 504

Sorgho A., Chemin L., Kam Z. S., Foster T., Carignan C., 2020, Monthly Notices of the Royal Astronomical Society, 493, 2618

Sotillo-Ramos D., et al., 2021, Monthly Notices of the Royal Astronomical Society, 508, 1817

Spekkens K., Sellwood J. A., 2007, The Astrophysical Journal, 664, 204

Stern J., Fielding D., Faucher-Giguère C.-A., Quataert E., 2019, Monthly Notices of the Royal Astronomical Society, 488, 2549

Stern J., Fielding D., Faucher-Giguère C.-A., Quataert E., 2020, Monthly Notices of the Royal Astronomical Society, 492, 6042

Stern J., Fielding D., Hafen Z., Su K.-Y., Naor N., Faucher-Giguère C.-A., Quataert E., Bullock J., 2023, Accretion onto Disk Galaxies via Hot and Rotating CGM Inflows (arxiv:2306.00092)

Stewart K. R., Bullock J. S., Wechsler R. H., Maller A. H., Zentner A. R., 2008, The Astrophysical Journal, 683, 597

Stewart K. R., Kaufmann T., Bullock J. S., Barton E. J., Maller A. H., Diemand J., Wadsley J., 2011, The Astrophysical Journal, 738, 39

Stewart K. R., Brooks A. M., Bullock J. S., Maller A. H., Diemand J., Wadsley J., Moustakas L. A., 2013, The Astrophysical Journal, 769, 74

Stewart K. R., et al., 2017, The Astrophysical Journal, 843, 47

Stierwalt S., Haynes M. P., Giovanelli R., Kent B. R., Martin A. M., Saintonge A., Karachentsev I. D., Karachentseva V. E., 2009, The Astronomical Journal, 138, 338

Strateva I., et al., 2001, AJ, 122, 1861

Struck C., 2006, Galaxy Collisions — Dawn of a New Era, doi:10.1007/3-540-30313-8_4.

Struck C., Smith B. J., 2012, Monthly Notices of the Royal Astronomical Society, 422, 2444

Su Y.-C., et al., 2022, The ALMaQUEST Survey. VIII. What Causes the Velocity Discrepancy between CO and H{\alpha} Rotation Curves in Galaxies? (arXiv:2206.05913)

Swaters R. A., Sancisi R., van der Hulst J. M., 1997, The Astrophysical Journal, 491, 140

Sweet S. M., et al., 2013, MNRAS, 433, 543

Sweet S. M., Drinkwater M. J., Meurer G., Bekki K., Dopita M. A., Kilborn V., Nicholls D. C., 2014, ApJ, 782, 35

Sweet S. M., Drinkwater M. J., Meurer G., Kilborn V., Audcent-Ross F., Baumgardt H., Bekki K., 2016, MNRAS, 455, 2508

Taylor R., Davies J. I., Jáchym P., Keenan O., Minchin R. F., Palouš J., Smith R., Wünsch R., 2016, Monthly Notices of the Royal Astronomical Society, 461, 3001

Team T. C., et al., 2022, Publications of the Astronomical Society of the Pacific, 134, 114501

Tejos N., et al., 2021, arXiv:2105.01673 [astro-ph]

Tempel E., et al., 2014, A&A, 566, A1

Teodoro E. M. D., Fraternali F., 2014, Astronomy & Astrophysics, 567, A68

Toomre A., 1977, Mergers and Some Consequences

Toomre A., Toomre J., 1972, The Astrophysical Journal, 178, 623

Tremaine S., Weinberg M. D., 1984, Monthly Notices of the Royal Astronomical Society, 209, 729

Tumlinson J., Peeples M. S., Werk J. K., 2017, ARA&A, 55, 389

Urrejola-Mora C., Gómez F. A., Torres-Flores S., Amram P., Epinat B., Monachesi A., Marinacci F., de Oliveira C. M., 2022, The Astrophysical Journal, 935, 20

Väisänen P., Reunanen J., Kotilainen J., Mattila S., Johansson P. H., Ramphul R., Romero-Cañizales C., Kuncarayakti H., 2017, Monthly Notices of the Royal Astronomical Society, 471, 2059

Veilleux S., Kim D. C., Sanders D. B., 2002, The Astrophysical Journal Supplement Series, 143, 315

Verdes-Montenegro L., Yun M. S., Williams B. A., Huchtmeier W. K., Del Olmo A., Perea J., 2001, Astronomy and Astrophysics, v.377, p.812-826 (2001), 377, 812

Verheijen M. A. W., Oosterloo T. A., van Cappellen W. A., Bakker L., Ivashina M. V., van der Hulst J. M., 2008,] 10.1063/1.2973599, 1035, 265

Veronese S., de Blok W. J. G., Walter F., 2023, Extended Neutral Hydrogen Filamentary Network in NGC 2403 (arXiv:2301.13526)

Vulcani B., et al., 2018, Monthly Notices of the Royal Astronomical Society, 480, 3152

Vulcani B., et al., 2021, The Astrophysical Journal, 914, 27

Wakker B. P., van Woerden H., 1997, Annual Review of Astronomy and Astrophysics, 35, 217

Walker I. R., Mihos J. C., Hernquist L., 1996, The Astrophysical Journal, 460, 121

Walker S. A., Bagchi J., Fabian A. C., 2015, Monthly Notices of the Royal Astronomical Society, 449, 3527

Walter F., Brinks E., de Blok W. J. G., Bigiel F., Kennicutt Jr. R. C., Thornley M. D., Leroy A., 2008, The Astronomical Journal, 136, 2563

Wang J., et al., 2013, Monthly Notices of the Royal Astronomical Society, 433, 270

Wang E., Wang J., Kauffmann G., Józsa G. I. G., Li C., 2015, MNRAS, 449, 2010

Wang J., et al., 2023, FEASTS: IGM Cooling Triggered by Tidal Interactions through the Diffuse HI Phase around NGC 4631 (arXiv:2301.00937)

Watts A. B., et al., 2023, Monthly Notices of the Royal Astronomical Society, 519, 1452

Westmeier T., et al., 2021, MNRAS, 506, 3962

Whiting M. T., 2012, Monthly Notices of the Royal Astronomical Society, 421, 3242

Wijesinghe D. B., et al., 2012, MNRAS, 423, 3679

Wotta C. B., Lehner N., Howk J. C., O'Meara J. M., Oppenheimer B. D., Cooksey K. L., 2019, The Astrophysical Journal, 872, 81

Wyder T. K., et al., 2009, The Astrophysical Journal, 696, 1834

Yamagata T., Noguchi M., Iye M., 1989, The Astrophysical Journal, 338, 707

Yeager T. R., Struck C., 2019, Monthly Notices of the Royal Astronomical Society, 486, 2660

Yeager T. R., Struck C., 2020, Monthly Notices of the Royal Astronomical Society, 492, 4892

Yu N., Ho L. C., Wang J., Li H., 2022, The Astrophysical Journal Supplement Series, 261, 21

Yuan T. T., Kewley L. J., Sanders D. B., 2010, The Astrophysical Journal, 709, 884

Zahedy F. S., Chen H.-W., Johnson S. D., Pierce R. M., Rauch M., Huang Y.-H., Weiner B. J., Gauthier J.-R., 2019, Monthly Notices of the Royal Astronomical Society, 484, 2257

Zaragoza-Cardiel J., Smith B. J., Rosado M., Beckman J. E., Bitsakis T., Camps-Fariña A., Font J., Cox I. S., 2018, The Astrophysical Journal Supplement Series, 234, 35

Zhang S., et al., 2023, Science, 380, 494

Zhu J., Putman M. E., 2023, Census of Gaseous Satellites around Local Spiral Galaxies (arXiv:2303.00763)

Zhu M., et al., 2021, The Astrophysical Journal, 922, L21

Zschaechner L. K., Rand R. J., Heald G. H., Gentile G., Kamphuis P., 2011, The Astrophysical Journal, 740, 35

Zschaechner L. K., Rand R. J., Heald G. H., Gentile G., Józsa G., 2012, The Astrophysical Journal, 760, 37

Zschaechner L. K., Rand R. J., Walterbos R., 2015, The Astrophysical Journal, 799, 61

Zucker C., Walker L. M., Johnson K., Gallagher S., Alatalo K., Tzanavaris P., 2016, ApJ, 821, 113

de Blok W. J. G., Walter F., Brinks E., Trachternach C., Oh S.-H., Kennicutt R. C., 2008, The Astronomical Journal, 136, 2648

de Blok W. J. G., et al., 2014, Astronomy & Astrophysics, Volume 569, id.A68, 11 pp., 569, A68

de Blok W. J. G., et al., 2016, in MeerKAT Science: On the Pathway to the SKA. p. 7 (arXiv:1709.08458)

de Blok W. J. G., et al., 2018, The Astrophysical Journal, 865, 26

de Vaucouleurs G., de Vaucouleurs A., Corwin Jr. H. G., Buta R. J., Paturel G., Fouque P., 1991, Third Reference Catalogue of Bright Galaxies

van Albada T. S., Bahcall J. N., Begeman K., Sancisi R., 1985, The Astrophysical Journal, 295, 305

van der Marel R. P., Franx M., 1993, The Astrophysical Journal, 407, 525

van der Velden E., 2020, The Journal of Open Source Software, 5, 2004

Appendices

A GaussPy+

1. Noise estimation and signal identification (see figure 2 and appendix figure B.1 in Riener et al. 2019).
   (a) Mask out broad features in the spectrum by using a Markov chain to estimate the probability that a consecutive number of positive or negative channels is due to noise.
   (b) Calculate the Median Absolute Deviation (MAD) using the unmasked negative channels.
   (c) Mask out all consecutively negative or positive channels of features that contain an intensity value higher than $\pm 5 \times$MAD.
   (d) Calculate the RMS noise from the unmasked channels.
   (e) To get an accurate estimation of the goodness of fit, the calculation is restricted to identified channels with signal. A padding parameter ensures that a user-defined minimum number of channels is used for the goodness of fit calculation.
   (f) Consecutive negative channels with at least one channel with a value lower than a user-defined threshold ($\sim 5 \times \sigma_{rms}$) are identified as negative noise spikes and are masked out from the goodness of fit calculations.
2. Training set creation.
   (a) A routine selects 300 random spaxels and decomposes it using an SLSQP optimization algorithm and least squares statistic. Initial guesses are provided by estimating the number of local positive maxima in the spectrum. Unsatisfactory fits are removed from the training set.
3. Original GaussPy algorithm.
   (a) The training set is used to find the optimum smoothing parameters α_1 and α_2 using a momentum-driven gradient descent algorithm.
   (b) Derivative spectroscopy is employed on the two smoothed spectra of each spaxel to determine the number of Gaussian components (n) and initial guesses for μ_i, A_i, and σ_i (see figure 1 in Lindner et al. 2015).
   (c) GaussPy then uses the Levenberg-Marquardt algorithm to perform a non-linear least-squares fit.
4. Quality control and refitting.
   (a) In-built quality control. A refit of the spectrum is attempted if:
      i. the FWHM value of a component is outside a user-defined range.
      ii. a component's signal-to-noise ratio is below a user-defined limit.
      iii. the integrated area of a Gaussian component falls below a user-defined significance limit.
      iv. the residuals fail one of the two normality tests that examine the null hypothesis that the residual resembles a normal distribution.
   (b) Optional quality control.
      i. Negative peaks in the residual can indicate a poor fit and thus are flagged for refitting.

ii. Gaussian components with an FWHM more than twice the second broadest component can be flagged and refit.
iii. Blended Gaussian components can be flagged and refit.
iv. The fit to the spectrum of a spaxel is flagged if it has a different number of components compared to the fits to the immediate neighbouring spaxels.

(c) The original GaussPy algorithm performs an unrestricted least squares fit which can introduce unphysical results. The improved fitting routine in GaussPy+ attempts to improve the fit based on the residual and certain user-selected quality criteria (See figure 7 in Riener et al. 2019).
i. The best-fit result of GaussPy is evaluated against the quality criteria introduced above. All the components not satisfying any of the criteria are removed from the best-fit solution and the spectrum is refit with the remaining fit components. This procedure is repeated until all of the leftover fit components satisfy all quality criteria.
ii. New Gaussian components are added iteratively based on positive peaks in the residual to improve the best-fit solution. This procedure is repeated until there are no positive peaks in the residual or no new best fit could be assigned. The new best fit is accepted if its AICc value is lower than that of the previous best fit.
iii. Optionally, negative residual features, broad components and blended components are flagged and refit using specialised routines.

5. Spatially coherent refitting.
(a) Phase 1: local coherence (see figure 8 in Riener et al. 2019).
i. The fit results from the improved fitting routine are flagged if:
A. there are negative peaks in the residual.
B. there are Gaussian components with a broad FWHM or if a component is broader by a user-defined factor than the broadest component in more than half of its neighbours.
C. there are blended components in the fit
D. the normalised residuals do not pass the normality tests
E. the number of components differs by more than one from its neighbours.
ii. The fit solutions of the neighbouring spectra are used to refit individual components of the flagged spectrum. The routine loops through all the neighbouring fit solutions in increasing order of χ^2_{red} to select initial guesses for the refitting. If one of the input guesses leads to an improved fit, the refitting is terminated, otherwise, the spectrum is passed to the next step.
iii. The fit solutions of the neighbouring spectra are used to refit the complete flagged spectrum. The routine again loops through the fit solution of neighbouring spectra to adopt initial guesses for refitting. If one of the input guesses leads to an improved fit, the refitting is terminated, otherwise, the spectrum is passed to the next step
iv. An initial guess is obtained by grouping the fit results of the neighbouring spectra in a parameter space spanned by velocity centroid and FWHM. After refitting a decision is made based on a comparison of the total flag value (F^{new}_{tot} and F^{old}_{tot}).

A. $F_{tot}^{new} > F_{tot}^{old}$ - The new fit is rejected.
B. $F_{tot}^{new} = F_{tot}^{old}$ - The new fit is accepted if it has a smaller AICc value than the initial best fir solution.
C. $F_{tot}^{new} < F_{tot}^{old}$ - The new fit is accepted if the normalised residual passes the normality tests. This is to test whether the new solutions reduced the F_{tot}^{new} by incorrectly removing valid components.

(b) Phase 2: global coherence (see figure 10 in Riener et al. 2019).
i. The velocity centroids of the Gaussian components along the four main directions are grouped and assigned weights. Total of 16 neighbours are considered with the closest neighbours getting assigned a higher weight than the farthest neighbours.
ii. A total weight is computed for each group of centroids by summing the weights of the spectra within the group.
iii. A refit to the central spectrum is attempted if it does not have the required Gaussian components inferred from the groups that met the required total weight threshold.
iv. The weight threshold is chosen by default as a value that can only be attained in the horizontal or vertical direction if two immediate spectra and an additional spectrum further out belonged to the group.
v. The refitting procedure is only run after the spatial consistency of the centroid position is determined for all the spectra in the dataset.

B J1250-20

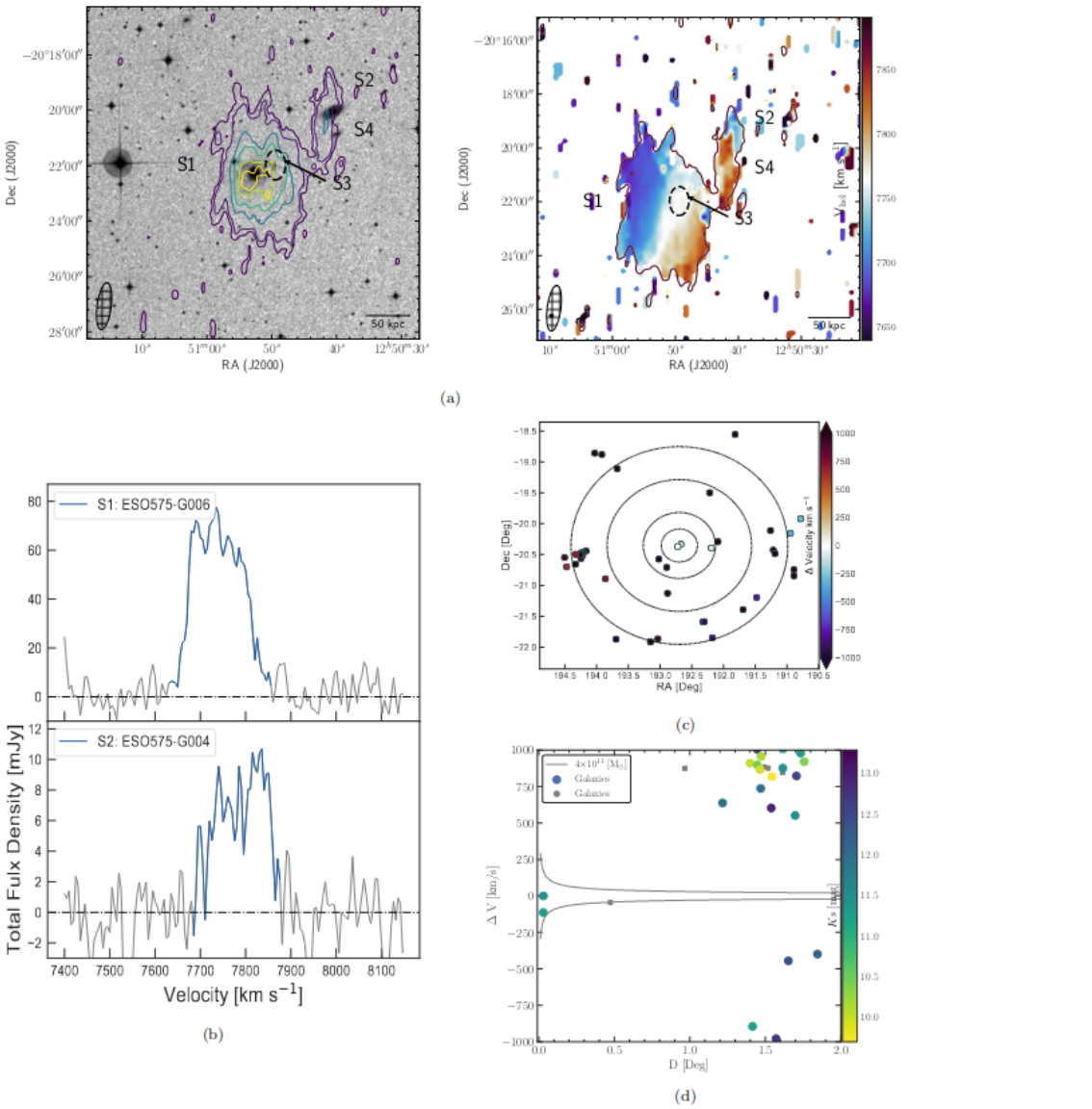

Figure B.1: Figure from D21 Appendix. **a) Left:** The HI emission in the J1250-20 group. The HI emission is shown by the contours overlaid on the optical DSS-B band image. The HI column density contours are 3.5, 7, 20, 30, 40, and 45 $\times 10^{19}$ cm^2. **a) Right:** The velocity field of the J1250-20 group within the limit from 7640 to 7890 kms^{-1}. The group members that are detected in HI within their field of view are marked - S1, S2, S3, and S4. The lowest HI column density contours are shown(3.5×10^{19} cm^2). **b)** Panels of the HI spectra for S1 and S2. The enhanced colour shows where the spectrum was integrated in D21. **c)** The extended field of J1250-20 centred on the weighted mean of the group. The black circles denote the radii of 0.5, 1, 2 and 3 Mpc. The projected separation between S1 and galaxies in a 4° field is shown. **d)** Projected angular separation of the galaxies within the field versus recessional their projected velocity separation with S1. Grey solid curved lines show simple caustics curves for a potential of $4 \times 10^{11} M_{\odot}$, assuming that all sources are at the J1250-20 distance of 114 Mpc.

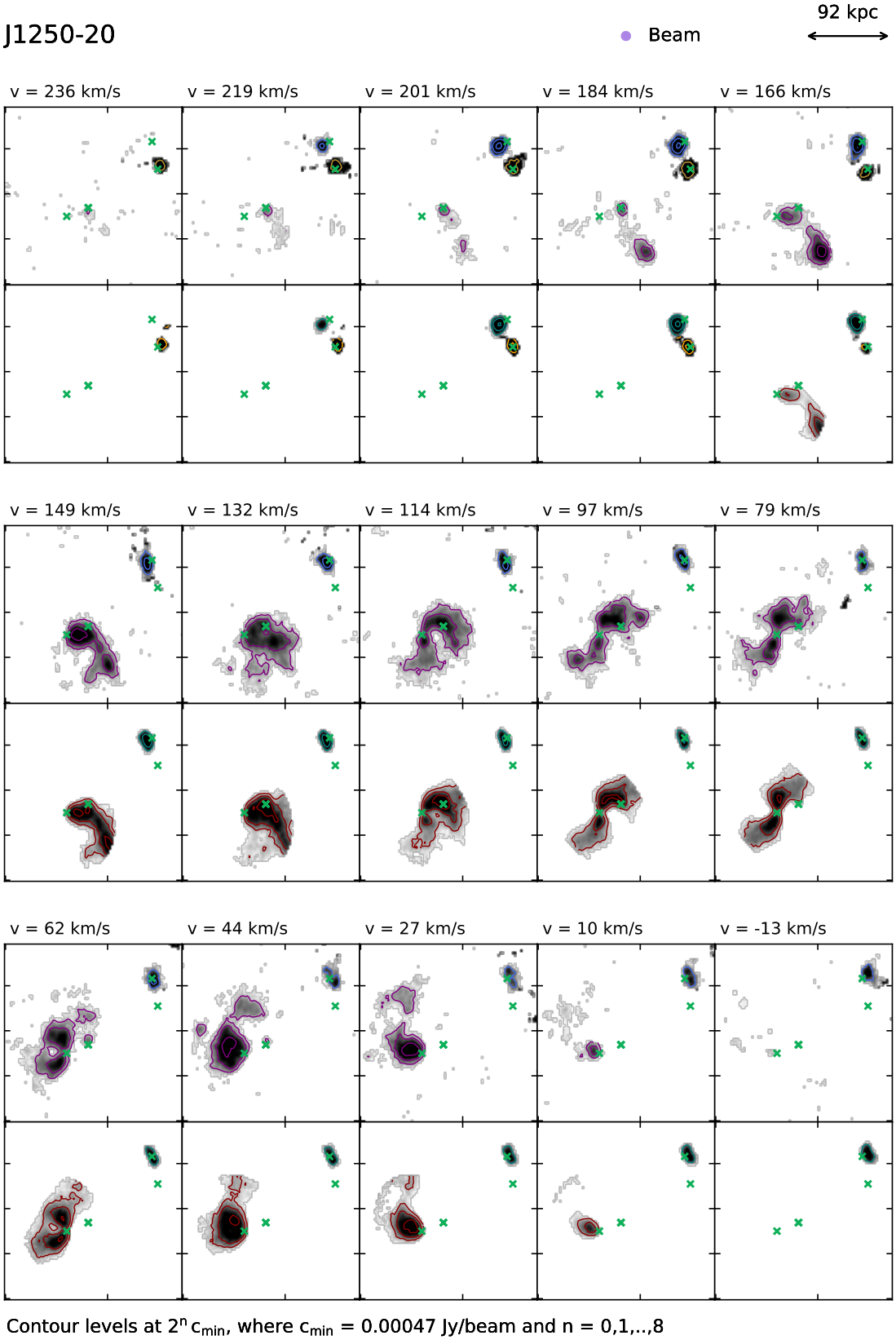

Figure B.2: Channel maps showing the structure of the neutral gas in J1250-20. The bottom panel in each channel show the ^{3D}BAROLO model of S1, S2, and S4. We note anomalous gas emission in the data in regions not modelled as a disc. Due to the close interaction between S1 and S2, for separation, we utilized SlicerAstro to identify the planes without gas above a certain threshold.

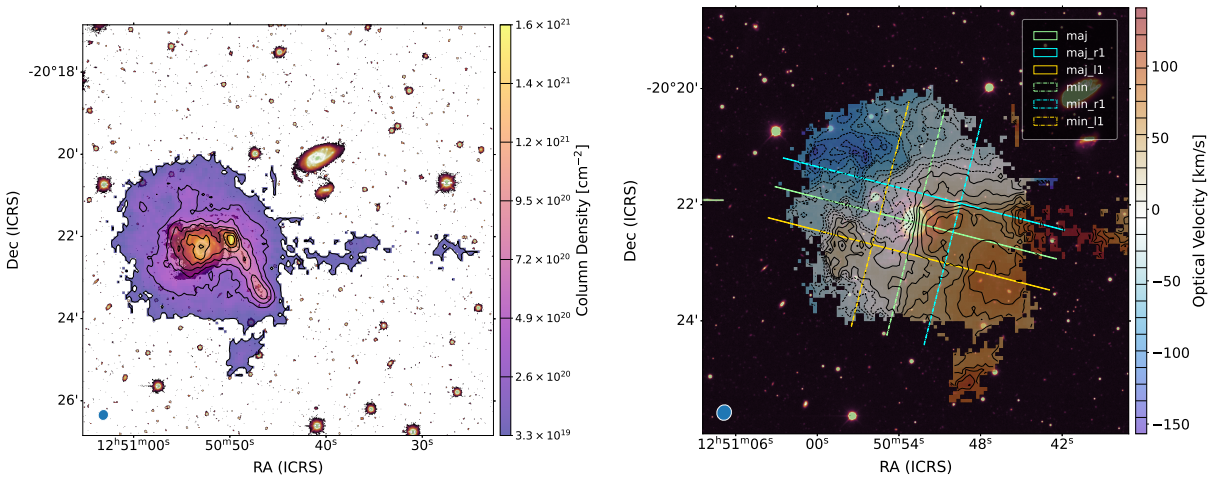

Figure B.3: **Left panel:** Total intensity map of J1250-20:S1 overlaid on DECam g-band image. The contours correspond to the respective column density levels denoted by the colorbar. **Right panel:** Velocity field of J1250-20:S1 overlaid on DECam g-band image. The contours correspond to the difference between the systemic velocity and the line-of-sight velocity. The PV slices extracted along the lines annotated in the plot are shown in figure B.4.

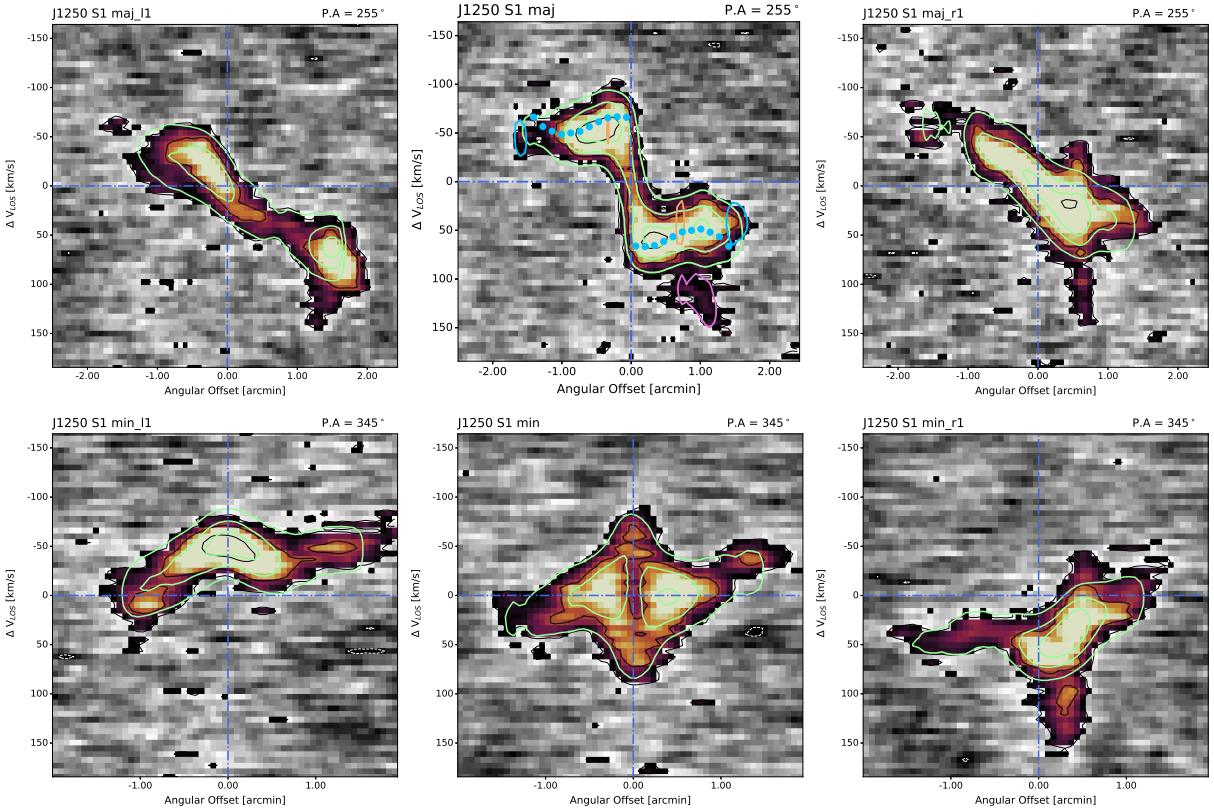

Figure B.4: PV slices of J1250-20:S1 with ^{3D}BAROLO contours of the corresponding model slice overlaid. **Top row:** slices extracted along or parallel to the major axis. *Top left panel:* a slice of the SE side. *Top middle panel:* slice along the major axis. *Top right panel:* a slice of the NW side. **Bottom row:** slices extracted along or parallel to the minor axis. *Bottom left panel:* a slice of the approaching side. *Bottom middle panel:* a slice along the minor axis. *Bottom right panel:* a slice of the receding side.

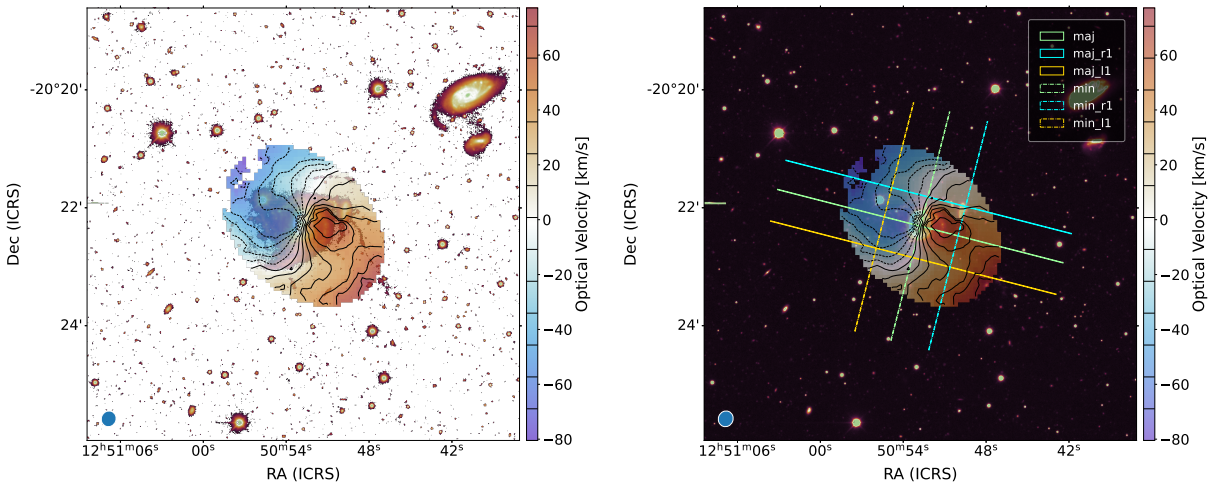

Figure B.5: Same as figure B.3 but for the disc Gaussian model. The PV slices extracted along the lines annotated in the plot are shown in figure B.6.

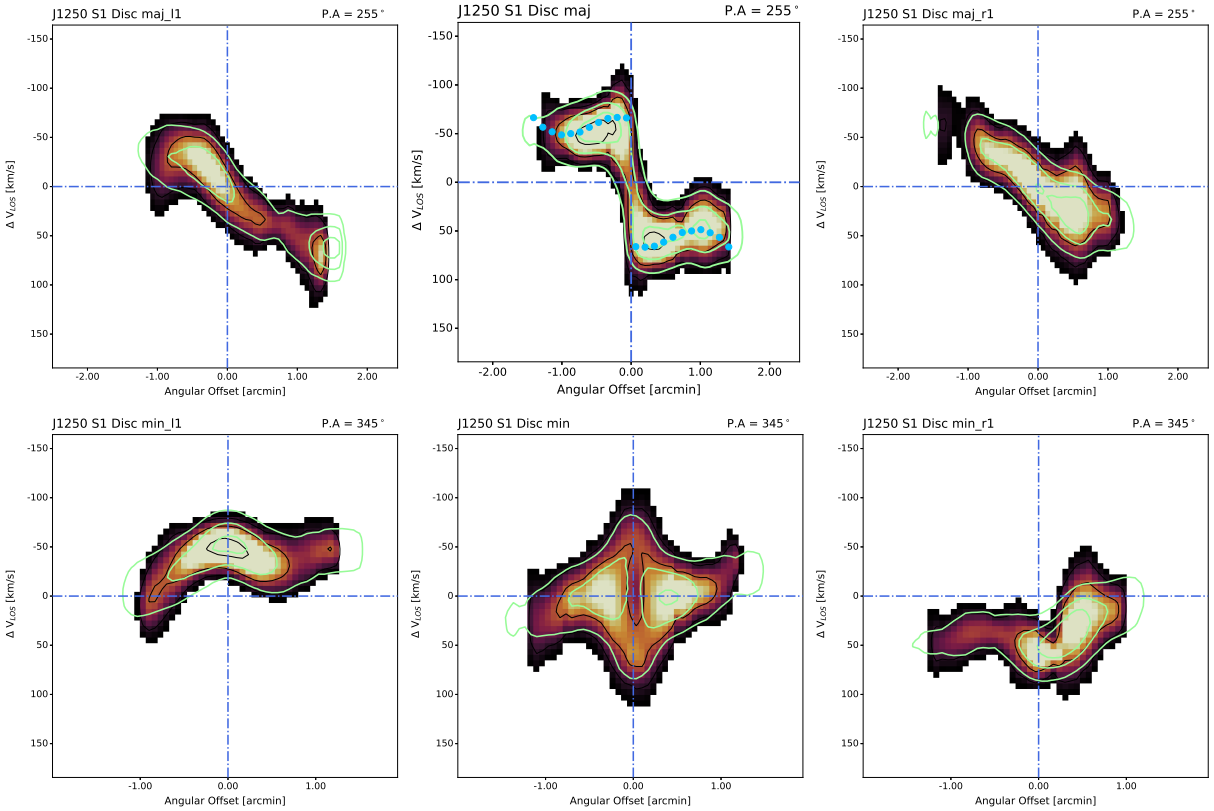

Figure B.6: Same as figure B.4 but for the disc Gaussian model.

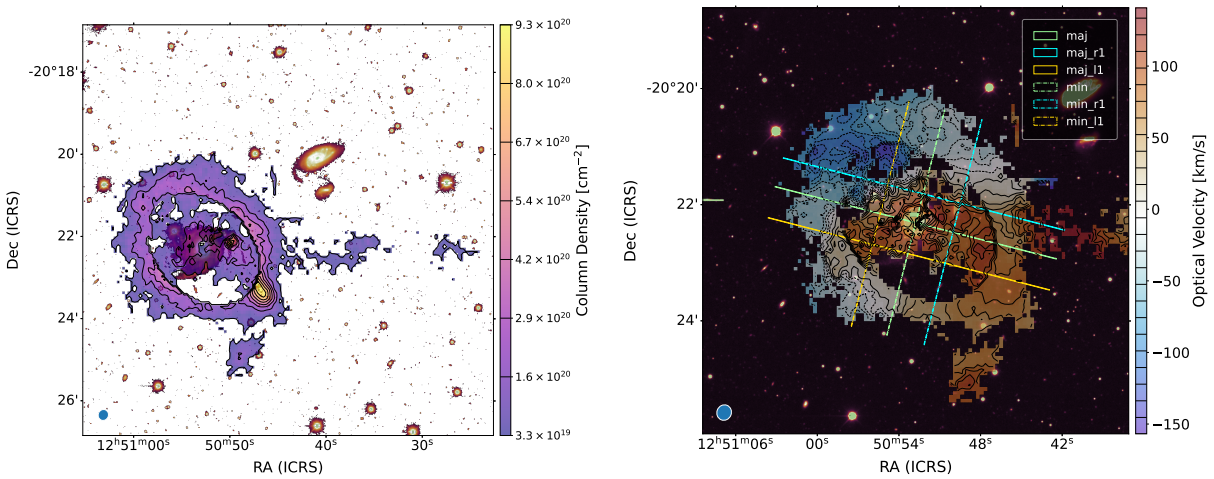

Figure B.7: Same as figure B.3 but for anomalous gas obtained by subtracting the disc Gaussian model from the data. The PV slices extracted along the lines annotated in the plot are shown in figure B.8.

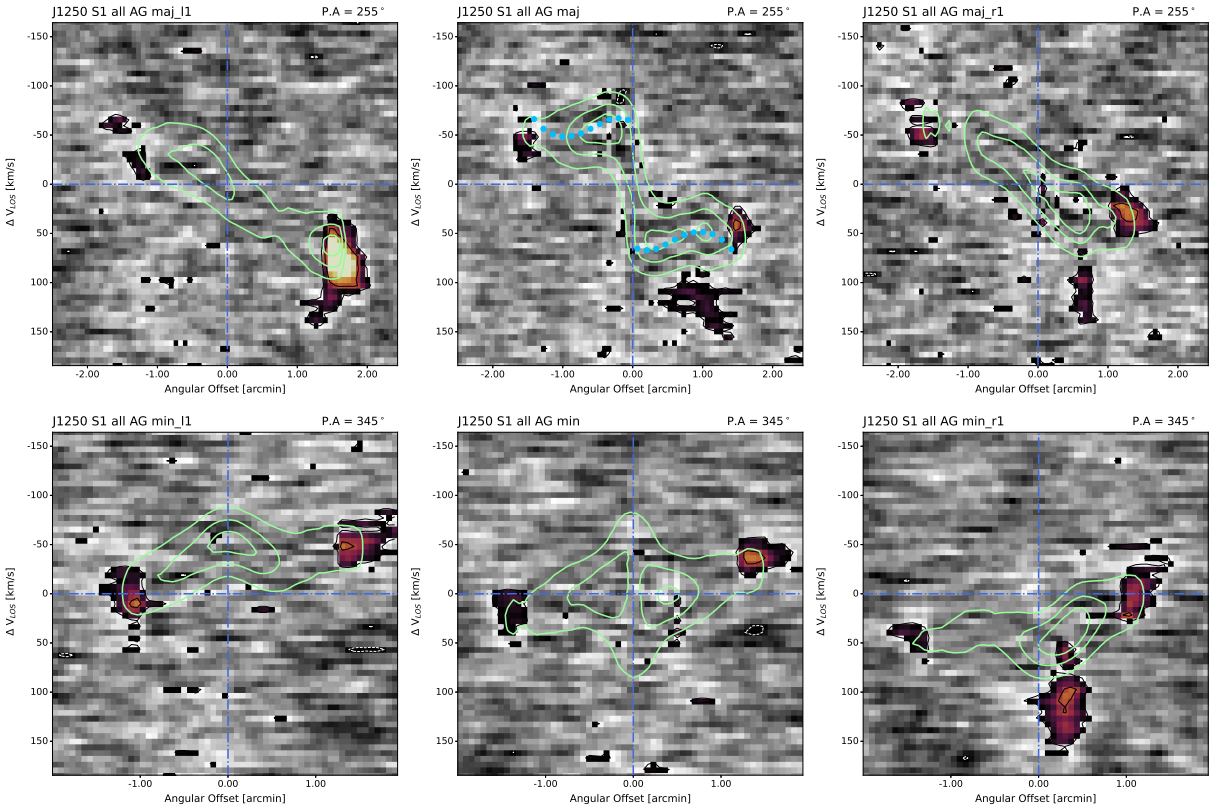

Figure B.8: Same as figure B.4 but for the disc subtracted anomalous gas.

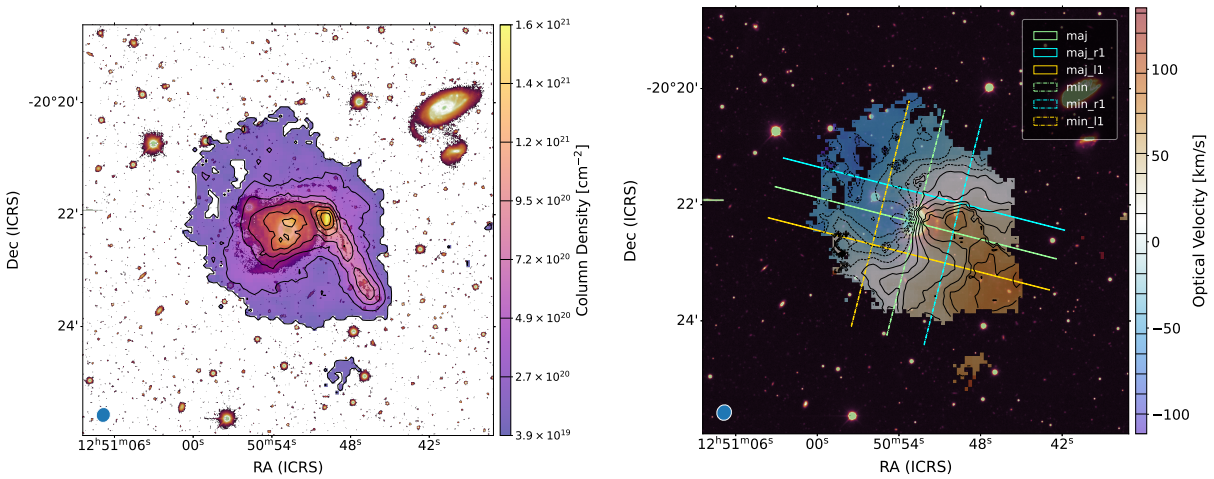

Figure B.9: Same as figure B.3 but for the full Gaussian model. The PV slices extracted along the lines annotated in the plot are shown in figure B.10.

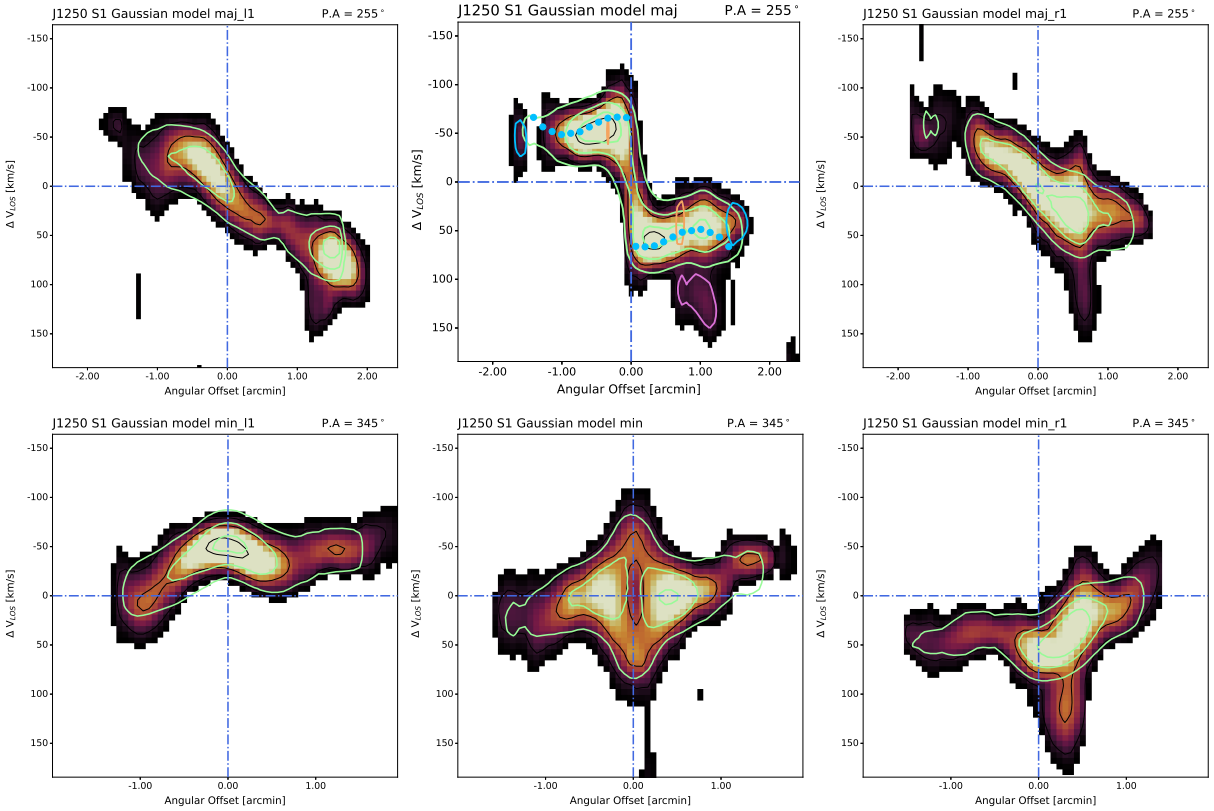

Figure B.10: Same as figure B.4 but for the full Gaussian model.

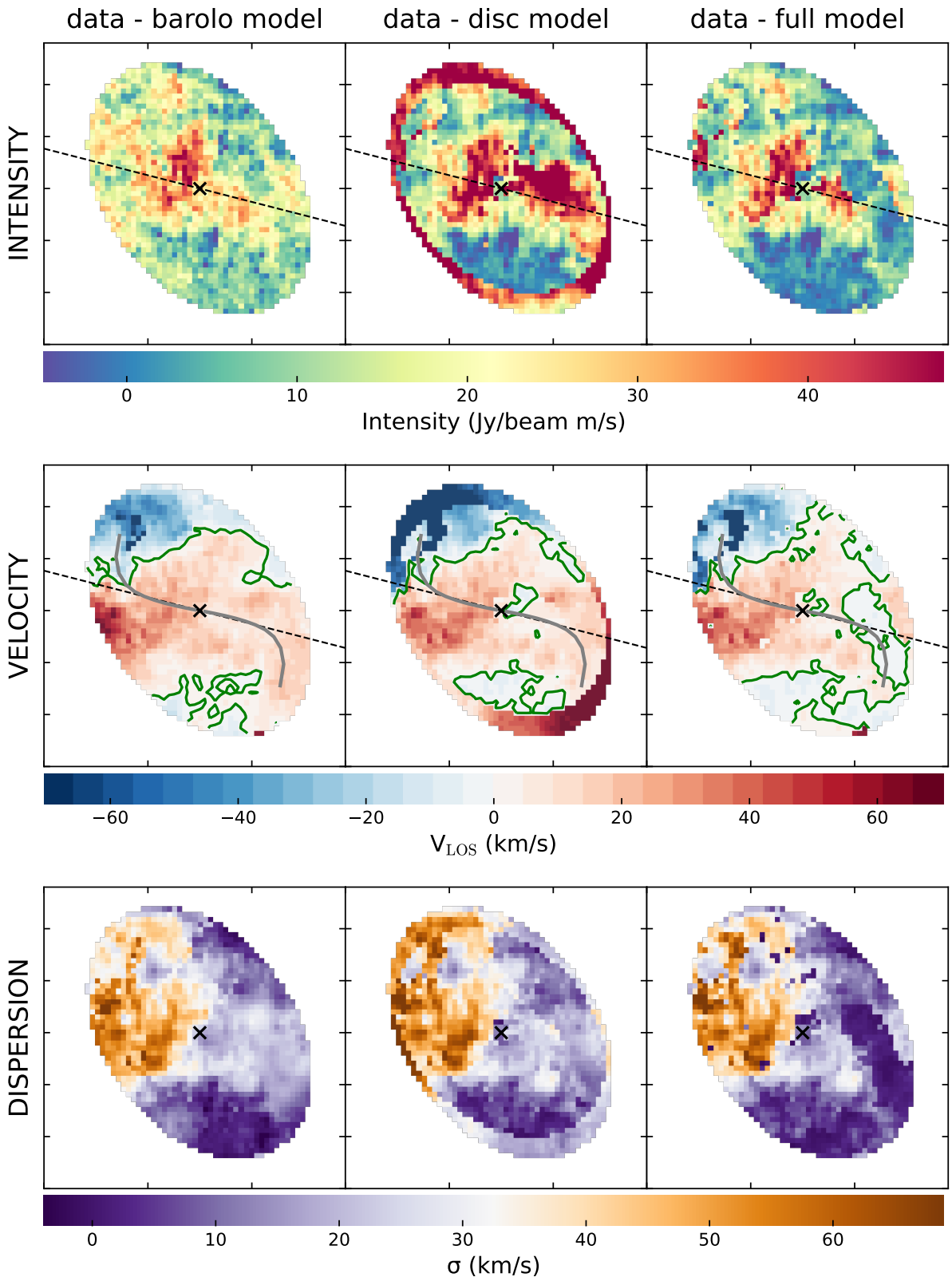

Figure B.11: 2D residual maps for intensity (first row), velocity field (second row), and dispersion (third row) of J1250-20:S1. 2D maps of the ^{3D}BAROLO model (first column), disc Gaussian model (second column), and multi-component Gaussian model (third column) are subtracted from the maps of the elliptical masked disc data. The 'x' denotes the centre and the dashed line denotes the P.A. obtained from tilted ring modelling. The green contour in the first moment demarcates the $0\,\mathrm{km\,s^{-1}}$ line at the systemic recession velocity.

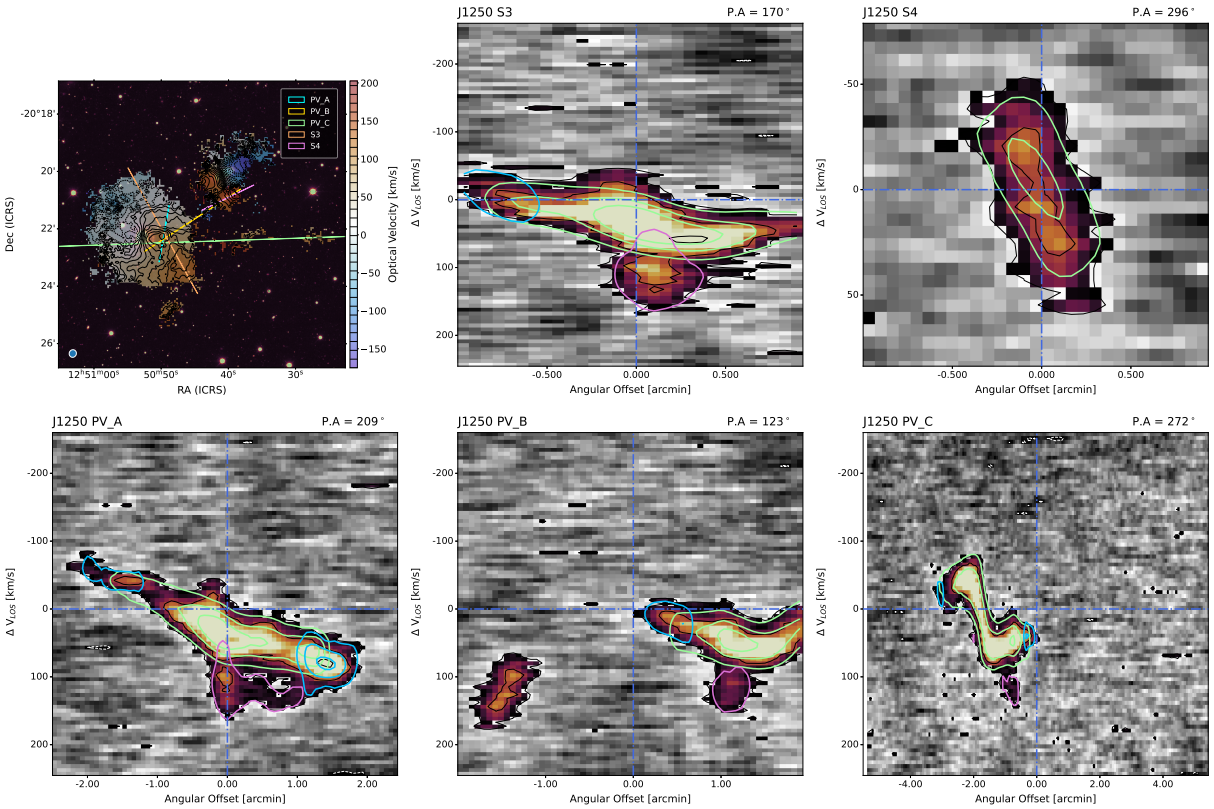

Figure B.12: *First panel:* Velocity field of J1250-20 overlaid on DECam g-band image. The lines along which the subsequent PV slices were extracted are also annotated. *Second panel:* The major axis PV of Mkt5 with ^{3D}BAROLO model contours and rings defined for tilted ring modelling overlaid. *Panels 3-5 (left to right):* PV slices of the western tails.

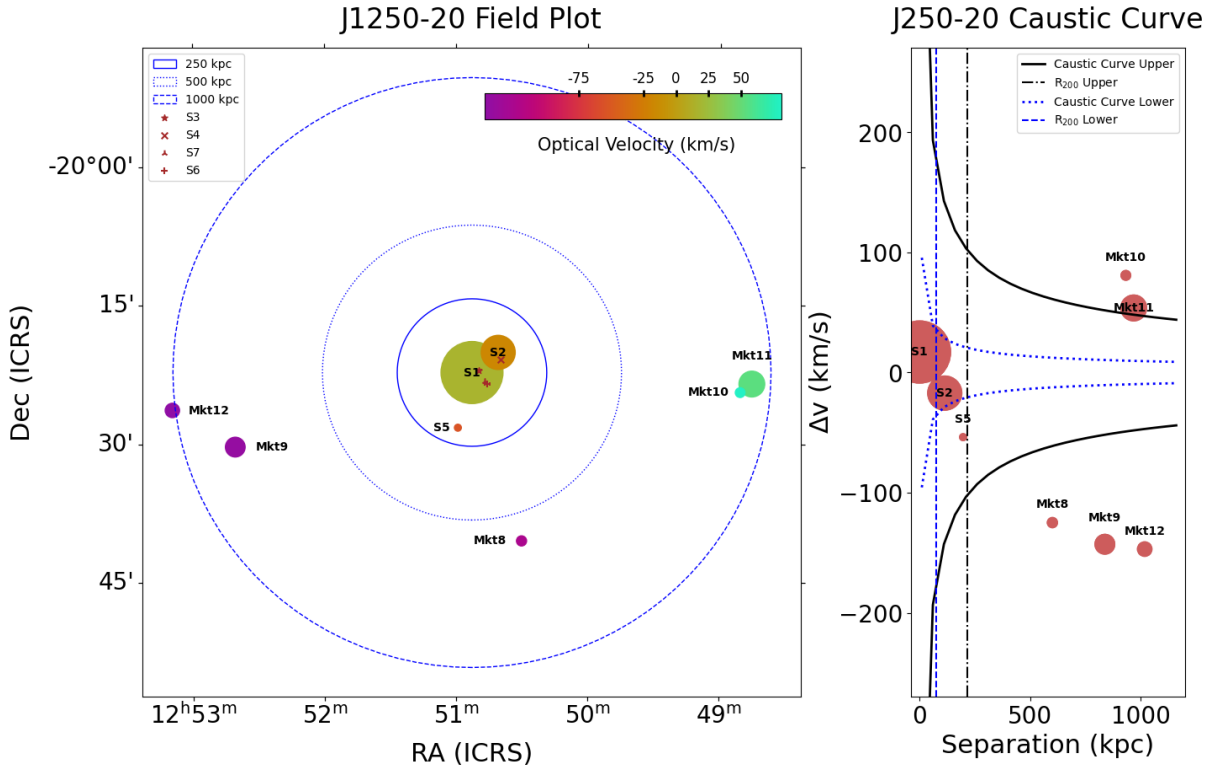

Figure B.13: Plots describing field of J1250-20. The markers are scaled by the HI masses. **Left panel:** the blue circles show projected separation from the centre at 250 kpc, 500 kpc and 1 Mpc respectively. The positions of dwarf galaxies that are interacting S1 & S2 are also indicated. **Right panel:** simple caustic curve and the positions of the galaxies in the field with respect to their projected separation from S1. V_{sys} is assumed to be the average of S1's and S2's systemic velocities.

C J1403-06

C.1 J1403-06:S1

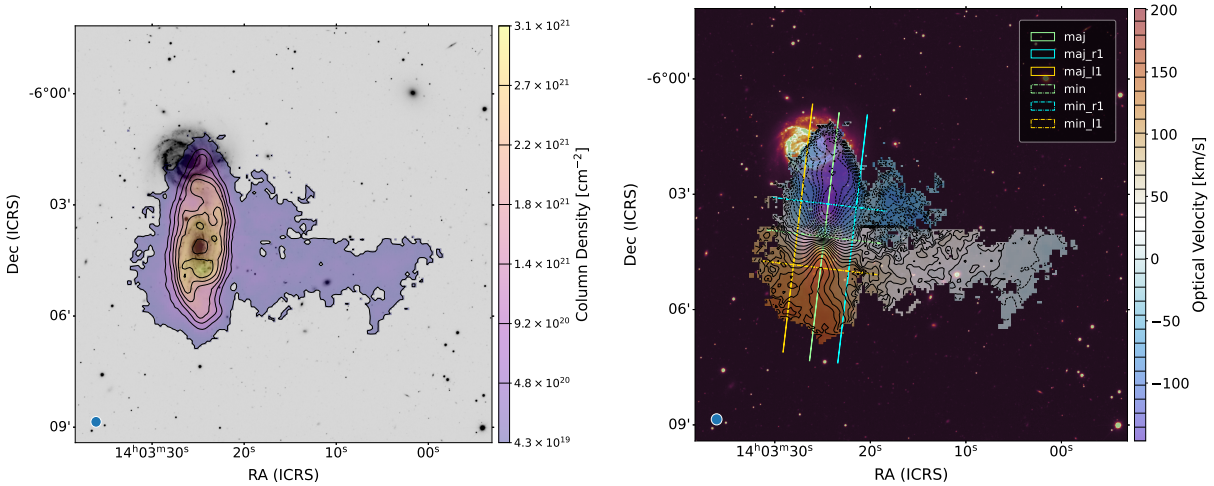

Figure C.14: **Left panel:** Total intensity map of J1403-06:S1 overlaid on DECam g-band image. The contours correspond to the respective column density levels denoted by the colorbar. **Right panel:** Velocity field map of S1 overlaid on DECam g-band image. The contours correspond to the difference between the systemic velocity and the line-of-sight velocity. The PV slices extracted along the lines annotated in the plot are shown in figure C.15.

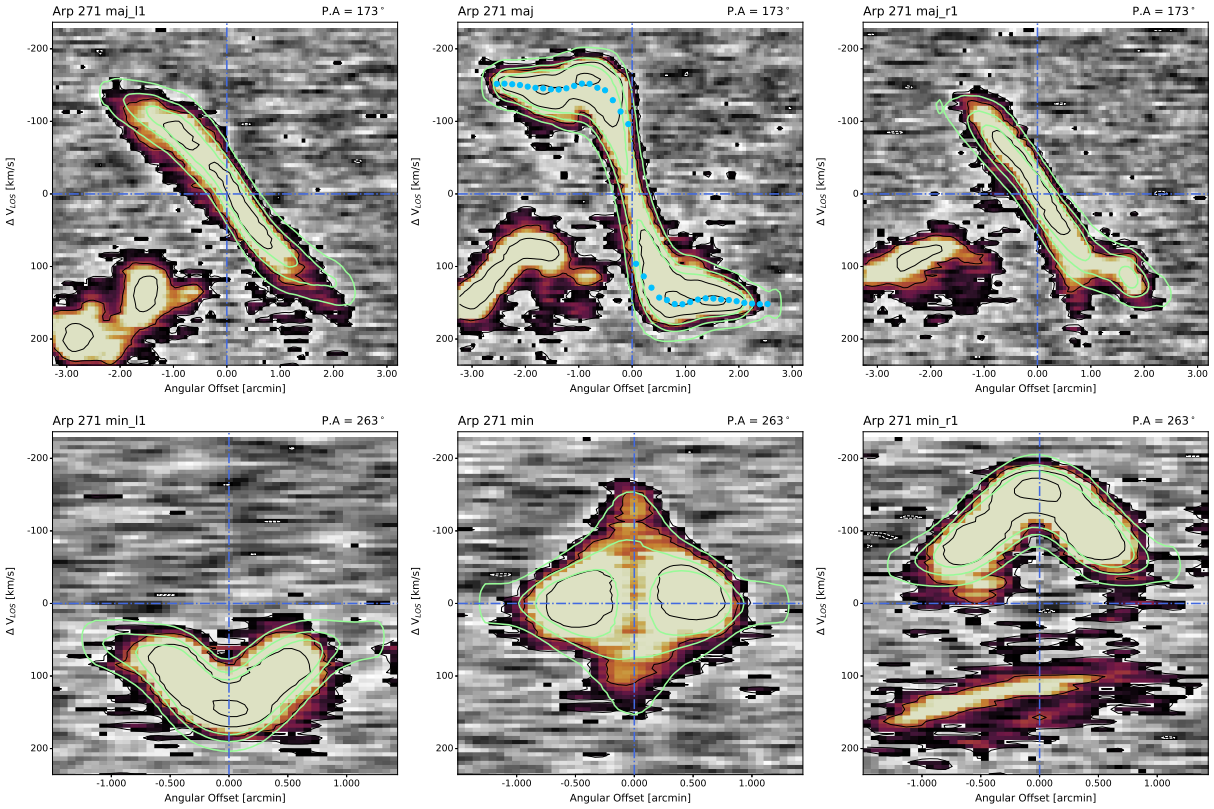

Figure C.15: PV slices of J1403-06:S1 with ^{3D}BAROLO contours of the corresponding model slice overlaid. **Top row:** slices extracted along or parallel to the major axis. *Top left panel:* a slice of the far side. *Top middle panel:* slice along the major axis. *Top right panel:* a slice of the near side. **Bottom row:** slices extracted along or parallel to the minor axis. *Bottom left panel:* a slice of the receding side. *Bottom middle panel:* a slice along the minor axis. *Bottom right panel:* a slice of the approaching side.

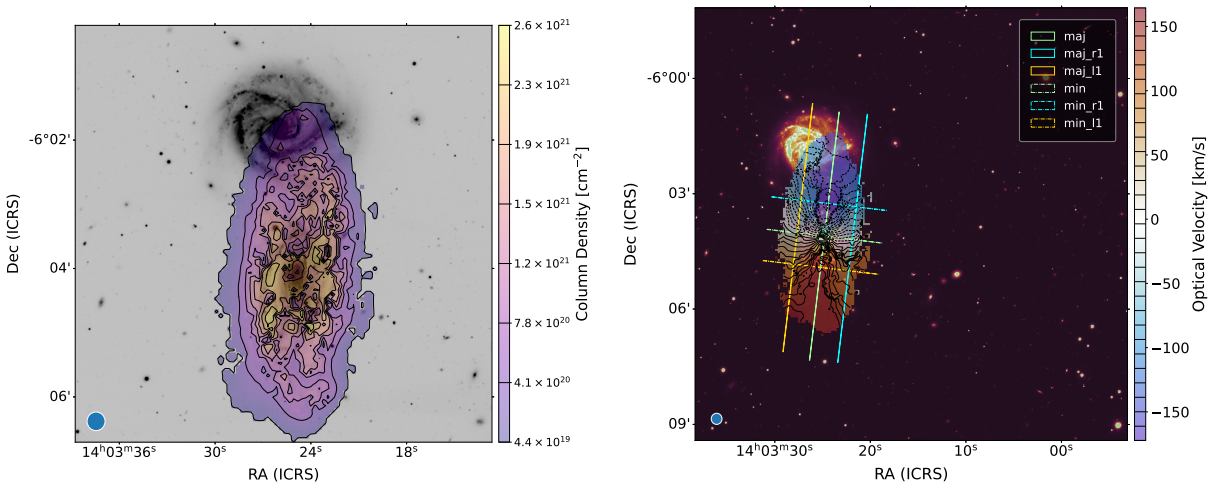

Figure C.16: Same as figure C.14 but for the disc Gaussian model. The PV slices extracted along the lines annotated in the plot are shown in figure C.17.

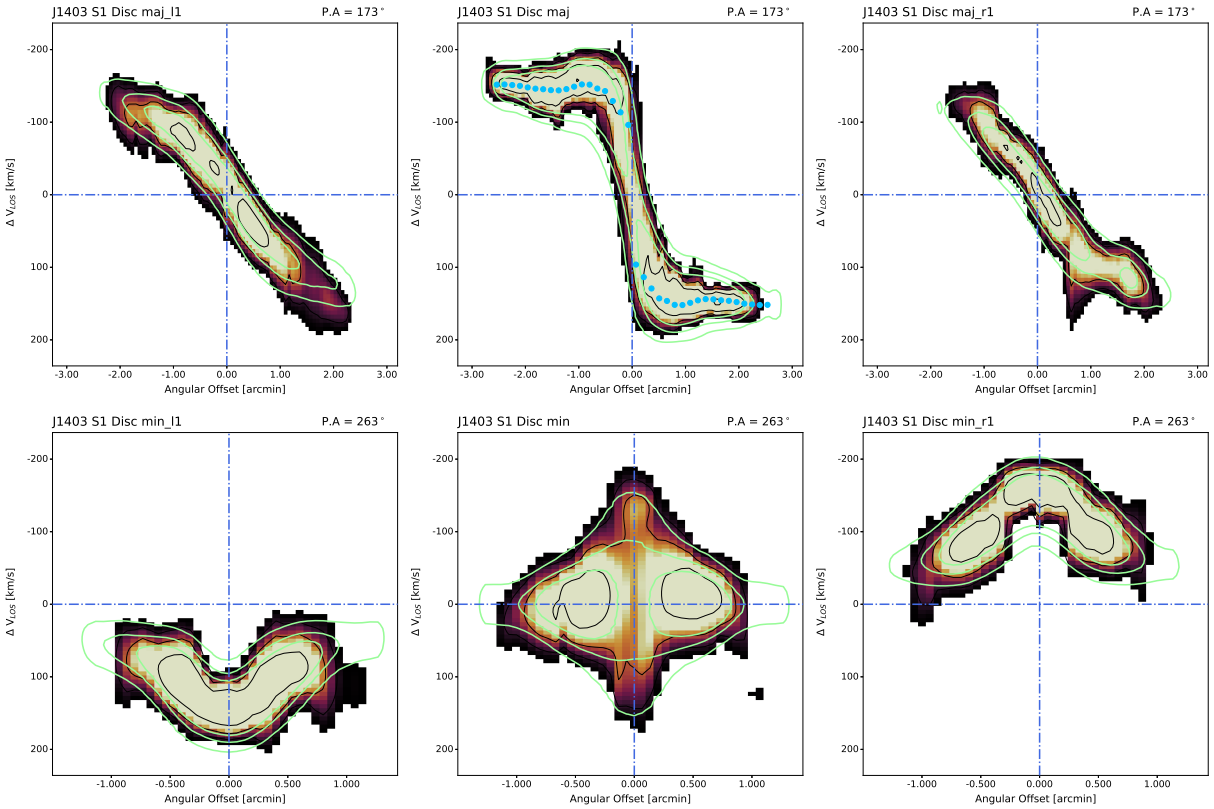

Figure C.17: Same as figure C.15 but for the disc Gaussian model.

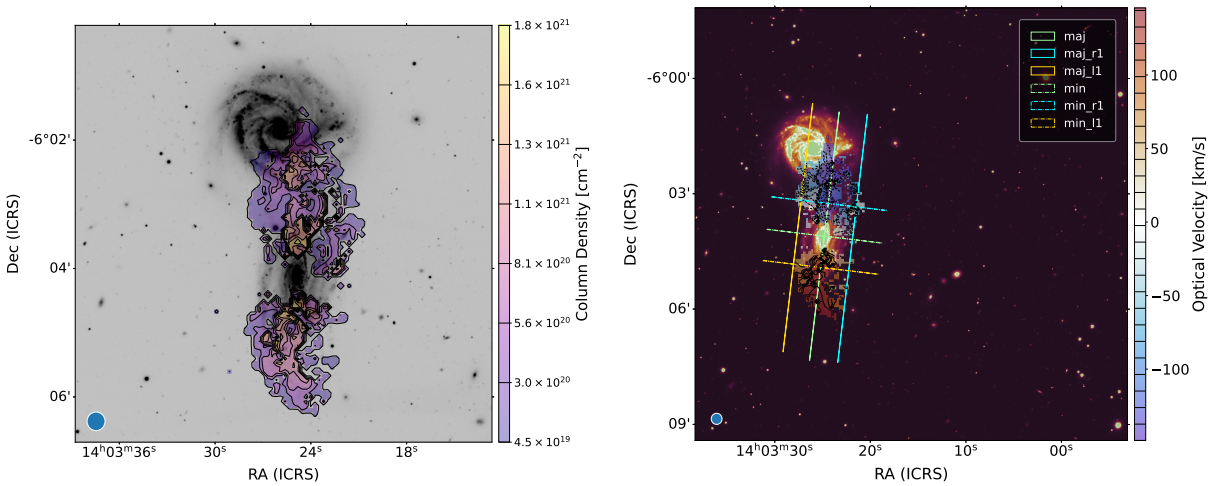

Figure C.18: Same as figure C.14 but for the EPG Gaussian model. The PV slices extracted along the lines annotated in the plot are shown in figure C.19.

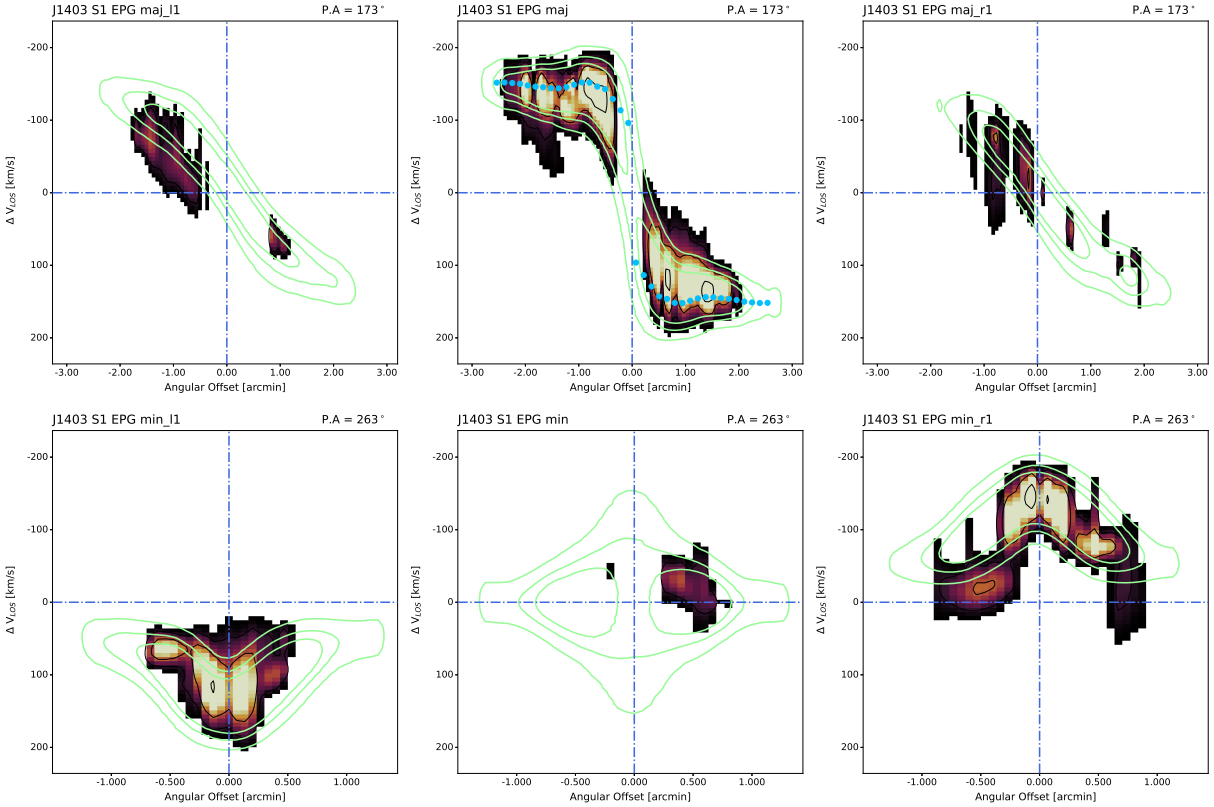

Figure C.19: Same as figure C.15 but for the EPG model.

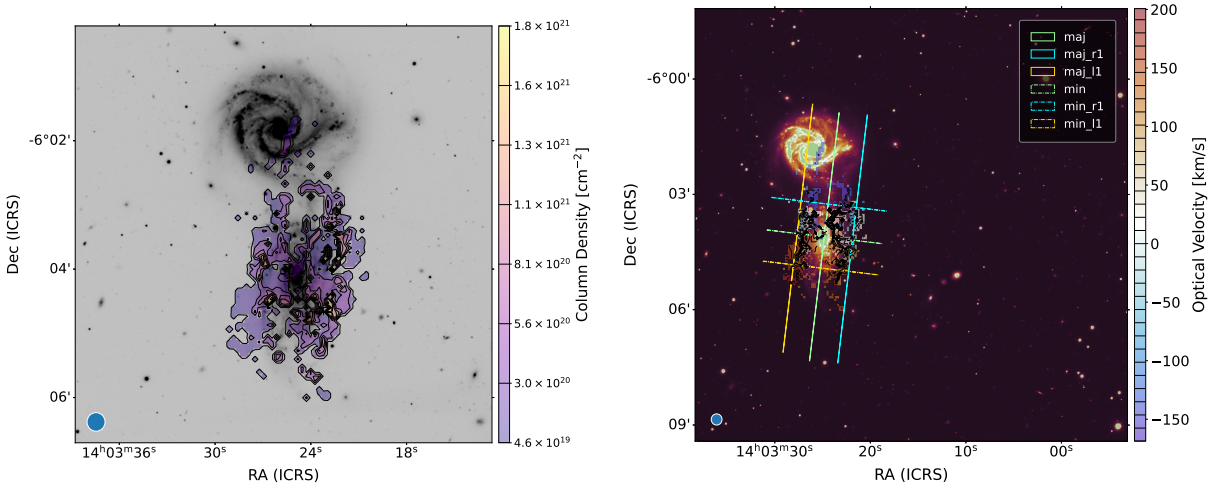

Figure C.20: Same as figure C.14 but for the leading Gaussian component model (FC). The PV slices extracted along the lines annotated in the plot are shown in figure C.21.

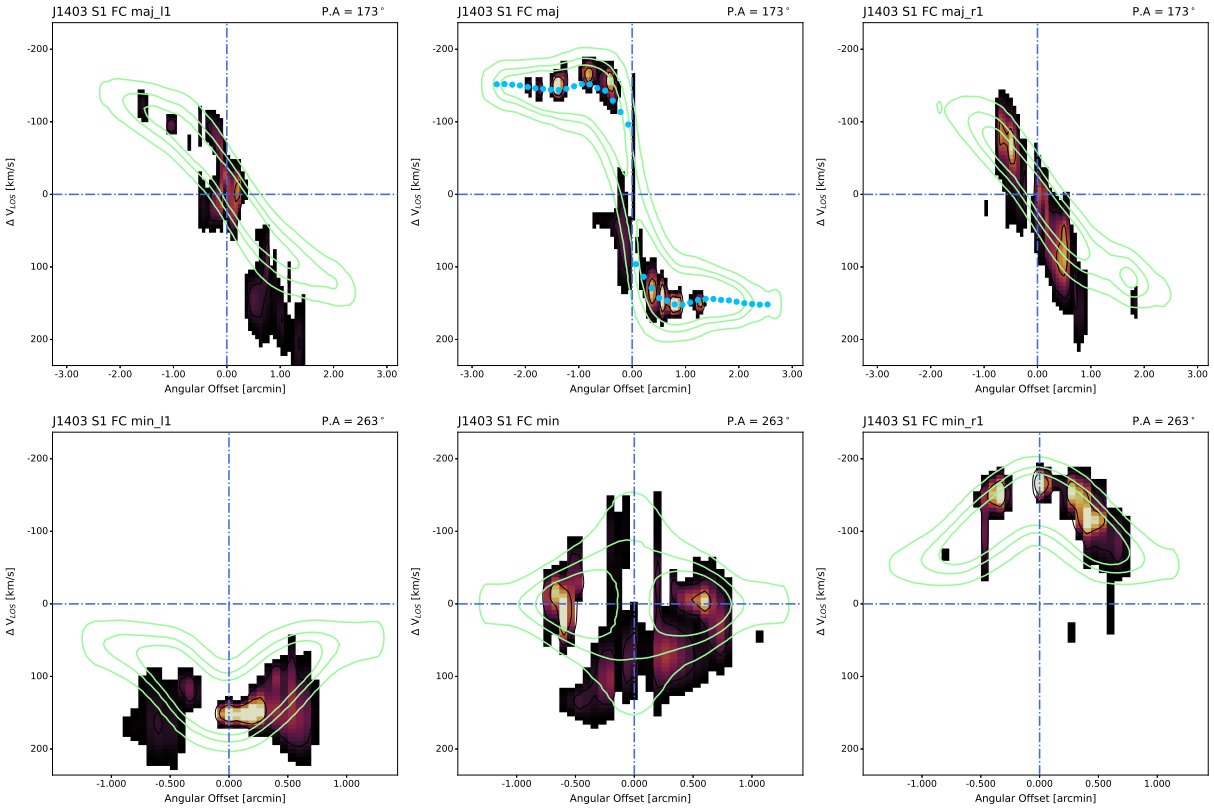

Figure C.21: Same as figure C.15 but for the leading Gaussian component model (FC).

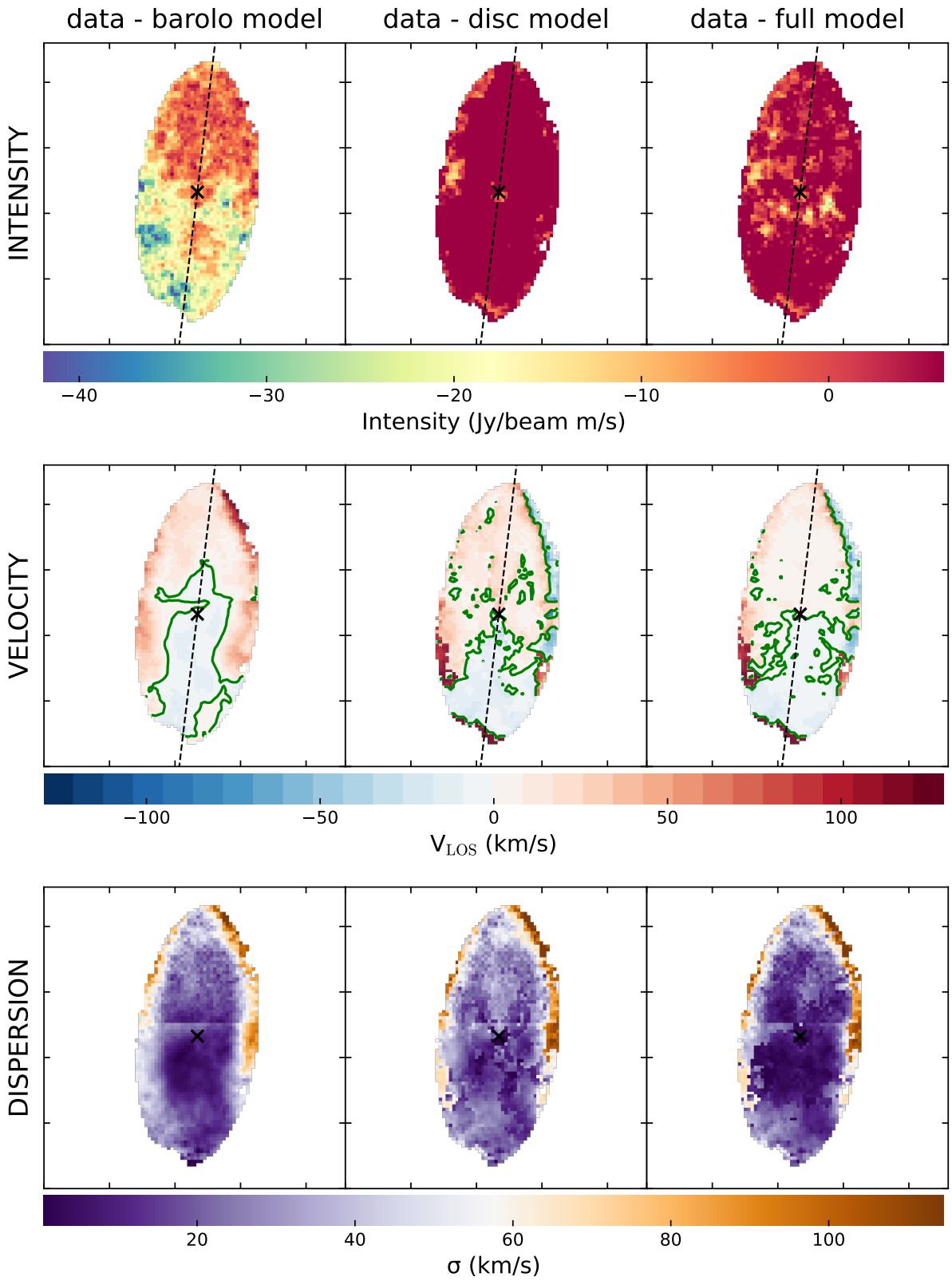

Figure C.22: 2D residual maps for intensity (first row), velocity field (second row), and dispersion (third row) of J1403-06:S1. 2D maps of the ^{3D}BAROLO model (first column), disc Gaussian model (second column), and multi-component Gaussian model (third column) are subtracted from the maps of the elliptical masked disc data. The 'x' denotes the centre and the dashed line denotes the P.A. obtained from tilted ring modelling. The green contour in the first moment demarcates the $0\,\mathrm{km\,s^{-1}}$ line at the systemic recession velocity.

C.2 J1403-06:S2

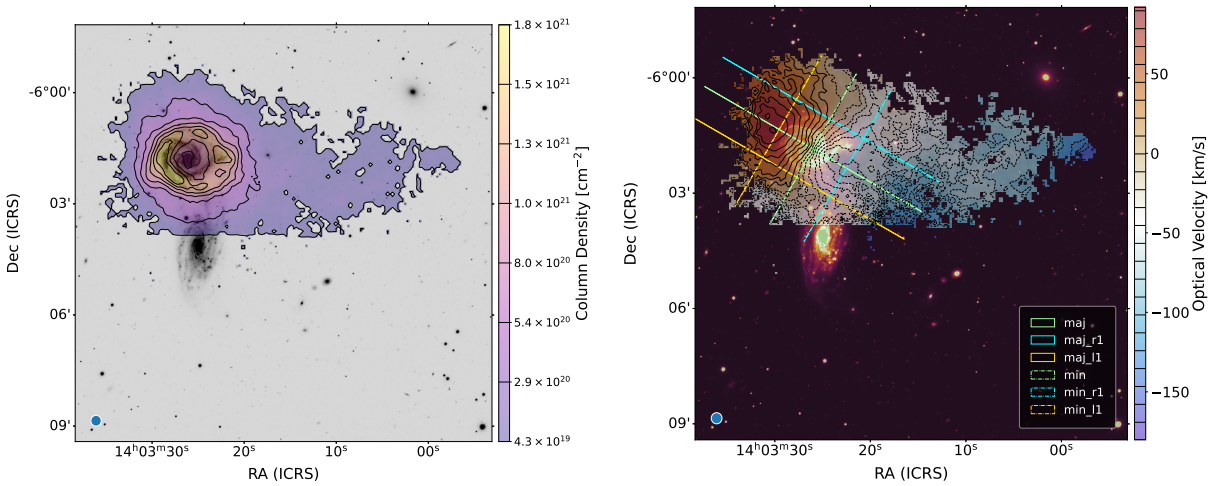

Figure C.23: **Left panel:** Total intensity map of J1403-06:S2 overlaid on DECam g-band image. The contours correspond to the respective column density levels denoted by the colorbar. **Right panel:** Velocity field map of S2 overlaid on DECam g-band image. The contours correspond to the difference between the systemic velocity and the line-of-sight velocity. The PV slices extracted along the lines annotated in the plot are shown in figure C.24.

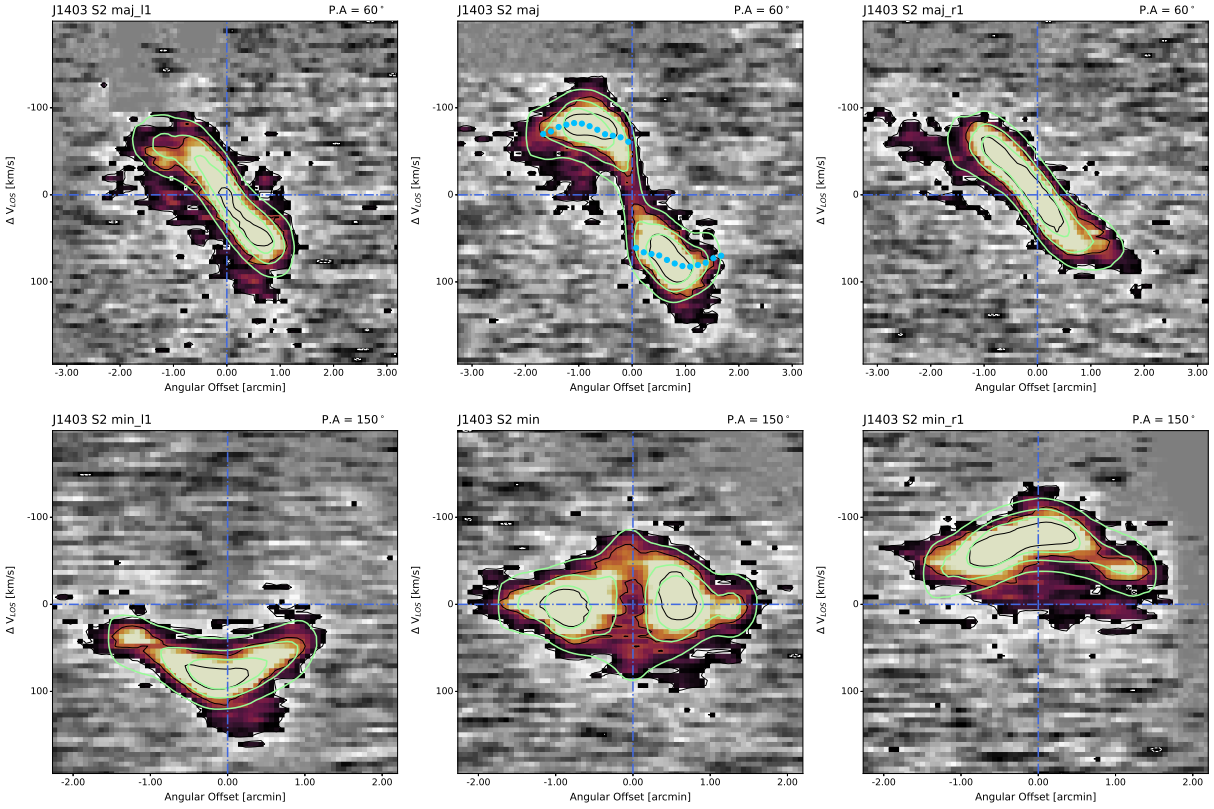

Figure C.24: PV slices of J1403-06:S2 with ^{3D}BAROLO contours of the corresponding model slice overlaid. **Top row:** slices extracted along or parallel to the major axis. *Top left panel:* a slice of the near side. *Top middle panel:* slice along the major axis. *Top right panel:* a slice of the far side. **Bottom row:** slices extracted along or parallel to the minor axis. *Bottom left panel:* a slice of the receding side. *Bottom middle panel:* a slice along the minor axis. *Bottom right panel:* a slice of the approaching side.

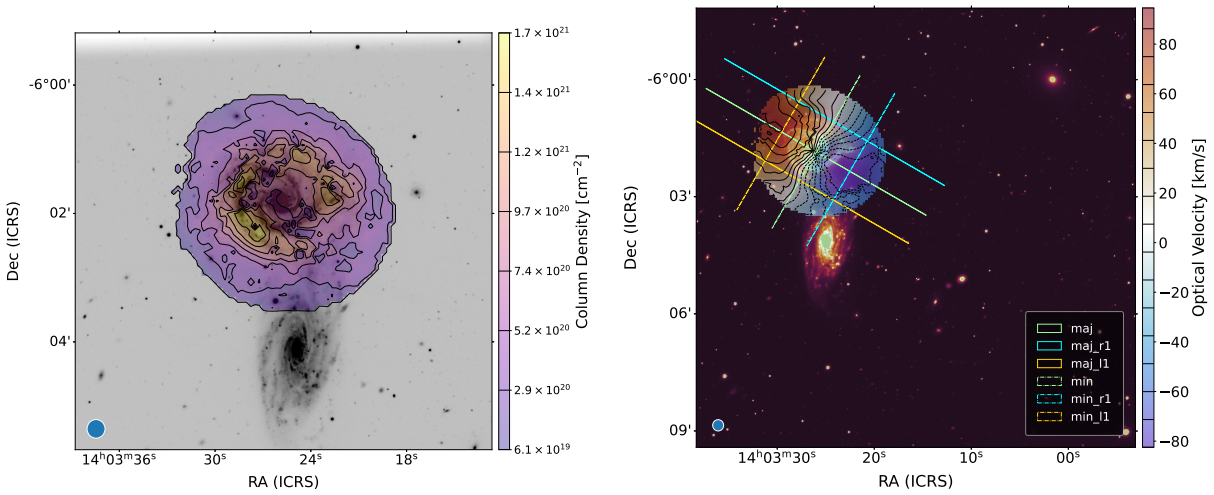

Figure C.25: Same as figure C.23 but for the disc Gaussian model. The PV slices extracted along the lines annotated in the plot are shown in figure C.26.

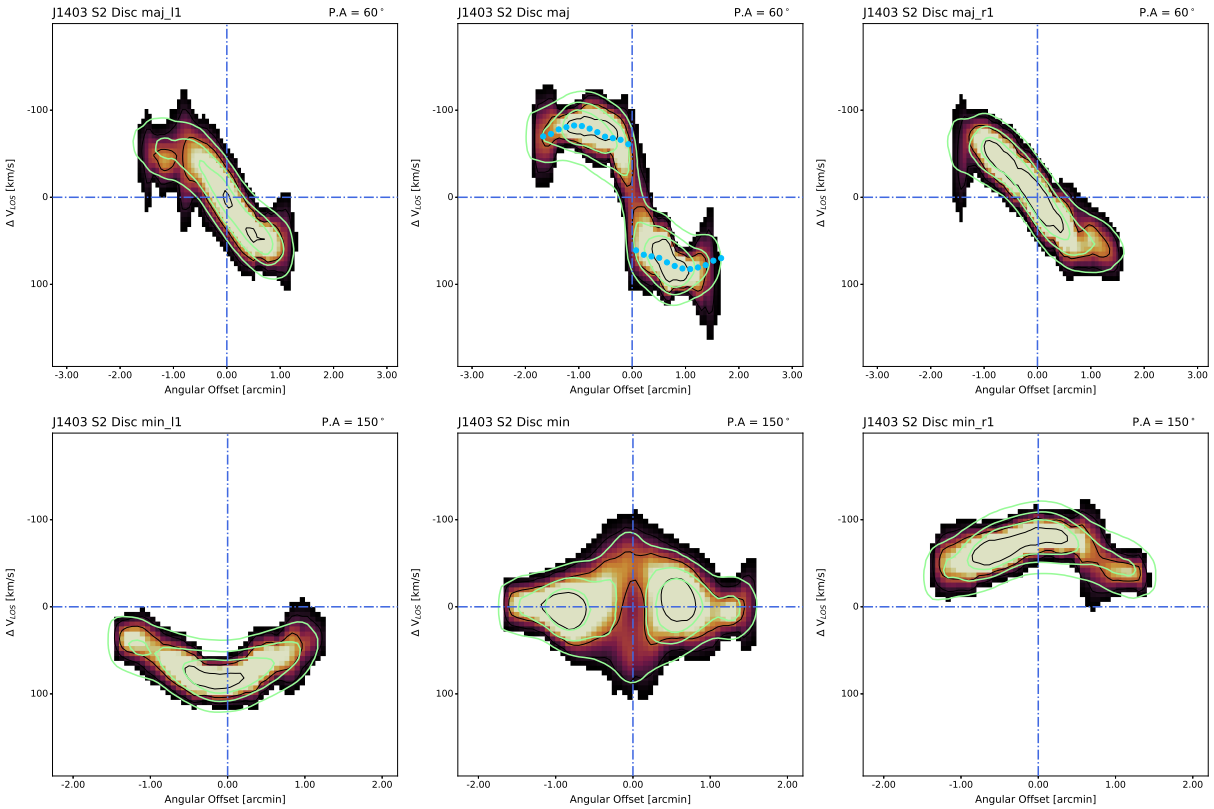

Figure C.26: Same as figure C.24 but for the disc Gaussian model.

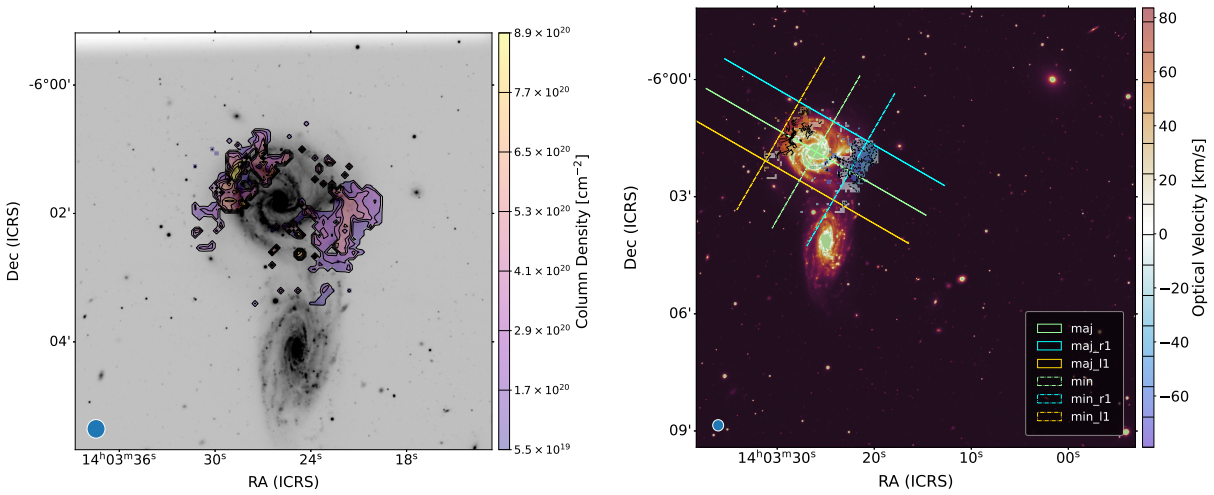

Figure C.27: Same as figure C.23 but for the EPG Gaussian model. The PV slices extracted along the lines annotated in the plot are shown in figure C.28.

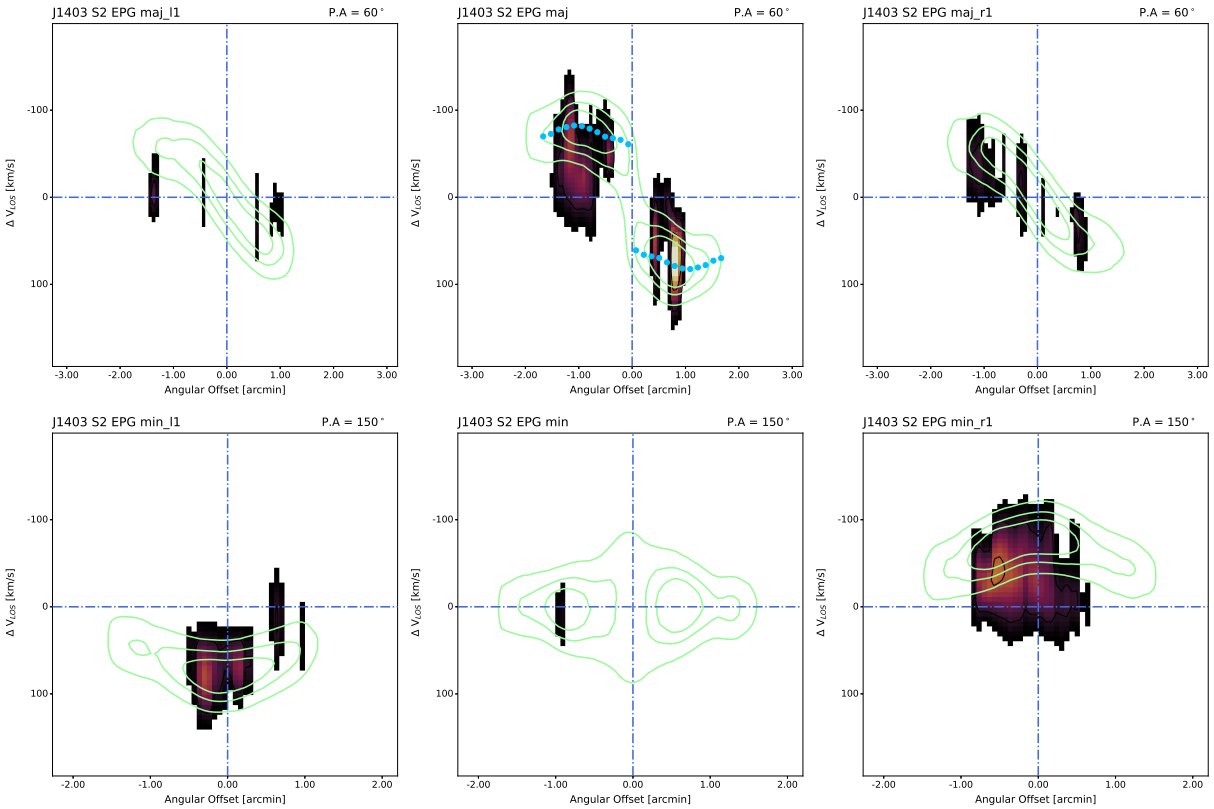

Figure C.28: Same as figure C.24 but for the EPG Gaussian model.

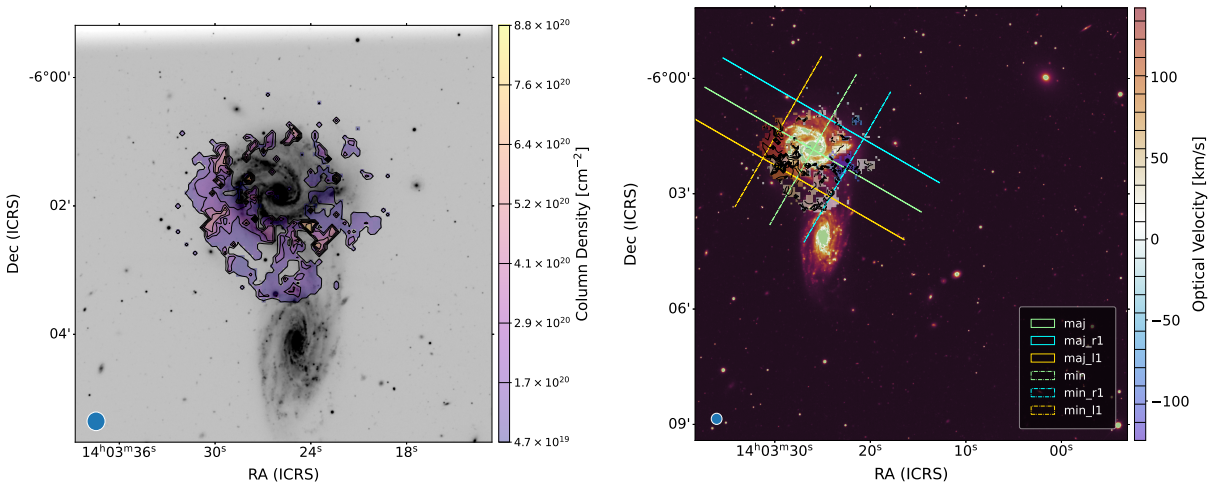

Figure C.29: Same as figure C.23 but for the leading Gaussian component model (FC). The PV slices extracted along the lines annotated in the plot are shown in figure C.30.

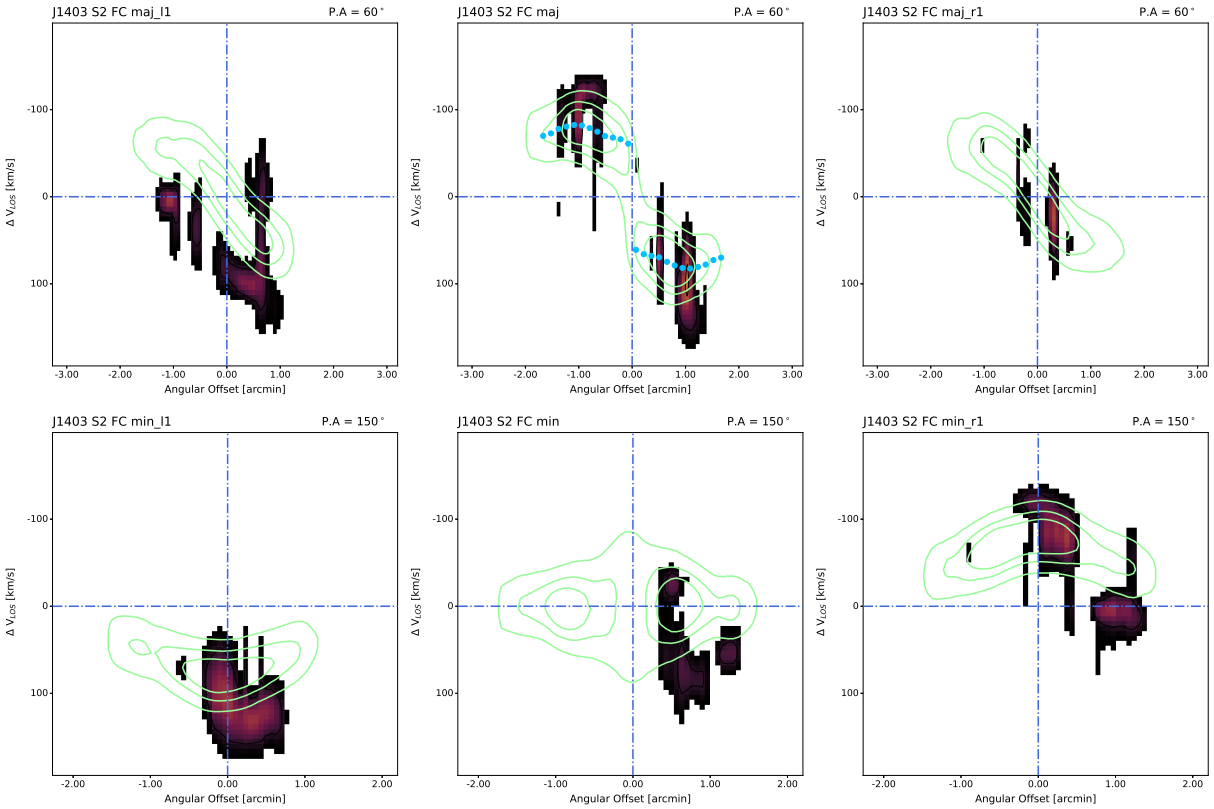

Figure C.30: Same as figure C.24 but for the leading Gaussian component model (FC).

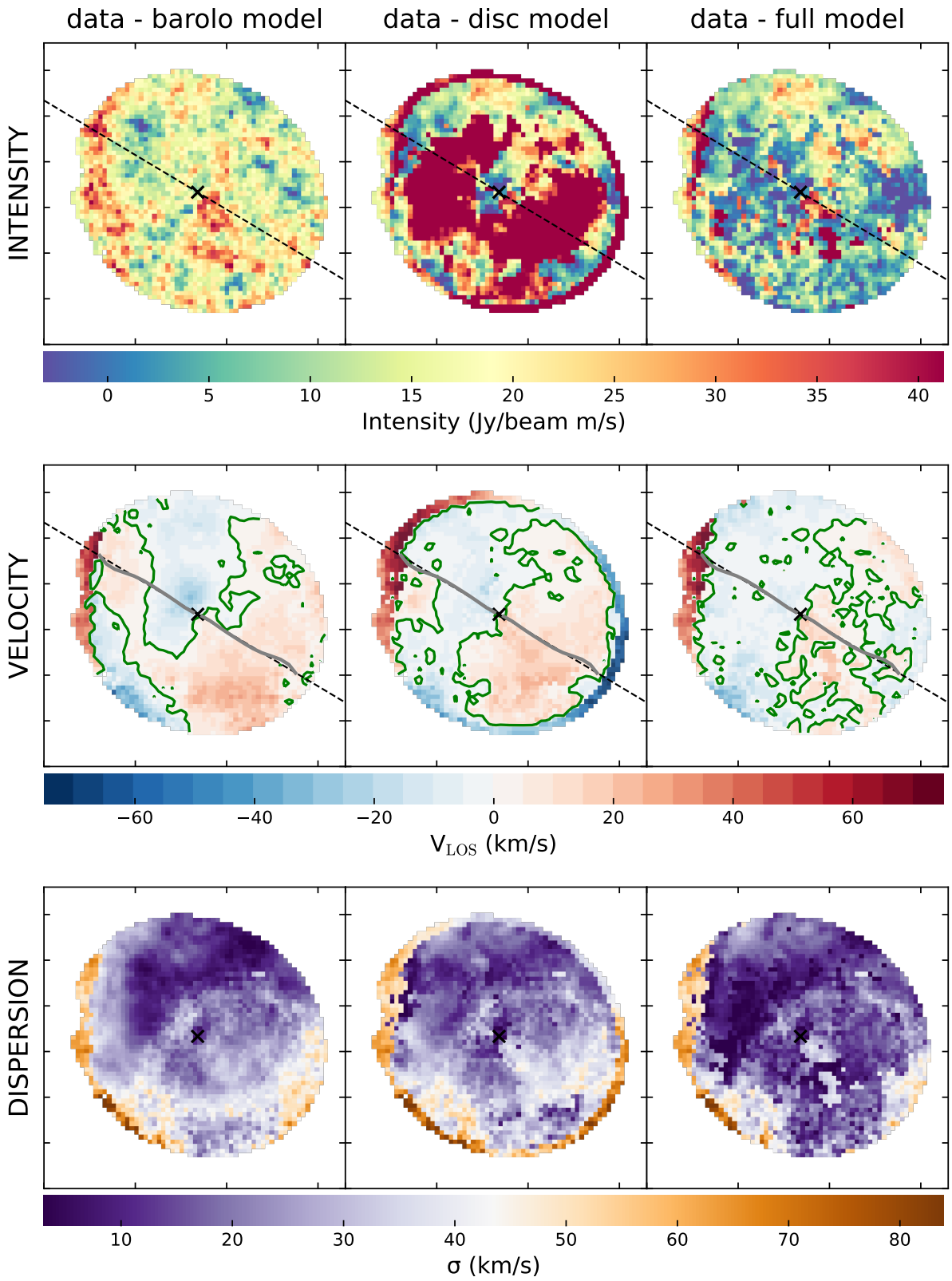

Figure C.31: 2D residual maps for intensity (first row), velocity field (second row), and dispersion (third row) of J1403-06:S2. 2D maps of the ^{3D}BAROLO model (first column), disc Gaussian model (second column), and multi-component Gaussian model (third column) are subtracted from the maps of the elliptical masked disc data. The 'x' denotes the centre and the dashed line denotes the P.A. obtained from tilted ring modelling. The green contour in the first moment demarcates the $0\,\mathrm{km\,s^{-1}}$ line at the systemic recession velocity.